UiT
THE ARCTIC
UNIVERSITY
OF NORWAY

Department of Geology

Basin analysis and diagenetic investigations of Early and Middle Triassic sediments on Mariaholmen, Svalbard

—

Henrik Erevik Riise

GEO-3900 Master's thesis in Geology – Spring 2016

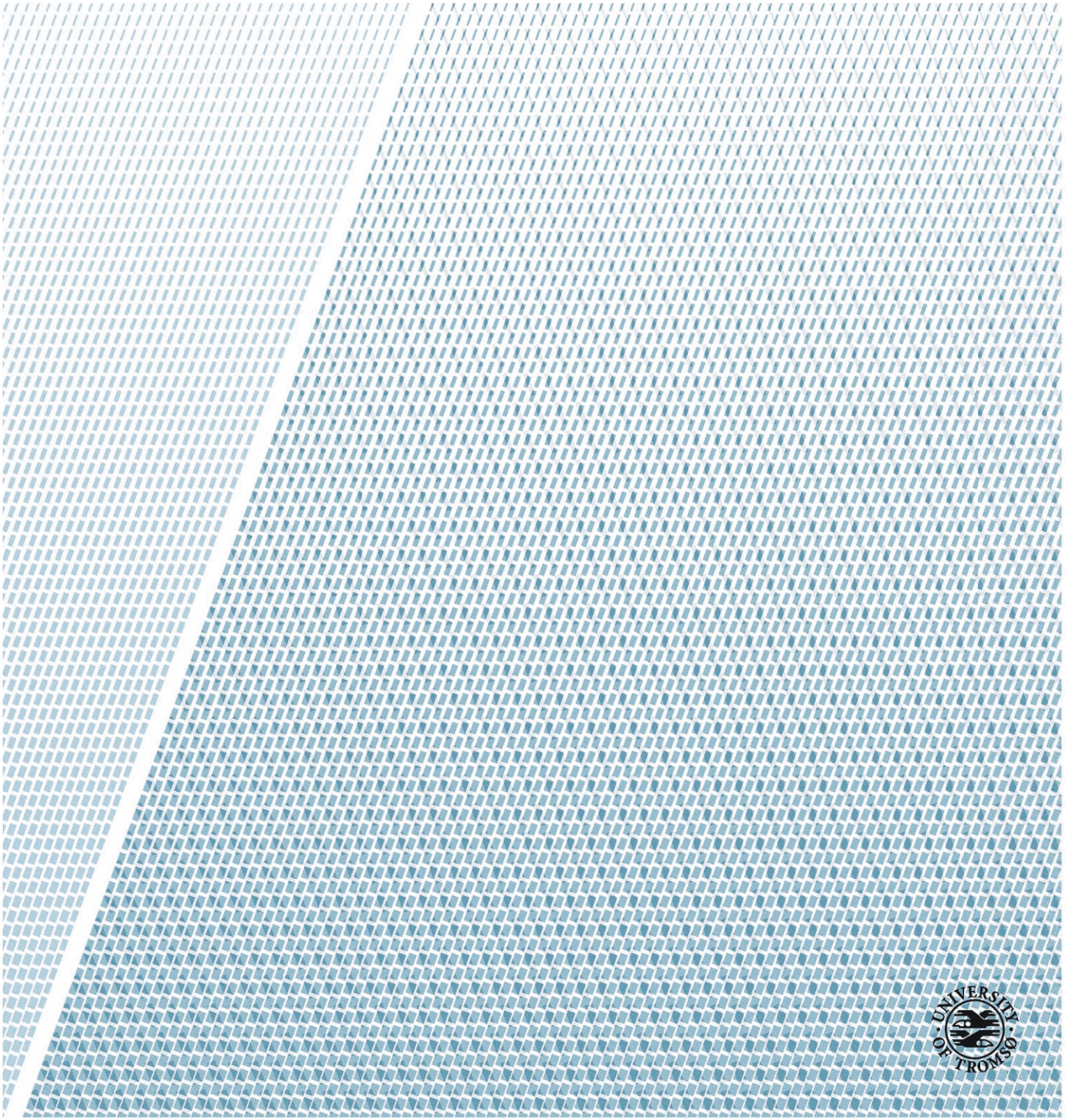

En stor *takk*,

til mor, far og Karoline

- takk for at dere har holdt ut og for all støtte.

ABSTRACT

Subsequent to a widespread hiatus at the top of the Permian on western Svalbard, the Triassic Vardebukta, Tvillingodden and Bravaisberget formations were deposited. In this thesis, the sedimentology, geochemistry and diagenesis are investigated to determine the depositional environment and basinal setting of the Triassic deposits.

In the investigated profile on Mariaholmen, only the upper part of the the Vardebukta Formation (from immediately below the *Myalina* layer) is exposed. The formation consists of interbedded sandstone and siltstone beds interpreted as sandy subtidal platform deposits. The lower Tvillingodden Formation consists of shale and siltstone interbedded with occasional sandstone beds, these deposits are interpreted as prograding prodelta clinoforms and bottomsets. The upper half of the Tvillingodden Formation represents a gradual transition to the Skilisen Bed and barrier tidal inlet lag deposits. The Bravaisberget Formation marks the transition from relatively shallow waters at the top of the Tvillingodden Formation to the onset of shale and siltstone deposits interpreted as prodelta clinoforms and bottomsets.

Five discrete sequences were recognised on Mariaholmen. All sequences were interpreted to represent either transgressive or regressive intervals of a prodelta environment situated next to a relatively large westerly delta. Within this environment river switching occurs in the westerly delta, and multiple hardgrounds and barrier structures are developed.

Trace fossil assemblages vary from proximal *Cruziana* ichnofacies to archetypal *Cruziana* ichnofacies. *Trypanites* ichnofacies is also recorded at the Skilisen Bed level. The trace fossil assemblages in conjunction with the sedi-

mentological investigations limit the water depths to the interval from upper offshore to lower/middle shoreface.

Geochemical proxies such as TOC, TS, $\delta^{13}C_{Org}$, V and Ni of the shales and shaly siltstones indicate a prevailing anoxic to dysoxic bottom-water conditions during deposition of the fine grained terrigenous deposits. However, oxygenated seawater is likely brought in frequently by flooding and storm events, which despite the oxygen-deficient bottom-water conditions during deposition of the fine-grained terrigenous sediments in the shale and siltstone allow for a thriving trace fossil fauna at the interface between fine and coarse grained beds and in the lower parts of decimetre thick beds. Discrete levels rich in nektonic ammonites in the shale also indicate that despite of anoxic to dysoxic bottom-water, the overlying water masses must have been oxygenated at these levels.

Acid dissolution of subordinate carbonate beds throughout the profile provided further information on the depositional environment, based on fauna and flora.

A diverse crinoid fauna indicates that the crinoids either recovered quicker, or that several clades possibly survived the Permian-Triassic extinction event in the northern Tethys.

A large $\delta^{13}C_{Org}$ excursion, which globally correlates with multiple localities, indicate that the Mariaholmen succession encompasses the Smithian.

Rock-Eval measurements of shales and siltstones show a predominance of kerogen type-III and type-IV, pointing to somewhat potentially gas-prone source rocks. Large-scale tectonic events in the Cenozoic and Mesozoic, and thick overburden prior to the Neogene erosion resulted in high burial temperatures, and as a result very little hydrocarbon potential remains within the sediments on Mariaholmen. The sediments are over-mature and pyrobitumen is found in diagenetic calcite and quartz veins.

ACKNOWLEDGEMENTS

First of all, I would like to thank my advisor Assoc. Prof. Nils-Martin Hanken (University of Tromsø - The Arctic University of Norway) for unsurpassed support and fruitful discussions throughout the process. I would also like to thank my co-advisor Dr. Jesper Kresten Nielsen (MOL Norge AS) for his dedication.

Also worthy of much appreciation is Prof. Dr. Hab. Alfred Uchmann (Jagiellonian University), Assoc. Prof. Dr. Błażej Błażejowski (Polish Academy of Sciences) and Michał Lofek (Jagiellonian University) for their participation in the field work and on subsequent studies.

I would like to extend my gratitude to Assoc. Prof. Dr. Hab. Mariusz A. Salamon (Uniwersytet Śląski), Dr. Przemysław Gorzelak (Polish Academy of Sciences) and Dr. Bruno Ferré for the cooperation on our Crinoid paper. I appreciate the help from Prof. Dr. Hans Arne Nakrem (University of Oslo) with identification of bryozoans.

The area investigated is protected by Norwegian landscape protection legislation, as such I would like to thank for the dispensation to sample the locality granted by the district governor of Svalbard, Sysselmannen.

At University of Tromsø - The Arctic University of Norway, I would like to thank Karoline Myrvang and Jannicke Kuvås for help with parts of the sample preparation and analysis.

I am grateful for *Kong Haakon den 7des utdannelsesfond for norsk ungdom* and Statoil ASA's funding of the field work, and last but not least, thanks to Lundin Norway AS for funding the preparation and analysis of the large number of samples.

I would also like to thank my fellow students at the University of Tromsø for a great period in my life, I am especially grateful for all the fun and games in "Brakka" and at "Passivhuset" with Torgeir, Morten and Arne — thanks a lot!

CONTENTS

LIST OF FIGURES

LIST OF TABLES

1

INTRODUCTION

1.1 THE ASPECTS OF THIS WORK

This work focuses on a coastal profile on Mariaholmen, Svalbard, 77°40'48" N, 14°48'47" E (Figure 1.2), which consists of the upper part of the Vardebukta Formation, the Tvillingodden Formation and the lowermost part of the Bravaisberget Formation. The investigated succession is dominated by clastic prodelta sediments, and consist of coastal and shallow marine sandstones, silty shales, shales and subordinate carbonates. Rich trace fossil assemblages are found throughout the sequence except for in the darkest silty shale and shale which have been deposited under anoxic and dysoxic bottom-water conditions.

Situated within the Tertiary fold-thrust belt, the succession has a steep dip to the east (~90°). About 90 m of the lowermost part of the Vardebukta Formation is covered by Quaternary deposits. The upper parts of the Bravaisberget Formation are highly tectonically disturbed; as a consequence, these parts of the sequence were not studied.

In this thesis, the Mariaholmen succession is studied through sedimentary analysis in combination with geochemical proxies, diagenetic investigations and ichnology to give a holistic interpretation of the depositional environment.

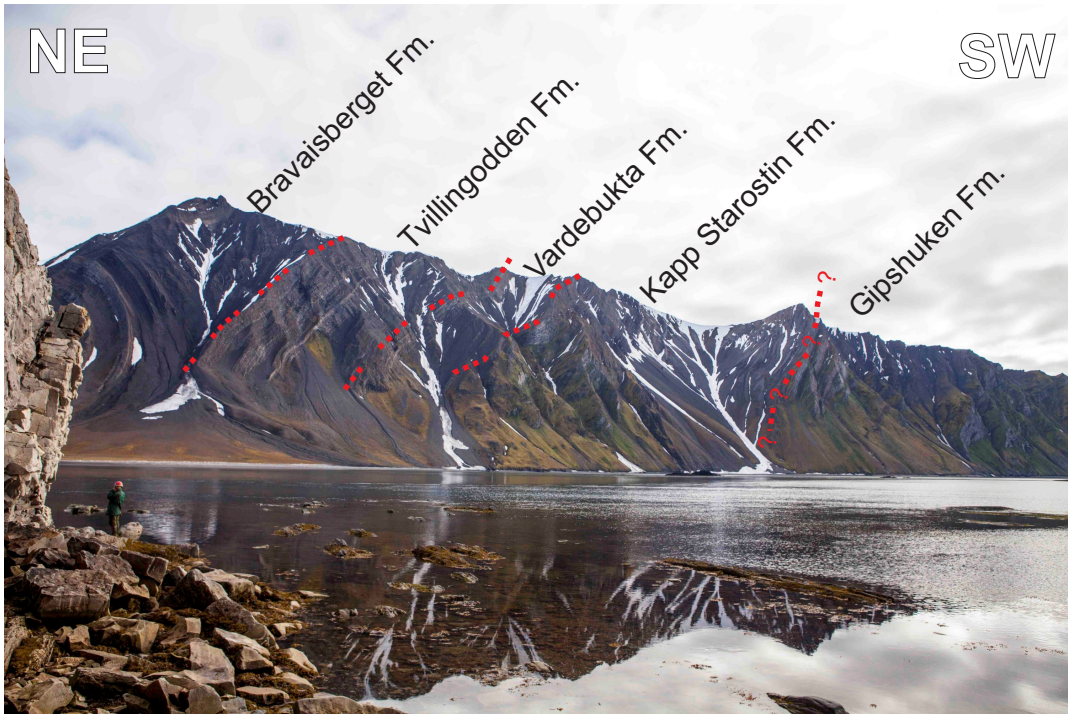

Fig. 1.1: Example of Tertiary tectonic influence immediately south of Mariaholmen. Photo taken approximately from the Skilisen Bed. Stratigraphic outline from Maher et al. (1986). Geologist for scale.

1.2 THE PERMIAN-TRIASSIC MASS EXTINCTION

During the Late Permian and the Early Triassic the supercontinent Pangea was relatively tectonically stable (Ramberg et al., 2007). Despite the stable continent conditions, what is now Siberia was colliding with Baltica and Kazakhstan (Torsvik et al., 2008), a collision coincident with the extrusion of the Siberian Traps, one of the worlds largest igneous provinces (Renne and Basu, 1991). Surrounding Pangea were major subduction zones that relate to the occurrences of rifting found in the Norwegian Greenland region where the sediments of Svalbard were deposited (Torsvik et al., 2008).

Towards the top of the Early Permian there was a significant and abrupt change from the carbonates of the Gipsdalen and the Bjarmeland

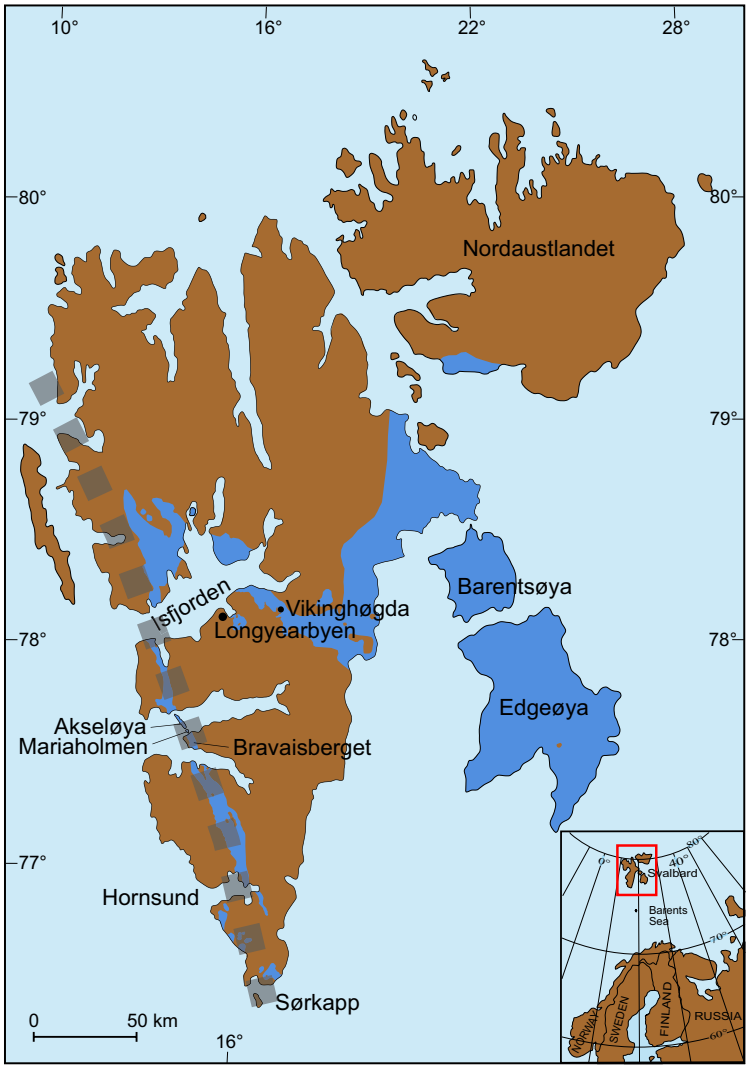

Fig. 1.2: Geographic location of Svalbard archipelago and relevant locations. Black stippled line shows the location of the western Spitsbergen fold belt (Krajewski et al., 2007). Extent of Triassic deposits in blue.

Groups that span almost 40 Ma, to the Tempelfjorden Group (Artinskian to Kazanian) consisting of cool spiculite deposits with interbedded units of sandstone and carbonate (Worsley, 2008). This change in lithology has been interpreted to reflect the change in climate that occurred when the formation of the Urals cut off the warm water supply from the Tethys ocean (Worsley, 2008).

The division between the Palaeozoic Era and Mesozoic Era was earlier defined by the first occurrence of the ammonoid *Otoceras woodwardi* and

the bivalve *Claraia* (Erwin, 1994). The first appearance of the conodont *Hindeodus parvus* has later been ratified by the International Union of Geological Sciences (IUGS) as the onset of the Triassic Induan stage (Hongfu et al., 2001). Occurrences of *Hindeodus parvus* have not yet been published on Svalbard, however, conodonts observed on Svalbard do correlate with assemblages in the Canadian Arctic where *Hindeodus parvus* has been observed (Nakrem et al., 2008). The ICS place the Permian-Triassic boundary at 252.17 $\pm$0.06 Ma (Cohen et al., 2013)

The end of the Permian period is marked by the largest extinction event recorded in the history of the Earth (Hochuli et al., 2010) (LPE). The timing of the Permian-Triassic extinction has been determined to 251.4 $\pm$0.3 Ma by dating ash beds at Meishan in China (Bowring et al., 1998). Jin et al. (2000) also place the extinction at 251.4 Ma ago, lasting approximately 500 ka. More recent work done by Shen et al. (2011) estimate the End-Permian mass extinction to have its peak immediately before 252.28 $\pm$0.08 Ma ago, with the peak being shorter than 20 ka, and the entire extinction interval to have lasted less than 200 ka. . The end-Permian extinction may have eradicated as much as 95% of marine species (Benton and Twitchett, 2003) and 70% of vertebrate families (Sahney and Benton, 2008). Even insects suffered their only recorded mass extinction (Labandeira and Sepkoski, 1993).

It was initially, and is still difficult to comprehend what could have caused the End-Permian mass extinction (Erwin, 1994; Benton and Twitchett, 2003). There are several different theories as to how and why the extinction occurred - many of which can be combined and compared, however, some workers also argue for vastly different mechanisms initi-

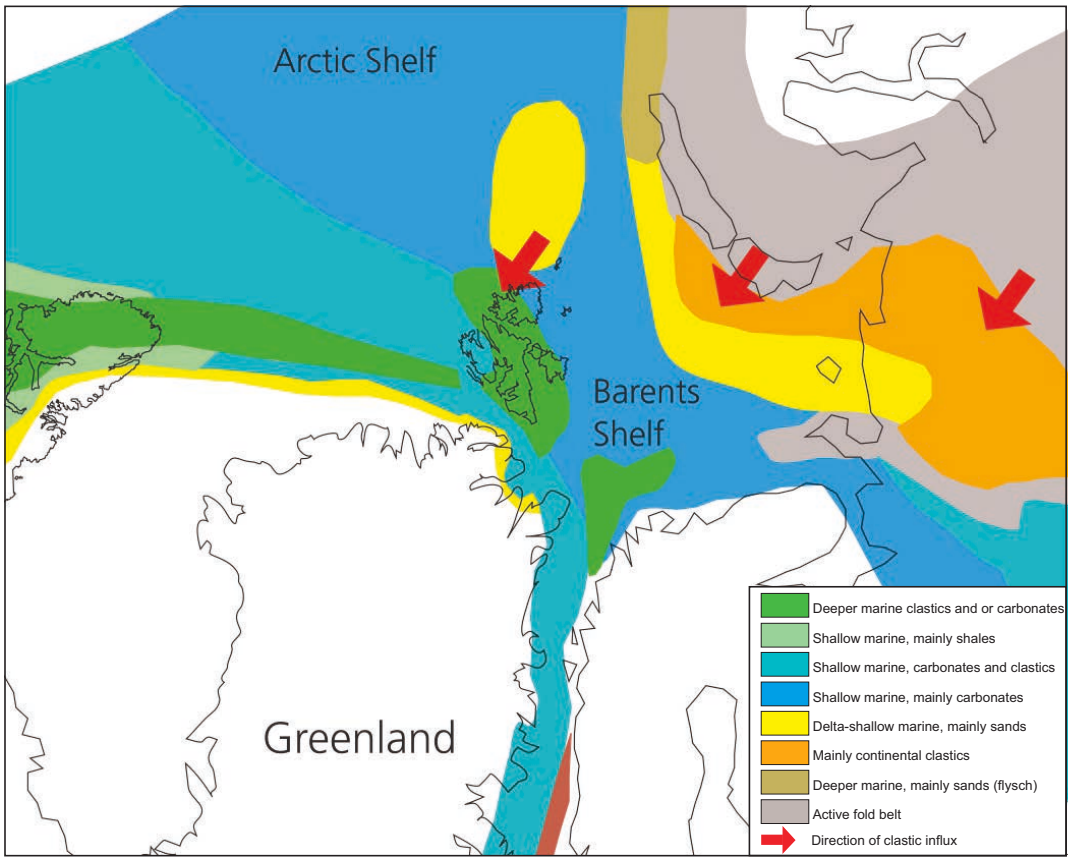

Fig. 1.3: Late Permian depositional environment in the arctic. Modified after Torsvik et al. (2008).

ating the LPE event. Their theories differ, some have an asteroid impact as the primary mechanism (Becker et al., 2001; Becker, 2002; Kaiho et al., 2001) while others suggest that it is caused by galactic cycles comparable to the Milankovitch cycles of the solar system (Harfield and Camp, 1970; J. John Sepkoski, 1989), other controversial theories include cosmic ray jets (Dar et al., 1998) and supernova explosions (Ellis et al., 1996). While these workers propose interesting ideas they are not generally accepted as mechanisms initiating the LPE event (c.f. Erwin (1993, 2015) and Benton (2015)) it cannot be ruled out that they might have been concurrent with the mechanisms that has generally been accepted to initiate the LPE event.

According to Benton and Twitchett (2003) it was prior to 1995 difficult to determine both the timescale and mechanisms initiating the event, however, further research has provided more information: As mentioned in the preceding text the boundary has now been dated precisely (Shen et al., 2011); a better dating of the Siberian Traps has been presented (Reichow et al., 2009); common patterns are found when comparing successions compromising the Late Permian and Early Triassic globally (Wignall and Hallam, 1992; Nielsen et al., 2010) and studies of carbon and oxygen isotopes of the different successions also indicate environmental turmoil (Holser et al., 1989; Wignall and Twitchett, 1996, 2002).

According to Erwin (1994) a likely cause for the End-Permian mass extinction is caused by the Late Permian regression leading to loss of habitat for ocean dwelling organisms. This again to some degree caused climatic instability, which further supported by the Siberian Volcanism led to environmental and ecological collapse due to increasing amounts of CO_2 (Erwin, 1994). Erwin (1994) believes some anoxia and global warming developed, but not that this is the cause. At the onset of the Triassic, the rapid transgression is believed to have ruined the terrestrial habitats close to the shore, causing the decline in insects and vertebrates Erwin (1994).

What Benton and Twitchett (2003) summarise as causes are not vastly different from those of Erwin (1994), but additional research sheds some more light on the event. They suggest that the initial global warming that lead to the extinction event is triggered by the onset of the eruptions in the Siberian Traps, which is anticipated to have initiated

the melting of gas hydrate bodies (this is also one possible explanation for the large shift in ^{12}C values observed). This melting of gas hydrate bodies is then expected to have increased the temperature enough to release further amounts of gas hydrates leading to a spiralling effect of further and further release - until a threshold most likely was met (Benton and Twitchett, 2003). This threshold must then have been outside what the systems on earth could handle in terms of CO_2, leading to the largest extinction in the history of the Earth (Benton and Twitchett, 2003).

Svensen et al. (2009) have also shown that the Siberian Traps venting possibly also lead to the exhumation of gasses from hydrocarbon bearing evaporites and coal deposits. This exhumation was due to sills within a basin containing both coal and evaporites (which were also petroleum bearing). As the sills were emplaced, the evaporites, coal and petroleum deposits were subjected to contact metamorphism which produced large quanta of CH_4, CO_2, SO_2 and halocarbons. The amount of carbon gases released from the petroleum and coal bearing formations are also sufficient to account for the excursion in ^{12}C noted above. Svensen et al. (2009) points out that the amounts of halocarbons generated are a factor of 10 higher than what is required to sufficiently disturb the atmosphere in regards to ozone (which in turn could lead to ecosystem collapse). The timing of the events observed by Svensen et al. (2009) tie well onto the LPE onset measured by Shen et al. (2011), 252 $\pm$0.4 vs 252.28 $\pm$0.08 Ma ago, respectively.

In addition to the end-Permian extinction event, there is also a second possible abrupt Middle Permian extinction event of Capitanian age. It

is viewed both as a major extinction event (Stanley and Yang, 1994; Bond et al., 2010, 2015) and as low point in biodiversity during the Permian (Yang et al., 2000; Clapham et al., 2009; Groves and Wang, 2013). Initially this event had only been observed and studied in detail in tropical areas (todays China) by workers such as Jin et al. (1994); Shen and Shi (1996) and Bond et al. (2010). However, Bond et al. (2015) have also shown the same extinction patterns in the boreal Spitsbergen.

The discovery of Bond et al. (2015) is important as it shows that the Capitanian biotic crisis was not only confined to the tropical areas of todays China, but was also found in the boreal areas of Spitsbergen, implying that the biotic crisis had a wider impact than first thought. Bond et al. (2015) also show (based on conodont dating), that this boreal event correlate to similar observations on Greenland. However, it should be noted that further correlation and dating is necessary (also pointed out by Bond et al. (2015)) in order to determine the timing of these events. For instance, Bond et al. (2015)'s revision of the biostratigraphic age (which is based on little evidence) of the Upper Permian deposits on Greenland (Ravnefjeld Formation and Wegener Halvø Formation) does not agree with the stratigraphic scheme of Stemmerik et al. (2001).

1.3 EARLY TRIASSIC FAUNAL RECOVERY

Subsequent to the end-Permian extinction event, the temperatures at equatorial latitudes were exceptionally high from the Griesbachian through the Spathian (Sun et al., 2012), at higher latitudes elevated temperatures are also recorded for the Early Triassic (Kidder and Worsley, 2004).

The high temperatures has an inverse relationship to the changes in biodiversity (Sun et al., 2012), and likely played an instrumental role in the recovery following the end-Permian mass extinction (Sun et al., 2012). Due to elevated temperatures at high latitudes, the Permian coal forests disappeared (Kidder and Worsley, 2004), an eventually the forests could no longer migrate further polewards (to compensate for higher temperatures) because of light limitations (Kidder and Worsley, 2004).

Worldwide, the Griesbachian stage deposits have low oxygen conditions in both shallow and deep water settings (Twitchett, 1999). It is suggested that the faunal recovery was prolonged due to this widespread marine anoxia (Hallam, 1991). Twitchett et al. (2004) describe a rare normally oxygenated environment of Griesbachian age where the recovery is substantially quicker than the common anoxic environments, confirming that widespread anoxia lead to a prolonged recovery.

Immediately following the mass extinction, trace fossil tiering below the water-sediment interface is virtually absent and gradually increases towards the Spathian (Twitchett, 1999). Trace fossil fauna diversity show similar patterns; immediately following the mass extinction the fauna consist of solely of fodinichnial traces followed by vertical domichnia (Twitchett, 1999). A worldwide reappearance of *Rhizocorallium* isp. occur first in the Spathian (Twitchett, 1999). The brachiopod fauna recovery occur in the late Griesbachian (Chen et al., 2005). However, the re-population of brachiopods appear to have a preference for regions where pre-extinction and surviving brachiopods are rare (Chen et al., 2005), and as a result the Triassic brachiopod fauna is sparse

(Chen et al., 2005). Lingulid brachiopods on the other hand appear after the end-Permian extinction as an ecological opportunist, but only in areas where they were found prior to the extinction event (Zonneveld et al., 2007).

1.4 REGIONAL GEOLOGY

1.4.1 *Triassic of Svalbard and the Barents Sea*

The Triassic is considered a relatively tranquil period in earths history (Ramberg et al., 2007), however, Svalbard moved fairly rapidly during the Triassic (Torsvik et al., 2008). Even though Pangea during the Triassic was relatively stable (Torsvik et al., 2008) and similar to what is found for the Permian (Dietz and Holden, 1970; Torsvik et al., 2008), Pangea shifted approximately 15° during the period from Early Triassic to Rhaetian (Torsvik et al., 2008). This resulted in a shift of Svalbard from a little below 45° N to approximately 60° N (Smith and Briden, 1977).

During the Triassic the clams thrived, and eventually more or less replaced the brachiopods. The terrestrial flora of the Triassic bear evidence of an arid climate not significantly different from the Permian, but large coal deposits can also be found (Ramberg et al., 2007). The terrestrial fauna is dominated by the rise of Dinosauria and the tiny, but important ancestors of the early Mammalia (Ramberg et al., 2007).

Triassic deposits are found throughout the Svalbard archipelago. First described by Buchan et al. (1965) the stratigraphy has since been re-

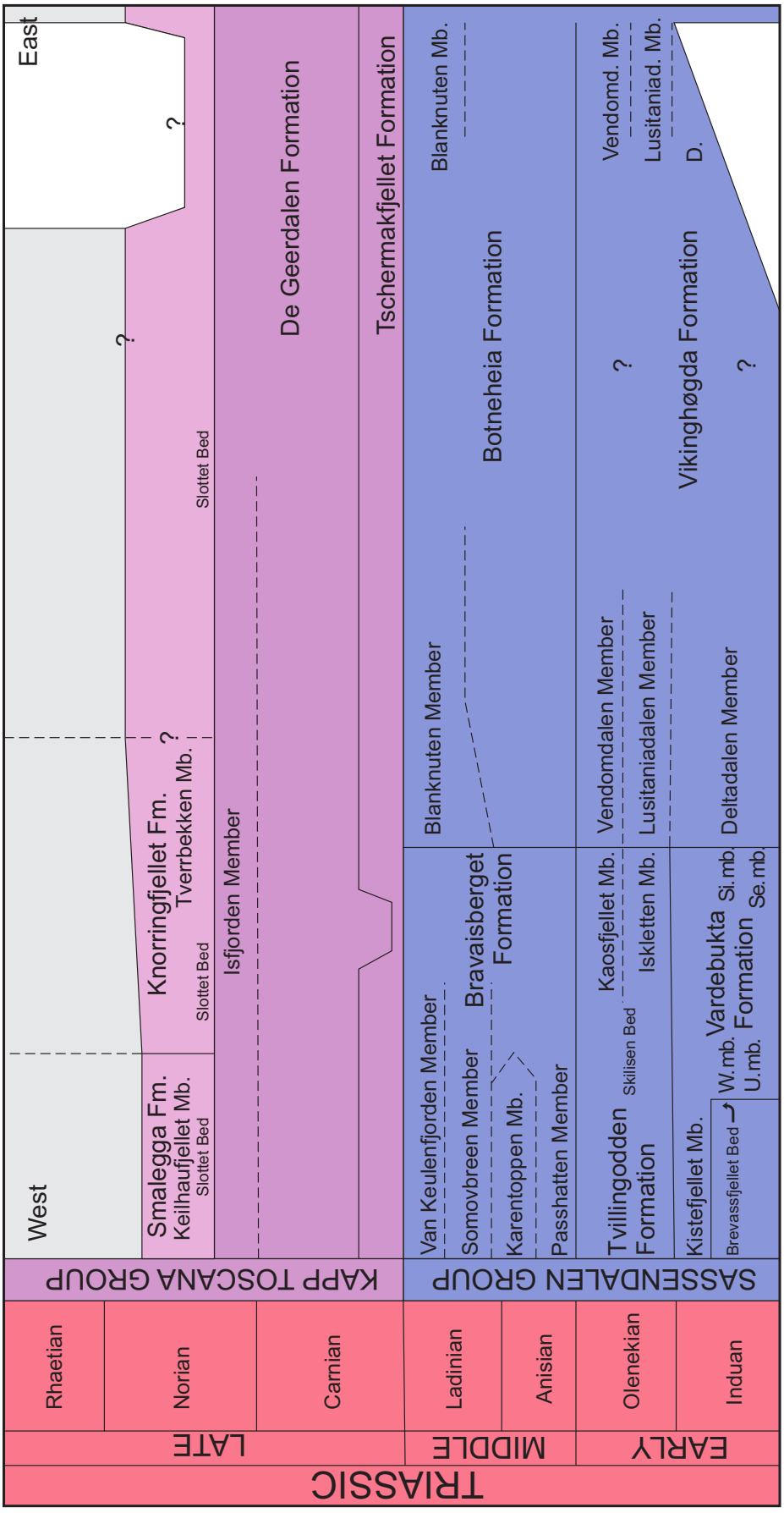

Fig. 1.4: Triassic stratigraphy on Svalbard. Modified after Mørk et al. (1999a).

vised by Mørk et al. (1982) and Mørk et al. (1999a). According to palaeogeographical reconstruction of Early Triassic (Mørk et al., 1999a) there was a land area to the west of Svalbard resulting in coast parallel sandstone and shale deposits in western Spitsbergen representing coastal, deltaic and shallow marine environments (Figure 1.6). These facies grade into dark shales with minor siltstone and sandstone deposits which were deposited in a basinal setting further to the east (Mørk et al., 1982, 1999a). Sedimentation occurs predominantly from the west during Early Triassic, eventually shifting to an eastern provenance area during lower-Ladinian. (Glørstad-Clark et al., 2010). The basin extended southwards forming an extensive embayment of the Panthalassa Ocean into the northern margin of the Pangea supercontinent (Riis et al., 2008; Worsley, 2008). During the Triassic the epicontinental seaway between the Baltic and North American continent gradually closed (Worsley, 2008; Riis et al., 2008; Glørstad-Clark et al., 2010).

The Permian-Triassic boundary at Svalbard has traditionally been placed at the top of the Kapp Starostin Formation where there is an abrupt change from glauconitic sandy or spiculite facies to black organic-rich shales, siltstones and finer grained sandstones of the Vardebukta Formation (Mørk et al., 1982; Gruszczyński et al., 1989; Mørk et al., 1989, 1999a). However, there has been debate whether the boundary between the Kapp Starostin Formation and the Vardebukta Formation is continuous or not on Svalbard, c.f. summary by Dustria et al. (2013), who also gave evidence for a major Late Permian transgression. Palynological investigations indicate that the Permian-Triassic boundary is located within basal parts of the Vardebukta Formation (Vigran et al.,

2014; Uchman et al., In Press). This is also supported by $\delta^{13}C_{Org}$ chemostratigraphy (Wignall et al., 1998) and similar studies of the lateral equivalent Vikinghøgda Formation situated further to the east (Dustria et al., 2013) and of biomagnetostratigraphy (Hounslow and Nawrocki, 2008).

The boundary between the Vardebukta Formation and the overlying Tvillingodden Formation has traditionally been regarded as corresponding to the Induan/Olenekian boundary (see summary by Mørk et al. (1999a)). However, magnetostratigraphic investigations by Hounslow and Nawrocki (2008) have provided greater chronostratigraphic detail than biostratigraphy alone, indicating that the Vardebukta Formation extends into the Olenekian rather than terminate near the Induan-Olenekian boundary. Mørk et al. (1989); Mørk (1994) and Mørk et al. (1994) show the presence of a major early Olenekian transgression in the circum-arctic area. Characteristic fossil assemblages (conodonts, ammonoids, bryozoans and bivalves) in the Tvillingodden Formation indicate an Olenekian age (Mørk et al., 1999a; Nakrem et al., 2008; Hounslow et al., 2014). Palynological investigations by Vigran et al. (2014) correlate the Tvillingodden Formation with the *Naumovaspora striata* composite assemblage zone (early Olenekian/Smithian).

There are two different sandy grainstone levels in the lower part of the Triassic succession which serve as marker horizons in the western part of Svalbard (Mørk et al., 1982, 1999a). These levels are:

1. The *Myalina* layer carbonate from the upper part of the Vardebukta Formation contains a coquina of skeletal fossils dominated by the bivalve *Myalina*. Conodonts have been extracted from the

same stratigraphic level on several localities on Spitsbergen, and these microfossils indicate an upper Griesbachian/Lower Dienerian age (see summary by Nakrem et al. (2008)). However, biomagnetostratigraphic investigations by Hounslow and Nawrocki (2008) have given better chronostratigraphic resolution indicating an upper Griesbachian (Commune zone according to the ammonoid stratigraphy and magnetostratigraphic correlation).

2. The Skilisen Bed from the upper part of the overlying Tvillingodden Formation has formally been defined by Mørk et al. (1982). The bed consist of sandy grainstone containing a rich fauna dominated by small spiriferids and bivalves. Locally there are also massive crinoidal grainstone banks. The conodont fauna indicates an upper Smithian age (Nakrem et al., 2008)

In the following subsections I will give a brief description of the formations studied in this paper and the formations adjacent in the stratigraphy.

1.4.2 *Sassendalen Group*

Sassendalen Group consists of five different formations and ranges from the Induan to the transition from the Ladinian to the Carnian, covering the lower two thirds of the Triassic stratigraphy on Svalbard (Mørk et al., 1999a). In the west, the Sassendalen Group consist of Vardebukta, Tvillingodden and Bravaisberget Formation, while in the east it is represented by the Vikinghøgda and Botneheia Formation (Mørk et al., 1999a). All in chronological order.

1.4.2.1 *Western Svalbard*

VARDEBUKTA FORMATION AND TVILLINGODDEN FORMATION

The formations were initially defined by Buchan et al. (1965), but the current formal definition is from Mørk et al. (1982): The Vardebukta Formation is of Induan age, and represent only the first 1.5 Ma of the Triassic. Shale, siltstones and sandstones make up the general composition of the formation. The lower part of Vardebukta Formation consists of grey shales resting conformably on the dark silica cemented spiculites in the Kapp Starostin Formation of late Artinskian - Kazanian age (Tempelfjorden Group) (Mørk et al., 1999a). The Vardebukta Formation is exposed along the Tertiary fold and thrust belt in the west of Spitsbergen (Mørk et al., 1999a). The formation is relatively similar moving southwards from the Festningen profile, but it should be noted that the amount of sandstone decreases southwards (Mørk et al., 1982).

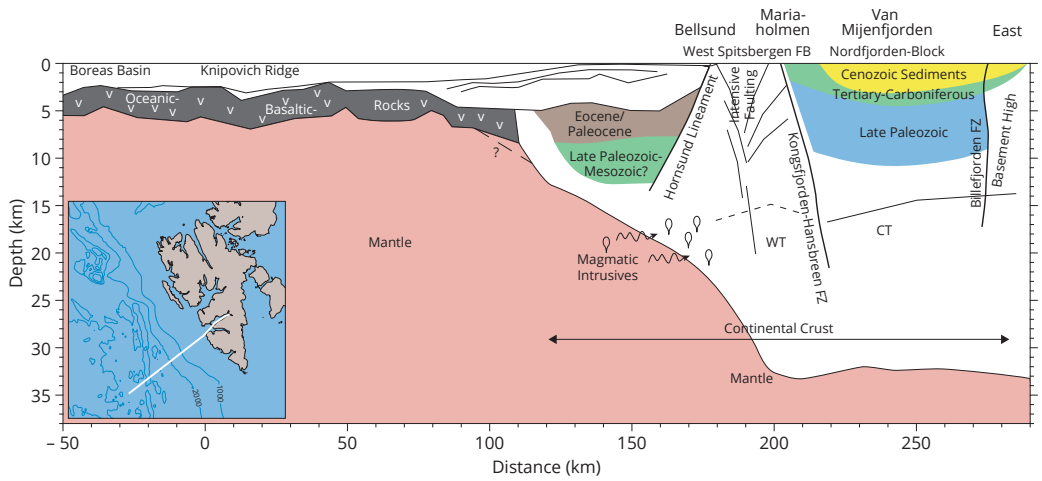

Fig. 1.5: Spatial distribution of sedimentary deposits, oceanic basaltic rocks and continental crust along the southwest - northeast axis on Svalbard. Notice the varying thickness of deposits along the profile. WT: western terrane. CT: central terrane. Modified after Ritzmann et al. (2002).

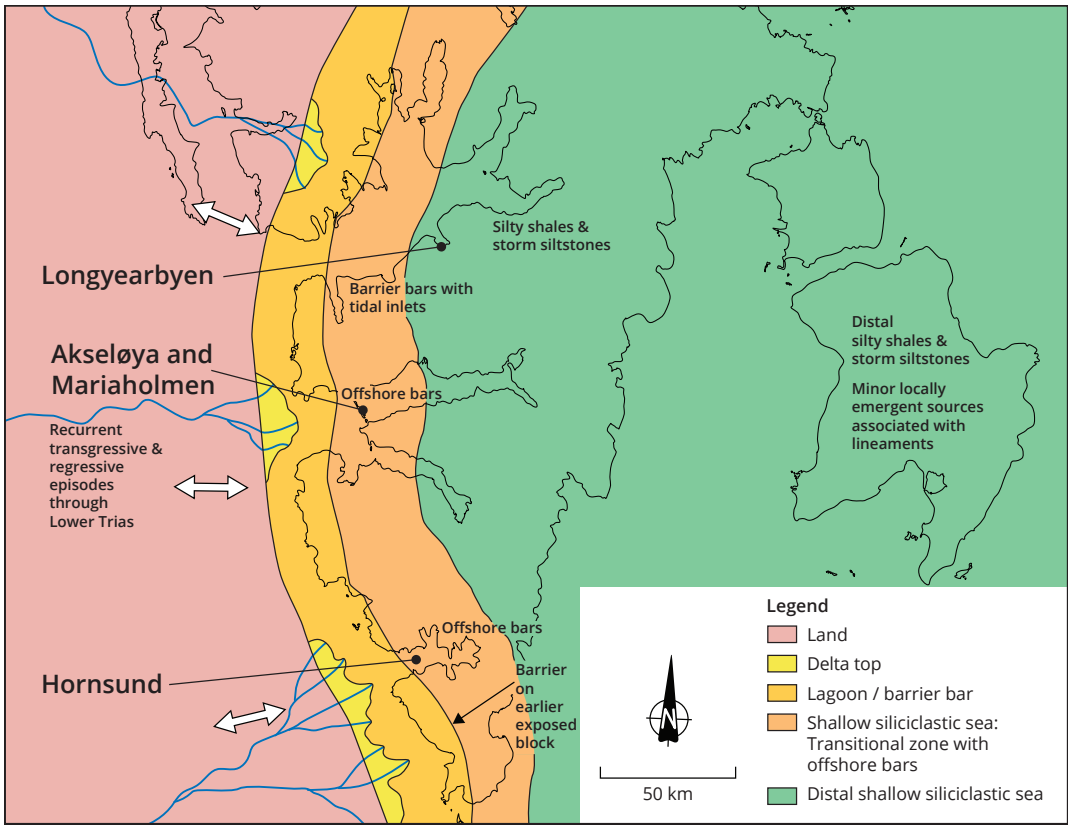

Fig. 1.6: Overview of the Early Triassic depositional environment at Svalbard. Notice how Mariaholmen is situated within a transitional siliclastic sea where sediments are primarily derived from the land area situated somewhere to the west. Modified after Mørk et al. (1982).

It is suggested that the deposits found in the south are offshore bars formed in open marine environments Mørk et al. (1982).

Shale characterise the first 75 m of the Vardebukta Formation with periodic occurrences of siltstones where fossil fauna is generally relatively sparse (Mørk et al., 1982, 1999a). After this interval, the frequency of siltstone intervals gradually increases to approximately 140 m above the Permian Triassic boundary(Mørk et al., 1982, 1999a). From this level, the formation is now recognised by a 90 m thick sandstone unit ending at around 230 m (Mørk et al., 1982, 1999a). Within this package both fossils and bioturbation are commonly found (Mørk et al., 1982). In the centre of the 90 m thick sandstone unit, cross bedded sandstone beds

with mud flakes and abundant *Myalina* bivalves are found (Mørk et al., 1982). Onward from 230 m above the Permian-Triassic boundary, the sequence is again characterised by shale and siltstone (Mørk et al., 1982, 1999a). The Vardebukta Formation is believed to represent a Early Triassic shallow-marine coastal environment with prograding deltaic lobes with offshore bars (Mørk et al., 1982).

Approximately 300 m above basis the boundary between the Vardebukta Formation and Tvillingodden Formation is found (Mørk et al., 1999a). The boundary definition is based on the transition from the distinct silty shales of the Vardebukta Formation to finely laminated non-bioturbated shales (Mørk et al., 1999a). The Tvillingodden Formation is composed mainly of mudstones, shales and siltstones and is of Olenekian age (Mørk et al., 1982).

The Tvillingodden Formation first and current definition is by Mørk et al. (1982), Tvillingodden Formation is however, a redefinition of the Sticky Keep Formation described by Buchan et al. (1965). The Tvillingodden Formation, like the Vardebukta Formation, is also found in the tertiary fold and thrust belt on western Spitsbergen.

The Tvillingodden Formation stratotype starts with finely laminated shale beds with a gradual transition upward into finely laminated sandstone and shale beds (Mørk et al., 1999a). Some wave ripples and bioturbation can be found, but it is not common in the lower parts of the formation (Mørk et al., 1982). In the Tvillingodden Formation sandstones commonly containing the trace fossil *Rhizocorallium* isp. become more abundant towards the top (Mørk et al., 1982). Found towards the top of the formation are also sandstones with abraded bivalves and

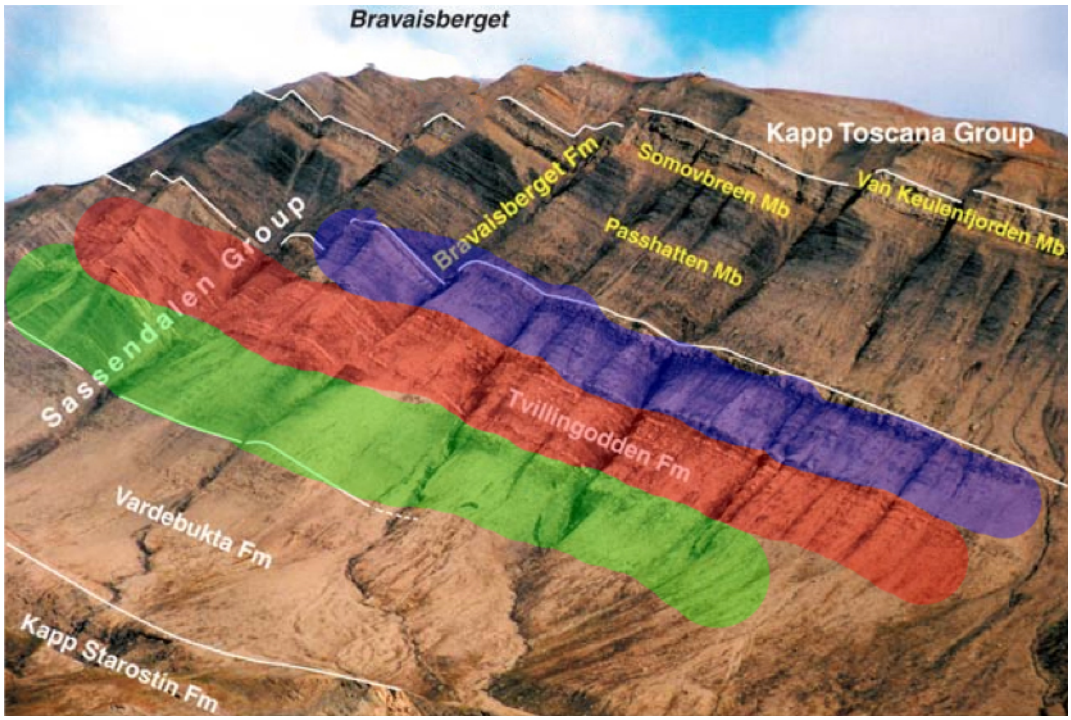

Fig. 1.7: The Vardebukta Formation representing a large coarsening upwards sequence that can be observed above the Permian Kapp Starostin Border. It is followed by the coarsening upwards sequences of the Tvillingodden Formation (marked in green, red and blue). Overlying the Tvillingodden Formation are the shales of the Passhatten Member. They are followed by the Somovbreen Member and Van Keulenfjorden Member sandstones. The latter three representing the Bravaisberget Formation. Modified after Krajewski et al. (2007).

brachiopods and the Skilisen Bed carbonates (Mørk et al., 1982). The Tvillingodden Formation has a total of three coarsening upwards sequences (Figure 1.7).

BRAVAISBERGET FORMATION

First defined by (Mørk et al., 1982), the Bravaisberget Formation represents the Middle Triassic in the western fold and thrust belt areas on the Svalbard archipelago. Bravaisberget is over-mature in the west due to the tectonics of the fold and thrust belt (Krajewski et al., 2007). On

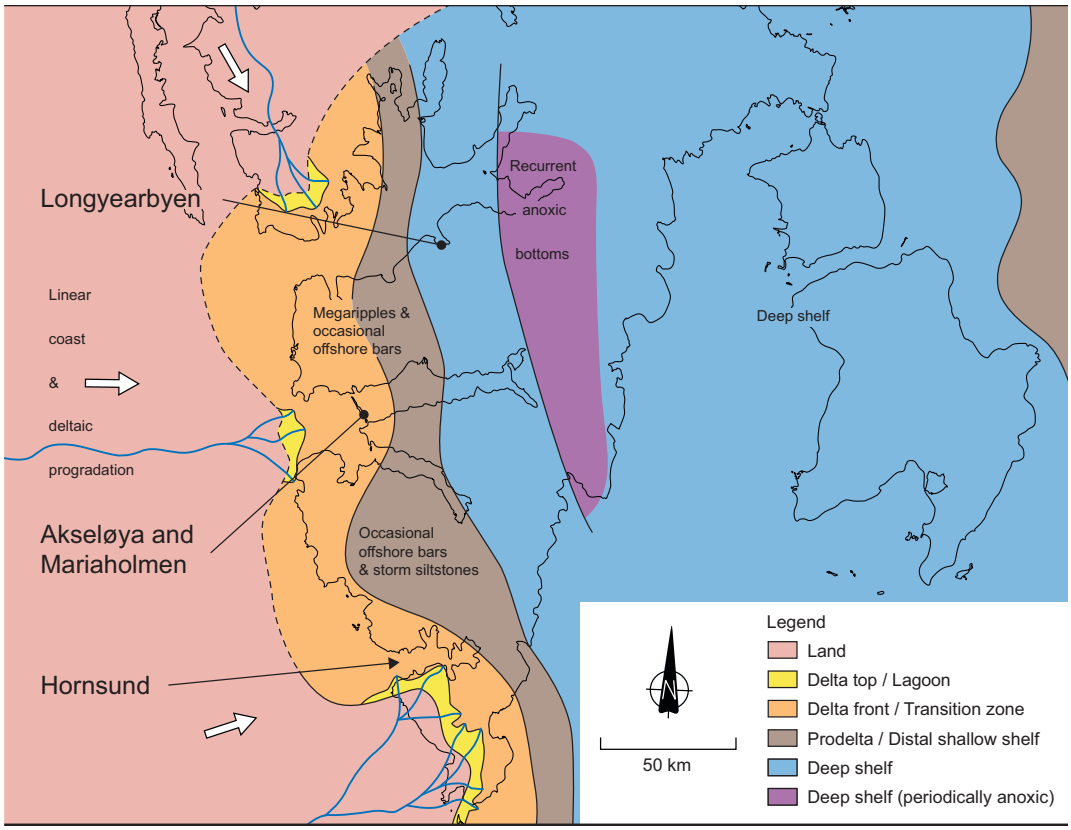

Fig. 1.8: Middle Triassic depositional environment. White arrows indicate sediment transport direction. Modified after Mørk et al. (1982).

the rest of Svalbard, the formation is mature to early mature except for locations where it has been exposed to contact metamorphism (Krajewski et al., 2007). According to Mørk et al. (1982); Krajewski (2000) and Krajewski et al. (2007) deposition occurred in a broad shelf basin bordered by lands areas dominated by deltas in what is now the west and southwestern areas of offshore and onshore Svalbard. Since the sediments found in the western parts of Svalbard are generally coarser than those of the east, deposition in this part of the epicontinental basin has been interpreted to occur from west to east (Buchan et al., 1965; Mørk et al., 1982). An overview of the depositional environment of the Middle Triassic on Svalbard can be found in Figure 1.8

The Bravaisberget Formation found at Bravaisodden on Nathorst Land is the stratotype (Mørk et al., 1999a). It was deposited in the Middle Triassic, and range from the beginning of Anisian to the end of Ladinian (249.5 Ma to 228.7 Ma) with a thickness of 209 m at the stratotype (Mørk et al., 1999a). The formation base is defined by a sharp contact of soft black mudstone resting conformably on the cliff forming sandstones of the underlying Tvillingodden Formation (Mørk et al., 1982). The Bravaisberget Formation forms one large coarsening upwards sequence and is divided into four members from bottom to top, Passhatten Member, Karentoppen Member, Somovbreen Member and Van Keulenfjorden Member (Mørk et al., 1999a). At the stratotype, only Passhatten Member, Somovbreen Member and Van Keulenfjorden Member are found (Mørk et al., 1999a). Karentoppen Member is restricted to western Sørkapp Land, forming a wedge between Passhatten Member and Somovbreen Member (Mørk et al., 1999a). Bravaisberget Formation is subdivided into two regressive sequences of Anisian and Ladinian age (Mørk et al., 1989).

At the stratotype of Bravaisberget Formation, five phosphorite bearing conglomerate layers are found (Krajewski et al., 2007). These layers are thought to represent high biological productivity (Krajewski et al., 1994), marking the onset of Middle Triassic transgression (Krajewski et al., 2007). The conditions lasted throughout Passhatten Member (Krajewski et al., 2007). Black shales recurrently develop in-between the phosphorite bearing conglomerates (Krajewski et al., 2007), and this is thought to reflect the interplay between high energy environments dominated by coarser clastic sediments and low energy organic prone

environments(Krajewski et al., 2007). Krajewski et al. (2007) relates this to morphological variations of a shelf, where the coarser phosphorite beds are postulated to be elevated sediment bars situated in areas of finer grained organic sediments.

The phosphorite, as in all of the Middle Triassic in Svalbard is mainly found as nodules and peloids (Krajewski, 2000; Krajewski et al., 2007). Phosphorite sequences are mainly found in the Passhatten Member where they exist in siltstone-sandstone beds as:

- Allochthonous phosphorite that have been reworked, winnowed and redeposited.
- Pristine autochthonous phosphorite that have formed *in situ*.
- Phosphorite consisting of a mixture of allochthonous and autochthonous origin.
- Rare occurrences of condensed phosphorite.

Not counting the four sequences of Passhatten Member there are two more episodes of phosphporite observed in the stratotype, one towards the base Somovbreen Member and a thin discontinuous phosphorite lag bed at the base of the Van Keulenfjorden Member (Krajewski et al., 2007).

Passhatten Member

Passhatten Member is defined and described by Krajewski et al. (2007), it is a 160 m thick member of Anisian age. Passhatten Member is the lowermost member of Bravaisberget Formation, and is subdivided into 8 sequences (Krajewski et al., 2007).

Sequences 2, 4, 6 and 8 are black shales with occasional interbedded phosphate horizons (Krajewski et al., 2007). The black shale sequences have varying amounts of coarser grained interbeds, and Passhatten Member's black shales are most commonly fissile (Krajewski et al., 2007). There are four different varieties of shale described in the Passhatten Member: sandy silty shale with weak fissility, fissile silty shale, fissile illite dominated mud-shale and very fissile clay-shale, the most prevalent shale type is the illite dominated mud-shale (Krajewski et al., 2007).

Throughout the shales it's common to find varying amounts very fine silt to coarse silt quartz grains blended in the shales, feldspar contributes as the secondary detrital component (Krajewski et al., 2007). Organic material observed throughout the member is generally amorphous, although some herbaceous and wood components are observed along with localised occurrences of bivalves, fish teeth and vertebrae (Krajewski et al., 2007). Pyrite is also found both in the microcrystalline and framboidal form (Krajewski et al., 2007).

The shale in Passhatten Member varies from non-laminated to densely-laminated, the shale laminae are generally 0.2 cm to 2 cm and vary from continuous to discontinuous seams and lenses (Krajewski et al., 2007). This combined with undulation of the black shales and low angle cross-laminated and ripple-laminated internal structures indicates that bottom water currents were present during deposition of the Passhatten Member (Krajewski et al., 2007).

Sequence 1, 3, 5 and 7 are the phosphorite bearing sequences in Passhatten Member described in the previous Bravaisberget Formation paragraph.

As observed in most shales, also found within the Passhatten Member's black shales are interbeds of sandstone and siltstone beds, the thickness of these interbeds vary from 5 cm up to 2.9 m (Krajewski et al., 2007). The sandstone and siltstone beds are generally fossiliferous, with ammonoids found throughout beds, which can be used for biostratigraphy (Krajewski et al., 2007). The content of biogenic components such as bivalves tend to increase towards the upper part of the Passhatten Member (Krajewski et al., 2007). Detrital size fractions vary from bed to bed, and also within beds. Boundaries to the black shale vary from sharp to gradual (Krajewski et al., 2007).

Abrupt facies change generally coincides with an increase in diagenetic carbonate cement dominated by microspar relative to the fairly abundant detrital clay particles observed in the pores when facies undergo a gradual transition (Krajewski et al., 2007). It is worth noting that these two varieties are conveniently discerned in the field through weathering colour which is graded from yellow to dark grey representing maximal calcite cement versus maximum detrital content, respectively (Krajewski et al., 2007).

As opposed to the black shales where almost no bioturbation are observed, the sandstone and siltstone beds of Passhatten Member are generally intensely bioturbated (Krajewski et al., 2007). At the transitional margins of the beds, fine lamination graduates to finely bioturbated sediments (Krajewski et al., 2007). This bioturbation coupled with

benthic fauna is interpreted to reflect recurrent development of aerobic bottom water conditions throughout the deposition of Passhatten Member (Krajewski et al., 2007). The beds originated as a result of two different mechanisms; winnowing and reworking of the black shale sediments constitutes the first mechanism, requiring recurrent increases of sea bottom activity which is consistent with the features observed in the shale (Krajewski et al., 2007). The second mechanism is progradation of coarser grained sediments onto the muddy bottom water conditions of Passhatten Member, and indication of deposition on morphological slopes, which agree well with observed slumping and redeposition of phosphorite horizons (Krajewski et al., 2007). Some thicker beds suggest interplay between the aforementioned mechanisms (Krajewski et al., 2007).

Karentoppen Member

Karentoppen Member is restricted to western Sørkapp Land (Mørk et al., 1999a), and as mentioned earlier can not be found in the stratotype at Bravaisberget. Karentoppen Member form a wedge between Passhatten Member and Somovbreen Member, where it represents deltaic distributary sandstones (Mørk et al., 1999a). As such Karentoppen Member is characterised by herringbone cross-bedded sandstones in the bottom which fine upwards to planar laminated sandstones, and in the midst of the succession two conglomerate beds are found (Mørk et al., 1999a). Bioturbation can be observed throughout the entire member, grading from high energy burrows to normal marine bioturbation towards the top (Mørk et al., 1999a).

Somovbreen Member

Somovbreen Member is situated stratigraphically directly above Karentoppen Member, but in the stratotype it is found conformably on top of Passhatten Member (Mørk et al., 1999a). Including the already described phosphorite bearing layer, the Somovbreen Member consist of very fine to fine grained silty sandstones and sandy siltstones (Krajewski et al., 2007).

Generally, a low clay content is observed, however, detrital feldspar is commonly found alongside detrital rutile at some levels (Krajewski et al., 2007). Bioturbation is common throughout the sequence, and *Taenidium* isp. dominates the finely bioturbated lower part of the sequence (Krajewski et al., 2007). Bioturbation in the Somovbreen Member often show a succession of trace fossils that could reflect increasing energy levels (Krajewski et al., 2007). Some organic material can be found throughout the section, and it is dominated by land derived wood fragments (Krajewski et al., 2007).

In Somovbreen Member the pore space has been filled by carbonate cement very similar to that of the underlying Passhatten Member (Krajewski et al., 2007). It is dominated by calcite microspar with odd occurrences of rhombs which consist of ferrous dolomite (Krajewski et al., 2007). Scattered pyrite is observed forming both micro crystals and rare framboids (Krajewski et al., 2007).

Van Keulenfjorden Member

Van Keulenfjorden Member was first defined by Pčelina (1983), this is also the current definition. Resting conformably on top of Somovbreen Member, its onset is marked by a thin lag horizon consisting of re-

worked and rounded sandy phosphate nodules Pčelina (1983). As Somovbreen Member, Van Keulenfjorden Member consist mainly of sand stone and silt stone (Mørk et al., 1999a). At Bravaisberget the Van Keulenfjorden Member consists of two coarsening upwards units. Albeit being coarsening upwards units, the range only spans the fractions from silt to fine sand stone. Mørk et al. (1999a) reports that the Van Keulenfjorden Member's lower section in the stratotype (Bravaisodden) is carbonate cemented while the upper section is silica cemented. Krajewski et al. (2007) on the other hand reports that throughout the section logged at Bravaisberget, silica cement overgrowing detrital grains and filling pore space is common throughout the entire Van Keulenfjorden Member. The only carbonate cement observed by Krajewski et al. (2007) is dolomite in the form of minute rhomb's ranging from 30 µm to 100 µm in size, in fact, they recognise it as a quartz-dominated dolomitic rock.

1.4.2.2 *Central and Eastern Svalbard*

VIKINGHØGDA FORMATION

Vikinghøgda Formation first described by Mørk et al. (1999b), is a redefinition of the Deltadalen Member and Sticky Keep Member in the now unused Barentsøya Formation. Deltadalen Member is still encompassed by Vikinghøgda Formation, while Sticky Keep Member is replaced by Lusitaniadalen Member and Vendomdalen Member respectively (Mørk et al., 1999a). Vikinghøgda Formation is time-equivalent to the Vardebukta Formation of western Spitsbergen (Mørk et al., 1999a). The formation generally consists of grey shales and silty shales, with

ancillary siltstones and carbonate beds where plenteous of septarian nodules are found at several levels Mørk et al. (1999b). Overall the Vikinghøgda Formation represents several transgressive-regressive events, and each individual member has its base at a regionally recognisable transgression Mørk et al. (1999b). The Vikinghøgda Formation has been deposited in moderately deep marine shelf environments (Mørk et al., 1999a). See figure 1.8 for an overview of Middle Triassic depositional environments. Vikinghøgda Formation directly overlies the Permian Kapp Starostin Formation, and at the stratotype, the formation is 250 m thick Mørk et al. (1999a). The boundary to the underlying Kapp Starostin Formation is defined where the soft weathering sandstones of the Deltadalen Member rest on top of the glauconitic Permian sandstones. (Mørk et al., 1999a).

Deltadalen Member

First discussed by Mørk et al. (1982), the Deltadalen Member's current definition can be found in Mørk et al. (1999b). Deltadalen Member was deposited during the Induan stage, and primarily consists of shale and sandstone (Mørk et al., 1999b).

The lower part of the member consists of silty shale with thin and medium thick beds of sandstone, while the remaining part of the member consists of greenish-grey silty shale, siltstone and sandstone (Mørk et al., 1999b). In the sandstone beds, hummocky cross bedding, wave ripples and planer lamination fining upwards is observed, carbonate concretions and marine fossils are also present (Mørk et al., 1999b).

Deltadalen Member's contact with the Permian Kapp Starostin Formation at the stratotype, e.g. the Permian-Triassic boundary in central

and eastern Svalbard has small channels such as gutter casts filled by medium grained sandstone and irregular shaped pits and groves that combined resembles a karstified surface (Mørk et al., 1999b). The top of the Kapp Starostin Formation is also fractured and cherty with a brown weathering coloured surface, this weathering crust at the top of Kapp Starostin Formation erosional surface indicates an exposure of the top Permian prior to deposition of the Deltadalen Member (Mørk et al., 1999b). Similar features have been observed by Mørk et al. (1982) at Edgeøya. At the equivalent boundary in the neighbouring Lusitaniadalen, no such features can be observed, albeit there is a yellow-weathering bed at the boundary (Mørk et al., 1999b). Deltadalen Member's sandstone layers repeatedly show hummocky cross bedding, often with rippling in the upper levels of the beds, bioturbation throughout the Deltadalen Member is sparse (Mørk et al., 1999b). The reoccurrence of hummocky lamination is a common indication of a depositional environment above storm base (Leeder, 2011). This would also be consistent with the commonly accepted model for the Early Triassic on Svalbard where the stratotype of Deltadalen Member is situated in-between the coastal environments of Vardebukta Formation a mere 75 km to the west and the more distal depositional environments to the east on Edgeøya and Barentsøya (Mørk et al., 1999b).

Lusitaniadalen Member

First described (and currently defined) by Mørk et al. (1999b), Lusitaniadalen Member is named after a valley next to Vikinghøgda mountain. The Member was deposited in early Olenekian, and it consists mainly of mudstone and occasional sandstones (Mørk et al., 1999b).

The Lusitaniadalen Member's contact with the underlying Deltadalen Member is defined where dark grey laminated silty mudstones sharply overlies the hummocky laminated sandstones of the Deltadalen Member (Mørk et al., 1999b).

The mudstones of Lusitaniadalen Member are generally finely laminated, and throughout the member only sparse bioturbation has been observed (Mørk et al., 1999b). Towards the base of the member it is dominated by dark grey silty laminated mudstones, and some metres above the base, sandstones appear (Mørk et al., 1999b). The sandstones are arranged in subtle coarsening upwards sequences, and like the sandstones in the underlying Deltadalen Member, some sandstones feature Hummocky cross bedding and cross lamination (Mørk et al., 1999b). From approximately 15 m above the base of the member, small carbonate nodules appear in some horizons, and 25 m above the base a distinct horizon containing septarian concretions can be observed (Mørk et al., 1999b). Calcite concretions are also common from the middle of the Lusitaniadalen Member and up (Mørk et al., 1999b).

The concretions are thought to have been formed during early diagenesis as the surrounding shales have been deformed around the nodules as well as the enclosed fossils are intact (Mørk et al., 1999b). Not counting the first 30 m, fossils such as ammonoids, bivalves and vertebra remains are recognised throughout the Lusitaniadalen Member (Mørk et al., 1999b).

Vendomdalen Member

Like the Lusitaniadalen Member, Vendomdalen Member was also first described (and currently defined) by Mørk et al. (1999b). It is named

after a valley south east of the Vikinghøgda Mountain (Mørk et al., 1999b). The boundary between Vendomdalen Member and Lusitaniadalen Member is defined where the silty shale with siltstone beds of Lusitaniadalen Member is replaced by the dark grey uniform mudstones of Vendomdalen (Mørk et al., 1999b).

Vendomdalen Member is mainly made up of silty dark grey mudstones with occasional thin and medium bedded yellow weathering silty dolomite beds (Mørk et al., 1999b). The yellow weathering ferrous, dolomite beds formed during early diagenesis are indicative of the Vendomdalen Member, and they can be recognised throughout central Spitsbergen. Commonly found in Vendomdalen Member are also dolomite nodules (Mørk et al., 1999b). These nodules are usually in the size range of up to tens of cm in diameter. Some flattened nodules may have a horizontal extent of several m, but will still only be around 0.5 m thick (Mørk et al., 1999b). Occasional calcite concretions can be found towards the top of the member (Mørk et al., 1999b). As in Lusitaniadalen Member, also in Vendomdalen Member faint coarsening upwards sequences can be observed, grading from laminated shale to silty mudstones (Mørk et al., 1999b). These are capped by one of the aforementioned dolomite beds or lenses, each of these sequences are between 3 m and 12 m thick (Mørk et al., 1999b).

The upper 50 m of Vendomdalen Member is made up of planar laminated sooty grey mudstone, with thin dolomite beds (Mørk et al., 1999b). At the top of the member is pronounced silty/sandy dolomite bed with abundant poorly preserved ammonoid imprints and some ripple lamination (Mørk et al., 1999b). The Vendomdalen Member is

thought to represent distal shelf deposits, below wave base (Mørk et al., 1999b). Organic material has accumulated due to low oxic content of the bottom water (Mørk et al., 1999b).

The descriptions of the Vendomdalen Member also fit well with the models for the area, throughout the member, the depositional environment transition to a more distal deposition seen as finer grained sediments.

BOTNEHEIA FORMATION

The Botneheia Formation is time-equivalent to the Bravaisberget Formation of western Spitsbergen (Krajewski, 2008; Mørk et al., 1999a). The formation consists of Muen Member and Blanknuten Member (Krajewski, 2008). The Botneheia Formation is an organic rich fine-grained clastic succession, and as such it is considered interesting in regards to petroleum exploration (Krajewski, 2008). The Botneheia Formation represents one large (2^{nd} order) transgression-regression cycle which encompasses two additional transgression cycles (3^{rd} order), the 3^{rd} order cycles are followed by stepwise regression (Krajewski, 2008). The rises in sea level were concurrent with deterioration of bottom water environments (Krajewski, 2008). In Muen Member the bottom-water environment is oxic, this environment gradually becomes dysoxic (Krajewski, 2008). Blanknuten Member is initiated with the same dysoxic environments, but gradates into an euxinic environment in the middle of the member (Krajewski, 2008). The Svalbard euxinia is terminated by a regional regression (Krajewski, 2008).

The Botneheia Formation has exposures on the eastern half of Spitsbergen, Barentsøya, Edgeøya and the southwestern areas of Nordaustlandet (Mørk et al., 1999a). It has also been observed in cores on the Barents Shelf (Riis et al., 2008).

Muen Member

First described by Krajewski (2008), the Muen Member represents the lower 65 m of the Botneheia Formation (54 m in the type section described by Mørk et al. (1999a)). Deposited during the Anisian (Krajewski, 2008) it is the time equivalent of the western Passhatten Member. Muen Member rests conformably on top of the Vikinghøgda Formation, and it mainly consists of shales and mudstone with repeating carbonaceous intervals (Krajewski, 2008). Irregular and scarce carbonaceous concretions throughout the Muen Member do occur (Krajewski, 2008). The upper pars of Muen Member are phosphorite bearing, and this part of the member is constrained between to carbonate cementstone beds which are rich in flattened ammonoids Krajewski (2008).

Muen Member's lower boundary is defined where there is an abrupt change from the Vikinghøgda Formation's dark grey mudstones and siltstones to the fissile shales of Muen Member (Krajewski, 2008). Commonly the Vikinghøgda Formation is terminated with 0.5 m to 2 m thick carbonate cementstone beds, this boundary between Muen Member and Vikinghøgda Formation marks the onset of a transgressive sedimentary cycle (Krajewski, 2008). The upper boundary of the Muen Member to the Blanknuten Member is marked by the onset of carbonate cementstone on top of Muen Member's soft fissile shales (Krajewski, 2008). An exception exist at the Blanknuten exposure, where no

cementstone layer is observed, in this location the boundary is defined at the onset of the cliff forming mudstones and shale towards the top of Botneheia Member (Krajewski, 2008).

Fine grained clastic sediments with a high content of organic material is the primary constituent of the Muen Member (Krajewski, 2008). Muen Member has been subdivided in five separate units; Unit 1 and 3 (3 m to 5 m and 7 m to 9 m thick, respectively) predominantly consists of black soft fissile shale, while the thicker units 2 and 4 (10 m to 22 m thick and 14 m to 16 m thick, respectively) mainly consist of dark grey to black mudstones and shale that is less fissile and more resistant to erosion (Krajewski, 2008). The basal phosphorite concentration horizon observed at the onset of the Middle Triassic succession on Svalbard is, however, not observed in the eastern exposures (Krajewski, 2008). In the two lower units rare large (at least 80 cm) carbonate concretions occur, the concretions are commonly either brecciated or septarian - where multiple cement generations fill the cracks, reptilian bone fragments are found in some concretions (Krajewski, 2008). Unit 5 is 13 m to 18 m thick and consists of black shales where macroscopic phosphate nodules, seams and lenses commonly occur, it is unit 5 that is contained within the previously mentioned carbonate cementstone beds (Krajewski, 2008). Phosphate found in unit 5 is generally in the pristine form, although allochthonous nodules from synsedimentary reworking do occur (Krajewski, 2008).

Blanknuten Member

Blanknuten Member was first described by Mørk et al. (1982) and later refined to its current definition by Mørk et al. (1999a), which have fur-

ther been improved by a better hypostratotype in Krajewski (2008). The Member was deposited in Late-Anisian to Ladinian, but there are still problems constraining the biostratigraphic relations in eastern Svalbard and as such the age of depositional onset and termination is not very certain (Mørk et al., 1999a). Possibly parts of the Anisian is missing at the top of Botneheia Formation. Its lower boundary to the underlying Muen Member is described in the previous paragraph .

Blanknuten Member mainly consists of fine grained clastic deposits such as mud stones and shales, both of which are enriched by organic carbon (Mørk et al., 1999a). Considerable amounts of phosphoric deposits are also found throughout the member, and the deposits with phosphorite can be found as seams, nodules and grains (Krajewski, 2008). The member is further subdivided into informal units; lower-, middle-, upper- and top Blanknuten phosphorite-bearing units (Krajewski, 2008).

The lower Blanknuten phosphorite-bearing unit is between 8 m to 11 m thick and embraces black shale intervals containing varying types of phosphate deposits such as: phosphorite conglomerates, grainstones, phosphatic cementstone beds and horizons of carbonate concretions (Krajewski, 2008). In the black shale intervals, the phosphate concretions are mainly pristine in nature (Krajewski, 2008). The allochthonous phosphate is found as seams and lenses of peloids and grains with sedimentary structures such as cross bedding and ripple lamination (Krajewski, 2008). Phosphate in carbonate cementstone shows an easily recognisable striped texture, and the phosphatic cementstone form distinct yellow weathering beds with lenticular and discoidal bodies

(Krajewski, 2008). The beds and layers of phosphorite grainstone and conglomerate interfinger with layers and seams of black shale creating a complex lithology, and is believed to be a result of sedimentary reworking, concentration and redeposition of the phosphates (Krajewski, 2008). Carbonate concretions occur in two distinct horizons in the lower Blanknuten phosphorite-bearing unit, they are septarian as a rule and can contain liquid bitumen (Krajewski, 2008).

The middle Blanknuten phosphorite-bearing unit is between 14 m to 16 m thick and consists of a thick organic rich shale that weathers into paper shale (Krajewski, 2008). The unit lacks macroscopic phosphate except for in a few levels of the unit (Krajewski, 2008). Two horizons of large carbonate concretions can be found in the unit, much like the underlying unit, also here the concretions are septarian/brecciated and sometimes contain liquid bitumen (Krajewski, 2008).

Upper Blanknuten phosphorite-bearing unit unit is between 2 m to 8 m thick and is encompassed by black shales with phosphate nodules both evenly spread and in horizons (Krajewski, 2008). Most of the phosphorite nodules are pristine, and their shape varies (Krajewski, 2008). Some distinct beds are very rich in fossils such as reptilian- and fish bone fragments, even complete and nearly complete reptilian fossils have been found in these layers (Krajewski, 2008).

Top Blanknuten phosphorite-bearing unit unit is 2 m to 7 m thick (Krajewski, 2008). Its lower part is dominated by phosphorite horizons, and it consists of two sandy cementstone layers either superimposed or separated by a thin black shale interval (Krajewski, 2008). As for the upper part, it is a black shale interval with primary phosphate nodules,

the unit is unconformably cut by an erosion surface at the top (Krajewski, 2008).

1.4.2.3 *Western Barents Sea area*

As the Barents Sea is relatively far away from the investigated Mariaholmen section. Only a brief overview of the Early and Middle Triassic stratotype formations will be given. The Barents Sea is made up of a complicated tectonic regime with several basins which have been filled at different times (Worsley, 2008). The basins have gone through various erosive end depositional events which involve both major subduction and subsequent erosion (Worsley, 2008). Unlike the Lower and Middle Triassic on Svalbard where deposition occurs from a land area to the west of Svalbard (Figures 1.6 and 1.8), deposition in the Lower and Middle Triassic in the western Barents Sea predominantly occur from the Fennoscandian Shield (Glørstad-Clark et al., 2010). This depositional trend is deduced from large-scale clinoforms with a dip direction towards WNW thus implying a provenance area to ESE (Riis et al., 2008; Lundschien et al., 2014).

URD FORMATION

First described by Krasil'ščikov and Livšic (1974), the Urd Formation's current definition is as per Mørk et al. (1982). Urd Formation's type section is found at Miseryfjellet on Bjørnøya (Mørk et al., 1999a) (Figure 1.9) where the slope forming shales of the Urd Formation overlie the cliff-forming siliceous rocks of the Permian Miseryfjellet Formation.

Fig. 1.9: Miseryfjellet on Bjørnøya as seen from the south. Here the steep cliffs of the siliceous Permian Miseryfjellet Formation is overlain by the softer fissile shales of the Triassic Urd Formation.

Urd Formation's lower boundary is defined by a sharp contact with a slight angular unconformity to the underlying Permian cliff forming rocks (Mørk et al., 1999a) (Figure 1.9). The Urd Formation is a time equivalent to the Sassendalen Group in the Spitsbergen area (Mørk et al., 1999a). Sandstones and siltstones grading upwards into silty shale make up the lower 22 m of the formation, while 40 m of silty shales with thin yellow weathering sandstone laminae represents the upper part of Urd (Mørk et al., 1999a). At the very top the 20 cm thick conglomeratic Verdande Bed is found.

STEINKOBBE FORMATION

Steinkobbe Formation is an offshore unit which is known from the Svalis Dome. It was first defined by Mørk and Elvebakk (1999) which is also current. The stratotype is from the shallow boreholes 7323/07-U-03, 7323/07-U-04, 7323/07-U-01, 7323/07-U-07 and 7323/07-U-09. The basal contact with the underlying Klappmyss Formation is defined at 107.05 m in core 7323/07-03 where its black organic-rich mudstones rest conformably on the siltstones of Klappmyss Formation where an abrupt increase in gamma ray logs can also be observed (Mørk and Elvebakk, 1999). It is the time equivalent to the Kobbe Formation, the lower Bravaisberget Formation and the lower Botneheia Formation (Mørk et al., 1999a).

Steinkobbe Formation is dominated by phosphatic and organic rich mudstones, though siltstone beds are also present (Mørk and Elvebakk, 1999). Its facies is equivalent to the Botneheia Formation on Svalbard, thus representing a deep open continental shelf environment (Mørk and Elvebakk, 1999). As it is more similar to the formations on Spitsbergen, it has not been grouped in the Ingøydjupet Subgroup described in the next paragraph (Mørk et al., 1999a).

HAMMERFEST BASIN AND SVALIS DOME

The formations of the Early Triassic in the Hammerfest Basin are all contained within the Ingøydjupet Subgroup which is assigned to the Early to Middle Triassic of the Southern Barents Sea area (Mørk et al., 1999b).

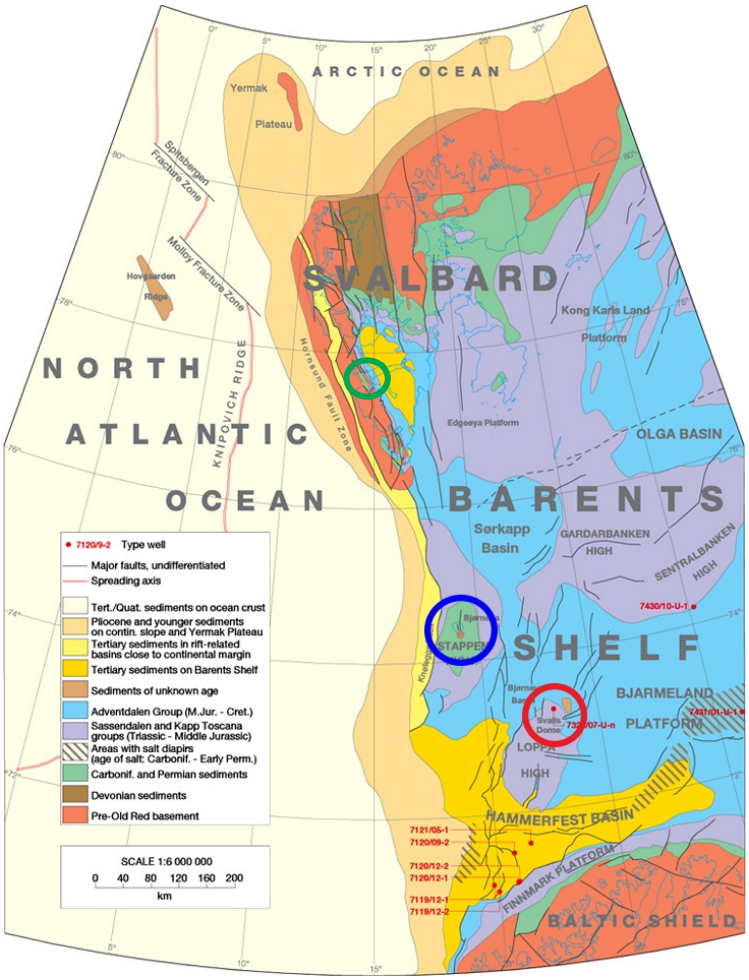

Fig. 1.10: Geological overview of western Barents Sea and Svalbard. Mariaholmen, Bjørnøya and Svalis Dome highlighted in green, blue and red, respectively. Modified after Mørk et al. (1999a).

Havert Formation

Havert Formation is an offshore unit which is known from the Hammerfest Basin, it was first described by Worsley et al. (1988), which is also the current definition. The stratotype and hypostratotype is from the exploration well 7129/12-2 and 7120/9-2 respectively (Mørk et al., 1999b). Being an offshore unit, Havert Formation's base is defined by increasing gamma ray and decreasing density response above the Palaeozoic deposits (Mørk et al., 1999b).

Havert Formation consist of medium to dark-grey shales interbedded by siltstones and sandstones (Mørk et al., 1999b). The formation consists of two coarsening upwards sequences, representing a shallow marine to open marine environments (Mørk et al., 1999b). It is a time equivalent to the Vardebukta Formation (Mørk et al., 1999a).

Klappmyss Formation

The Klappmyss Formation is an offshore unit which is known from the Hammerfest Basin. It was first described by Worsley et al. (1988), which is also the current description. The stratotype and hypostratotype is from the exploration well 7129/12-2 and 7120/9-2 respectively (Mørk et al., 1999a). The lower boundary to the Havert Formation is defined where there is a clear log break with an upward increase gamma ray, ITT and neutron porosity (Mørk et al., 1999b). Klappmyss Formation consist of medium to dark grey shales which transition upwards to alternating shale, siltstone, and sandstone (Mørk et al., 1999b). It is thought to represent shallow to open marine environments (Mørk et al., 1999b). Klappmyss Formation is a time equivalent to the Tvillingodden Formation on Spitsbergen (Mørk et al., 1999a).

Kobbe Formation

Kobbe Formation is an offshore unit which is known from the Hammerfest Basin. It was first described by Worsley et al. (1988), this is also the current definition. The stratotype and hypostratotype is from the exploration wells 7129/12-2 and 7120/9-2 respectively (Mørk et al., 1999a). Kobbe Formation's boundary to the underlying Klappmyss Formation is defined where an increase in gamma ray, ITT and neutron porosity

towards the basal shale is observed (Mørk et al., 1999b). A basal shale 20 m thick grades upwards to interbedded shales (Mørk et al., 1999b). The formation has more variation from platform to basin than the underlying formations (Mørk et al., 1999b). Not counting the transgressive shale pulse on the bottom of the formation, it represents build-out of clastic marginal marine regimes from the coastal areas to the south (Mørk et al., 1999b).

2

METHOD

2.1 OVERVIEW

This chapter summarises the methods used to obtain the data used in the project. It gives an overview of the methods and equipment used to produce the qualitative, quantitative and empirical data on which the thesis is based.

2.2 FIELD WORK AND METHODS

The field work was carried out on Mariaholmen, Svalbard, Norway during one month the summer of 2010.

The supereminent objective of the field work was to investigate the Triassic sequence on Mariaholmen, with special emphasis on palaeoenvironmemt and depositional setting. The profile on Mariaholmen was measured along the south and northeast coast and consists of an approximately 227 m thick conformable succession of Triassic sediments, and a lithological log was drawn in the scale 1:100.

During the field work multiple photographs representing both overview and detailed features were taken along with some detailed logs. A Canon 5D Mark II was used with the following optics: Canon 100 mm

f2.8L macro, Canon 16-35 mm f2.8L, Canon 24-70 mm f2.8L and Canon 70-200 mm f2.8L. The 100 mm macro was used for most of the detailed photographs in order to minimise optical distortion, the 16-35 mm is used for general overview photos while the 70-200 mm mainly was used for taking the panoramic mosaics of the profile.

Systematically, siltstone and shale samples were collected throughout the section. In the sequences dominated by siltstone and shale, samples were gathered with 1 m sample interval (see Appendix D).

Samples are named MXXX.X with the prefix M representing Mariaholmen and XXX.X is the height in m above the initial base of the profile. As a succession of 18.65 m was measured and added to the bottom of the log, this increment was added to the XXX.X number on samples to obtain correct height on the profiles and geochemical logs. This applies to both systematic and discrete samples.

Discrete samples were gathered throughout the sequence to assure that representative samples were collected from all facies. Thus the discrete samples consist of shales, siltstones, sandstone and carbonates. During all sampling great emphasis was placed on collecting unweathered samples to assure optimal geochemical and petrographic analysis.

All current, wind and feature directions are structurally restored compass measurements.

2.3 ROCK TYPE CLASSIFICATION

During field work, the grain size was determined using a loupe to compare the sediments to a grain size ruler. Due to the uncertainty related to this method, representative samples were later investigated in the laboratory using thin sections. Carbonate sediments were classified after Wright (1992) which is a revision of Dunham (1962) and Embry and Klovan (1971), while siliclastic samples were classified according the Udden-Wenthworth scale by Wentworth (1922) and the petrological scheme by Pettijohn et al. (1987). Carbonate porosity nomenclature is as defined by Choquette and Pray (1970).

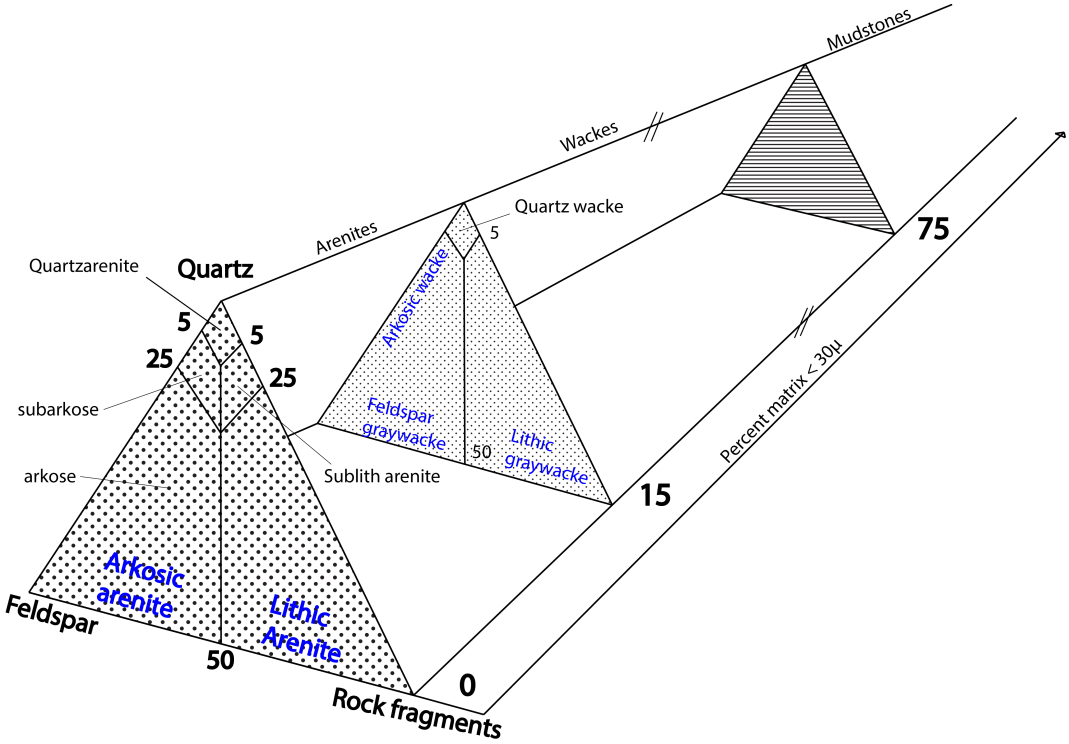

Fig. 2.1: Classification of sandstones. Modified after Pettijohn et al. (1987).

2.4 CUT AND POLISHED ROCK SAMPLES

All sandstone and carbonate samples gathered were cut in half perpendicular to the layering. The final polishing of the sawn surfaces was carried out with 600 grain carborundum powder and subsequently photographed using a Canon EOS 5D Mark II with a Canon Macro Lens EF 100 mm 1:2.8L. A Canon Speedlight 580EXII was used as light source.

All photographs were shot in the RAW format CR2 and transmitted directly to the computer using EOS Utility. Contrast and white balance was adjusted in Photoshop CS5 Camera Raw to make sure the colours were correct before converting to quality 12 JPEG. A 15% grey card was used for the white balance.

The polished sawn surfaces of the samples were first photographed dry, and subsequently with water added to the surface to enhance the visibility of sedimentary features.

2.5 GEOCHEMICAL ANALYSIS

2.5.1 *Preparation of systematic samples for geochemical analysis*

Approximately 100 g of unweathered sample material was selected for analysis. Remaining parts of the samples are stored in marked Zip-Lock bags for reference.

Selected samples were thoroughly washed and dried at low temperature of 40°C to avoid potential loss of hydrocarbons for 48 hours two consecutive times. The samples were ground for 30 seconds to a grain

size of 63 microns or less with a Siebtechnik sling and puck mill and transferred to new ziplock bags for further storage and analysis.

Prior to processing of each sample, the grinder was cleaned using hot water and analytic ethanol to remove any contamination from previous samples.

After grinding, the samples were dried overnight at 40°C to remove any remaining humidity.

2.5.2 *Total sulphur (TS)*

TS is defined as the total content of sulphur contained within a sample including both organic and inorganic sulphur compounds.

It is commonly assumed that most inorganic sulphur origin from pyrite sulphur and little, if any sulphur, is a product of organic compounds. There is one potential source of error pointed out by Berner and Raiswell (1984) which is the occurrence of sulphuric minerals such as barite, anhydrite and gypsum. No gypsum or anhydrite has been observed in hand specimens or thin sections. As seen in Figure 2.2, there is very little barium present throughout the section (~0.043%) thus only minute amounts of barite would be present. It is therefore assumed (as per Raiswell and Berner (1986)) that pyrite (FeS_2) is the only significant sulphur source.

Approximately 0.2 grams of each sample were transferred to ceramic crucibles. The crucibles were then weighed and equal amounts of LECOCEL II and Iron Chip Accelerator were added to enhance the combustion.

Analysis of the crucibles were performed using a LECO CS-200. The amount of CO_2 and SO_2 released during combustion was back-calculated to the total amount of sulphur and total amount of carbon in the sample. Prior to combustion the LECO CS-200 was calibrated using blank samples and reference samples. As a reference the international standard LKSD-1 consisting of lake sediments from Joe Lake and Brady Lake, Ontario, USA was used (Lynch, 1990). The standard has a high TC content of $12.3 \pm 0.031\%$ and a TS of $1.57 \pm 0.029\%$. The LECO CS-200 has a standard deviation of 0.5% for carbon and 1.5% for sulphur.

2.5.3 *Total organic carbon (TOC)*

Total organic carbon (TOC) is defined as the remnant carbon after treating the samples with hydrochloric acid. Volatile organic compounds are considered absent due to diffusion and as such, TOC consists solely of the remaining insoluble organic compounds.

In order to measure the TOC of the samples, all carbonate in the samples have to be removed by treating the weighed samples with 2M HCl. The powdered sample material was transferred to, and weighed in porous ceramic crucibles and thereby cautiously 3 ml HCl was added. Having sat for one hour at 65°C, the samples were rinsed in distilled water before the process of adding HCl and drying was performed once more. Upon completion of the second sequence of drying the samples were rinsed 8 times with distilled water to remove potential acid remnants and $CaCl_2$ formed during treatment.

The crucibles were left to dry for 48 hours at 40°C before being weighed and analysed using the LECO CS-200. It was calibrated using the same procedure as described above, and the internal standard 501 – 504 with 0.357% TC and 0.0276% TS was utilised.

TOC was measured using both LECO method and the Mass Spectrometry (MS) method. The MS derived TOC and LECO derived TOC measurements correlate very well (Figure 2.3) with an r of 0.96. All measurements discussed here relate to the LECO derived measurements.

2.5.4 *Negative LECO measurements*

A few negative values were measured with the LECO instrument, they have been redacted from the plots and graphs. However, they are included in Appendix D. Negative values measured is an indication that the actual value is below the detection limit of the instrument. Actual values when measuring negative are below the zero value set for the instrument through in-house and international standards used for calibration.

2.5.5 *X-ray fluorescence (XRF)*

Description of the method from XRF laboratory procedures for Department of Geology, University of Tromsø - The Arctic University of Norway, by Ravna (2011).

2.5.5.1 *Elements analysed*

A Bruker S8 Tiger wavelength dispersive XRF (WDXRF) located at University of Tromsø - The Arctic University of Norway's geology laboratory was used to obtain atomic element measurements.

WDXRF work by passing the rays through metal slits onto a crystal at a known angle. The crystal diffracts the X-rays and wavelengths can be measured in order to determine the elements. The laboratory has access to approximately 50 international geochemical standards (reference standards), the following elements were measured:

CaO, Sc, TiO_2, V, Cr, MnO, Fe_2O_3, Co, Ni, Cu, Zn, Ga, Rb, Sr, Y, Zr, Nb, Cs, Ba, La, Ce, Pb, Th

Of the elements measured, nickel, vanadium and barium are used herein.

2.5.5.2 *Sample preparation*

During sample preparation great care was taken to avoid potential contamination. Powder used was from the same grinding and crushing process described for the LECO analysis.

Table 2.1: Standard deviations and lower limit of detection for elements measured with XRF.

Element	Standard deviation (ppm)	Lower limit of detection (ppm)
Vanadium	10	3
Nickel	12	3
Barium	24	8

The trace elements are measured on solid pressed powder pellets with wax as binder. A mixture of rock powder and wax is pressed using a Beckman type 0025 ring press using the following procedure:

1. 9 g of rock powder was weighed using a "ship" and transferred to a glass container size 4 and sealed with a plastic lid

2. The powder was poured into an agate mortar with 9 tablets of POLYSIUS POLAB Mahlhilfe. It was mixed for 8 to 10 minutes to ensure homogeneity. No pressure was exerted on the pestle as to avoid material sticking to the mortar

3. A specially constructed double cylinder piston device was utilised for pressing the pellets. The smaller cylinder is put within the larger one, the mix was then transferred to the inner cylinder and levelled out using a glass rod. The piston was carefully inserted into the cylinders and the whole device is placed in a hydraulic press

4. Using the hydraulic press, the sample within the cylinder is exerted to 15,000 kg of pressure for approximately 3 minutes. The valve was then carefully opened to safely bleed off the pressure

5. The sample was extracted from the cylinder and put into a plastic container with a paper label and with markings on the side of the sample

This process was repeated for all 119 samples.

2.5.6 *Stable carbon isotope analysis*

The difference between isotopes of $^{12}C_{Org}$ and $^{13}C_{Org}$ were measured using mass spectrometry. $\delta^{13}C_{ORG}$ is defined as the difference between ^{12}C and ^{13}C of the organic material contained within a rock specimen after removing inorganic carbon. It is referenced to $\delta^{13}C_{V-PDB}$, where $\delta^{13}C_{V-PDB}$ is the $\delta^{13}C$ of a laboratory generated, cross-calibrated substitute to the original PDB termed Vienna Pee Dee Belemnite (Miller and Wheeler, 2012).

Description of method is from laboratory report by Iso Analytical in the United Kingdom.

Weighed sub-samples were taken from the sample vials, placed in universal tubes, acidified with 2M hydrochloric acid, mixed, oven heated at 60°C for 2 hours and left for 24 hours to allow all carbonate to be liberated as CO_2. The sample fractions were then isolated by centrifugation and the acid was then decanted. The samples were then washed twice using distilled water and centrifugation. After acid washing, the fractions were oven dried at 60°C. After drying, the samples were re-ground.

The samples were measured using an Elemental Analyser Isotope Ratio Mass Spectrometry (EA-IRMS). Tin capsules containing either sample or reference material are loaded into an auto-sampler on a Europa Scientific elemental analyser. Here they are sequentially loaded into a furnace operating at 1000°C where the samples are combusted in an oxygen rich environment further raising the sample temperature in the region of approximately 1700°C. Gasses produced during combus-

tion is swept up by a helium stream over a combustion catalyst (Cr_2O_3), copper oxide wires to oxidise hydrocarbons and silver wool to remove sulphur and halides.

The resultant gasses N_2, NOx, H_2O, O_2 and CO_2 are swept through a reduction stage containing pure copper wires held at 600°C. This step removes the O_2 and converts NOx to N_2. A magnesium perchlorate chemical trap removes the water. Carbon dioxide is separated from nitrogen by a packed column gas chromatograph held at an isothermal temperature of 100°C. Resultant CO_2 chromatographic peak enters the ion source of the Europa Scientific $20-20$ IRMS where it is ionised and accelerated. Gas species of different mass are separated in a magnetic field then simultaneously measured using a Faraday cup collector array to measure the isotopomers of CO_2 at m/z 44, 45 and 46.

Both references and samples are converted and analysed in this same manner. Analysis were performed as a batch process where a reference is followed by a number of samples and then another reference.

References used during analysis were IA-R001 (wheat flour $\delta^{13}C_{V-PDB}$ of $-26.43‰$). For quality control purposes check samples of IA-R001, IA-R005 (beet sugar, $\delta^{13}C_{V-PDB}$ of $-26.03‰$) and IA-R006 (cane sugar, $\delta^{13}C_{V-PDB}$ of $-11.64‰$) were analysed during batch analysis of the samples. The standard deviations after 44 samples, 22 samples and 22 samples, respectively, were 0.09‰, 0.09‰and 0.11‰.

IA-R001, IA-R005 and IA-R006 are calibrated against and traceable to IAEA-CH-6 (sucrose, $\delta^{13}C_{V-PDB}$ of $-10.43‰$). IAEA-CH-6 is an inter-laboratory comparison standard distributed by the International Atomic Energy Agency (IAEA) in Vienna.

The total ion beam data were used to determine the carbon percentage of the acid washed samples. This data along with the weight loss data from the acid washing was used to calculate the organic carbon percentage (% TOC) for each sample.

2.5.7 *Rock-Eval pyrolysis*

Measurements were performed using a Rock-Eval 6 instrument. The analysis was performed by Applied Petroleum Technology AS. Rock-Eval 6 has a sensitivity of 12 ppm for CO and 25 ppm for CO_2, with a temperature range from 100 to 850°C. The temperature increase rate can be adjusted in 0.1°C steps from 0.2 to 50°C/minute. S1, S2 and S3 error margin is <10% and T_{Max} error is ±3°C

Rock-Eval measurements are performed by gradually heating the powdered sample specimen under non-isothermal conditions. Released hydrocarbons are monitored and measured. As temperature gradually increases different constituents of hydrocarbon are released, forming the S1, S2 and S3 peaks. After Behar et al. (2001).

2.6 PETROGRAPHY

A total of 46 thin sections were prepared at University of Tromsø - The Arctic University of Norway's geology laboratory. The thin sections are 30 µm thick, polished and without lacquer or cover glass.

2.6.1 *Standard optical microscopy*

Leica Z16 APO Macroscope was used for taking overview photos of the thin sections while conventional microscopy was conducted using a Leica DMLP polarising microscope.

2.6.2 *Reflected light, optical microscopy*

Reflected light microscopy was conducted with a Leica DMLP. During microscopy the transmitted light was shut to optimise the reflected light. The reflected method was mainly used to study opaque minerals such as pyrite and iron oxides such as hematite. Reflected light is also useful for distinguishing between pyrite and pyrobitumen as pyrite looks like brass in reflected light while pyrobitumen is black.

2.6.3 *Photography during microscopy*

When taking pictures under plane polarised light, cross polarised light and reflected light a Canon 5D mounted on the Leica DMLP and Leica Z16AP was utilised along with Canon EOS Utility. White balance was calibrated to the light source on the microscopes.

All pictures of thin sections are marked with one of the following descriptions: PL - plane polarised light, XL - cross polarised light, RL - reflected light.

2.6.4 *SEM*

A Hitachi TM3000 low-vacuum scanning electron microscope with a 5 kV to 15 kV accelerating range and 15x to 30000x magnification fitted with a Bruker Quantax 70 EDS system with 1% accuracy was utilised to perform SEM imaging and element identification.

2.7 CARBONATE BULK DISSOLUTION IN ACETIC ACID

Blocks of carbonate rock were dissolved in diluted and buffered acetic acid to obtain insoluble residues such as conodonts, phosphatised moulds, fish fragments, clasts and plant fragments. The following method which has been described by Jeppson et al. (1999) was utilised.

In order for the process of dissolution to occur at a fairly rapid pace the samples were crushed using a jaw-crusher in order to significantly increase the effective surface area of the samples.

Large tanks were fitted with fine-meshed nets suspending the samples at the centre of the tanks. 45 l acetic acid (10% CH_3COOH), 5 l previously used mix (as acetate buffer) and 100 g tetrasodium phosphate ($Na_4P_2O_7$, to increase phosphorous saturation to minimise apatite dissolution) were mixed and added to the tanks.

The tanks were let to sit for months (where new water was continuously added as it evaporated) until the material had fully dissolved leaving only the non-calcareous material. The insoluble residue was polluted by $Ca(COOH)_2$, a bi-product of the reaction which was removed by repeated rinsing using tap water. Subsequently the insoluble

residue was wet sieved, recovering all fractions > 0.25 mm. All fractions were investigated using a binocular macroscope, but only parts of the 0.25 mm to 0.5 mm were investigated due to time constraints.

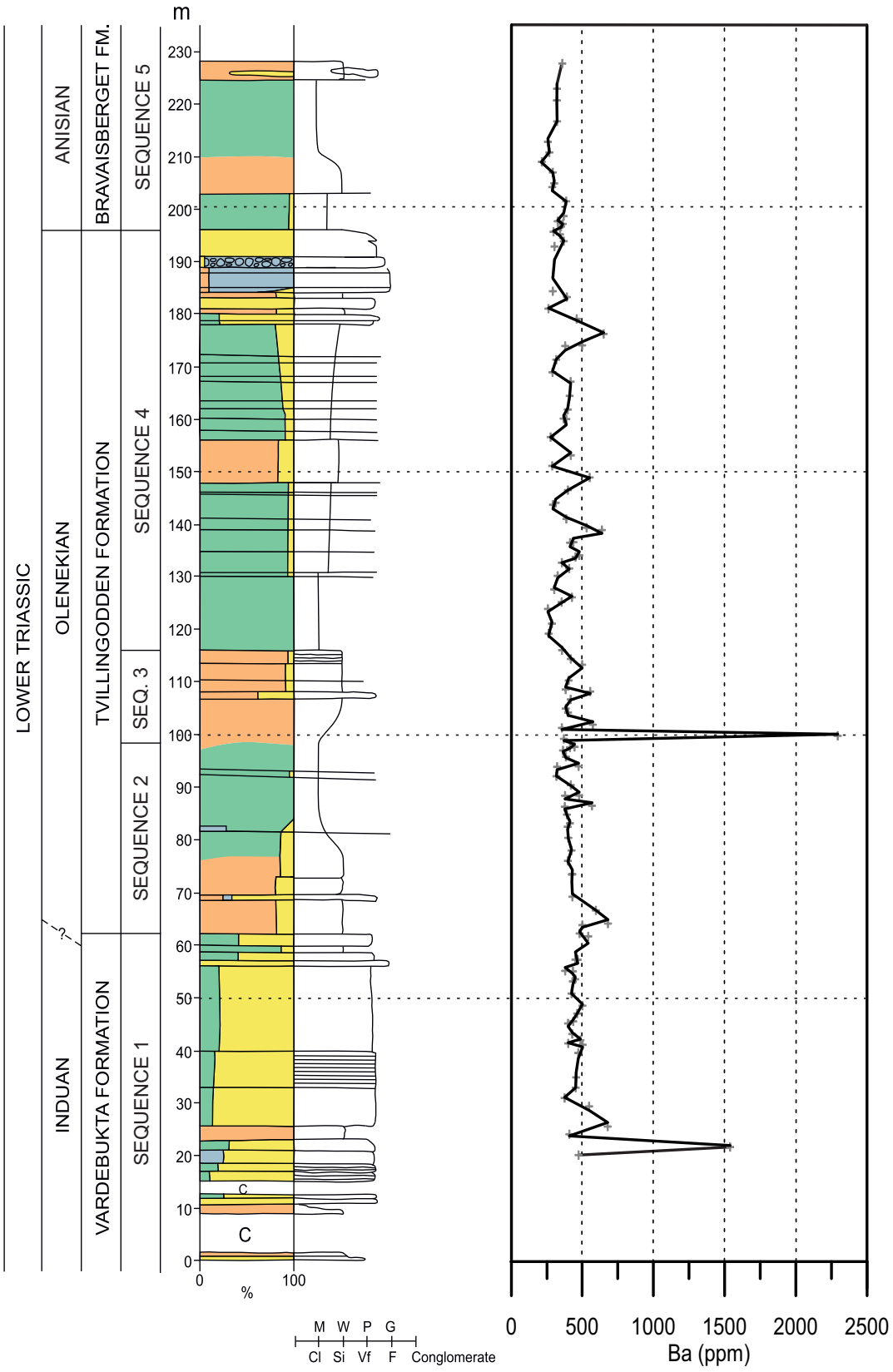

Fig. 2.2: The concentration of barium present in analysed samples. The high values at 20 and 100 m could indicate that the sample contains parts of a vein. Curve is weighted average, discrete points denoted by +. For lithology legend see Figure 3.3.

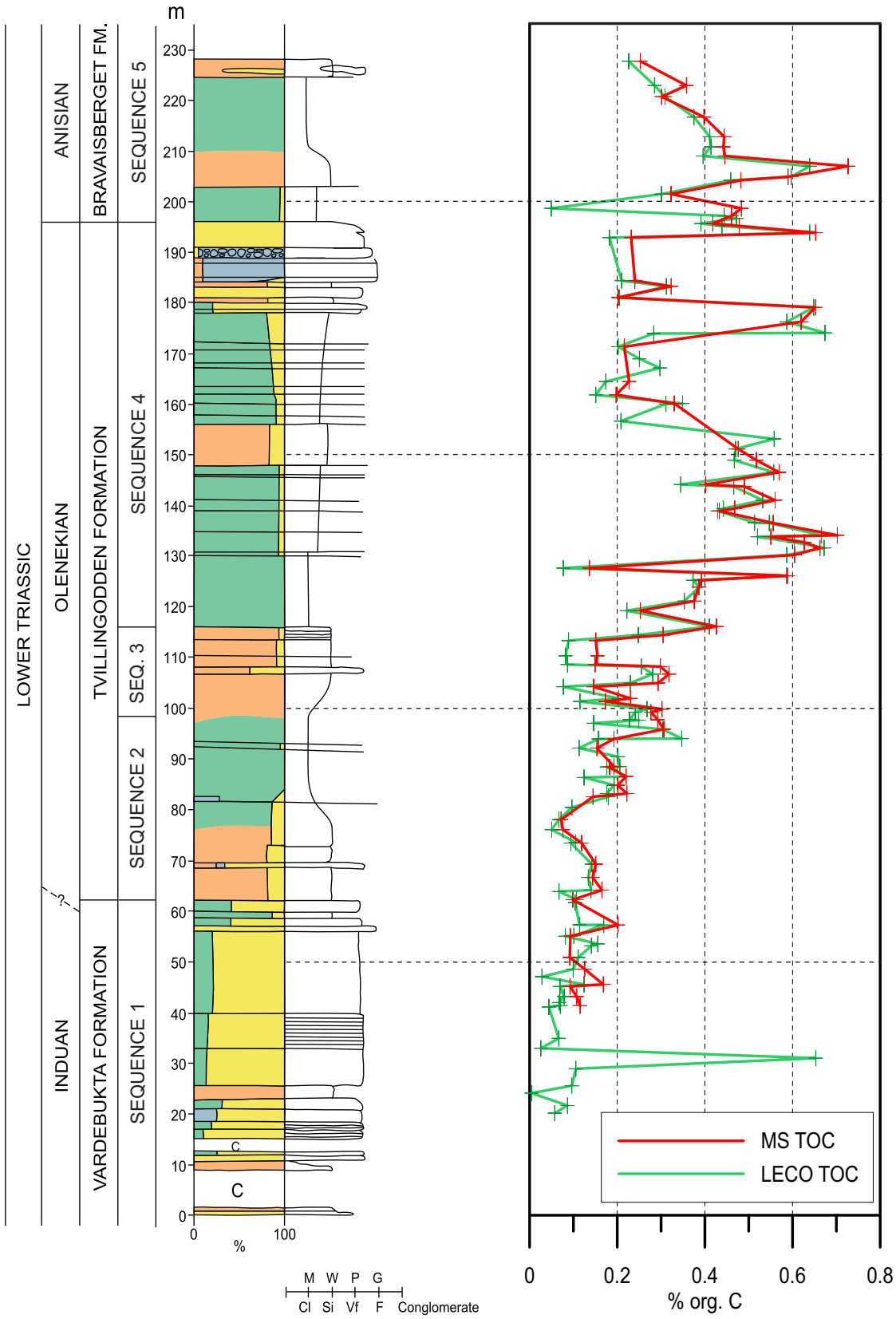

Fig. 2.3: Comparison of LECO total organic carbon (green) and mass spectrometry (red) total organic carbon measurements. Measurements based on the two different methods correlate reasonable well. For lithology legend see Figure 3.3.

3

SEDIMENTOLOGICAL INVESTIGATIONS

In this chapter, a sedimentological description of the Triassic Vardebukta, Tvillingodden and Bravaisberget formations on Mariaholmen will be given. All distances given are in m above the base of the Mariaholmen profile. The base is the first non-covered exposure of the Vardebukta Formation on south-east coast of Mariaholmen.

3.1 GENERAL CHARACTERISTICS

The Triassic sediments studied on Mariaholmen is composed of a 227 m thick succession consisting mainly of sandstone, siltstone and shale with subordinate beds of carbonate grainstones. Based on field observations and measurements of variations in sedimentological and lithological features, the Mariaholmen succession has been subdivided into five distinct sequences (Figure 3.3).

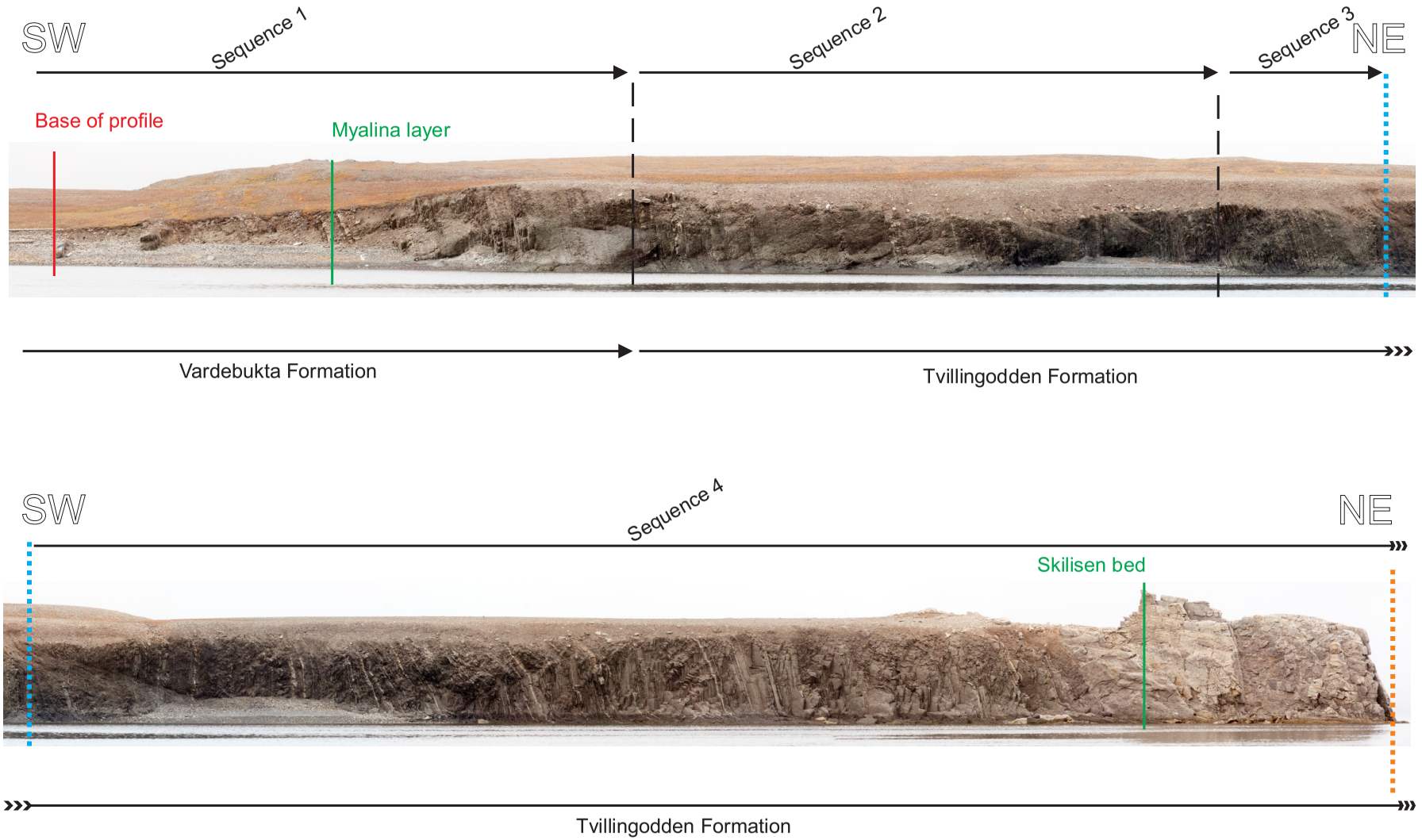

Fig. 3.1: Overview of the Triassic deposits along the south coast of Mariaholmen. Four of the sequences are shown, sequence five is only visible on the eastern side of Mariaholmen (Figure 3.2). The blue dashed line indicate identical position. The orange dashed line represents identical position in Figure 3.2.

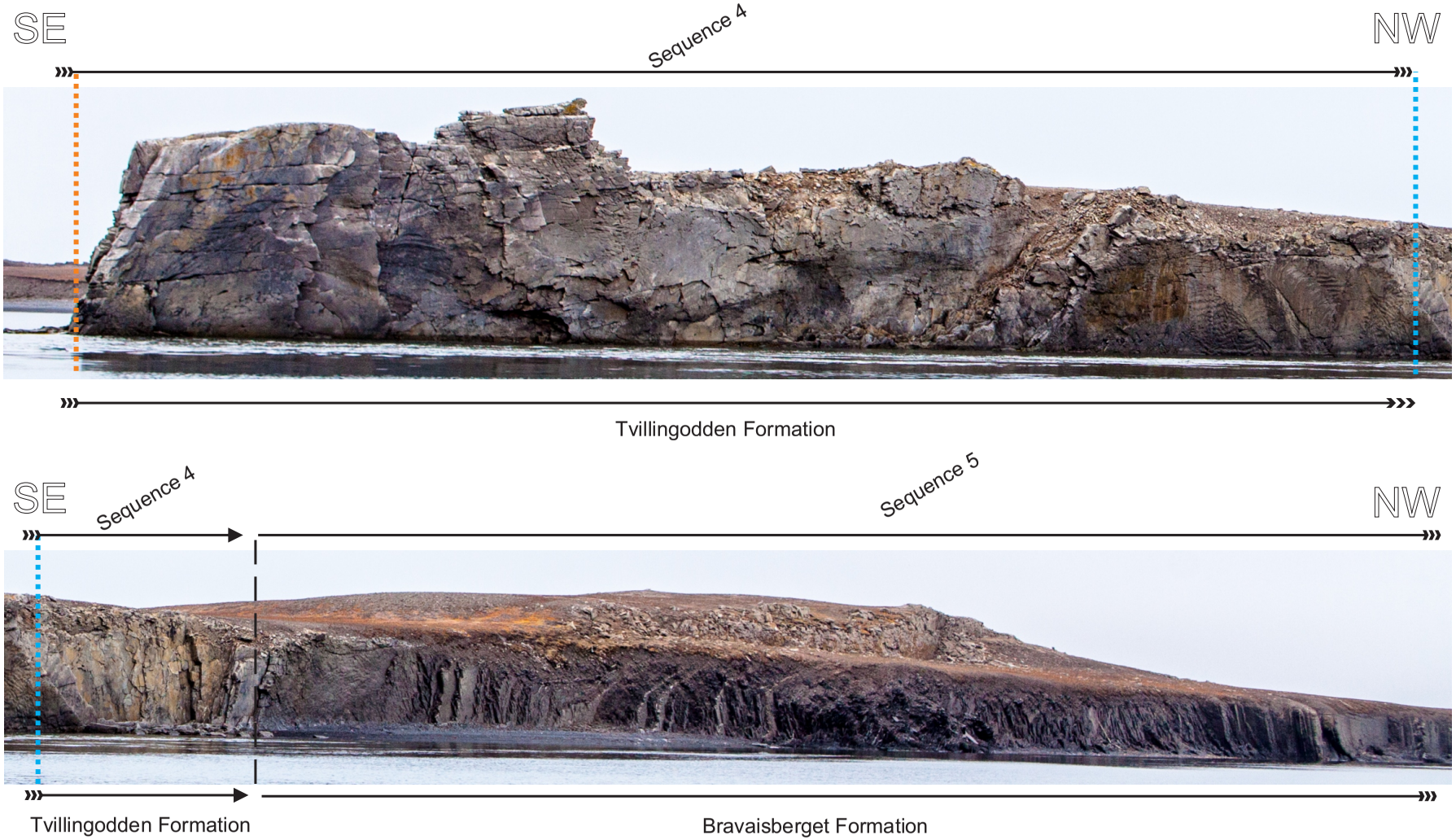

Fig. 3.2: Overview of the Triassic deposits along the east coast of Mariaholmen. Sequence four above approximately 190 m level, sequence five up to approximately 220 m level. The blue dashed line indicate identical position. The orange dashed line indicate identical position in Figure 3.1.

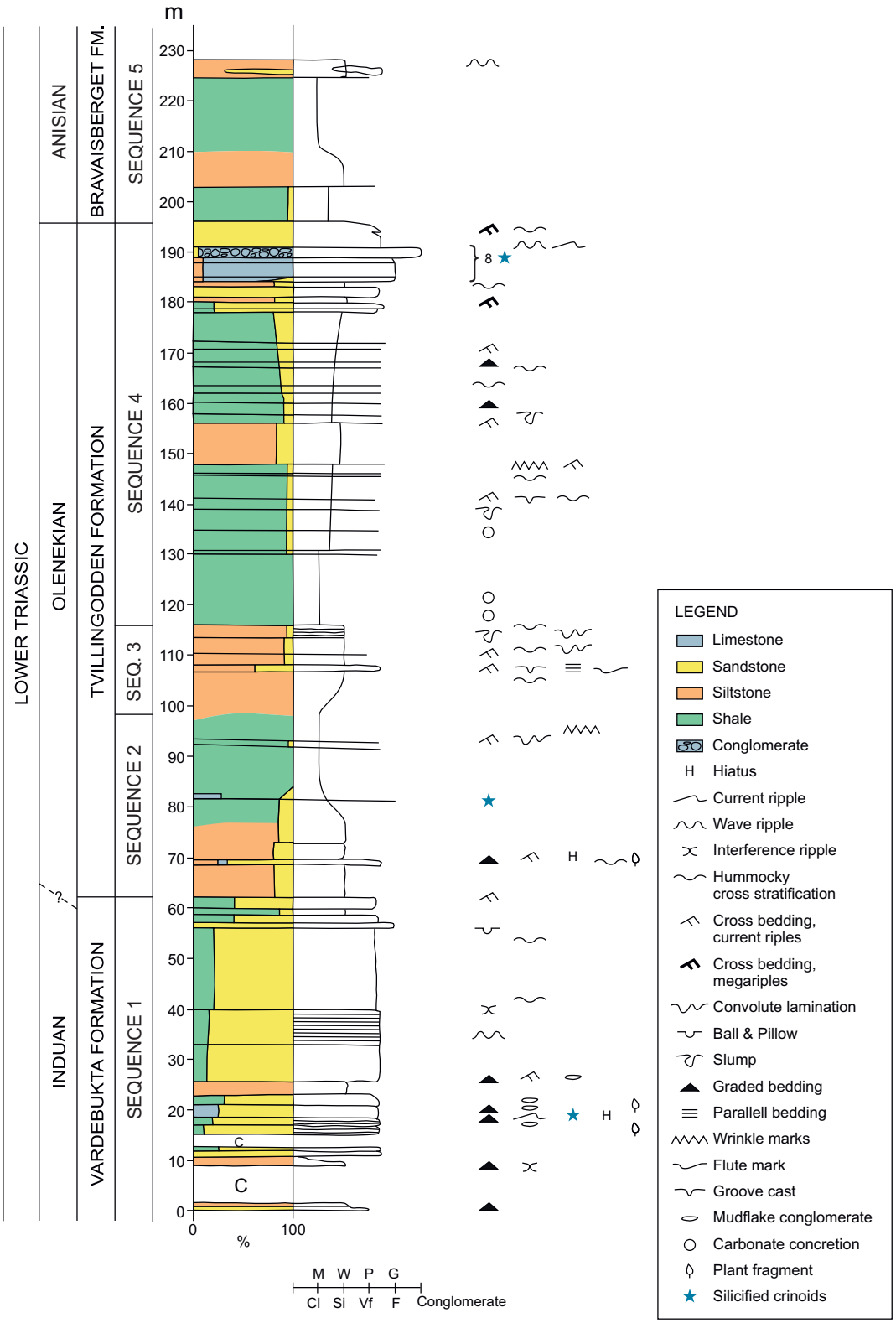

Fig. 3.3: Lithological log of the Mariaholmen profile. Legend seen here applies to all other logs in this thesis.

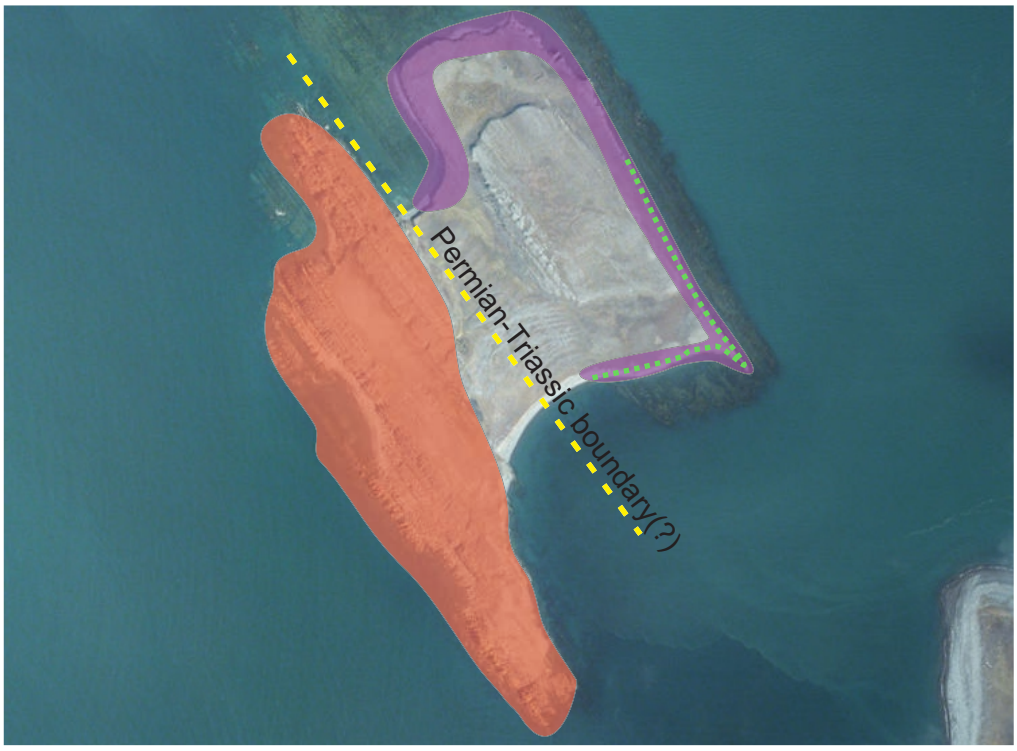

Fig. 3.4: Arial photography of Mariaholmen. Uncovered Permian deposits shaded in orange, yellow stippled line is estimated Permian-Triassic boundary. Area shaded in purple shows coastal exposures of Triassic sediments. Green stippled line shows position of lithological log. Photo from Norsk Polarinstitutt.

3.1.1 *General overview*

The following five subsections contain an overview of the depositional sequences of Mariaholmen. Individual descriptions and discussions of sedimentary features, trace fossils, fauna and diagenesis are found in the proceeding Sections 3.2, 3.3, 3.4, 3.5, 3.6 and 3.7.

3.1.1.1 *Sequence 1*

The first sequence starts at the base of the non-covered Vardebukta Formation on Mariaholmen, and terminates at approximately 62 m with the onset of distinctly siltier deposits.

Fig. 3.5: *Myalina* layer (~30 cm) and adjacent carbonate grainstones at 19 m to 20 m above base. The upper and lower boundaries are between yellow lines. Rightmost yellow line mark 20 m. The *Myalina* layer form a sharp contrast to the over- and underlying sandstone beds. Stratigraphic up to the right.

In the lower part of the sequence (from approximately 0 m to 20 m), the formation consists of sandstone and some few siltstone benches. The *Myalina*-bearing carbonates (Figures 3.5, 3.6 and 3.7) which is commonly observed in the Lower Triassic of the western Svalbard (Mørk et al., 1982, 1999a) are found just below the top of this sequence .

Upwards from the 20 m level, the siltstone content and frequency gradually increases while the thickness of the sandstone beds decrease. In the lower part of the 20 m to 60 m interval, there are abundant thick sandstone benches with thin interbeds of siltstone and shale such as the example in Figure 3.8. When approaching the 60 m level, the deposits have changed to decimetre thick interbedded siltstone with decimetre thick sandstone beds.

Sandstone beds found in the first sequence often have normal graded bedding, and sedimentary features such as interference ripples, cross bedding, current ripples, wave ripples and hummocky cross stratification. Occasional parallel lamination and slumping is also observed.

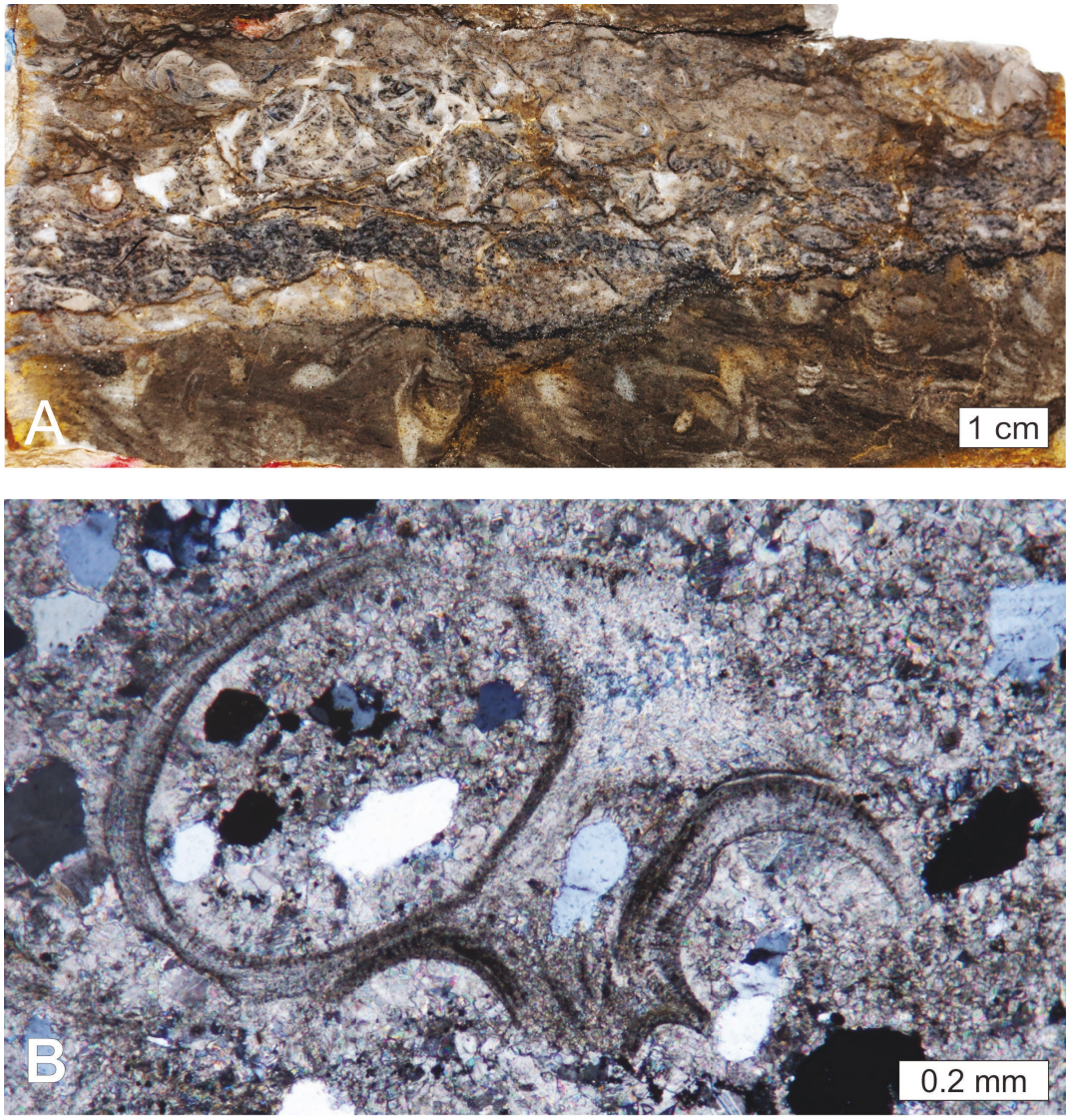

Fig. 3.6: A: Polished slab at 20.10 m from the *Myalina* layer rich in skeletal material. Notice how the disarticulated bivalve shells are oriented at random angles indicating rapid deposition. B: Thin section (XP) of the bryozoan *Arcticopora* found within the *Myalina* layer.

Fig. 3.7: Polished slab from Mariaholmen with a very distinct gradation in the skeletal material. At the top of the specimen, a clear phosphatised hardground can be seen (red arrow). 19.10 m above base.

3.1.1.2 *Sequence 2*

Sequence 2 is the interval covering 62 m to 98 m above the base. It represents the gradual onset of finer material with a transition from the siltstones with occasional sandstone beds at the onset of the Tvillingodden Formation (Figure 3.9), to deposits above 85 m where sandstones are virtually absent (Figure 3.10).

The sequence terminates at 98 m in beds of siltstones and shales such as those seen on the right hand side of Figure 3.10. In the few sandstone beds found throughout the sequence, hummocky cross-stratification, cross bedding and current ripples are found. Within the sequence tool marks such as flute casts and grove casts were observed (Figure 3.11). Also ball and pillow structures is recorded in the sequence (Figure 3.21).

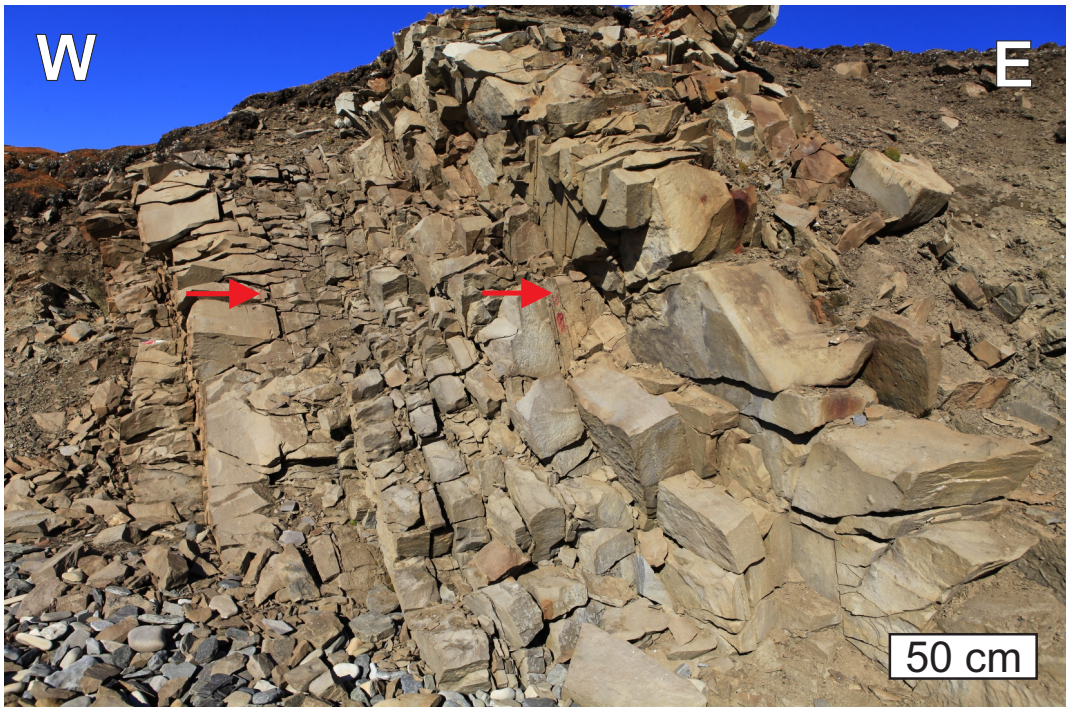

Fig. 3.8: Lower part of the first sequence. Notice the benching of sandstones with very thin claystone layers between benches. Arrows (from left) indicate 27 m and 28 m from base.

3.1.1.3 *Sequence 3*

Sequence 3 is a short, minor, coarsening upwards interval ranging from 98 m to 116 m. As seen in Figure 3.12, this sequence grades from the shale at the top of sequence 2 back to fine grained siltstone deposits with occasional sandstone beds. Within the sequence features such as cross bedding, convolute lamination, hummocky cross stratification, parallel bedding and slumping are observed.

3.1.1.4 *Sequence 4*

Sequence 4 reaches from 116 m to 196 m above the base of the profile. This sequence represents the longest coarsening upwards sequence on Mariaholmen. Initially, the sequence consists of finely bedded siltstone

Fig. 3.9: From the lower part of sequence 2. Siltier material characterises the deposition after the onset of the Tvillingodden Formation. The red arrow is at 79 m above base. Stratigraphic up to the right.

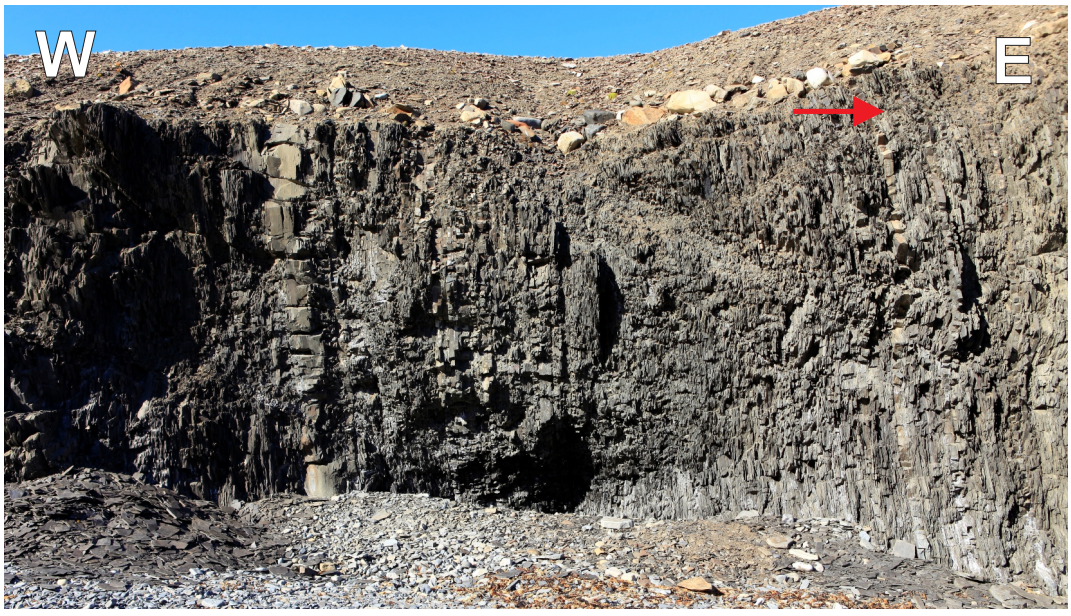

Fig. 3.10: Termination of sequence 2 at 98 m (red arrow). This part of the succession consists mainly of interbedded siltstone and shale. Stratigraphic up to the right.

Fig. 3.11: Groove cast from the underside of a sandstone bed in sequence 2. It is approximately 4 cm wide and minimum 80 cm long

Fig. 3.12: Photo from 106 m above base (red arrow). The occurrence of siltstone and occasional sandstone beds has increased compared with the underlying sequence. Stratigraphic up is to the right.

and shale beds. However, the sequence gradually transitions into higher energy environments with an increasing amount of siltstone and sandstone beds. At the top of the fourth sequence, it is characterised by sandstone and carbonate beds.

At approximately 185 m, the Skilisen Bed carbonate, which can be found in the Tvillingodden Formation throughout the southwestern Svalbard (Mørk et al., 1999a), are found (Figures 3.13 and 3.32). After the Skilisen Bed, a polymict conglomerate consisting of large blocks up to 1 m (Figure 3.14) are found before the sequence terminate in fine grained sandstone beds.

Within the sequence, two layers containing strata bound concretions are found. Within the finer grained beds, features such as slumping, wrinkle marks, convolute lamination and flute casts can be seen. While in the coarser grained beds, features such as cross bedding, hummocky cross stratification and graded bedding become more common toward the top of the sequence. At the top of the sequence, numerous oc-

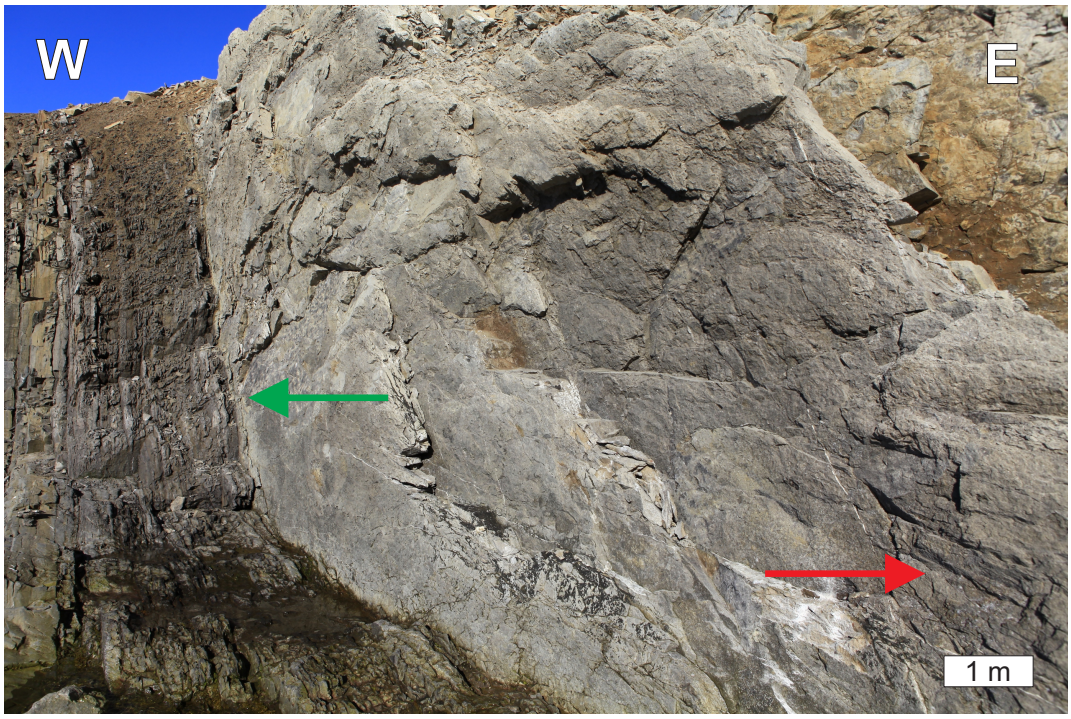

Fig. 3.13: Base of Skilisen Bed as seen on Mariaholmen at 187.5 m (red arrow). Notice how the underlying beds have been slightly eroded (green arrow).

currences of wave ripples, trough cross-bedding, parting lineation are found (Figures 3.18 and 3.19) .

3.1.1.5 *Sequence 5*

Sequence 5 starts at 196 m with the onset of abruptly siltier sediments following the sandstones of sequence 4. Throughout the sequence, there is a steady increase in the amount of shale representing increasingly lower energy in the depositional environment (Figure 3.15). At the very top of the sequence, a sandstone channel is intersecting the shale at 227 m. This channel fill has no visible sedimentary structures, while directly underneath the channel, sandstone beds with wave ripples are found. Further upward, the sediments are tectonically disturbed and have not been investigated.

Fig. 3.14: Polymict conglomerate immediately above the Skilisen Bed at 189.15 m above base. A: Large angular to sub-rounded clasts found throughout the bed. Red arrow: approximate location of B. B: Polished slab with examples of the smaller clasts found within the conglomerate. The clasts are sub-rounded and well-rounded, and lithology varies between sandstone, carbonate grainstone and phosphorite. Overlying sediments drape over the leftmost grey clast indicating an erosive contact.

Fig. 3.15: Photo of the lower part of the Bravaisberget Formation as seen on Mariaholmen. The sandstone beds from the upper part of the Tvillingodden Formation have been replaced by interbeds of shales and siltstones. Red arrow at 225 m.

3.2 SEDIMENTARY FEATURES

3.2.1 *Cross-stratification*

3.2.1.1 *Hummocky cross-stratification*

Hummocky cross-stratification is found in sandstone beds throughout the succession, however, the hummocky cross-stratification is most common in three levels:

- Upper half of sequence one, 40 m to 60 m.
- Throughout sequence three, 98 m to 116 m.
- Upper two thirds of sequence four, 140 m to 196 m.

Hummocky cross-stratification found on Mariaholmen is observed in fine-grained sandstone beds (decimetre thick) with mm thin laminae (Figures 3.17 and 3.16) where a mix of first, second and third order boundaries (Cheel and Leckie, 1993; Dott and Bourgeois, 1982; Campbell, 1966) are observed at various locations. The hummocky cross-stratification observed has mm scale tangential cross bedding. Alternating layers of very fine grained silt and sand with both sparse bioturbation (Figure 3.16) and in some examples more bioturbated (Figure 3.17) are typical for the hummocky cross-stratification on Mariaholmen.

It is common for hummocky cross-stratification to appear as single beds with finer grained material as deposits become more distal (Cheel and Leckie, 1993), it should thus be reasonable to assume that the beds on Mariaholmen represent relatively distal deposition.

Hummocky cross-stratification was first described by Campbell (1966) and later defined by Harms et al. (1975). The processes developing hummocky cross-stratification have been discussed for decades, and have yet not been fully understood (Harms et al., 1975; Dott and Bourgeois, 1982; Duke et al., 1991; Becker et al., 2001; Peters and Loss, 2012; Morsilli and Pomar, 2012; Basilici et al., 2012).

Hummocky cross-stratification deposition is described by Dott and Bourgeois (1982) as waning of storm waves followed by fair weather sedimentation and burying. Hummocky cross-stratification is most commonly formed by redeposition below normal fair-weather wave-base of fine sand (Dott and Bourgeois, 1982; Duke et al., 1991; Peters and Loss, 2012). This fine sand is delivered offshore by flooding rivers, and/or by storm-wave scouring of the shoreface and/or shoals (Dott and Bourgeois, 1982; Duke et al., 1991; Peters and Loss, 2012). Hummocky cross-stratification is formed on the shoreface and shelf by waves, and is considered to represent a wave-dominated setting. (Dott and Bourgeois, 1982; Duke et al., 1991; Peters and Loss, 2012).

Hummocky cross-stratification beds typically have a sharp basal contact to the underlying bed. Beds of hummocky cross-stratification consist of randomly oriented antiform hummocks and synform swales that form relatively thin (1 mm to 2 cm) laminae (Dott and Bourgeois, 1982). Each lamina is thought to represent a wave or wave train, while the bed as a whole is believed to represent a storm event (Dott and Bourgeois, 1982). Hummocky cross stratification, unlike any other depositional sedimentary feature, has a vertical cross section that looks identical from all sides (Dott and Bourgeois, 1982).

Table 3.1: Water depths at which hummocky cross-stratification commonly form. Modified after Morsilli and Pomar (2012).

Min (m)	Max (m)	Dep. Setting	Age	Locality	Reference
5	30	-	-	-	Harms (1979)
-	3.8	Fore beach	Recent	North Sea	Reineck and Singh (1986)
2	5	Nearshore	Pliocene	Italy	DeCelles and Cavazza (1992)
15	40	Open shelf	Cretaceous	Oregon	Hunter and Clifton (1982)
10	40	Open shelf	Jurassic	Denmark	Surlyk and Noe-Nygaard (1986)
14	24	Offshore	Recent	North Sea	Gadov and Reineck (1969)
-	160	Offshore	Recent	Bering Strait	Nelson (1982)

Fig. 3.16: Polished slab of fine grained sandstone with very little bioturbation which results in well-preserved sedimentary features. Mm scale tangential cross bedding with partial erosion in the lower right. Hummocky cross-stratification with 2^{nd} and 3^{rd} order laminae boundaries. 2^{nd} order laminae at cm scale, while 3^{rd} order laminae are at a mm scale (1st order boundary is not present in this sample). From 69.45 m above base.

It has been debated whether hummocky cross-stratification can be used as an indicator of absolute water depths (Morsilli and Pomar, 2012). However, as can be seen in the summary found in Table 3.1, there is a large spread in the proposed water depths. Peters and Loss (2012) show through empirical data from the Gulf of Mexico, that using sedimentary structures as indicators of water depth (even relative) is difficult. This difficulty arises as there is no distinct depth of wave penetration corresponding to either storm or fair-weather wave bases (Peters and Loss, 2012).

Fig. 3.17: Polished slab of fine grained sandstone. In the lower two thirds, the primary lamination has been disturbed by bioturbation. At the top of the bioturbated unit, there is a clear 1st order boundary before the onset of hummocky cross-stratification which also include 2nd and 3rd order laminae boundaries. From 36.65 m above base.

Also proposed as a mechanism for the formation of hummocky cross-stratification, is the reworking occurring when internal waves (gravity waves) propagate along the pycnocline break on the shelf (Morsilli and Pomar, 2012). This create episodic events of turbulence, induced up-slope currents, down-slope currents and oscillatory currents which together lead to the formation of hummocky cross-stratification (Morsilli and Pomar, 2012).

3.2.1.2 *Wave and current ripples*

Wave and current ripples are common throughout the succession on Mariaholmen and are usually seen as cross bedding in cross sections (Figure 3.18). However, at the top of sequence four huge exposure surfaces were observed (Figure 3.19) with well-preserved ripples on the bedding planes. Palaeocurrents observed from the current ripples show a directional trend from N-NW (Table E.1 in Appendix E).

3.2.1.3 *Trough cross-bedding*

Approximately 190 m above base, multiple occurrences of trough cross-bedded mega-ripples were observed. The trough cross-bedding is seen as several metre long and approximately 1 m wide trains of ripples on large bedding planes exposed at the top of sequence four (Figure 3.19). These bedding planes also allowed for the measurement of trough cross-bedding angles. These measurements show that they have a prevailing palaeocurrent direction between 315° and 360° with an average of 340° (Table E.1 in Appendix E).

Trough cross-beds typically form by migration of subaqueous three dimensional dunes or as a result of high energy current ripples. As the trough cross-beds on Mariaholmen appear as mega-ripples, they most likely represent dune migration.

Fig. 3.18: Example of mega-ripple cross bedding with two bed sets from 192.65 m above base.

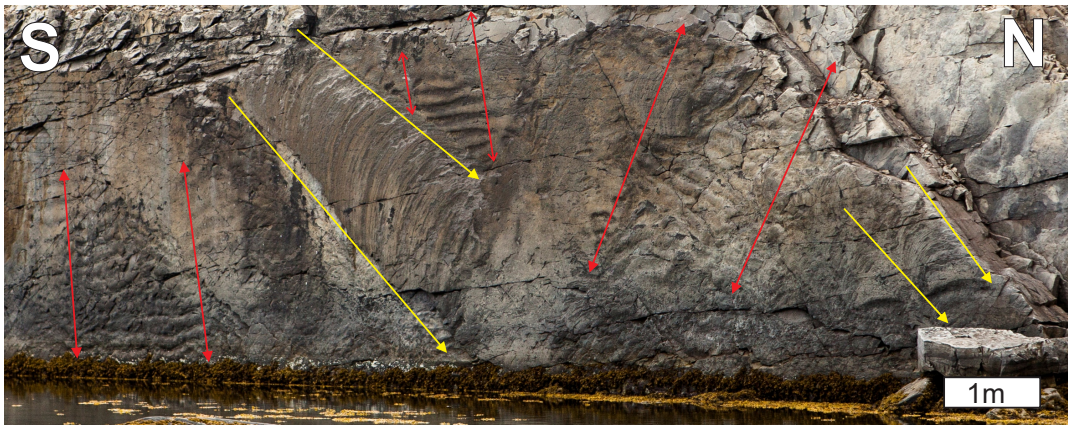

Fig. 3.19: Sedimentary features as seen at the bedding plane at 190 m above base. Areas between red arrows represent wave ripples, areas situated between yellow arrows represent trough cross-bedding. Yellow arrows thus show the direction of the palaeocurrent. Wave ripples and trough cross-bedding appear on the same bedding planes, the leftmost trough cross-bed cuts the wave ripples.

3.2.2 *Deformation*

3.2.2.1 *Convolute lamination*

Convolute laminations are generally developed in sediments that have been rapidly deposited (Allen, 1977). The beds are continuous and the convolution does not affect the bed thickness (Dzulynski and Smith, 1963). Convolute lamination develops when the rapidly deposited sediments are disrupted after deposition, for instance when a change in loading occurs so that the overburden pressure equals the pore pressure (Owen, 1987). This leads to a weight transfer from the grain contacts to the fluid which results in liquefaction (Owen, 1987). Other mechanisms include slope failure, breaking waves, flood surges, over steepening, earthquakes, groundwater movement (Owen, 1987). There is no need for an unstable bulk density gradient at the time of deposition to form convolute lamination (Allen, 1977).

Fig. 3.20: Convolute lamination situated between two beds of planar laminated siltstone. The upper part of the convoluted unit was eroded prior to the deposition of the overlying siltstone. Polished slab from 92.95 m above base.

Convolute lamination does not give an indication of the depositional environment, but serve only as a fossil record of the forces that acted upon the sediments immediately following deposition (Dzulynski and Smith, 1963). Convolute lamination can be found both as a slight over steepening and/or tilting of sedimentary features, or as more commonly seen on Mariaholmen, as narrow upturned laminae which are often truncated at both the top and bottom surface (Figure 3.20).

3.2.2.2 *Ball-and-pillow*

Ball-and-pillows were observed in one single level (56.8 m). They are situated in a 0.8 m thick fine grained sandstone bed where the lower half have ball-and-pillow development (Figure 3.21). The largest pillow has a height of 26 cm and is 70 cm wide. Metre sized ball-and-pillow structures are also present on Mariaholmen´s northern exposure, approximately 600 m from the measured profile (Figure 3.21), showing that the ball-and-pillow structures has a certain lateral extent.

Ball-and-pillows are a variant of soft sediment deformation. The ball-and-pillow structures consist of round masses of clastic sediment (typically sand) slumped downwards into a matrix, ball-and-pillow structures are interpreted to represent an extreme form of a load structure (Owen, 2003). Load structures are events of partial to complete inversion of sediment layers where high density sediments overlie lower density sediments (Allen, 2003). For load structures to form there must be a trigger mechanism (such as: earth quakes, abnormal pore pressure increases or a sudden appearance of coarser deposits), both the high and low density sediments must also have little or no compaction and be fully water saturated (Allen, 2003).

Fig. 3.21: A: Ball-and-pillow as seen at 56.8 m (green arrows). The pillows are not separated from the sandstone bed. Stratigraphic up is to the right. B: Ball-and-pillow structures (green arrows) as seen at the northern unmeasured exposure on Mariaholmen. At this location the ball and pillows are detached from the overlying sandstone bed. Stratigraphic up is to the left.

3.2.3 *Wrinklemarks*

Wrinklemarks were observed at three levels on Mariaholmen, specifically at 114 m, 148 m and 170 m above basis. The wrinklemarks found have either scour texture or ridge texture. The wrinklemarks on Mariaholmen have millimetre scale, where the distance between crests are between 3 mm to 5 mm, with an amplitude of 0.5 mm to 2 mm (Figures 3.22 and 3.23). The scour shaped wrinklemarks, have through diameters of 2 mm to 5 mm. The wrinklemarks on Mariaholmen are found either adjacent to, or in close proximity to hummocky cross-stratification, which indicates that they have been formed between fair weather and storm weather basis.

Wrinklemarks are morphological biosignatures formed at the sediment-water interface in wave-dominated environments by microbial mats (Mariotti et al., 2014).

Wrinklemarks are commonly observed in the ancient geological record (Ordovician or older) and seldom in modern sediments (Hagadorn and Bottjer, 1997; Mariotti et al., 2014). They were earlier interpreted as a product of wind shear, sediment loading and current waning (Hagadorn and Bottjer, 1997). However, Hagadorn and Bottjer (1997) suggest that wrinklemarks likely represent the formation of algal mats. Wrinklemarks are therefore thought to be mainly preserved in the ancient record as the relatively intense bioturbation destroying the mats have occurred since the Ordovician (Hagadorn and Bottjer, 1997; Mata and Bottjer, 2009). Wrinklemarks were by Noffke et al. (2001) proposed as a new sedimentary structure: microbial induced sedimentary struc-

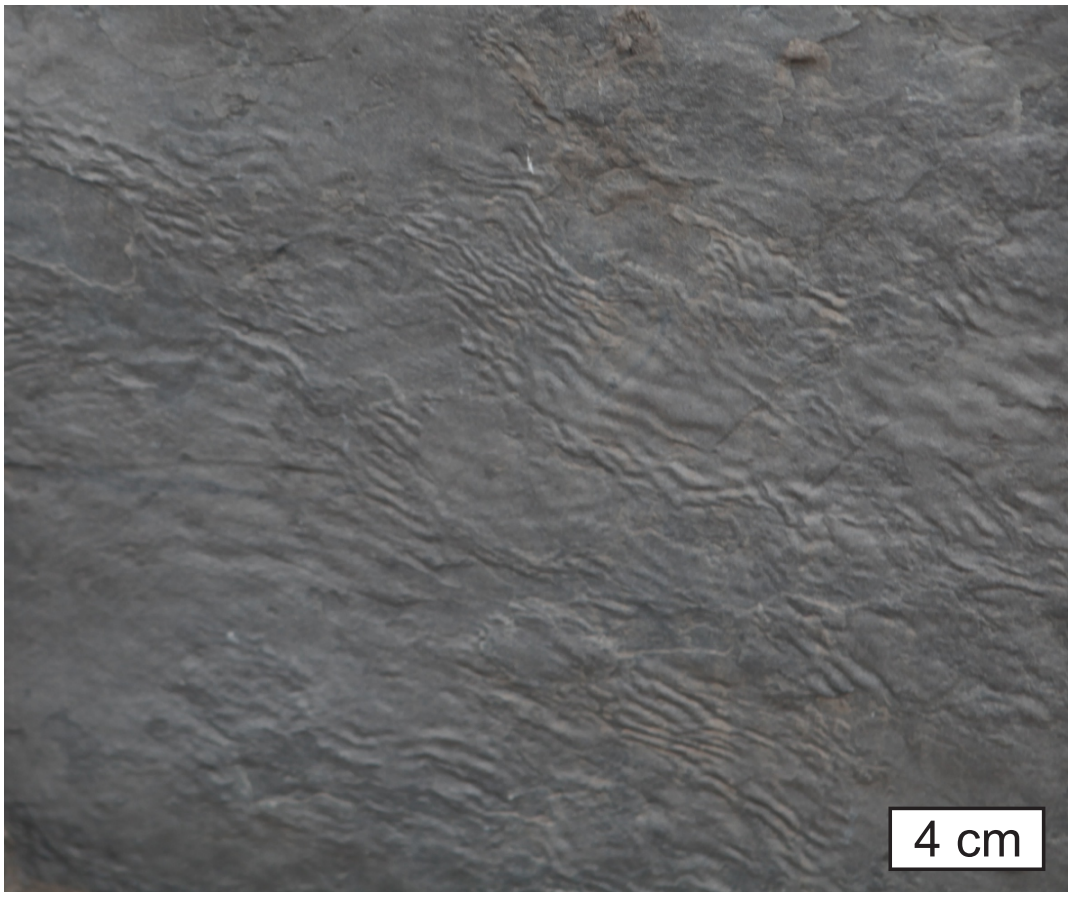

Fig. 3.22: Field photo of wrinklemarks of the ridge variant from 148 m above base. The surface of the bed is slightly undulating, and the wrinklemarks have varying directions, but the ridges had an average direction of 70°/270°.

tures. Noffke et al. (2002) showed that mat colonisation occurs where fine grained quartz sand is deposited in areas with flow is sufficient enough to sweep the finer grained mud from the surfaces, but not strong enough to erode the algal mats.

Porada et al. (2008) suggested that wrinklemarks of the kinneya type (parallel flat-topped ridges) is formed when oscillating groundwater flow below algal mats in the intratidal and subtidal zone. Periodic reversal of flow is suggested as the mechanism behind the ripple structures at the interface with the overlying microbial mat. However, Mariotti et al. (2014) highlights that the model established by Porada et al.

(2008) does not cover issues related to restricted grain size or ridges and pits on the same surface. With wave-tank experiments, Mariotti et al. (2014) further demonstrated that wrinklemarks form not by direct movement of sand grains, but by wave action on millimetre sized, light microbial fragments, which in turn produced sand ridges and scour pits.

Ridged wrinkles are formed when rounded microbial mat fragments transport sand grains from depressions to ridges, while pitted wrinkles form when microbial mat aggregate anchored to the sediment oscillate to create the pits (Figure 3.24) Mariotti et al. (2014).

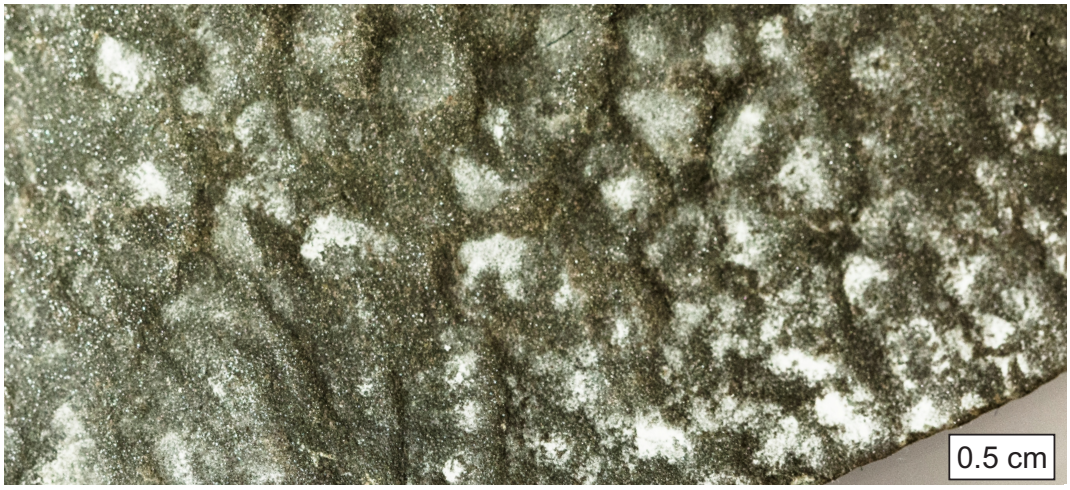

Fig. 3.23: Wrinklemarks as seen at 95.7 m above base. Scour marks (pit) have an average diameter of roughly 2 mm to 5 mm.

Though mainly common in the ancient record, wrinklemarks have been reported as an anachronistic facies occurring in the aftermath of mass extinctions and environmental stress throughout the post-Ordovician Phanerozoic (Mata and Bottjer, 2009; Mariotti et al., 2014; Woods, 2014). During the post-Ordovician Phanerozoic, the wrinklemarks are found mainly in the intertidal and storm-dominated subtidal environments (Mata and Bottjer, 2009).

Specifically, Pruss et al. (2004); Mata and Bottjer (2009) have described the occurrence of wrinkle structures in association with hummocky cross-stratification in Triassic sediments. They suggest that the proliferation and preservation of these microbial mats is a result of reduced infaunal bioturbation after the Permian-Triassic extinction event.

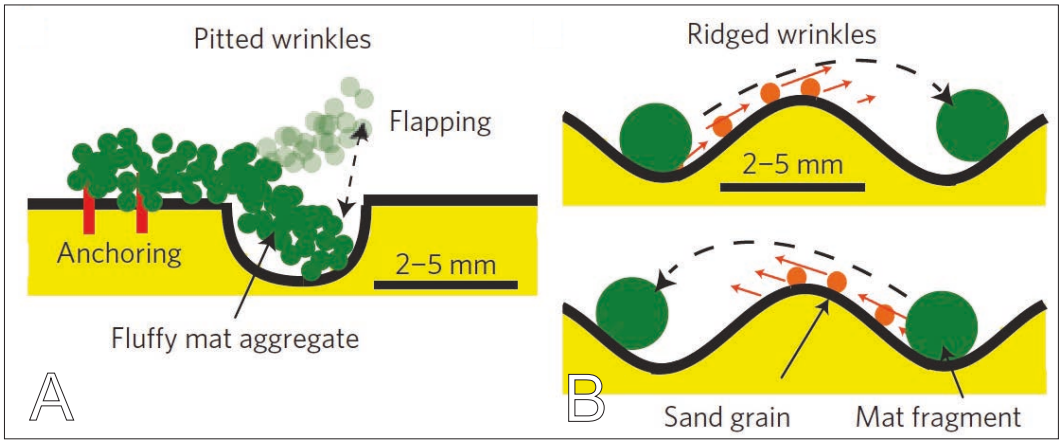

Fig. 3.24: Formation of wrinklemarks. A: Forming of pitted/scour wrinklemarks occur when anchored microbial mat material oscillate to create pits in the sediment. B: Forming of ridged wrinklemarks occur when rounded microbial mat material transport sand grains from depressions to ridges. Modified after Mariotti et al. (2014).

3.2.4 *Tempestites*

The tempestites on Mariaholmen (Table 3.2) are observed in relatively thin, fine grained sandstones (Figure 3.25). These sandstones frequently contain skeletal material such as disarticulate bivalves, disarticulated inarticulate brachiopods and crinoid fragments. The skeletal material has a random orientation, with an upwards decrease in both size and abundance within the individual tempestite beds (Figure 3.26). The bivalves are most frequently disarticulated and have often been micritized prior to redeposition. Some bivalves also have *Trypanites* isp. borings.

Figure 3.25 show the location of the tempestite at the 103m to 104 m level where multiple beds of similar sandstone beds are present. Considering the abundance of similar sandstone beds, it seems reasonable to assume that tempestites on Mariaholmen are more abundant than the samples presented in Table 3.2. The relatively poor exposures on Mariaholmen led to significant difficulty in observing features within sandstone beds in the field.

Table 3.2: Tempestites seen in samples from Mariaholmen.

Height (m)	Sample name
1.15	M-17.5
20.35	M1.7
20.45	M1.8
103.85	M85.2
103.95	M85.3
104.35	M85.7

Tempestites are sedimentary features produced during storm events (Aigner and Reineck, 1982). Prevailing high energy conditions bring large amounts of coarse grained material relatively near the sea shore into suspension (Myrow and Southard, 1996). This mixture of sediments and water subsequently move as a gravity (density) driven flow that eventually redeposits the suspended sediments in deeper water (Myrow and Southard, 1996).

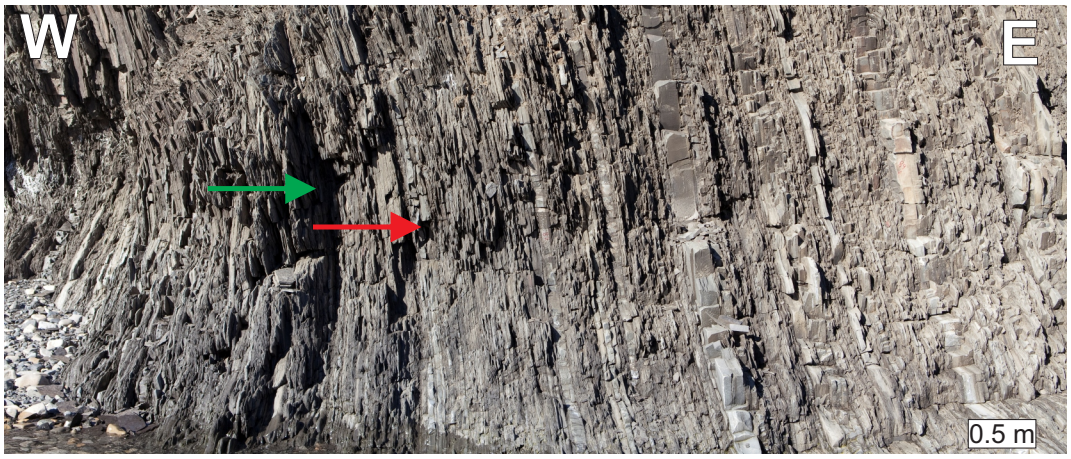

Fig. 3.25: Siltstone with frequent sandstone beds interpreted as tempestites. Red and green arrow: location of tempestite at 104.35 m and 103.85/103.95 m respectively. Stratigraphic up to the right.

Fig. 3.26: Polished slab of tempestite at 20.35 m. Fine grained sandstone that is very rich in skeletal material. Notice how the skeletal material decrease upwards in both size and abundance. In the lower part the skeletal material has a random sorting possibly indicating rapid deposition, while in the upper third the larger shells are oriented with convex up an indication that currents have had time to orient the bivalves. Bioturbation and lamination is absent within the tempestite.

3.2.5 *Hardgrounds*

3.2.5.1 *Hardground at 19.05 m*

At the 19.05 m level, a hardground is observed in a hand specimen. The hardground is seen in a sandy grainstone bed that can be subdivided into three parts. The lower unit consists of terrigenous material rich in thin bivalves, and lingulid fragments. The middle part is very rich in disarticulated bivalves. The smaller bivalve shells have a chaotic orientation, while the larger shells are oriented with the convex side facing upwards. Cm-scale angular clasts of sandstone are seen in the two lower parts.

Table 3.3: Hardgrounds observed in hand specimens from Mariaholmen.

Height (m)	Sample name	Lithology
19.05	M0.4	Sandy grainstone
68.65	M50	Sandy grainstone/ grainstone
192.65	M174.0A	Sandy grainstone

The top of the middle part is draped by a clear erosional surface with a dark phosphate rim (Figure 3.28). In the erosional surface, small borings (*Trypanites* isp.) occur throughout the specimen where they are preserved as mud infilled borings (Figure 3.27). The hardground has a micro-topography of a few cm. In thin section, phosphorite cement is observed at the hardground, indicating very slow deposition. Within the hardground there is a gradual downwards decrease in phosphate cement, the total phosphate cement thickness is approximately 0.4 mm to 0.5 mm.

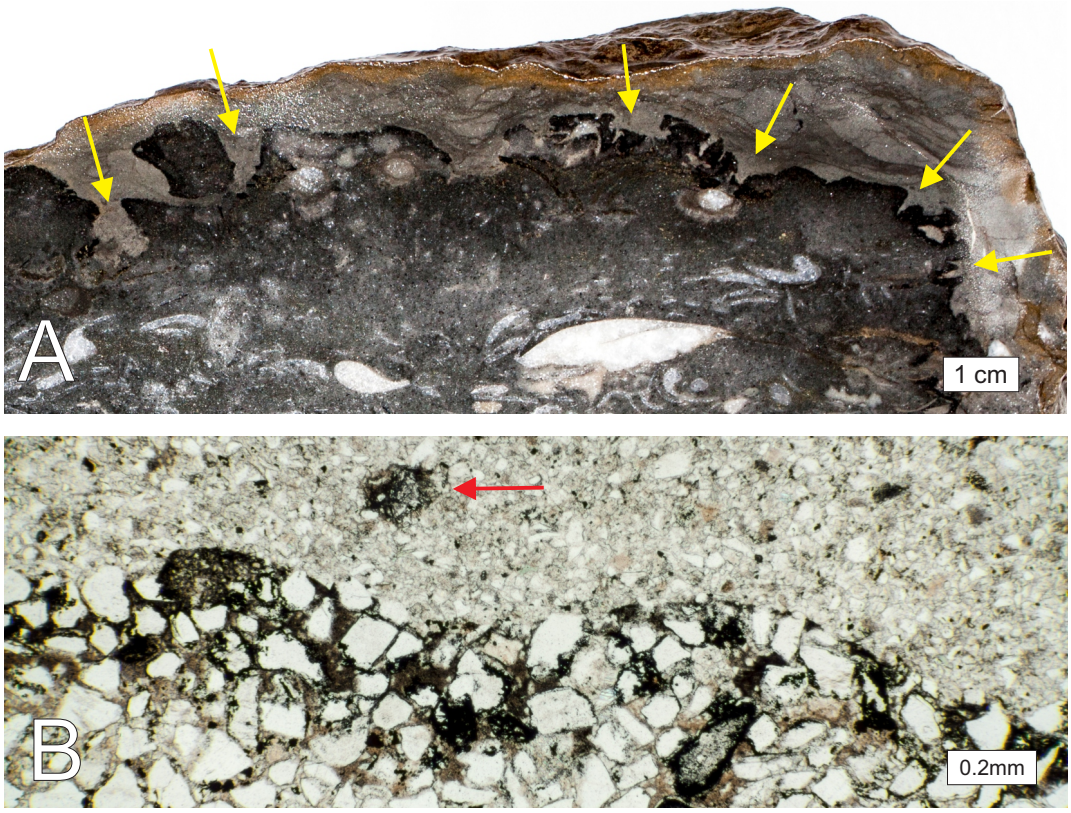

Fig. 3.27: Details of polished slab of hardground at 19.05 m above base. A: Notice the borings (arrows) and micro-topography. B: Micrograph of thin section (PL) where the uppermost part of the hardground is phosphatised (black colour). Some of the quartz extend to the outside of the hardground surface. There is also a prominent decrease in quartz grain size above the hardground. Red arrow indicates the location of a phosphorite clast situated within the matrix above the hardground.

3.2.5.2 *Hardground at 68.65 m*

The hardground was observed within a very sandy grainstone divided into two graded layers. Bivalve shells are plentiful towards the bottom of both layers. A partial erosion with a micro-topography of a few cm is seen in the top of the lower layer. Within this erosion surface, borings are seen (*Trypanites* isp.). At the erosional surface, the quartz grains are phosphate cemented (Figure 3.29).

3.2.5.3 *Hardground at 192.65 m*

Situated 192.65 m above basis is a planar laminated, carbonate cemented sandstone with scattered crinoid fragments. A marked erosional surface with a micro-topography of 3 mm to 4 cm is seen towards the top of the hand specimen. The hardground surface has a gently undulating surface, with only a few steep angles (Figure 3.30A). Above the hardground, multiple clasts of varying size, roundness and lithology are observed (Figure 3.30). Clasts above and below the hardground surface are similar, albeit the clasts above the hardground are significantly smaller in size. The erosional surface is marked by a dark horizon which is similar in appearance to the hardgrounds observed at 19.05 and 65.65 m.

3.2.5.4 *Hardground summary*

Formation of hardgrounds generally require two prerequisites to be met. There has to be an extended pause in the sedimentation, and carbonate deposits must be present (Flügel, 2010). On Mariaholmen hardgrounds were found at three levels (see Table 3.3). The hardgrounds on Mariaholmen show no signs of encrustation, commonly observed on hardgrounds (Brett, 1988; Taylor and Wilson, 2003). Neither does the hardgrounds observed on Mariaholmen have any signs for ferruginous crusts covering the surfaces (Flügel, 2010).

3.2.6 *Conglomerate*

3.2.6.1 *Conglomerate at* 189.15 *m*

A large partially eroded carbonate cemented conglomerate is exposed at 189.15 m (Figure 3.14). The conglomerate has a 10 cm to 20 cm relief to the underlying sandstone, implying partial erosion of the sandstone prior to the deposition of the conglomerate. The sandstone surface/topography has slopes above the angle of repose indicating lithification before the conglomerate was deposited. The conglomerate is polymict, and is dominated by clast of sub-rounded to rounded carbonates in sizes from granules to boulders. The largest clasts are angular to subangular and are approximately 1 m wide, they are, however, quite flat with a thickness estimated to be between 15 cm and 20 cm (based on the thickness of the conglomerate bed). The remaining clasts are either carbonate cemented sandstone, bio-eroded grainstones or phosphorite (phosphorite clasts appear as pebbles). The orientation of the longest axis of the clasts is random with no imbrication observed.

3.2.6.2 *Conglomerate at* 192.65 *m*

Directly overlying the hardground found at 192.65 m (Section 3.2.5.3) is a polymict conglomerate. Subangular to rounded carbonate clasts is the major constituent of the conglomerate. Several 4 cm to 5 cm long well-rounded dark spiculite clasts (Figure 3.35), are also seen throughout the conglomerate. Also found are grey sandstone clasts, some of which are particularly well-rounded. The grey sandstone clasts are different from the sediments found on Mariaholmen which indicate that that

they have been transported from elsewhere within the provenance area. The conglomerate is matrix supported, where the clasts are situated in the matrix and are generally not in contact with other clasts. The orientation of the longest axis of the clasts is seemingly random and no imbrication has been observed. An overview of the various clasts seen at 192.65 m is found in Figure 3.31.

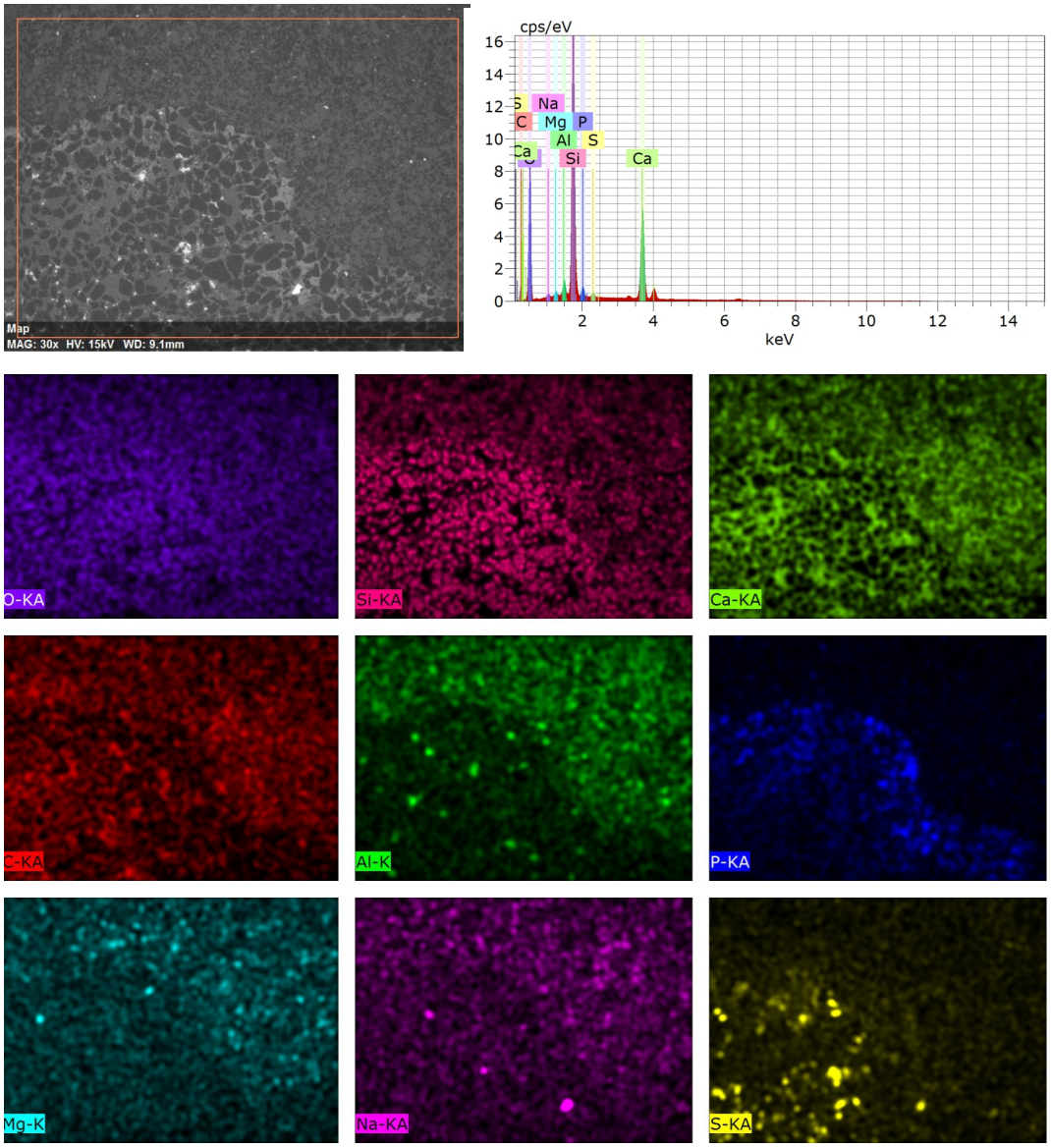

Fig. 3.28: SEM image and SEM-EDS of the hardground at 19.05 m. Phosphorous is confined to the hardground cement, and calcium also has an increase in this area which confirm phosphate in the form of apatite.

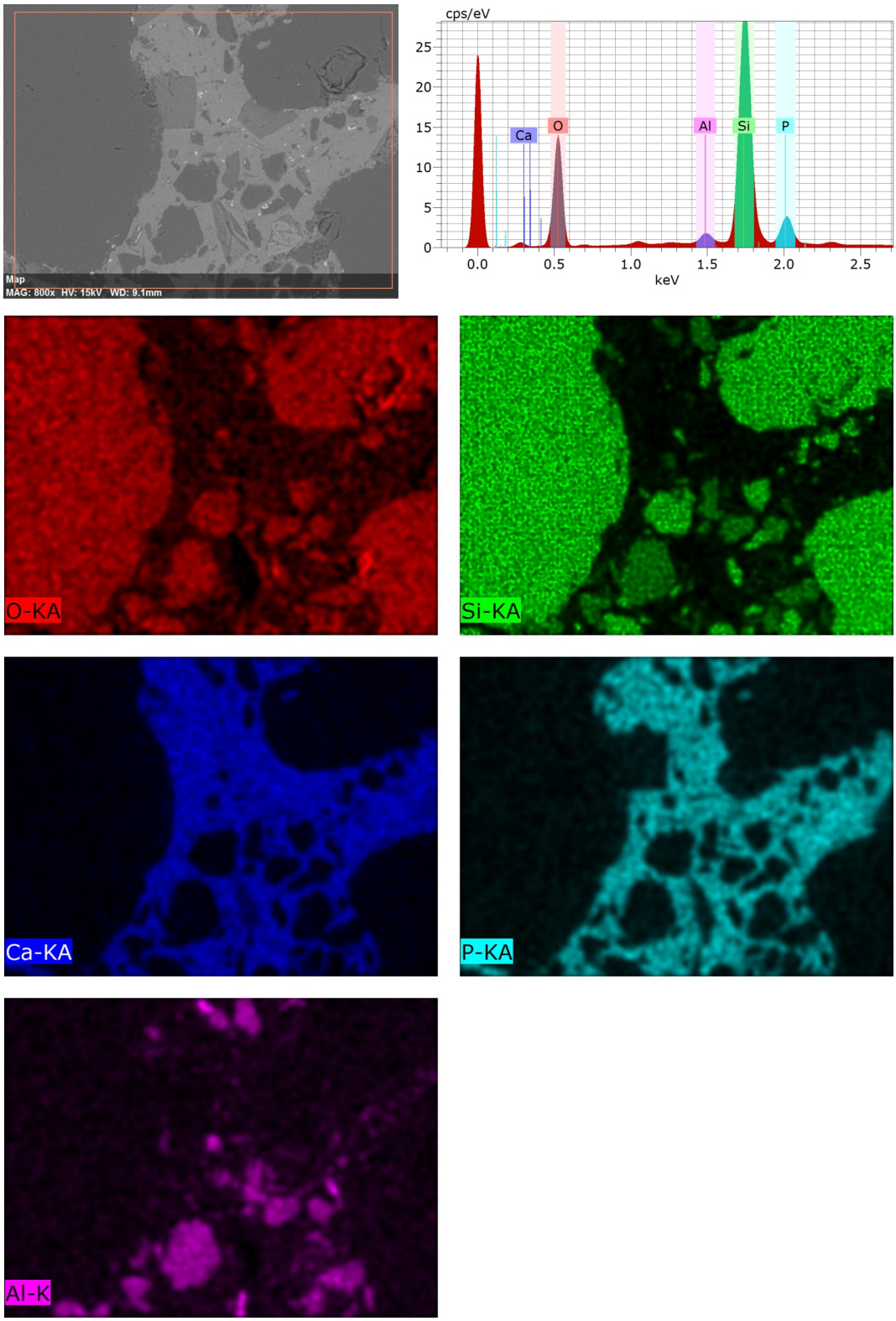

Fig. 3.29: SEM image and SEM-EDS of the hardground at 68.65 m. Phosphorus and calcium confirm that the hardground cement is apatite. The largest grains are quartz, while most of the smaller grains are feldspar (see Al map in purple)

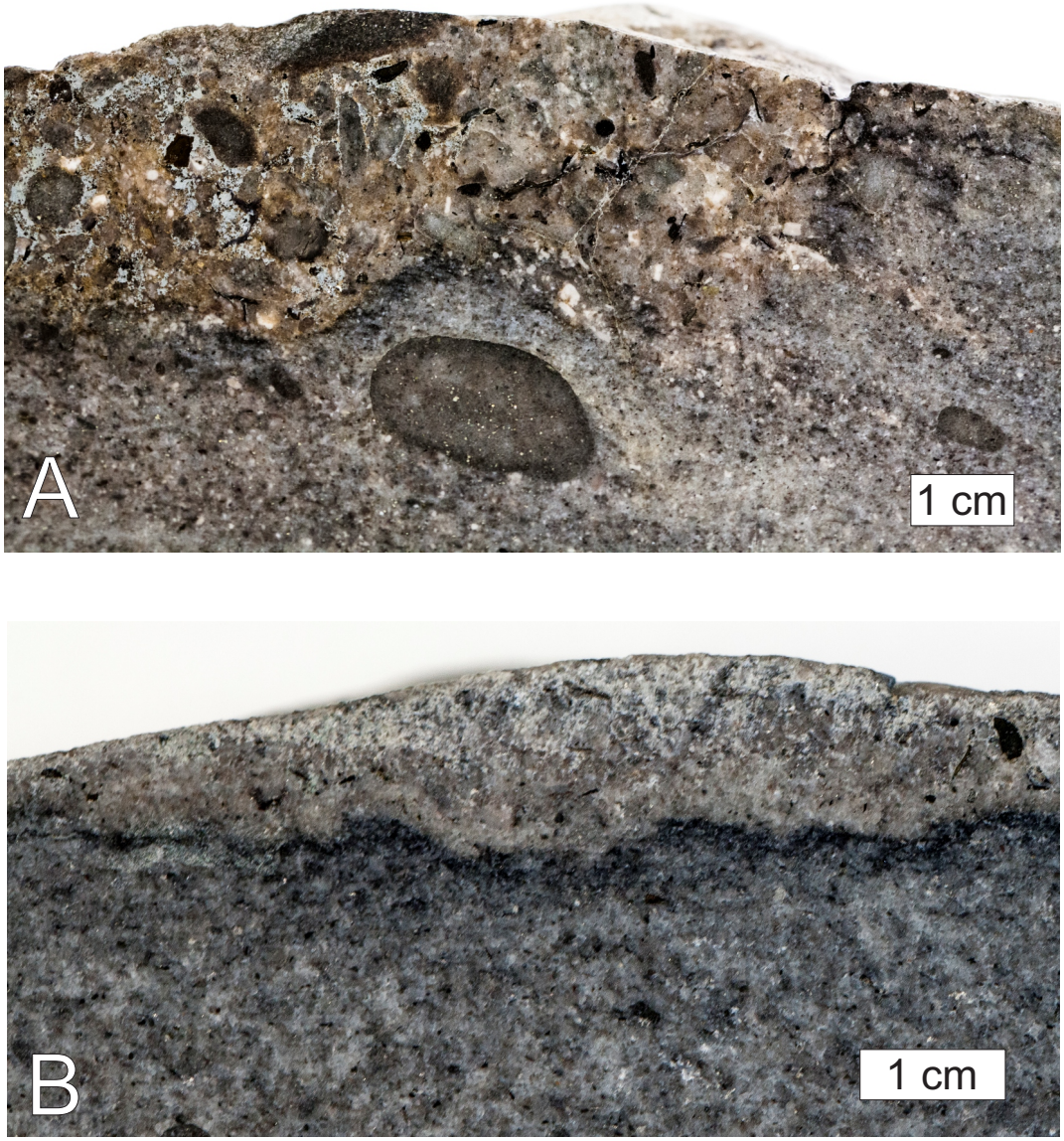

Fig. 3.30: Hardground as seen in polished hand specimen at 192.65 m above base. A: Phosphatised erosion surface. Well-rounded clasts are common above the draped surface, occasional clasts seen below. Well-rounded phosphate clasts appear only above the hardground, indicating that they have been eroded from the hardground. B: Phosphatised erosion surface. There are distinctly different sediments above and below the hardground; a clast bearing carbonate cemented sandstone overlain by a conglomeratic grainstone.

Fig. 3.31: A: Conglomerate as seen 192.65 m above base, clasts vary from large 30 cm subangular to well-rounded smaller clasts. B: Close-up of one of the well-rounded spiculite clasts seen on the surface at 192.65 m. C: Cut and polished slab from 192.65 m with angular to subangular sandstone and carbonate clasts. D: Cut and polished slab from 192.65 m with well-rounded elongated sandstone clasts with variable orientations of the long axis. Black clasts are phosphate cemented fine grained sandstone clasts.

3.3 CARBONATES

On Mariaholmen, carbonate deposition mainly occurred at two specific intervals:

- 18 m to 22 m, *Myalina* layer level
- 185 m to 189.15 m, Skilisen Bed level

Outside these two levels, only scattered thin <10 cm beds of carbonate occur. These scattered beds occur as grainstones or as very sandy grainstones (see Table F.1 in Appendix F for an overview of carbonate samples dissolved in acetic acid).

3.3.1 *Myalina layer*

As noted in Section 3.1.1.1, the *Myalina* layer is situated at approximately 19 m above base. The *Myalina* layer is a very fine, to fine grained sandstone/grainstone. On Mariaholmen, the layer is very rich in the *Promyalina* Sp. bivalve (Figure 3.7). This abundance of bivalves is in accordance with what is seen in the stratotype and throughout the western Svalbard (Mørk et al., 1999a).

The bivalves are mainly disarticulated. The smaller bivalves are randomly oriented, while the larger bivalves are oriented with the convex side facing upwards. Bivalves with borings of the bivalve shells are observed in thin section. The micritization described in Section 3.7.1.2 indicate that the Myalina layer have been situated within the photic zone.

Also found within the *Myalina* layer are crinoids, bryozoans, fragments of inarticulate brachiopods and bio-eroded articulate brachiopods which have had their shells bored by organisms prior to deposition (Figure 3.6 and 3.49).

3.3.2 *Skilisen Bed*

The Skilisen Bed is a pronounced fossiliferous carbonate bed found in the upper levels of the Tvillingodden Formation throughout the southwestern Spitsbergen. At the type location it marks the top of the formation (Mørk et al., 1999a). However, on Mariaholmen, the Skilisen Bed is approximately 4.15 m thick, and located 5 m below the top of the Tvillingodden Formation. The Skilisen Bed on Mariaholmen consists of a sandy carbonate, rich in bivalves, articulate brachiopods and inarticulate brachiopods, bryozoans and crinoid fragments. Occasional fish remains, gastropods, conodonts also appear (Figure 3.32). Some of the gastropods and bivalves are micritized.

Bivalves, brachiopods and crinoid fragments are the only macroscopic fossils observed in field and in hand specimens, while the other fossils have been observed in either thin section or as phosphatised moulds in the insoluble residue from dissolved carbonates (Figure 3.33).

In thin section it is observed that bivalves are frequently micritized, an indication of being within the photic zone. In a sample at 185.35 m, shells which have been micritized on both sides are observed, this is an indication that the shells could have been deposited within fair weather

wave base. Within the Skilisen Bed numerous clasts are also found, see Section 3.4.

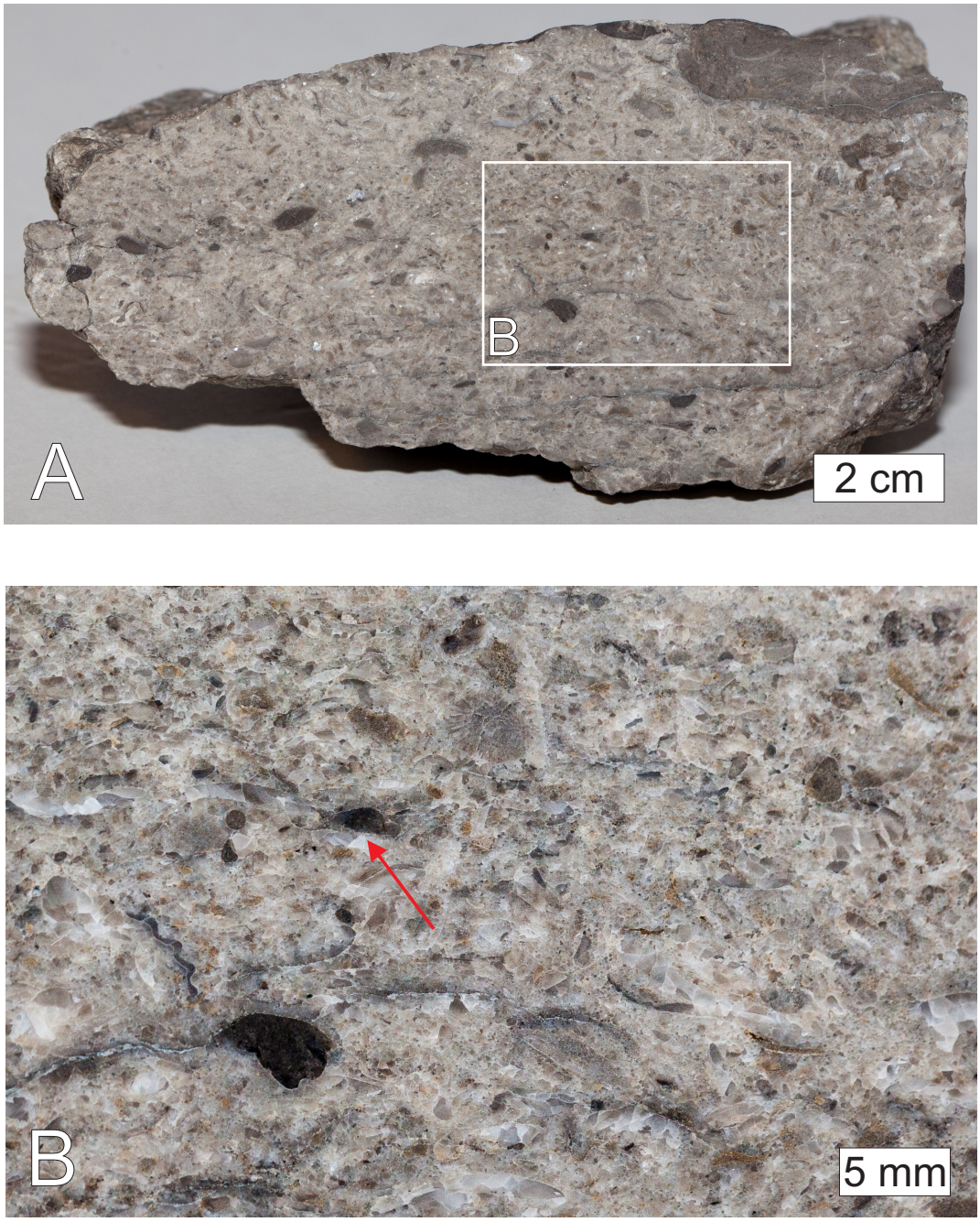

Fig. 3.32: A: Polished slab of grainstone at 187 m. This sample represent the Skilisen Bed as observed on Mariaholmen. Notice phosphorite nodules (black) and disarticulated brachiopod shells B: Detail from A, note how the middle phosphorite nodule has a fracture where it has broken (red arrow), while the lower phosphorite nodule is rounded. The bivalve shells and disarticulated brachiopod shells are not sorted with convex up, indicating fairly rapid deposition and burial.

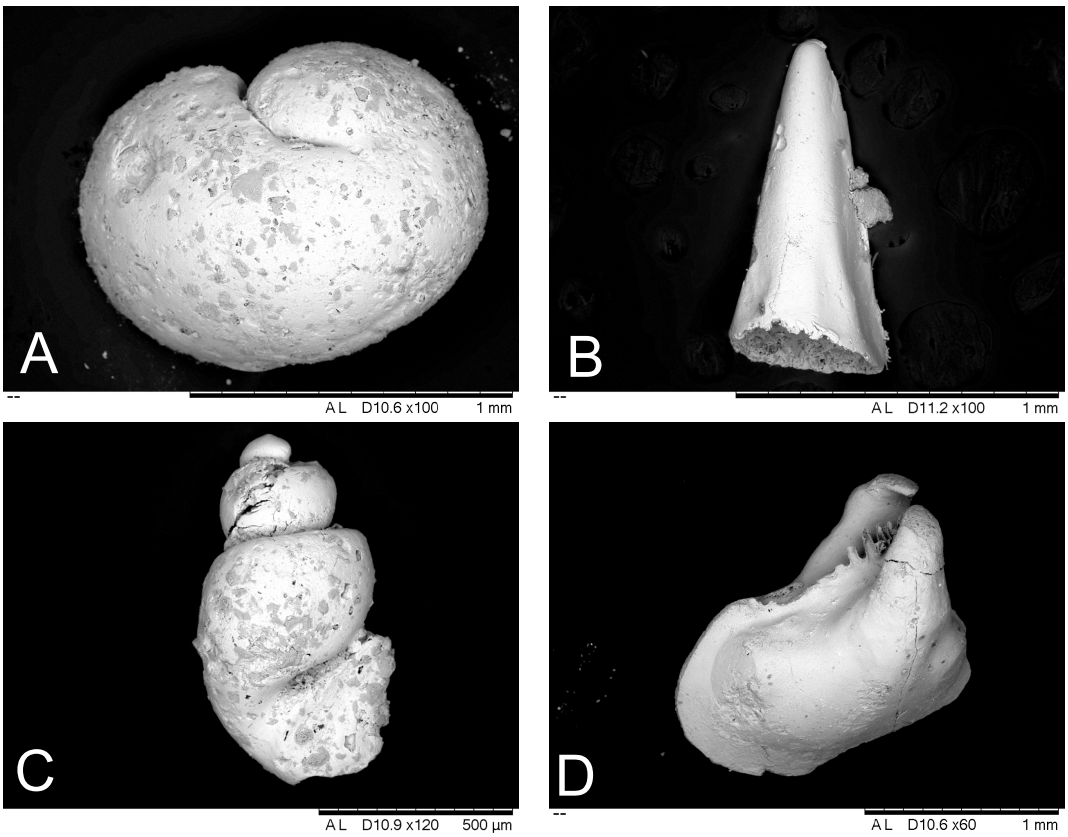

Fig. 3.33: SEM images of fossils from Skilisen Bed (185 m to 189.15 m). A: Internal mould of a planispiral gastropod, B: Fish tooth., C: Internal mould of a high spiral gastropod, D: Internal mould of a small articulated bivalve. All moulds have been phosphatised and have been recovered from the insoluble residue of dissolved carbonates.

3.4 CLASTS AND MINERALS

Large amounts of material from bulk samples and dissolved carbonates from Mariaholmen were sieved, sorted and subsequently identified. However, most of the clasts and minerals were found in the insoluble residue left after acid treatment, only the clasts and minerals from the lowermost levels of the succession are from bulk samples. An overview can be seen in Figure 3.38.

GLAUCONITE

In the insoluble residue after acid treatment, glauconite is found at three different levels. All levels with glauconite is in relation to the Skilisen Bed at the top of the Tvillingodden Formation. Glauconite is considered an authigenic mineral. It is believed to form outside an area of continuous sedimentation under the presence of some clay and mica (Einsele, 2000). Glauconitisation is a long lasting process (Einsele, 2000). The appearance of glauconite at certain levels imply that although the sedimentations might have been continuous at that interval, the sedimentation rates must have been very low.

SPICULITE CLASTS

On Mariaholmen, spiculite clasts are found throughout most of the Vardebukta Formation and the Tvillingodden Formation. Albeit present throughout the succession on Mariaholmen, the spiculite clasts are most abundant in upper levels of the Tvillingodden Formation.

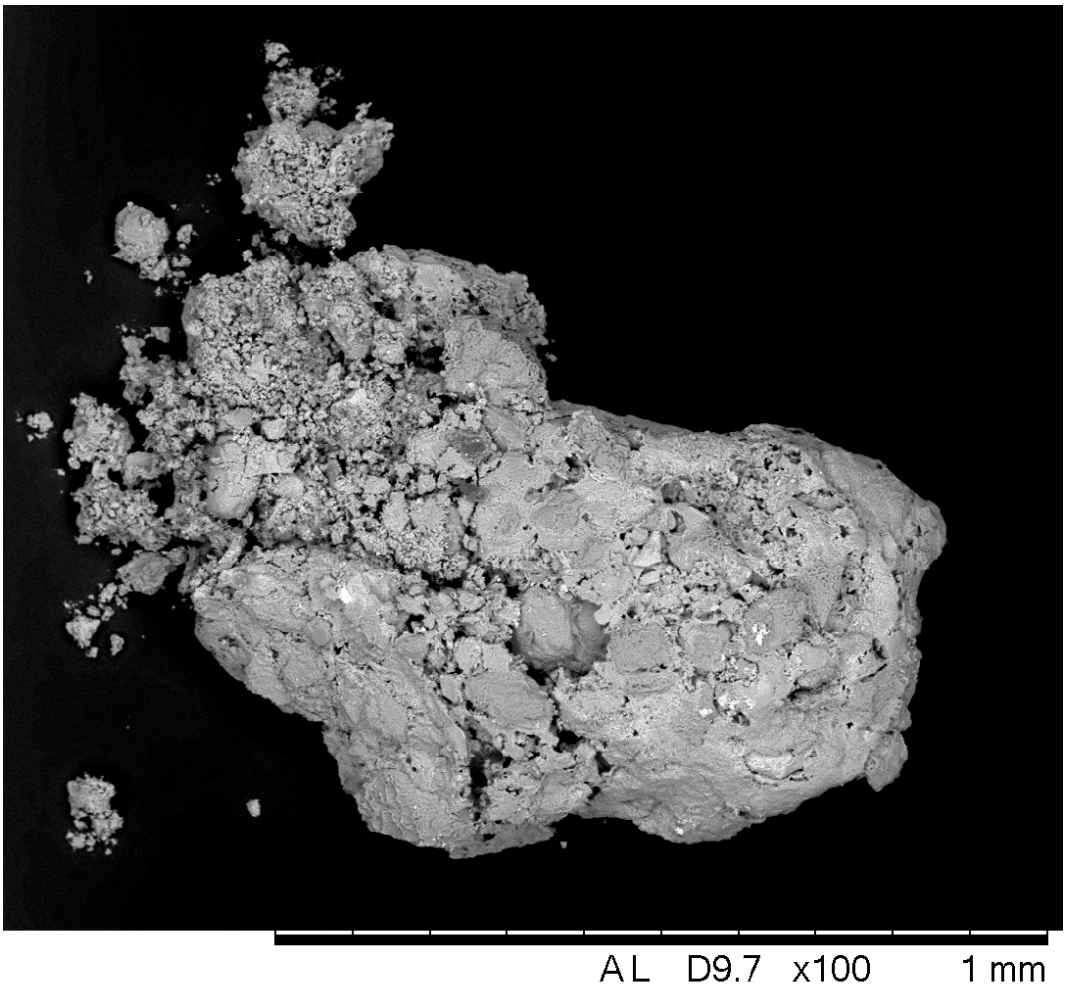

Fig. 3.34: SEM image of glauconite in fine grained deposit at 184.4 m.

The spiculite clasts (Figure 3.35), contain thin silica spicules from silica sponges which are encapsulated in a cryptocrystalline quartz matrix. These clasts have a strikingly close resemblance to the spiculites from the underlying Kapp Starostin Formation (Siedlecka, 1970; Ehrenberg et al., 2001; Blomeier et al., 2011). Indicating that the clasts have been derived from an area with subaerial exposure of the Kapp Starostin Formation.

SANDSTONE, CARBONATE AND PHOSPHORITE CLASTS

Sandstone and carbonate clasts of varying size (between the very coarse sand and medium gravel fractions) were observed throughout the profile. They are naturally weathered and different from their encompassing lithology. The clasts are generally quite well-rounded with varying elongation, although exceptions occur where some of the sandstone clasts are angular-subangular. The sandstone clasts have varying colours and texture, while the carbonate clasts are grainstones. This is an indication of varying or multiple provenance areas (Figures 3.36 and 3.37). As the clasts have no apparent similarities to the sediments in which they are confined, it seems reasonable to assume that they are dropstones. Dropstones are clasts posing a hydrodynamic paradox, with exotic or extra-basinal lithology with uncertain provenance (Bennett et al., 1996).

Dropstones are transported by a rafting agent (Bennett et al., 1996). Reasonable rafting agents for the dropstone clasts on Mariaholmen would be either within tree roots (Vogt and Parrish, 2012; Bennett et al., 1996), or possibly (however, less likely) on seaweeds as holdfasts (Bennett et al., 1996).

There appears to be a correlation between the clasts and depositional environment (Figure 3.38). In the coarser grained high energy depositional environments, clasts appear in relatively high numbers, while they are absent in the fine grained more distal deposits.

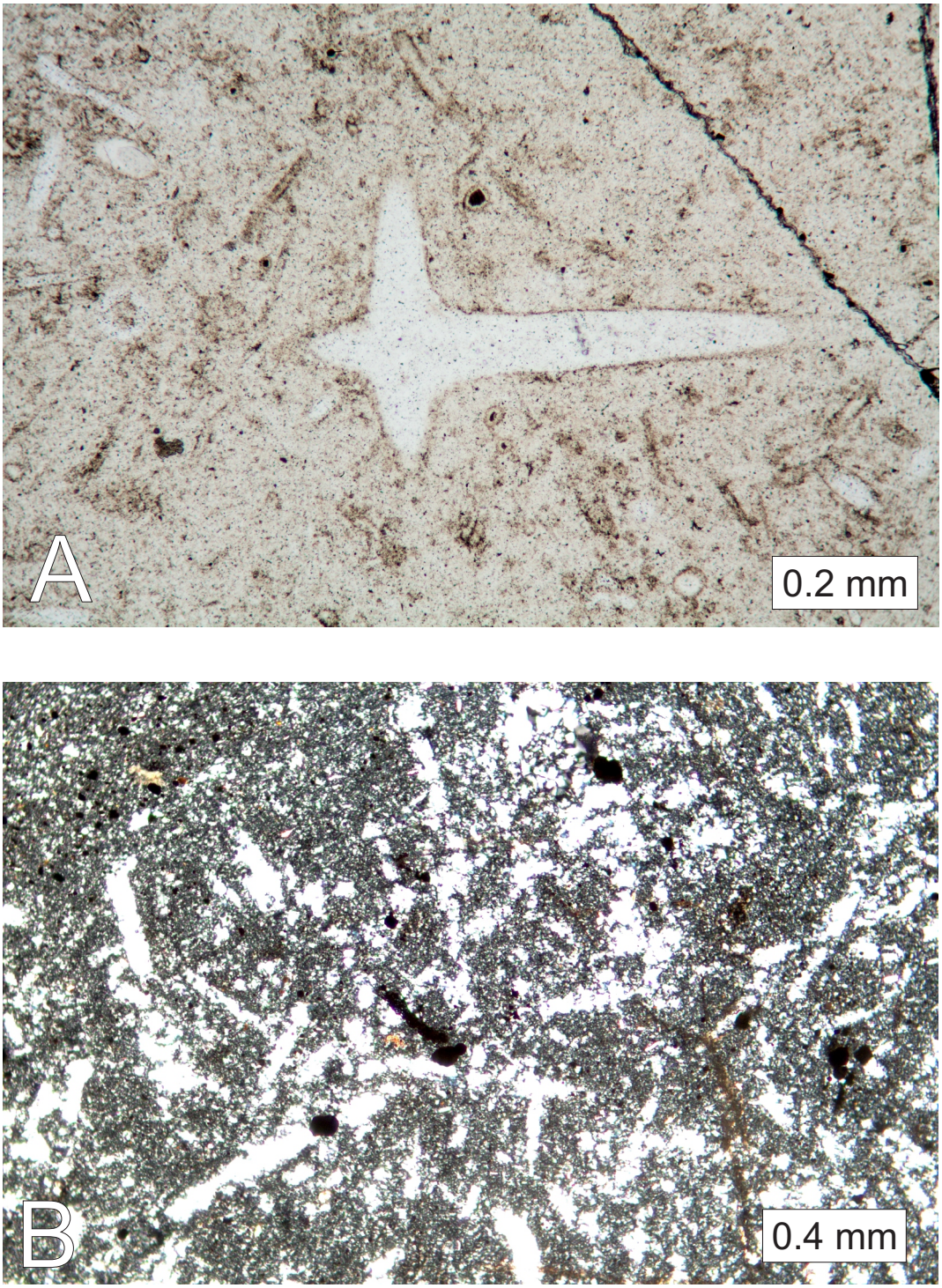

Fig. 3.35: A: Thin section (PL) micrograph of dark well-rounded clast from 192.7 m with well-preserved spiculite needle cross situated in a cryptocrystalline silica matrix. B: Thin section (XL) micrograph of dark well-rounded clast from 192.7 m with abundant spiculite needle fragments situated in a cryptocrystalline silica matrix.

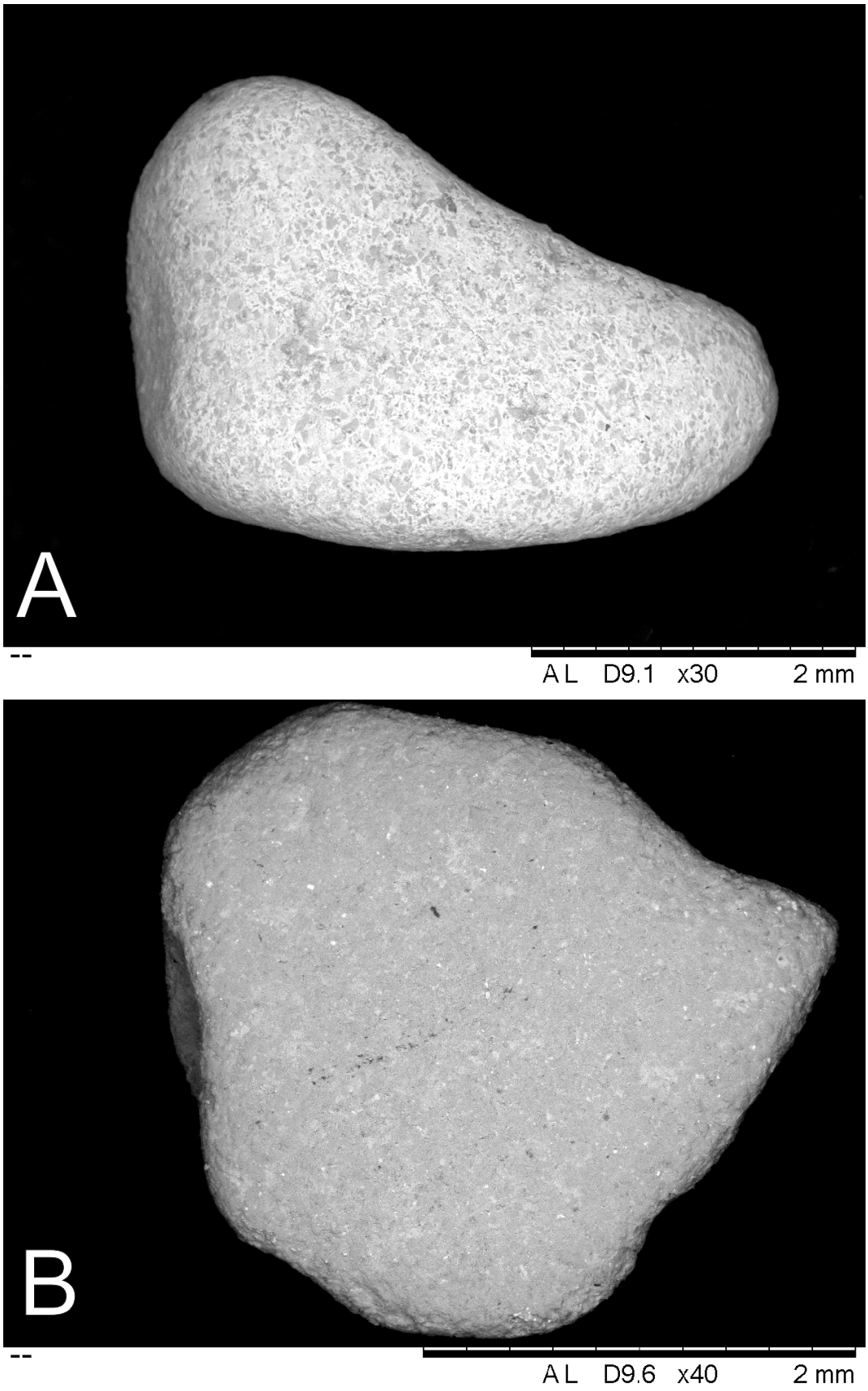

Fig. 3.36: Small clasts found on Mariaholmen. Composition determined by SEM-EDS (data in Appendix G). A: Siderite cemented sandstone clast from 18.95 m, B: Sandstone clast from 18.95 m with quartz grains and quartz cement. Some aluminium silicates are present (7.96% Al), most likely feldspar.

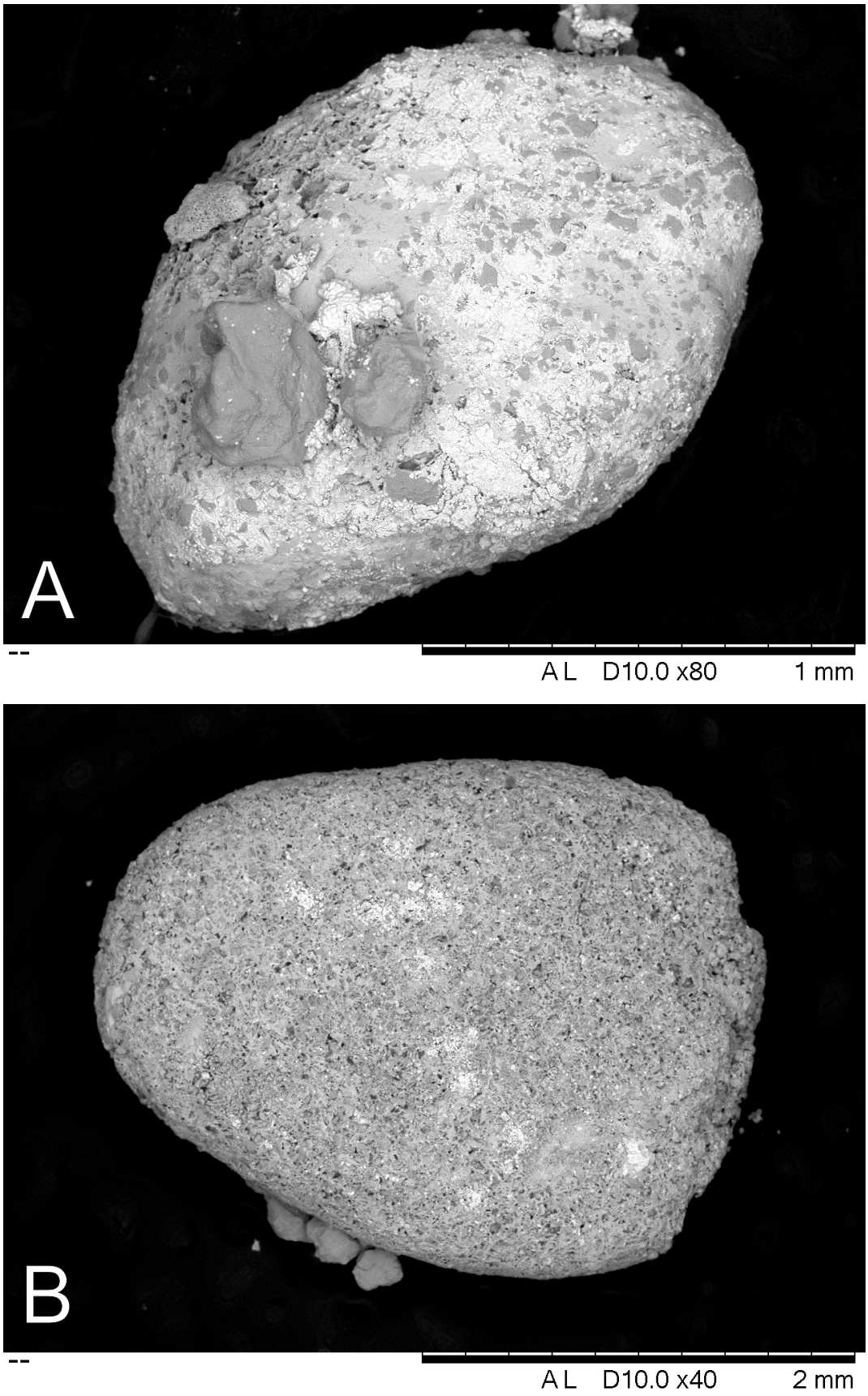

Fig. 3.37: Small clasts found on Mariaholmen. Composition determined by SEM-EDS (data in Appendix G). A: Phosphorite cemented clast from 192.65 m with sub-angular quartz grains and abundant pyrite. B: Clast of phosphorite cemented sandstone with some pyrite growth from 191.75 m.

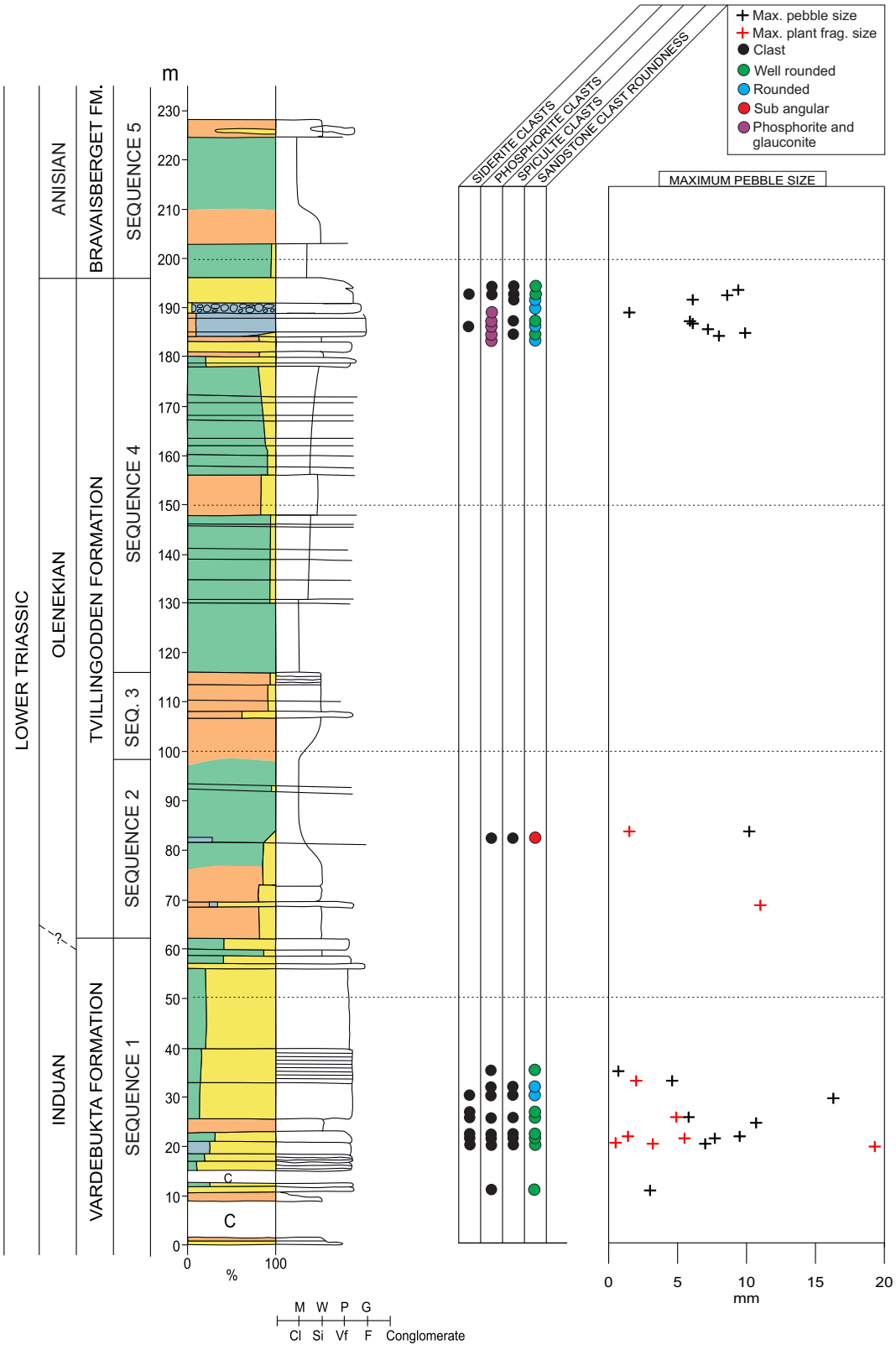

Fig. 3.38: Plant fragments, clasts and clast types found as insoluble residue from dissolved carbonates and from bulk shale samples on Mariaholmen. Even though spiculite clasts appear at several levels in the profile, they are not found above the Tvillingodden Formation. Legend can be found in Figure 3.3.

3.5 TRACE FOSSILS

Trace Fossils were not the main aspect of this thesis as they were studied in great detail in the unpublished Master's Thesis by Lofek (2012) which was part of the same project as this thesis. We carried out the fieldwork together and this section is partly based on his thesis.

As seen on Figure 3.39, the Triassic succession on Mariaholmen has been divided in 10 ichnofacies units. All the facies described by Lofek (2012) belong to variations of the *Cruziana* ichnofacies which aid in determining the palaeobathymetry

The ichnofacies concept was first introduced by Seilacher (1967) who defined the *Skolithos*, *Glossifungites*, *Cruziana*, *Zoophycos* and *Nereites* ichnofacies. The *Cruziana* ichnofacies found on Mariaholmen is further subdivided into archetypal, proximal and distal *Cruziana* ichnofacies.

The archetypal *Cruziana* ichnofacies which is a mixed association of horizontal, inclined and vertical burrows represent the shallow marine subtidal domain from below the fair weather wave base to deeper more quiet waters (MacEachern et al., 2007). Archetypal *Cruziana* ichnofacies spans from offshore to the distal lower shoreface, which equates prodelta to distal delta front environments (MacEachern et al., 2007).

Proximal *Cruziana* ichnofacies represent the shoreward transition from archetypal *Cruziana* ichnofacies to distal *Skolithos* ichnofacies (MacEachern et al., 2007). This transition zone represents depositional environments with moderate energy in the shallow subtidal zone, and it is characterised by silty sandstones and sandy siltstones with generally

lower diversity burrows than those of the archetypal *Cruziana* ichnofacies (MacEachern et al., 2007).

Distal *Cruziana* ichnofacies is the basinward transition from archetypal *Cruziana* ichnofacies to *Zoophycos* ichnofacies (MacEachern et al., 2007). Distal *Cruziana* ichnofacies is characterised by muddy siltstones and silty mudstones deposited in a quiescent bottom-water environment dominated by deposit-feeding structures, their associated dwelling structures and abundant grazing structures (MacEachern et al., 2007).

Trypanites ichnofacies is characteristic of lithified marine substrates such as reefs, hardgrounds, beach rock and other omission surfaces (MacEachern et al., 2007). The *Trypanites* ichnofacies correspond to long term bio-erosion on surfaces with little or no sedimentation. Characteristic trace fossils are sharp walled, unlined and cylindrical domiciles such as *Trypanites* isp. (MacEachern et al., 2007).

3.5.1 *Common trace fossils*

Out of the 24 trace fossils observed by Lofek (2012) on Mariaholmen the most common ones are: *Arenicolites* isp. (Figure 3.40), *Lockeia* isp. (Figure 3.41), *Helminthoidichnites* isp. (Figure 3.42), *Paleophycus* isp. (Figure 3.43), *Planolites* isp. (Figure 3.44) and *Rhizocorallium* isp. (Figure 3.45).

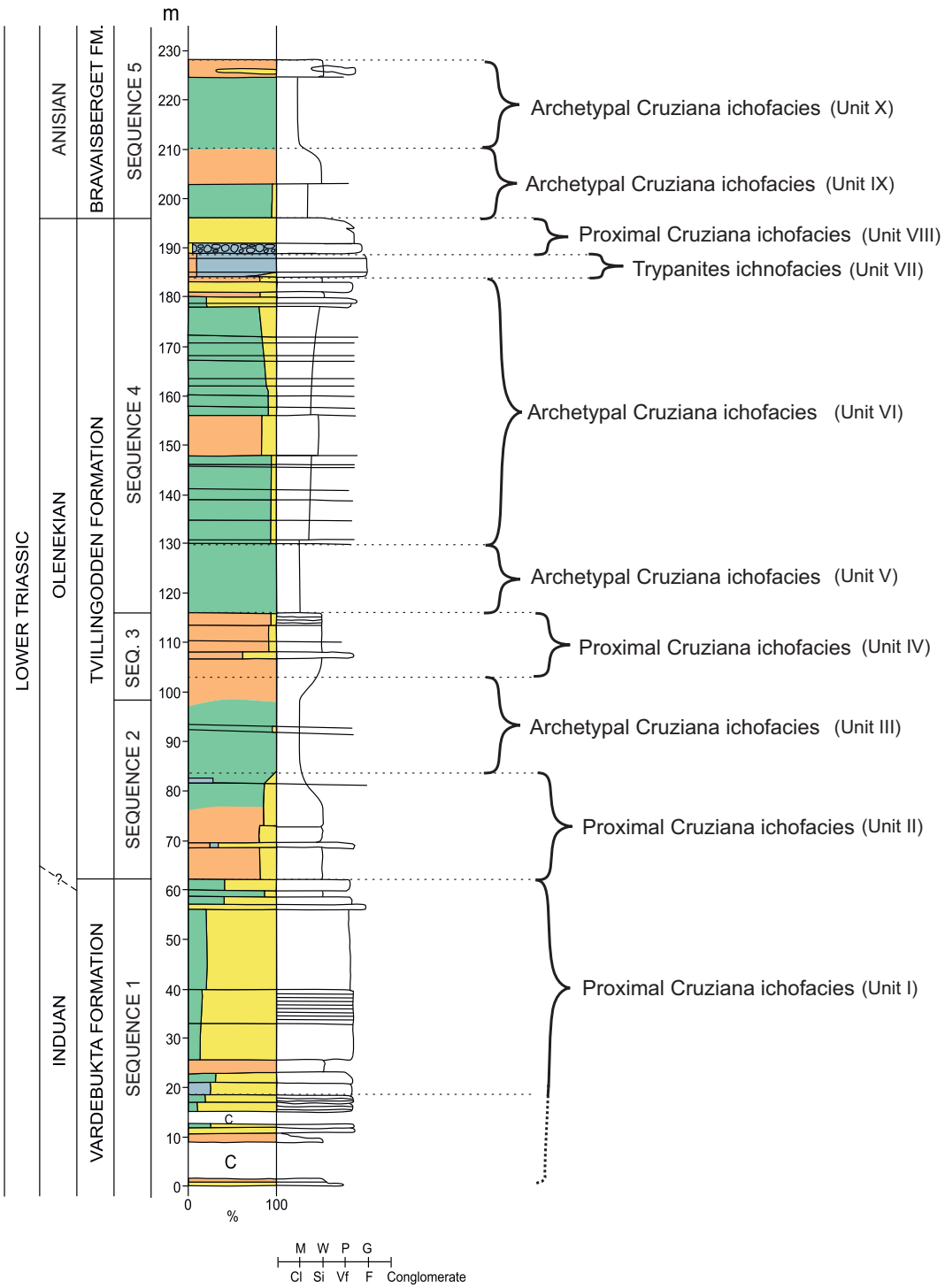

Fig. 3.39: Overview of ichnofacies on Mariaholmen. Unit boundaries after Lofek (2012). Legend in Figure 3.3.

Fig. 3.40: Longitudinal section showing a part of *Arenicolites* isp. within a sandstone bed on Mariaholmen

3.5.2 *Ichnofacies*

Unit I, Proximal *Cruziana* ichnofacies (18 m to 56 m)

The presence of vertical burrows such as *Arenicolites* isp. in sandy sediments point towards the *Skolithos* ichnofacies.

However, presence of horizontal trace fossils such as *Planolites* isp., *Diplopodichnus* isp., *Helminthoidichnites* isp., *Mulatina* isp., *Monomorphichnus* isp. and *Lockeia* isp. rules out the *Skolithos* ichnofacies, and therefore point towards a proximal variant of *Cruziana* ichnofacies where the *Skolithos* ichnofacies is introduced when high energy events occur.

Unit II, Proximal *Cruziana* ichnofacies (56 m to 81 m)

This unit consists of horizontal burrows with the appearance of diagonal burrows which still point towards proximal *Cruziana* ichnofacies, however, there is a shift towards deeper waters.

Fig. 3.41: *Lockeia* isp. as observed in the sandstones on Mariaholmen. Photo from Lofek (2012).

Unit III, Archetypal *Cruziana* ichnofacies (81 m to 104 m)

Some *Lockeia* isp. is found at the bottom part of the unit. The remainder of the unit contains mainly *Helminthoidichnites* isp. and *Planolites* isp. with single specimens of *Gordia* isp., *Imponoglyphus* isp. and *Chondrites* isp.

The appearance of *Helminthoidichnites* isp. and *Gordia* isp. in combination with an increase in fine grained material imply archetypal *Cruziana* ichnofacies.

Unit IV, Proximal *Cruziana* ichnofacies (104 m to 114.5 m)

Consisting mainly of *Helminthoidichnites* isp. and *Planolites* isp. with reappearance of *Arenicolites* isp.

This unit is interpreted as proximal *Cruziana* ichnofacies.

Fig. 3.42: *Helminthoichnites* isp. as observed on a slab of siltstone. Photo from Lofek (2012).

Unit V, Archetypal *Cruziana* ichnofacies (114.5 m to 128.5 m)

This 14-meter-thick unit is very deprived of trace fossils, and only *Helminthoidichnites* isp. was found.

The presence of *Helminthoidichnites* isp. indicates that also this section belongs to the archetypal *Cruziana* ichnofacies.

Unit VI, Archetypal *Cruziana* ichnofacies, (128.5 m to 182 m)

Unit VI start with *Helminthoidichnites* isp., *Kouphichnium* isp. and an upwards increasing amount of *Rhizocorallium* isp. Towards the top of the unit there are levels very rich in bioturbation containing *Diplopodichnus* isp., *Ptychoplasma vagans*, *Paleophycus* isp., *Kouphichnium* isp., *Planolites* isp., *Lockeia* isp. and *Asterichnus* isp. *Arenicolites* isp. is also found within sandstone beds.

Fig. 3.43: *Palaeophycus* isp. as observed in a sandstone slab on Mariaholmen. Photo from Lofek (2012).

Such a large ensemble of trace fossils is produced by a diverse fauna and must represent good environmental conditions at the time of deposition.

Even though there are *Arenicolites* isp. present, the unit still belong to the archetypal *Cruziana* ichnofacies as it is still dominated by horizontal traces produced by mobile fauna in the levels low energy siltstone and shale beds. The fact that the siltstone and shale beds are rich in trace fossil implies that the time between the deposition of high energy sandstone beds must have been long enough to develop favourable conditions for the fauna reported in the siltstone and shale beds.

Unit VII, *Trypanites* ichnofacies (182 m to 185.5 m)

Within this unit no trace fossils were reported in Lofek (2012), however,

Fig. 3.44: Sandstone slab from the upper levels of the Vardebukta Formation, rich in *Planolites* isp. Photo from Lofek (2012).

Trypanites isp. moulds were later found in the insoluble residue after acid treatment of carbonate slabs (Figure 3.47).

Unit VIII, Proximal *Cruziana* ichnofacies (185.5 m to 193 m)

This unit represents a higher energy depositional environment with proximal *Cruziana* ichnofacies. *Lockeia* isp., *Paleophycus* isp. and *Rhizocorallium* isp. are all common within the interval.

Unit IX, m Archetypal *Cruziana* ichnofacies (193 m to 211 m)

Rhizocorallium isp. is the most common trace fossil. It occurs both in beds of siltstone and shale. In addition, *Lockeia* isp. and *Paleophycus* isp. are also present. One large *Phoebichnus* isp. (Figure 3.46) was also seen. The large accumulations of *Rhizocorallium* isp. along with the absence of sand and the presence of *Phoebichnus* isp. indicates that this interval is of archetypal *Cruziana* ichnofacies.

Fig. 3.45: *Rhizocorallium* isp. in a shale slab from the lower levels of the Bravaisberget Formation.

Unit X, Archetypal *Cruziana* ichnofacies (211 m to 227 m)

Much like Unit IX, this unit is dominated by *Rhizocorallium* isp. trace fossils with some *Planolites* isp. and *Paleophycus* isp. confining it to the archetypal *Cruziana* ichnofacies.

Fig. 3.46: *Phoebichnus isp.* with numerous branching burrows, found in the Bravaisberget Formation on Mariaholmen.

3.5.3 *Borings*

Borings were found in all the insoluble residues after carbonate dissolution (Figure 3.49). The borings are found as moulds and have varying morphology where some form seemingly complex networks, others form solitary tubes (Figure 3.47), however, all borings are *Trypanites* isp. The borings were filled with silt and/or fine grained clastic sand together with scattered grains of glauconite. The infills are usually cemented with phosphorite and sometimes with minor amounts of pyrite. The moulds were therefore not affected by the acid treatment.

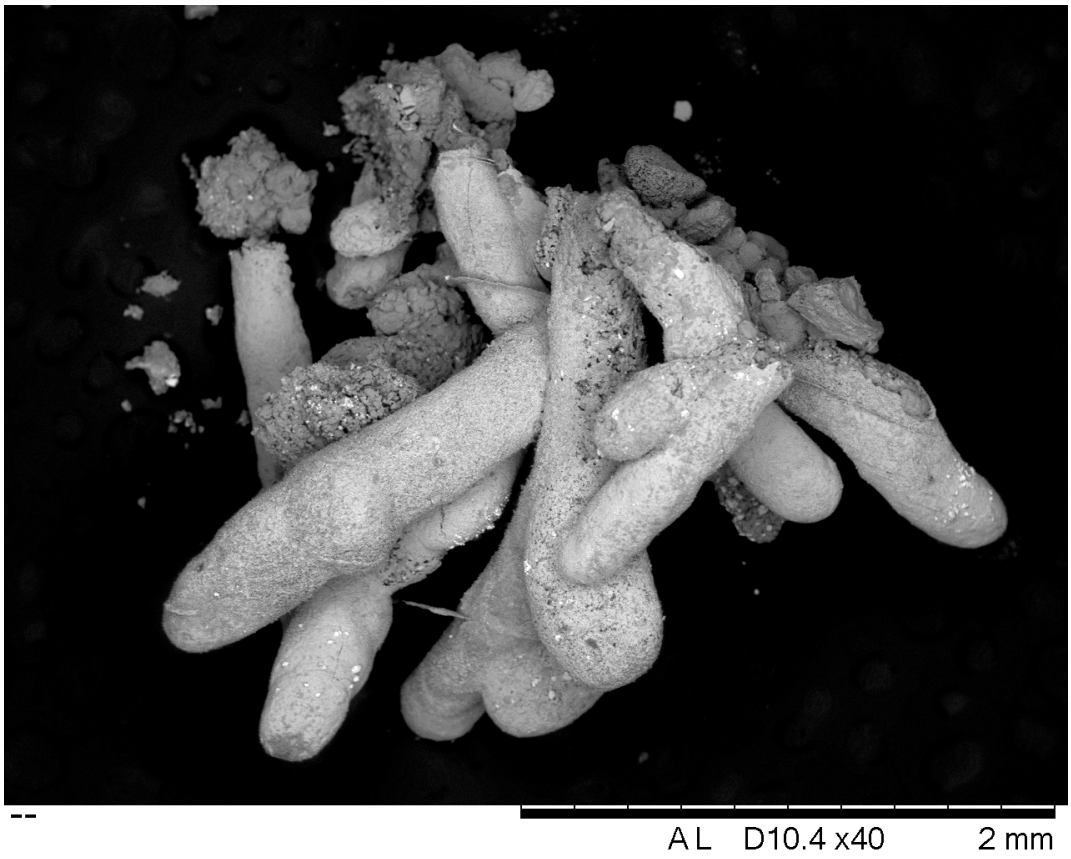

Fig. 3.47: SEM image from 20.3 m above base with multiple *Trypanites* isp. borings. Notice how the borings cross each other when older borings are intersected by newer borings. The borings are approximately 2 mm long and the diameter is ±0.4 mm

However, in some cases the borings were partly dissolved, indicating the presence of carbonate cement. The presence of phosphate cement indicates very slow sedimentation rates (Glenn and Garrison, 2003). There also appears to be multiple generations of borings. Multiple *Trypanites* isp. borings close to and crossing each other seemingly forming a network, but as the *Trypanites* isp. only bore solitary tubes, this must be different generations of borings crossing (Figure 3.47).

3.6 FAUNA

3.6.1 *Bivalves*

Fossil bivalves are found throughout the Mariaholmen succession. Although found in all lithologies, they are most abundant in carbonate beds. In siliclastic beds, the bivalves appear as either poorly preserved imprints or very compacted. The bivalves range in size from millimetre scale (Figure 3.33D) to centimetre scale (Figure 3.27A).

Bivalves generally appear as disarticulated shells. This is an indication of reworking prior to final deposition. However, exceptions occur and some complete bivalves are seen. The complete bivalves are well-preserved as moulds from the insoluble residue after carbonate dissolution (Figure 3.33).

The bivalves are commonly micritized, but it varies whether both sides of the shell have been micritized. In thin sections some of the bivalves are found to have had borings of the dissolved primary aragonite.

Bivalves on Mariaholmen are of both allochthonous and autochthonous origin. The presence of incomplete and abraded shells can indicate that bivalves are of allochthonous origin, while well-preserved complete bivalves and *Lockeia* isp., a bivalve resting trace (Uchman et al., 2004) indicates autochtonous origin.

Johnsen (1980) found the bivalve *Promyalina degeeri* sp. throughout both the succession on Mariaholmen and the Akseløya equivalent profile. Johnsen (1980) described *Promyalina degeeri* sp. as an epibyssal

bivalve that thrive in high energy shallow water shelf environments. Johnsen (1980) also found the bivalve *Unionites fassaensis* sp. throughout both successions. This bivalve is described by Johnsen (1980) to be semi-infaunal shallow burrowing.

3.6.2 *Gastropods*

On Mariaholmen gastropods are only found in thin sections and as moulds in the insoluble residue after carbonate dissolution. The gastropod moulds found are slightly abraded indicating some degree of reworking or possibly redeposition of the gastropod shells. As seen in Figure 3.33 the gastropods observed on Mariaholmen are either planispiral or high spiral.

3.6.3 *Ammonoids*

Ammonoids were observed at three levels (90 m, 136 m and 147.5 m). At these levels the ammonoids were numerous, but appear as poorly preserved imprints (Figure 3.48) or as compacted shells. As a consequence it was not possible to identify the genus or species.

3.6.4 *Brachiopods*

Observed on Mariaholmen are both articulate brachiopods and inarticulate brachiopods. The inarticulate brachiopods are seen throughout the succession, and are commonly found within polish slabs, in thin

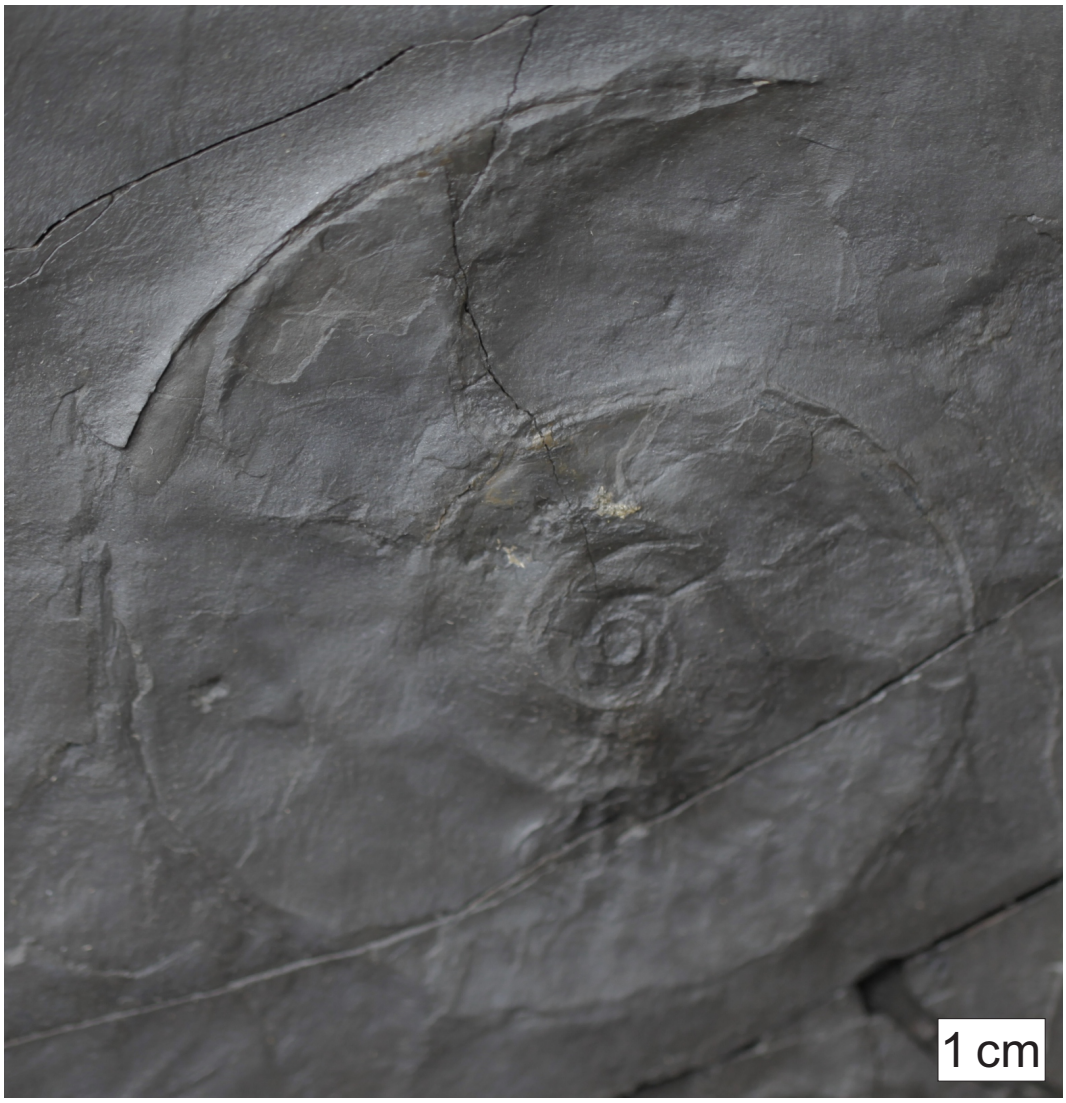

Fig. 3.48: Ammonoid impression as seen at 88.65 m where the ammonoids were numerous, but poorly preserved.

sections and as moulds from the insoluble residue after carbonate dissolution. Although found throughout the succession, the inarticulate brachiopods are by far outnumbered by the bivalves. In thin section some of the inarticulate brachiopods have been bored prior to deposition (borings were filled by the matrix).

3.6.5 *Bryozoans*

Nakrem and Mørk (1991) has described the bryozoans found on Mariaholmen. During our project, bryozoans were found at two distinct levels: 18.65 m (Figure 3.50) and 68.65 m. Nakrem and Mørk (1991) identified the bryozoans found on Mariaholmen as *Parolioclema*, which has later been transferred by Nakrem and Ernst (2008) to *Arcticopora*. The bryozoans found in this work also belong to the genus *Arcticopora*. *Arcticopora* is recorded from North America, Europe, Siberia, New Zealand, Japan and the Arctic region (Nakrem and Ernst, 2008), and is restricted to the Triassic (Griesbachian - Norian) (Nakrem and Ernst, 2008).

3.6.6 *Crinoids*

The crinoid fauna from Mariaholmen have already been described by Salamon et al. (2015a) and Salamon et al. (2015b) (see Appendix A and B).

3.6.7 *Fish remnants*

Fish teeth and scales are, as seen on Figure 3.49, found throughout the succession on Mariaholmen. Most commonly, the fish remnants were found in the insoluble residue after dissolved carbonates.

The fish teeth are often only very slightly abraded, while the scale fragments are substantially reworked. Table 3.4 describes fish teeth found on Mariaholmen. The fish teeth found on Mariaholmen are sim-

ilar to those found by Błażejowski (2004) in the equivalent Triassic formations in Hornsund on south-western Spitsbergen.

Table 3.4: Fish teeth found on Mariaholmen

Genus\Species	**Range**	**Known from**	**Author**
Hybodus sp.	Permian - Cretaceous	Worldwide	Fossilworks (2015)
Hybodus Sasseniensis	Dienerian - Spathian	Vardebukta Formation, Spitsbergen (Hornsund, Hyrnefjellet Mt. and Mariaholmen)	Stensiö (1921); Błażejowski (2004)
Lissodus angulatus	Dienerian - Spathian	Vardebukta Formation, Spitsbergen (Hornsund, Hyrnefjellet Mt. and Mariaholmen)	Stensiö (1921); Błażejowski (2004)
Acrodus spitzbergensis	Dienerian - Spathian	Vardebukta Formation, Spitsbergen (Hornsund, Hyrnefjellet Mt. and Mariaholmen)	Stensiö (1921); Błażejowski (2004)

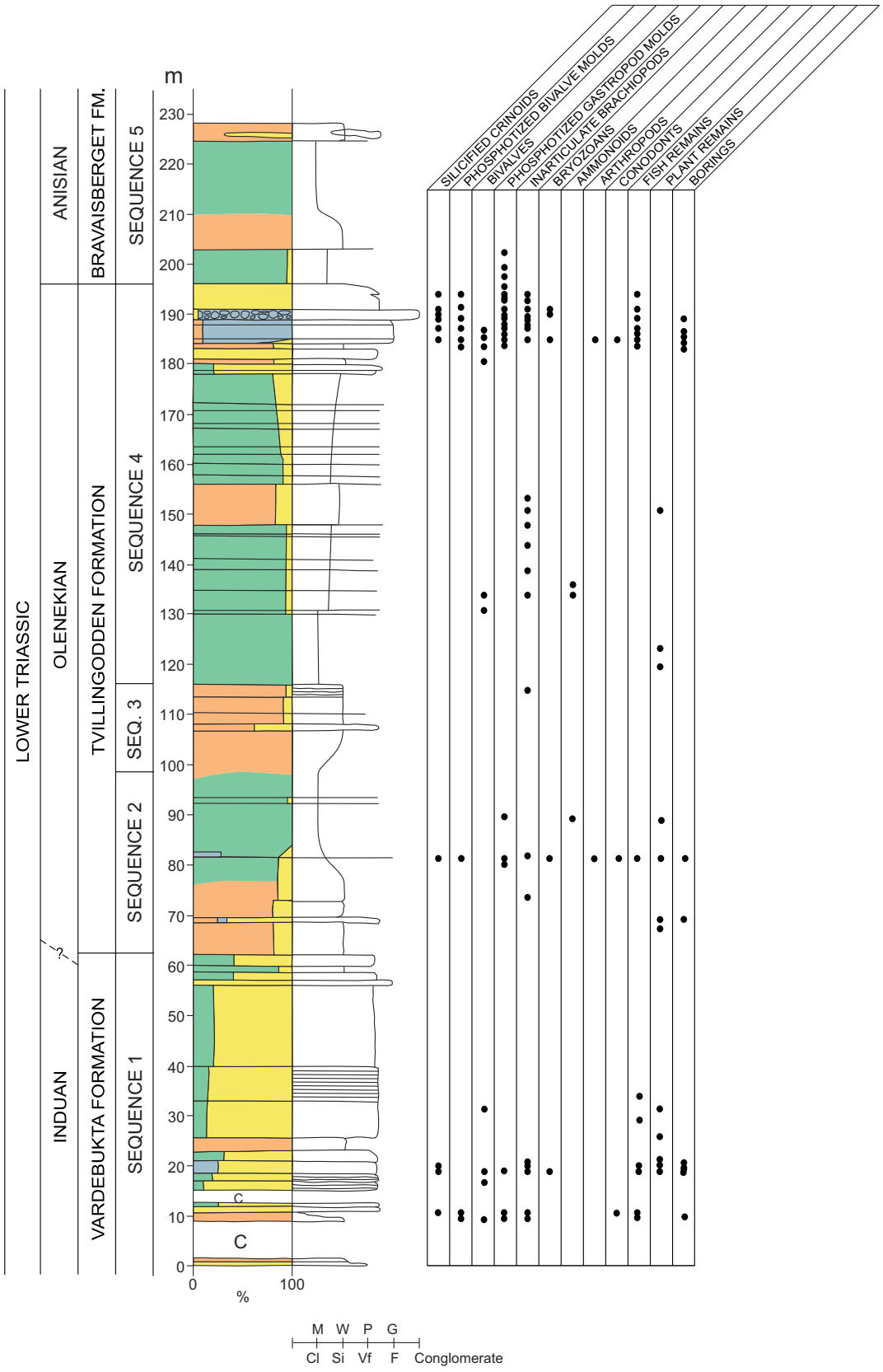

Fig. 3.49: Overview of fossils and fossil moulds from dissolved carbonates. Legend in Figure 3.3.

3.7 DIAGENETIC OBSERVATIONS

3.7.1 *General observations at discrete intervals*

3.7.1.1 19.05 *m above base*

At 19.05 m, as described in Section 3.2.5.1, and shown in Figures 3.28 and 3.27, a hardground is found. At the interface between the hardground and the subsequent sediments, there are bryozoans (Figure 3.50) with a thin carbonate cement coating the zooecia which were filled by a matrix that was subsequently phosphatised.

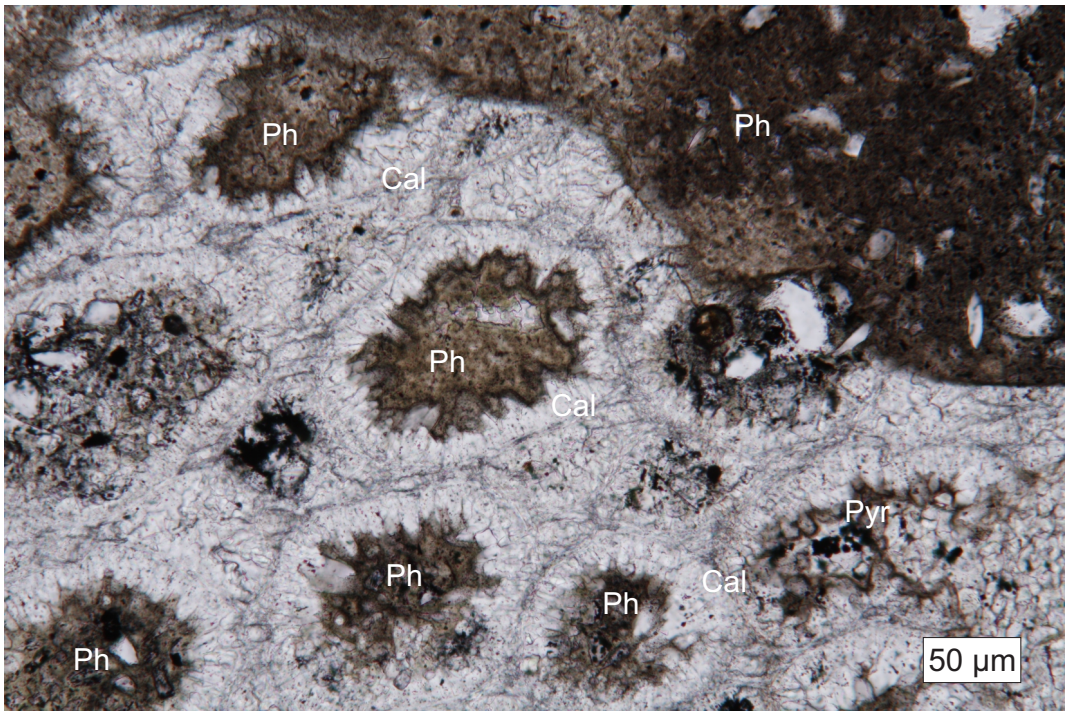

Fig. 3.50: Micrograph (PL) of transverse section of a bryozoan seen in thin section at 19.05 m. Note how the calcite cement (Cal) forms a thin rim around the zooecia which later were partially filled with matrix, before the phosphorite (Ph) fully cemented it. Note also how the calcite rim of the upper-right zooecia is cut off by the hardground, indicating early diagenetic cementation. Some pyrite (Py) is also seen.

3.7.1.2 19.15 *m above base*

The sample at 19.15 m consist of a sub-angular to sub-rounded fine grained calcite cemented sandstone rich in bivalves and with several rounded carbonate mudstone clasts. The clasts are likely to be extra-clasts as carbonate mudstones have not been observed elsewhere on Mariaholmen.

The bivalves originally consisted of aragonite that was dissolved after burial leaving behind a void. The voids were subsequently cemented with calcite preserving the bivalves as moulds. A micritized bivalve with a thin calcite cement generation which is filled with a fine grained matrix was observed in thin section (Figure 3.51). The fine grained material inside the bivalve have been calcite cemented and partially dolomitized.

From SEM and SEM-EDS (see Figure 3.52) it was found that the dark inner lining of the dolomite crystals consists of dolomite with equal amounts of Ca and Mg, while the outer zonation has depreciated values of Mg and increasing amounts of Fe and Ca, indicating changing pore water composition during crystal growth. The outer parts of the dolomite crystals show poikilotopic growth incorporating neighbouring clastic grains. (Figure 3.51D).

Micritization indicates that the bivalves were situated in the photic zone (Macintyre and Reid, 2003), and micritization on both sides along with the abrasion of bivalves show that the sediments have been moved by wave action. The bivalve fracture surfaces are also micritized. This shows that also the fragmentation of the bivalve shells has occurred in the photic zone, where the shell fragments subsequently rested on the

sea floor where they were micritized before final deposition. The lack of grain rounding can, however, indicate that wave action must have been somewhat limited.

Seen as a whole, the sediments at 19.15 m above base, were most likely deposited at the lower shoreface.

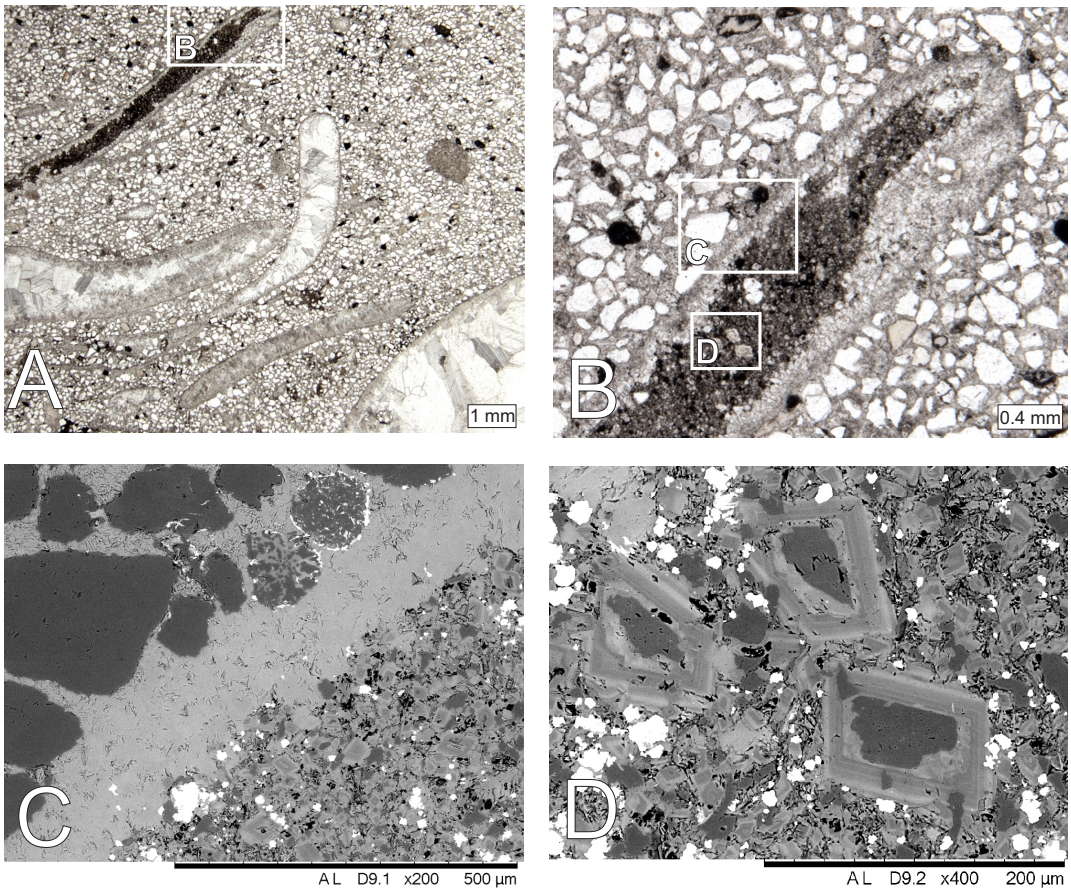

Fig. 3.51: Micrograph of thin section from sample 19.15 m above base. A: (PL) Overview of thin section, bivalves are micritized on both sides and are filled with calcite cement. B: (PL) Bivalve that was micritized on both sides, indicating wave action or reworking prior to burial. Subsequently a very early thin calcite cement precipitated on the walls in cavity created by the aragonite dissolution of the bivalve. After the calcite cement precipitated, the bivalve was exposed, abraded and filled with matrix. C: (SEM) Quarts grains are sub-angular to sub-rounded indicating transport before final deposition. D: (SEM) Dolomite crystals filling the porosity in an articulate bivalve. The outer parts of the dolomite crystals show poikilotopic growth incorporating neighbouring clastic grains.

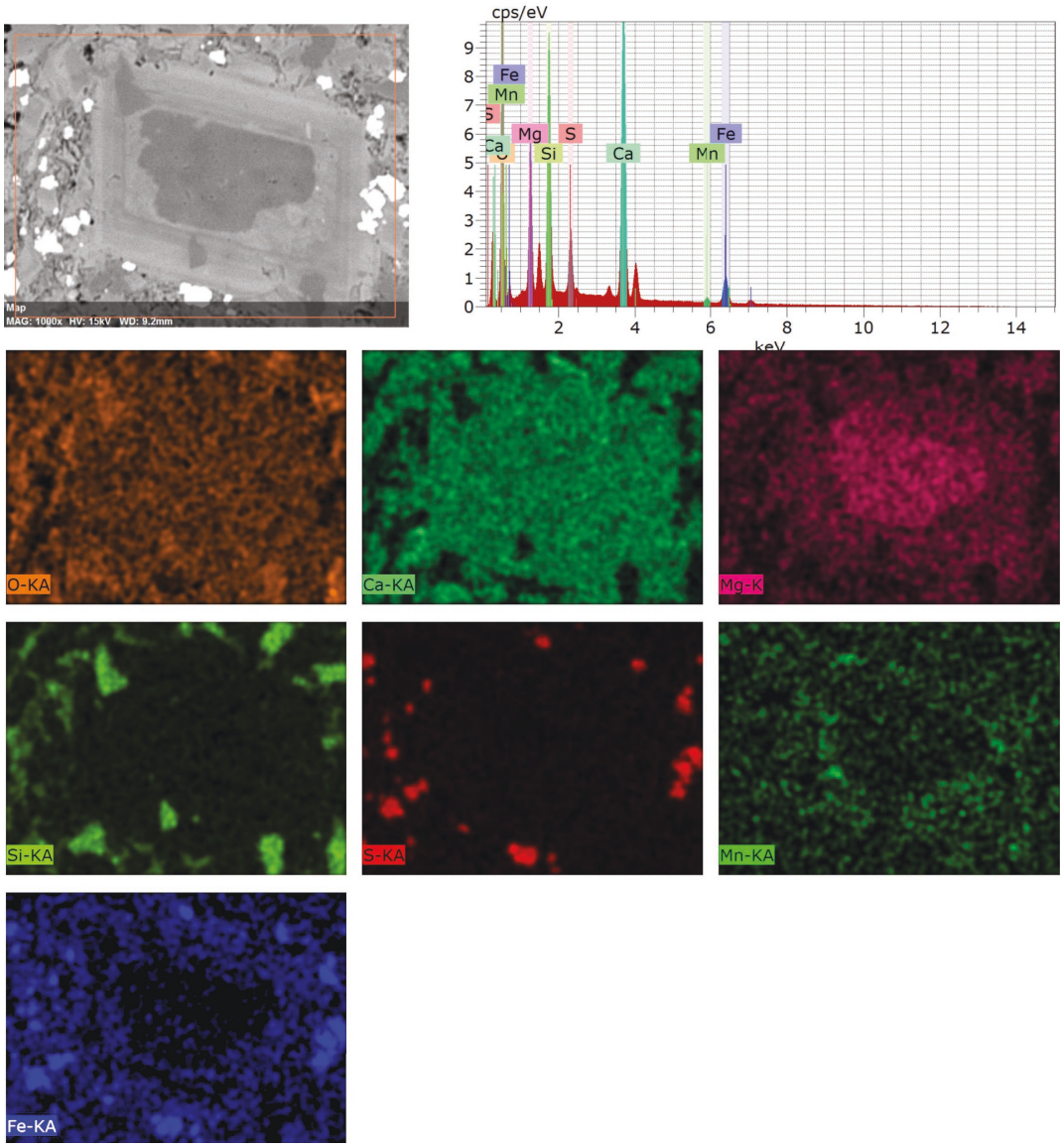

Fig. 3.52: SEM-EDS mapping analysis of a dolomite crystal within bivalve matrix show in Figure 3.51. The amount of Mg decreases from the centre of the crystal. Fe increases but this is somewhat subdued due to the very high concentration of Fe in pyrite. The S map show the location of the pyrite crystals, the S peaks also correlate with the bright spots on the Fe map.

3.7.1.3 34.15 *m above base*

In polished thin section of a parallel laminated sandstone located between two fully bioturbated sandstones at 34.15 m above base, angular to sub-angular quartz grains are situated in a microcrystalline calcite cement (Figure 3.53). The quartz grains have direct contact in the form of long and concavo-convex contacts (c.f. Taylor (1950)). Such contacts are a result of pressure dissolution of the quartz grains (Wilson and McBride, 1988), an indication of quite substantial burial (Bjørlykke and Høeg, 1997). The burial depth required for quartz dissolution is reported by Einsele (2000) to be >1 km and by Bjørlykke and Høeg (1997) to be between 2 km to 3 km.

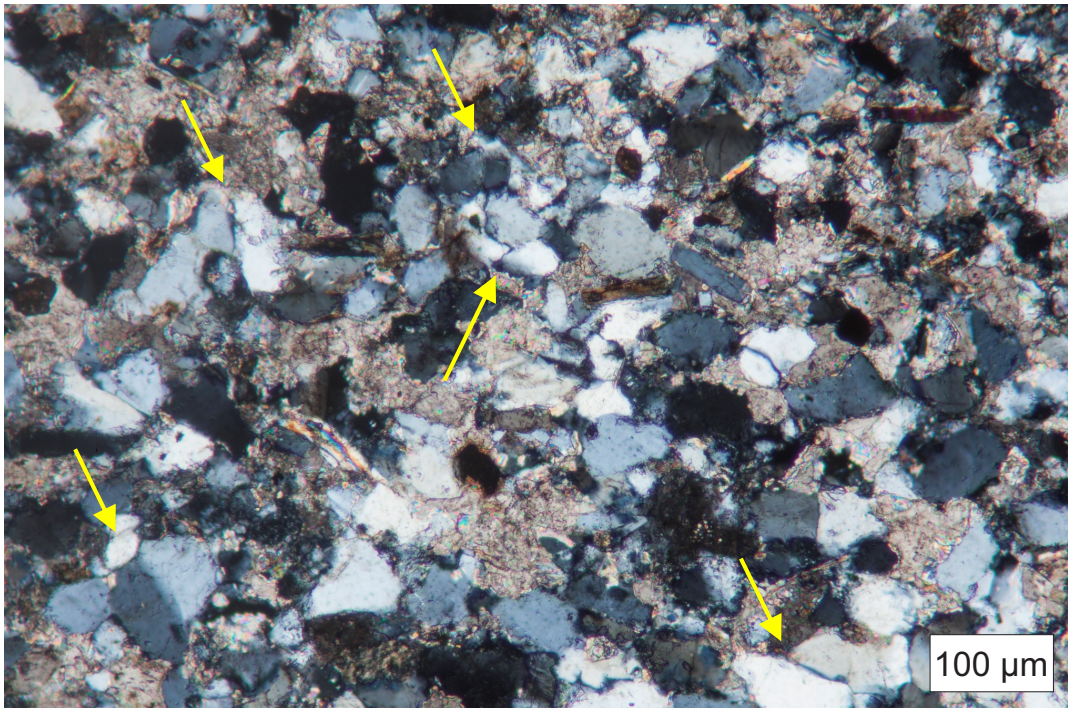

Fig. 3.53: Micrograph of thin section (XL) of a carbonate cemented sandstone from 34.15 m. Several quartz grains are characterised with concavo-convex and long contacts (yellow arrows).

3.7.1.4 *68.65 m above base*

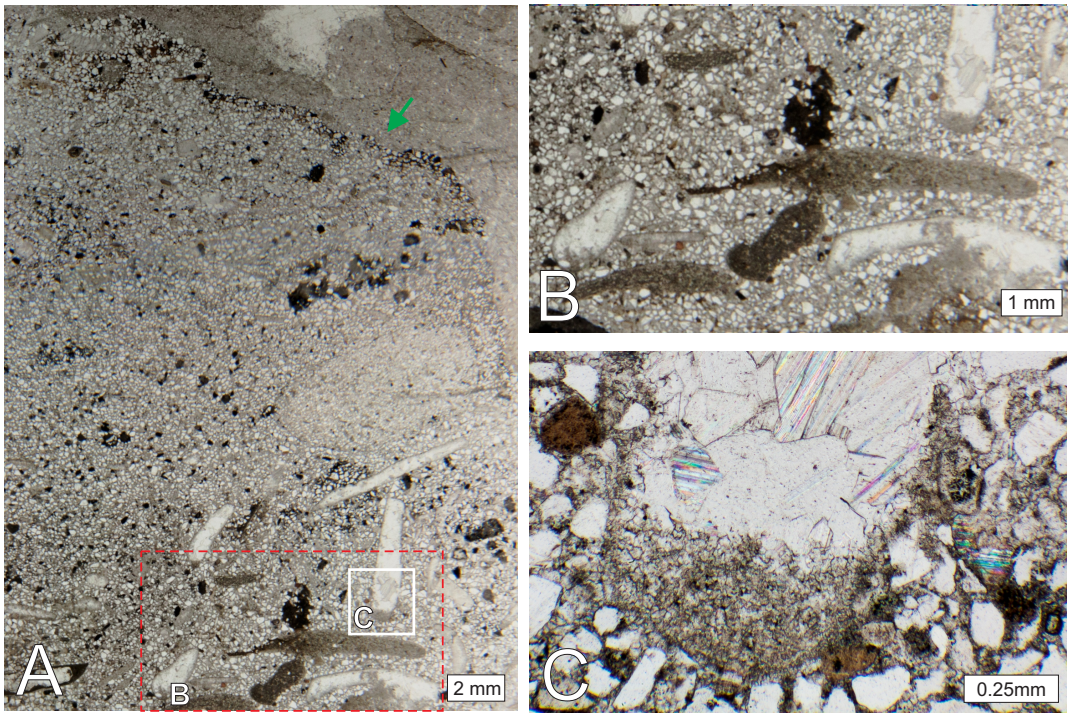

Fig. 3.54: Micrograph of thin section (PL) of sample at 68.65 m level. A: Green arrow show the location of phosphatised hardground. Note how the sediments are distinctly different above the hardground where the quartz grains are now absent. B: Bivalve which was mechanically abraded before deposition. The micritization show that the deposition of the bivalve could have occurred within the photic zone. Only the micritized outline is preserved after the dissolution of primary aragonite. Fine grained matrix fills the secondary cavity created by aragonite dissolution of bivalves C: Cavities partly filled by fine grained matrix.

The sample at 68.65 meter consist of a very sandy grainstone with sub-angular to sub-rounded quartz grains. Towards the top of the sample, a phosphatised hardground is observed (Section 3.2.5.2). Below the hardground, micritized bivalves are common, and there are occurrences where fine grained matrix is found within cavities (Figure 3.54). Some of the bivalves are entirely filled with matrix, while others have no matrix.

The matrix is most likely not vadose silt which require subaerial exposure (Dunham, 1969) as the matrix is resting directly on the micritized surface (Figure 3.54C). Since there is no evidence of a carbonate cement generation separating the matrix and micritized surface, the matrix was most likely introduced through small holes in the bivalve shells as they were washed back and forth on the sea-bottom

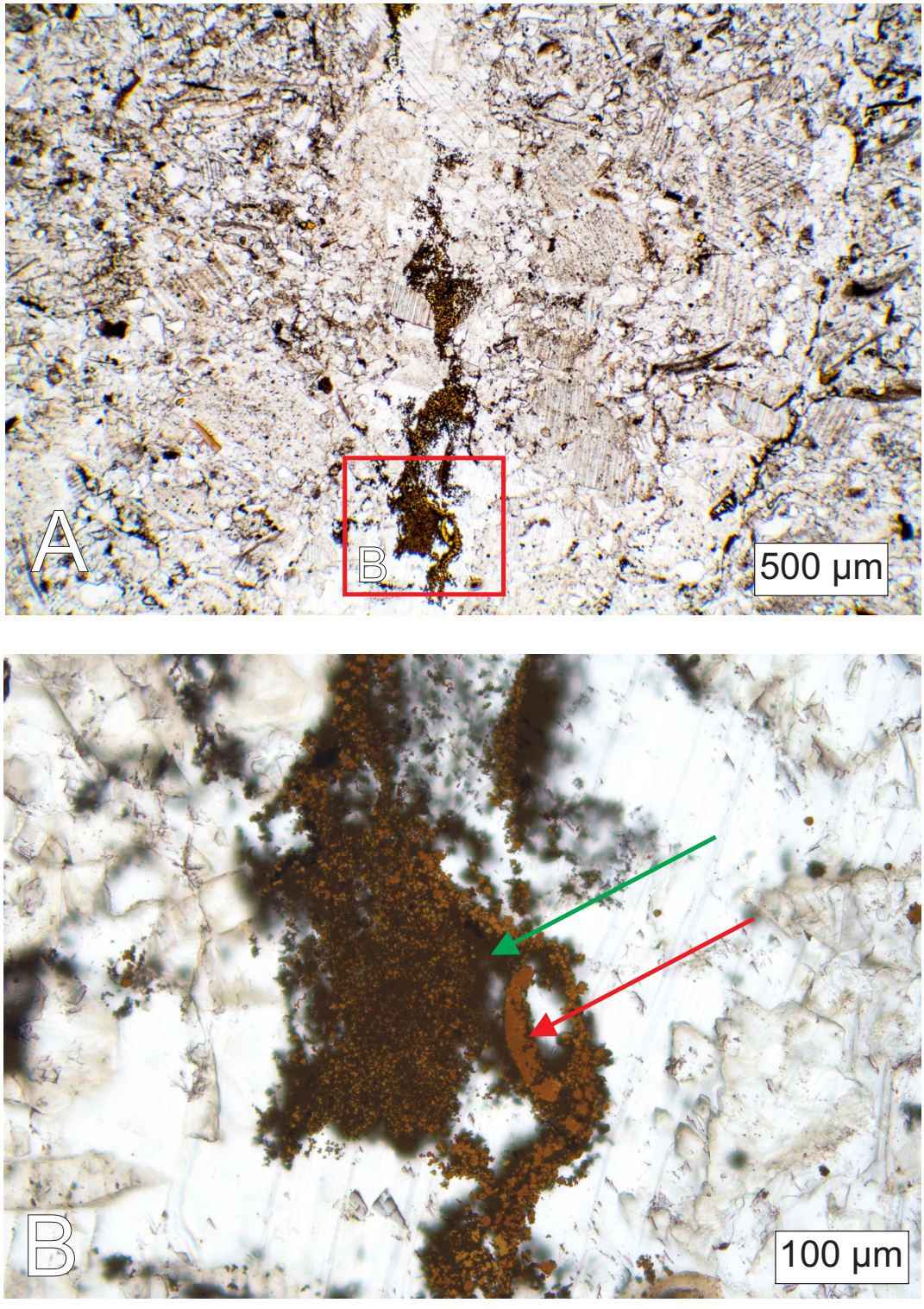

Fig. 3.55: Micrograph of thin section (combined PL and RL) from 185.35 m. A: Calcite cemented grainstone with abundant pyrobitumen and pyrite. Also note scattered phosphate fragments. B: Example of overgrowth pyrite (red arrow) in conjunction with pyrobitumen (green arrow). This combination of pyrite and pyrobitumen is found throughout the sample, either along stylolites or in fractures.

3.7.1.5 185.35 *m above base*

Situated within the Skilisen Bed, the sample at 185.35 m is a grainstone rich in disarticulated bivalve shells, some inarticulate brachiopods are also found. Many of the bivalve shells have been micritized and umbrella cement with large calcite crystals is commonly found underneath the bivalves, some of the shells also exhibit homogeneous prismatic microstructures. Two cement generations are present within the sample. The first cement generation is observed as a (at times slightly unclear) calcite cement in optical continuity with the micritized bivalve shells. The second cement generation is a relatively clear, blocky, drusy cement generation filling the remaining voids within the bivalve shells. A few of the larger crystals in the second cement generation are poikilotopic, incorporating neighbouring carbonate grains. Pyrite is found throughout the specimen, where it is found as framboid overgrowths as described by Sawlowicz (1993). The pyrite is often associated with a black opaque constituent interpreted to be pyrobitumen (Figure 3.55).

3.7.2 *Carbonate concretions*

3.7.2.1 28.34 *m above base*

At 28.34 m a pyrite rich carbonate concretion contained within a carbonate cemented sandstone bed is observed within a hand specimen (Figure 3.56). The pyrite appears to have grown within burrows; as umbrella effect below the bivalve shells; or as a complete replacement of bivalve shells. The complete bivalve replacement indicates pyrite growth after the initial aragonite dissolution, but prior to the phreatic calcite crystallisation observed elsewhere in the succession. In thin section, the quartz is found to have been subjected to pressure dissolution, and small bivalve fragments appear micritized. Along the fractures seen in Figure 3.56, a later calcite generation is seen.

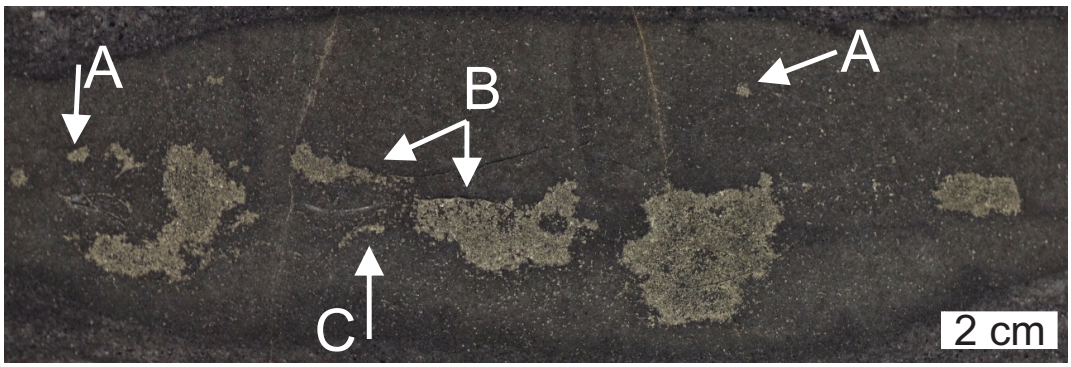

Fig. 3.56: Pyrite rich carbonate concretion within sandstone bed from 28.34 m above base. A: Possibly pyritized burrows, where early diagenetic pyrite crystallised prior to calcite cementation. B: Umbrella effect below shells where pyrite partly fills the void before calcite cementation. C: Pyritized bivalve.

3.7.2.2 123.15 *m above base*

At 123.15 m above base, a horizon of strata bound carbonate concretions was observed in a silty shale (Figure 3.57). The shape of the concretions are spherical to ellipsoidal and they range in size where the length of the longest axis varies from ~10 cm to ~40 cm. The concretions have fine parallel laminations and septarian fractures situated in a unclear carbonate matrix. The concretions at this level have at least two, possibly three cement generations (Figure 3.58). In the two concretions studied in thin section, the first cement generation appear as unclear brown calcite crystals, while the second (and possibly third generation) appear as a clear drusy calcite cement.

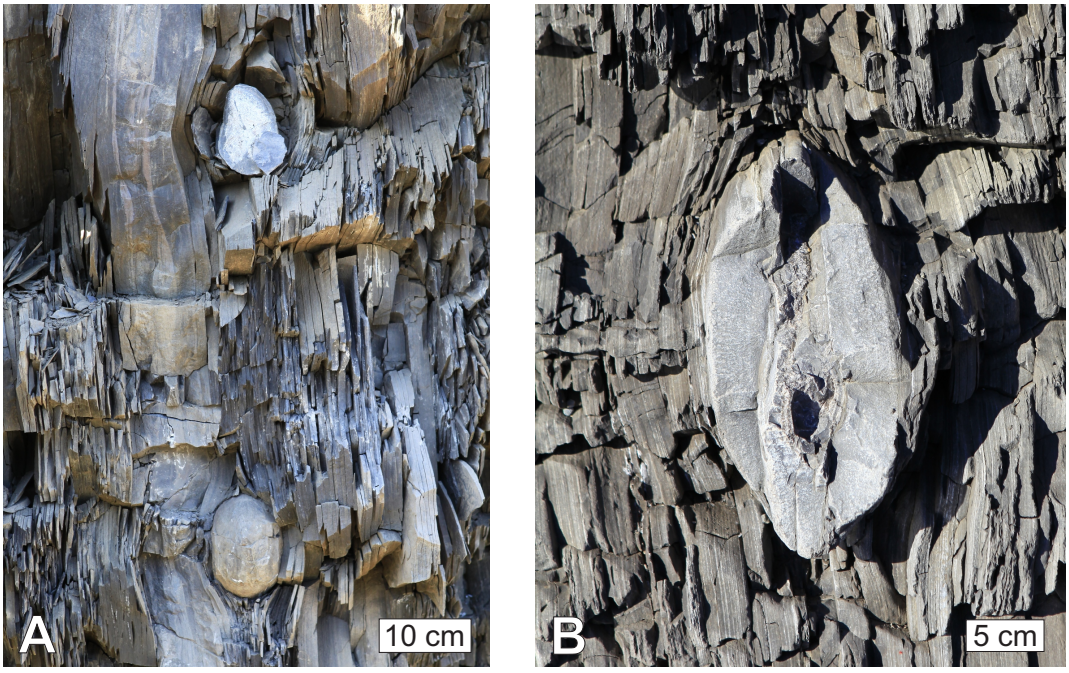

Fig. 3.57: Strata bound carbonate concretions. A: Concretions as seen at 134.25 m above base, upper concretion is fractured showing septaries. B: Fractured concretion with septaries at 123 m above base. A and B: Stratigraphic up is to the right.

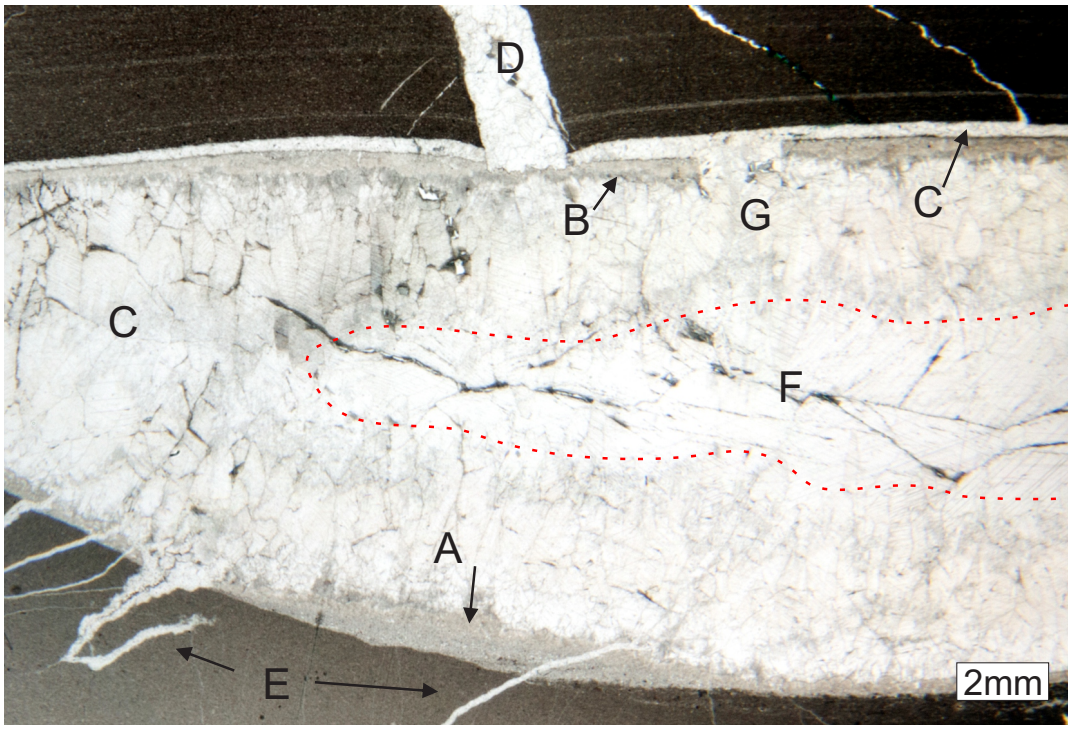

Fig. 3.58: Concretion at 123.15 m. A: Thin layer of fine grained matrix with varying thickness situated at the bottom of the septaries. B: 1st generation of cement. Slightly unclear carbonate which also cements the matrix in A. C: 2nd cement generation, the cement is now clearer than that of B, and it has a slightly blocky drusy appearance. D: 1st fracture generation with clean blocky calcite cement, which stops against B and C. E: 2nd fracture generation. Note how this generation cut through the 1st cement generation and stop against the 2nd. F: 3rd cement generation, differentiated from the 2nd by much clearer calcite cement. G: Breakage of the 1st cement generation, occurring some time before, or at the onset of the 2nd cement generation. Red: boundary between the 2nd and 3rd cement generations.

3.7.2.3 134.25 *m above base*

The concretions from the strata bound horizon situated in silty shales at 134.25 m (Figure 3.57) consists of finely laminated carbonate matrix with frequent septaries (Figure 3.59). The size of the concretions varies from ~10 cm to ~20 cm with a slightly elongated sphere shape. The septaries have two cement generations, the first generation appears to be rounded in its contact with the second generation, indicating a

partial dissolution before the onset of the second generation. The first cement generation must have undergone fracturing before the second generation precipitated as loose fragments of the first generation float within the second. However, this most likely happened after the rounding as the first generation's fragments that float within the second generation are not rounded.

3.7.2.4 *Summary*

Concretions usually form during early diagenesis, before the sediment is disrupted by compaction (Raiswell, 1976; Einsele, 2000). This provide a window of the sedimentary features relatively close to the time of deposition (Raiswell, 1976; Einsele, 2000). However, the exact depth range, and level at which they form have proven hard to establish (Raiswell and Fisher, 2000). Tens to hundreds of metres are, however, consistent with all evidence currently available (Raiswell and Fisher, 2000). Raiswell (1976) describe how the isotopic composition of carbonate concretions points to microbial processes with some incorporated seawater in the porewater for carbonate concretions forming at relatively shallow depths.

Septarian fractures are found within some concretions and are believed to have formed either as a result of shrinkage, dissolution or tensile stress (Raiswell and Fisher, 2000). Neither of these three processes provide supporting evidence for shallow formation (Raiswell and Fisher, 2000). However, according to Raiswell and Fisher (2000) a loose framework of cement resisting compaction could form at shallow

depths. This allows formation of septarian fractures and subsequent cementation at greater depths (Raiswell and Fisher, 2000).

3.7.3 *Hydrocarbons*

Traces of hydrocarbons in the form of pyrobitumen is seen at multiple stratigraphic levels on Mariaholmen. The pyrobitumen is mainly constrained to fractures, where it is contained within calcite and quartz cement (Figure 3.60). At the Skilisen Bed the pyrobitumen is also seen within the matrix (Figure 3.55). An indication that some porosity must have been left when the hydrocarbon migrated through the formations on western Svalbard.

In thin section the pyrobitumen appears as a dark to dark brown opaque element similar to that seen in Huc et al. (2000). This is however, as Møller and Friis (1999) state not certain proof of pyrobitumen, as the opaque fragments could also be various oxides.

The pyrobitumen was distinguished from oxides and other opaque minerals by study in reflected light microscopy. UV fluorescence light did however, not yield any results.

On Mariaholmen, mechanical crushing of the crystal surfaces in some samples did however, result in a characteristic smell of volatile sulphur-containing compounds present in hydrocarbons, which further strengthen the arguments for the opaque constituent to be pyrobitumen.

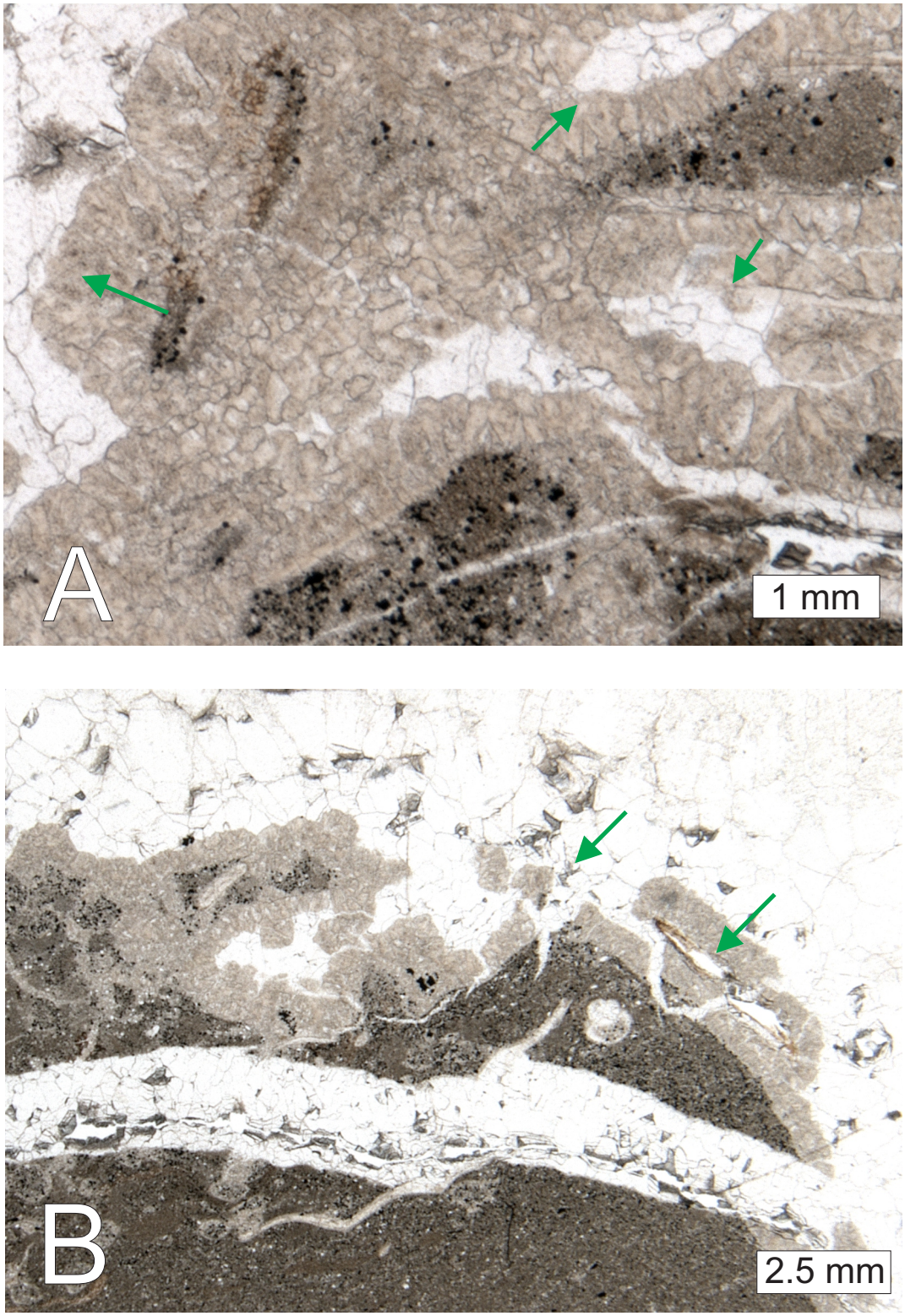

Fig. 3.59: Thin section (PL) of a septarie in a carbonate concretion at 134.25 m. A: 1st cement generation (brown) have been partially dissolved (green arrows) prior to precipitation of 2nd calcite generation. B: Fragments of 1st cement generation incorporated in the 2nd calcite generation.

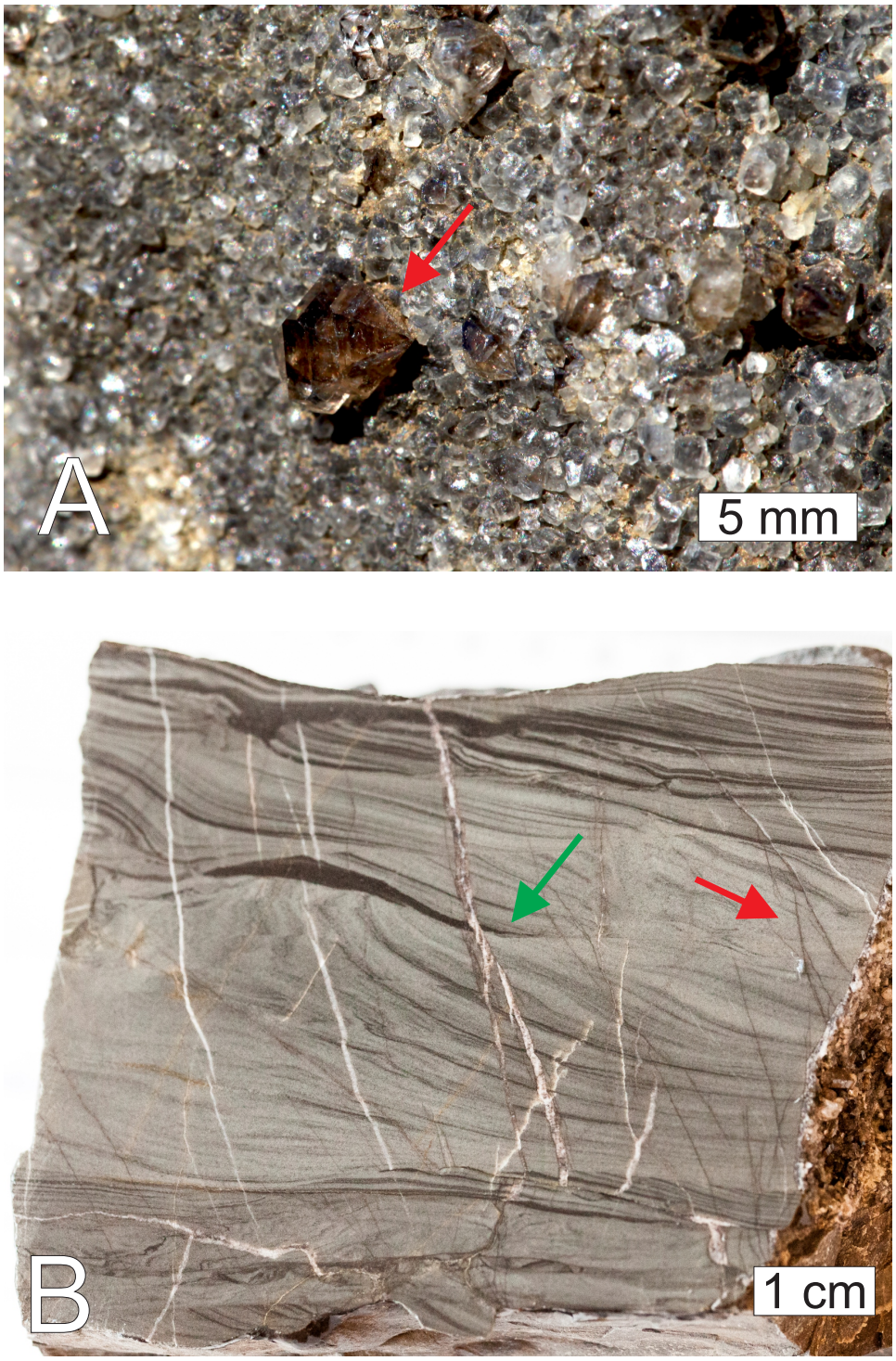

Fig. 3.60: From 140.65 m A: Pyrobitumen contained within quartz (red arrow) situated amongst dark calcite crystals with pyrobitumen inclusions. Seen in the outcrop on Mariaholmen. B: Polished hand specimen showing calcite veins containing pyrobitumen, the thicker veins (green arrow) have pyrobitumen along the lining with clean calcite in the centre, while the thin dark veins are filled with pyrobitumen filled (red arrow). Notice how the thick veins consistently intersect and cross the thin dark veins, indicating that the thick veins are younger than the thin veins. Thus the hydrocarbons most likely migrated through the formation prior to cementation of the thick fractures.

4

GEOCHEMICAL INVESTIGATIONS

This chapter cover the geochemical investigations, variances and statistics, followed by discussions. All geochemical data in tabular form can be found in Appendix D. All geochemical measurements have been performed on fine grained siliclastic deposits (shaly siltstones or shales). As high organic content normally gives a darker sediment colour (c.f. Arthur and Sageman (1994) and references therein), the geochemical variations for different sediment colours have also been investigated.

4.1 VANADIUM AND NICKEL

4.1.1 *Vanadium, nickel and vanadium/(vanadium+nickel) ratio data*

Vanadium and nickel measurements were performed on fine grained clastic sediments. Both the vanadium and nickel curves have very similar characteristics albeit shifted. The nickel has an average value of 35.48 parts per million (ppm) with a standard deviation of 9.76 ppm points, while the vanadium has an average of 93.89 ppm with a standard deviation of 30.06 ppm points. As seen on Figure 4.1, both vanadium and nickel have very frequent but small variations which lead to a fluctuant curve character.

There appear to be very little change in the V/(V+Ni) ratio throughout the succession. The total average ratio for the fine grained terrigenous sediments in the succession is 0.722, with a standard deviation of 0.029 (3.98% RSD). RSD is the relative standard deviation or coefficient of variation which is defined as the ratio of the standard deviation to the mean ($c_v = \frac{\sigma}{\mu}$). The low standard deviation indicates that there is not much change in the ratio throughout the profile.

When subdividing the succession, the lowermost sequence (0 m to 62 m) has an average ratio of 0.731 with a standard deviation of 0.028 (3.86% RSD), the second sequence covering (62 m to 98 m) has an average ratio of 0.727 with a standard deviation of 0.025 (3.44% RSD). As for the third sequence (98 m to 116 m), it also has an average ratio of 0.727 with a standard deviation of 0.027 (3.66% RSD). The fourth sequence has an average ratio of 0.728 with a standard deviation of 0.022 (3.04% RSD), while the fifth sequence has an average V/(V+Ni) ratio of 0.681 with a standard deviation of 0.016 (2.38% RSD).

4.1.2 *Discussion of vanadium, nickel and vanadium/(vanadium+nickel) ratio*

Several different trace elements can be used as indicators of bottom-water oxygenation and stratification. However, the V/(V+Ni) ratio has been shown to be especially useful. It was introduced by Lewan and Maynard (1982) and Lewan (1984) who used it to show that redox potential was the primary control on the ratio in bitumen and oils. It was, however, Hatch and Leventhal (1992) who showed that the ratio

can also be applied to whole rock samples. The method has since been used by, and further refined by multiple workers, (e.g. Arthur and Sageman (1994); Wignall (1994); Hoffman et al. (1998); Rimmer et al. (2004); Hansen et al. (2009)). They all show that this is a method which proves effective in depicting the oxygen variations in bottom-waters at the time of deposition.

Both vanadium and nickel are typically preserved under reducing conditions, i.e. at the deposition of fine grained material such as clay in low energy environments allowing stratification of the water column. Vanadium is preserved by a change in valence state in reducing environments (Wehrli and Stumm, 1989; Breit and Wanty, 1991; Wanty and Goldhaber, 1992; Calvert and Pedersen, 1993). Easily soluble vanadium compounds form increasingly less soluble compounds as vanadium is reduced from V^{5+} to V^{4+} and V^{3+} (V^{3+} at euxinic conditions), while nickel on the other hand does not go through a valence change, it's deposition increase with the availability of H_2S which leads to deposition of NiS (Wehrli and Stumm, 1989; Breit and Wanty, 1991; Wanty and Goldhaber, 1992; Calvert and Pedersen, 1993).

Ratio values used to discern the depositional bottom-water conditions used in this thesis were taken from Hatch and Leventhal (1992) (Table 4.1).

For the fine grained terrigenous deposits in the entire Mariaholmen succession, the levels are situated at the middle to lower end of "less strongly stratified water column", which has been interpreted as an equivalent to anoxic to dysoxic environments, and as such not very different from the TOC:TS ratio discussed in Subsection 4.4.2. How-

Table 4.1: V/(V+Ni) ratio bottom-water condition proxy based on analysis of clay-rich sediments.

Bottom-water condition	Ratio
Oxygenated bottom-water	<0.46
Weakly stratified dysoxic water column	0.46-0.60
Less strongly stratified water column	0.54-0.82
Strongly stratified water column	>0.82

ever, unlike the TOC/TS ratio, the V/(V+Ni) ratio does not show much variation throughout the succession. Differences in proxies are to be expected as they are based on vastly different principles. Varying content of coarser grained material such as silt is seen within the whole-rock samples, and as clay contain more vanadium (Wignall, 1994), this can lead to a relative decrease in vanadium. A decrease in vanadium could possibly shift the ratio somewhat towards oxic environments. As seen on Figure 4.1, the V/(V+Ni) ratio decreases somewhat towards normal marine environments within the sandier lower level between $30-40$ m.

For the succession between approximately $40-170$ m, the V/(V+Ni) ratio has a spiky appearance towards more oxic conditions, several of these spikes are adjacent to both sandstone beds and hummocky cross-stratification. As such this could be an indication of a slight oxygenation of the shale and siltstone beds deposited adjacent to sandstone beds of higher energy events such as storms. This appearance is also present where hummocky cross-stratification was not observed in the field. Consistent presence of bioturbation is also likely to affect the ratio in the sediments.

Although there is seemingly little variation in the bottom-waters measured with the V(V+Ni) ratio, both small and large depositional trends appear to be recorded.

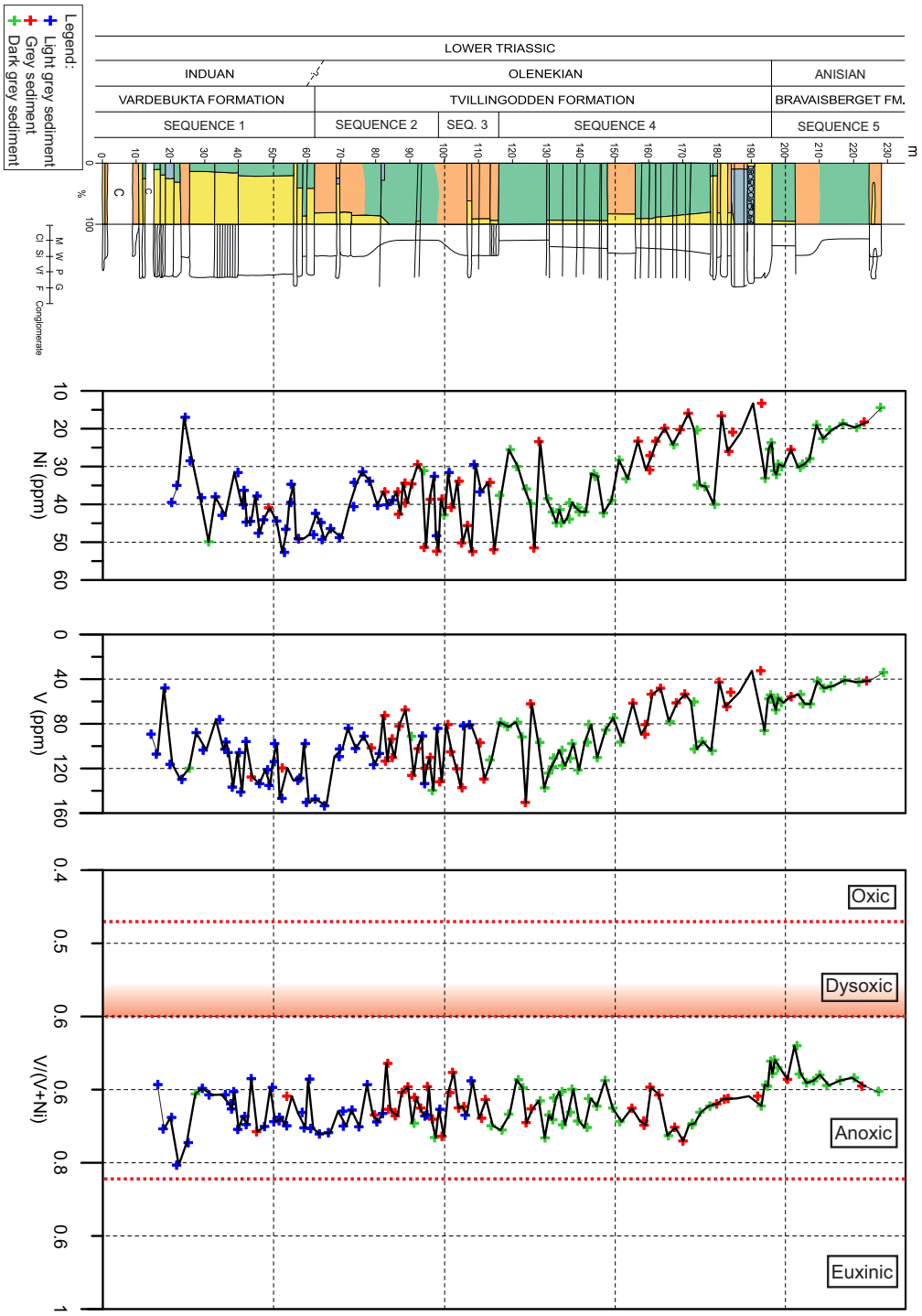

Fig. 4.1: Lithological log of the studied succession at Mariaholmen showing analysis of vanadium, nickel and V/(V+Ni) ratio data in fine grained clastic sediments. The curves are interpolated using moving average (over 3 data points). The raw data points are denoted by +. Ratio limits are from Hatch and Leventhal (1992).

4.2 TOTAL SULPHUR

4.2.1 *Total sulphur (TS) data*

Average TS values for the investigated section is 0.878% sulphur with a standard deviation of 0.608 pp (percentage point) (69.29% RSD). The total sulphur values vary from a minimum of 0.02% to a maximum of 2.67%.

The light grey and grey siltstones show average sulphur values of 0.459% and 0.521%, respectively, and standard deviation of 0.24 pp (61.62% RSD) and 0.51 pp (8.38% RSD), respectively. The dark grey fine grained siliclastic sediments gave an average sulphur value of 1.238%, which represent a ~2.5x increase compared to the grey fine grained siliclastic sediments, where the standard deviation was 0.60 pp (48.78% RSD). Furthermore, the sulphur and total organic carbon data (TOC will be described later) track the changes in depositional environment (Figure 4.3).

This trend is similar for a majority of the measured parameters, and thus it was chosen to subdivide the Mariaholmen profile chemostratigraphically with the same boundaries as described in Chapter 3: sequence 1 (0 m to 62 m), sequence 2 (62 m to 98 m), sequence 3 (98 m to 116 m), sequence 4 (116 m to 196 m) and sequence 5 (196 m to 227 m).

The deposits of the lowermost sequence (0 m to 62 m) have an average sulphur value of 0.37% with a standard deviation of 0.40 pp (109.00% RSD). The second sequence (62 m to 98 m) has the same average of 0.37% sulphur, but with a standard deviation of 0.42 pp

(113.23% RSD). The third sequence (98 m to 116 m) has a slight increase to an average of 0.99% sulphur with a standard deviation of 0.57 pp (57.67% RSD). Sulphur values in the fourth sequence (116 m to 196 m) further increase to an average of 1.18% sulphur, with a standard deviation of 0.74 pp (62.65% RSD). The uppermost fifth sequence (196 m to 227 m) has an average sulphur value of 0.90% with a standard deviation of 0.28 pp (31.15% RSD).

4.2.2 *Discussion of sulphur content*

Thin section studies indicate that pyrite is the only common sulphur bearing mineral in the succession and therefore all sulphur measured is assumed to be derived from pyrite. According to Berner (1983), the amount of pyrite formed during burial and diagenesis is highly dependent on three major factors:

1. Supply of decomposable organic matter
2. Available dissolved sulphate SO_4^{2-}
3. Available reactive detrital Fe-minerals

Berner (1983) describes how pyrite is formed during shallow burial where detrital Fe-minerals react with H_2S created by sulphate reduction by bacteria utilising organic matter as energy source. As seen on Figure 4.2, the initial product is not pyrite but metastable iron monosulphides that readily transform to pyrite under most conditions.

Bacterial reduction of sulphate can only occur under conditions where no oxygen is present (Berner, 1982). These conditions are met in most

marine fine-grained sediments (Berner, 1982). Organic matter deposited will act not only as a reducing agent and energy source for the bacteria, but also as a barrier hampering the migration of oxygen from the bottom-water into the sediments (Berner, 1983). This occurs because the oxygen is rapidly consumed at the water-sediment interface by oxic bacteria that convert the organic matter to CO_2, preventing oxygen from penetrating the sediment (Berner, 1983). As such anoxic conditions are met just centimetres below the water-sediment interface (Berner, 1983). Oxygen typically make its way to the sediments through diffusion; by bioturbation through ventilation of sediment (the biological pump according to Berner and Westrich (1985)) and wave/current stirring (Berner, 1983).

Berner (1983) also notes that the major controlling factor on early diagenetic pyrite formation in marine sediments is generally the availability of organic matter and its reactivity. Berner (1983) also points out that sufficient SO_4^{2-}, and Fe in terrigenous detrital minerals is generally readily available. However, Berner and Westrich (1985) observed that also the bioturbation of sediments affected the availability of oxygen below the sediment water interface. In addition, the bioturbation also alters the amounts of H_2S present within the sediments (oxidation due to diffusion). This will in turn lead to less pyrite formed and as such a reduction in potential sulphur amounts.

The amounts of sulphur formed is thus balanced by the bioturbation and bacterial activity at the water sediment interface.

Considering the sulphur values of the Mariaholmen succession as a whole, there appears to be a close correlation between depositional en-

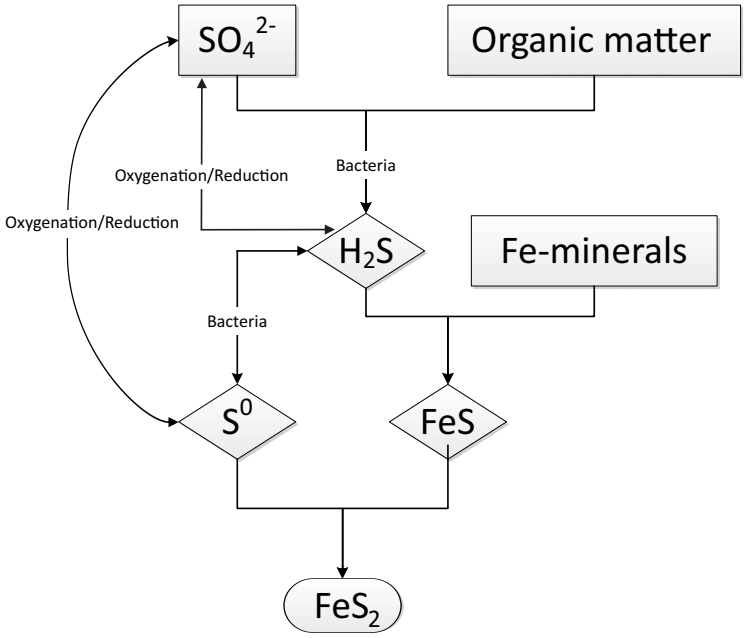

Fig. 4.2: Early diagenetic formation of sedimentary pyrite in marine sediments. S^{6+} in SO_4^{2-} can be directly reduced to S^{2-} in H_2S, and opposite, the S^{2-} H_2S can be directly oxidised to S^{6+} in SO_4^{2-}. The S^{6+} in SO_4^{2-} can also be reduced to S^{2-} in H_2S when anaerobic bacteria use the SO_4^{2-} during oxidation of organic matter. Regardless, the H_2S formed subsequently reacts with Fe-minerals to form FeS. The S^{2-} in H_2S can be oxidised by bacteria to produce S^0 (S^0 can also be reduced directly from SO_4^{2-}, or oxidised directly from S^0 to SO_4^{2-}). FeS and S^0 further react to form the end product FeS_2 (pyrite). Modified after Berner (1983); Jørgensen (1994); Canfield and Thamdrup (1994); Habicht and Canfield (2001).

vironment and sulphur levels. In the intervals with the highest abundance of sandstone the sulphur levels tend to be quite low. However, in siltstone, and especially in shale intervals the sulphur levels are substantially higher.

This is most likely related to more oxygen being present in the relatively higher energy environment where siltstones and shales situated within the coarser-grained sediments were deposited as compared to the intervals with deposition of mainly fine-grained material only.

As described in Section 3.5, the coarser grained sediments generally also have more vertical bioturbation in the form of trace fossils such as *Arenicolites* isp., vertical bioturbation can also introduce more oxygen to below the water-sediment interface, lowering the levels of H_2S available for pyrite formation.

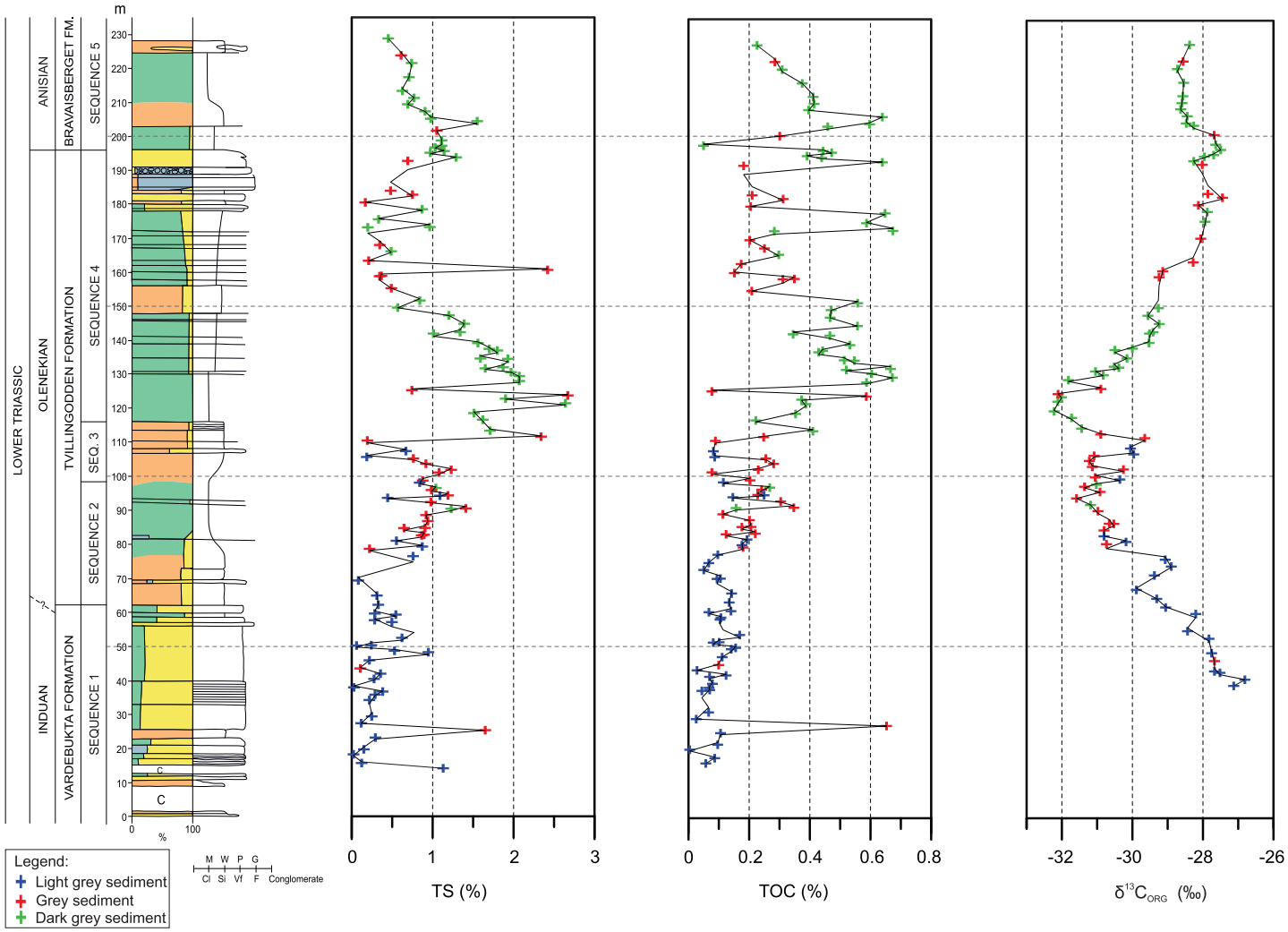

Fig. 4.3: Lithological log of the studied section against TS, TOC and $\delta^{13}C_{ORG}$ data. Curves are smoothed by moving average (over 3 points), where raw data points are denoted by +. All analysis have been carried out on fine grained siliclastics (shale or shaly siltstone). For legend see Figure 3.3.

4.3 ORGANIC CARBON

4.3.1 *Total organic carbon (TOC)*

Average TOC value for the fine grained terrigenous sediments is 0.27% with a standard deviation of 0.19 pp (68.86% RSD). Compared to the standard deviation values discussed for sulphur in Section 4.2.1, the standard deviation values for TOC might seem surprisingly low, but when considering the RSD, it is evident that it's due to generally lower values measured for TOC.

Looking at the sequence division of the succession, the lower unit (0 m to 62 m) show average TOC values of 0.11% with a standard deviation of 0.12 pp (115.35% RSD) the relatively high standard deviation for this unit is most likely a result of the peak seen on the log at 31 m. The second unit (62 m to 98 m) show a very slight increase in organic carbon with an average of 0.16% and a standard deviation of 0.07 pp (45.06% RSD). In the third unit (98 m to 116 m), the average TOC value is 0.20% with a standard deviation of 0.10 pp (50.00% RSD). Sequence 4 (116 m to 196 m) has an increase to 0.41% average TOC and a standard deviation of 0.17 pp (41.27% RSD). The fifth sequence (196 m to 227 m) has an average TOC value of 0.38% and a standard deviation of 0.14 pp (37.33% RSD).

For the light grey fine grained siliclastic sediments, the average total organic carbon is 0.10% accompanied by a standard deviation of 0.05 pp (48.51% RSD), while fine grained siliclastic sediments which were grey show average TOC values of 0.22% with a standard deviation of 0.10 pp

(44.31% RSD). The dark grey fine grained siliclastic sediments were measured at an average TOC of 0.45% with a standard deviation of 0.15 pp (32.44% RSD).

4.3.2 *Rock-Eval*

The Rock-Eval S1, S2 and S3 data generally show very low values, while the PI (Production index) and T_{Max} are relatively high. Data summary is given in Table 4.2, and complete data set in appendix Table D.4. As seen on Figure 4.4, the S3 data is quite variable in the lower unit, and this has a large impact on the Oxygen Index data. Such high values of S3 can occur if the TOC content is below 0.5%, and happens due to O_2 or CO_2 adsorption in the samples (Peters, 1986). Carbonate content could also impact S3 measurements (Peters, 1986), which is not unlikely as the peaks are all located within light grey fine grained siliclastic sediments.

Table 4.2: Statistics of Rock-Eval data

	Average	**Standard Deviation**	**RSD (%)**
S1 (mg/g)	0.07	0.09	129.28
S2 (mg/g)	0.1	0.11	109.91
S3 (mg/g)	0.43	0.27	62.15
T_{Max} (°C)	464	37	8
PI (wt ratio)	0.3	0.2	65.39
HI (mg HC/g TOC)	30	23	76
OI (mg CO_2/g TOC)	275	389	141

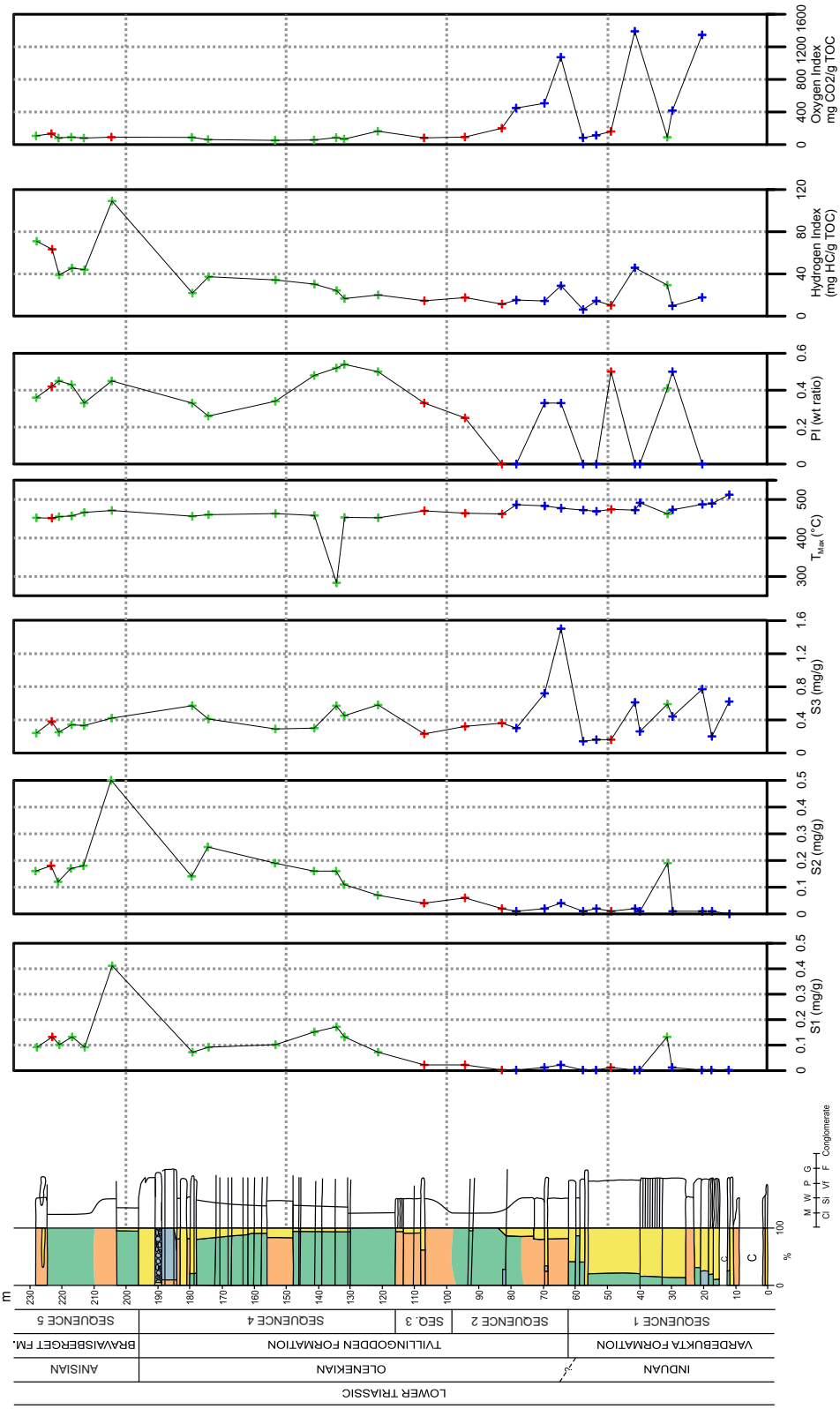

Fig. 4.4: Lithological log of the studied section against Rock-Eval data. The raw data points are denoted by +.

4.3.3 *Discussion of organic carbon*

Total organic carbon is the measure of organic richness in sedimentary rocks. It can also be used as a direct (and sometimes proportional) indicator of organic accumulation rates and productivity in the overlying water column (c.f. Schoepfer et al. (2015) and references therein). However, it should be noted that one should be careful when using TOC as direct indicator of organic richness. This applies for the sea bottom and in the overlying water column as there are multiple factors controlling the preservation of organic material in sediments. Such factors are diagenesis (maturation), variation in sedimentation rates, bioturbation and bottom-water conditions (Berner, 1982; Doyle and Garrels, 1985; Chinn, 1991; Kristensen et al., 1995; Schoepfer et al., 2015).

The fine grained terrigenous sediments in the Lower Triassic of Mariaholmen, has little, but some variation in total organic carbon. The values are generally quite low considering the fact that all the samples are taken from shale (with some slightly siltier samples). Also when comparing organic carbon values to the sulphur values (Figure 4.3), the organic carbon values are low. As seen in Section 4.3.1, the section as a whole has an average total organic carbon value of 0.27%. According to Miles (1989) and Chinn (1991), the global average total organic carbon content (determined using Rock-Eval) for all shales is between 0.8% and 0.9%, which is significantly higher than observed for the studied section. There are several possible causes covering these deviations from with the global average.

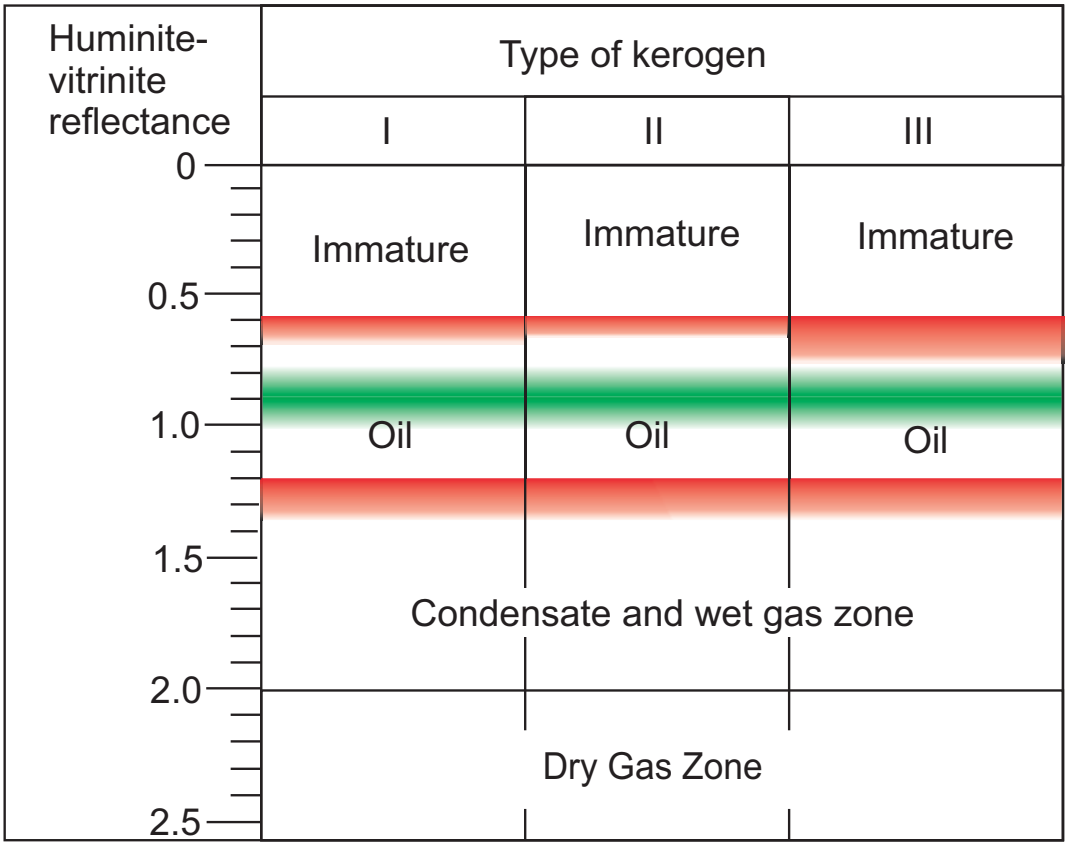

Fig. 4.5: Hydrocarbon generation in relation to vitrinite reflectance and kerogen type. Red indicates transition zone, green zone is peak oil generation level. Modified after Tissot and Welte (1984); Peters and Cassa (1994); Dembicki (2009).

Foremost, does our sampled material contain too high concentrations of silt as opposed to shale, and does this impact the measurements by a large extent? Through qualitatively studying the sampled material, it is evident that some silty material is present, albeit not much. Some silt is expected in the sediments that have a light grey colour (0.10% average TOC), and to some extent the sediments with a grey colour (0.22% average TOC). When further studying the most fissile and fine grained dark grey sediments, it becomes evident that something other than the silt content could be affecting the TOC levels as the dark grey

sediments measure at an average total organic carbon level of 0.45%. This is half the level of global shale average.

Following the sedimentation rate model, it has been shown that organic carbon content increases with increasing sedimentation rate (Ibach, 1982). However, when considering productivity and anoxicity alongside the sedimentation rate model, suboxic to anoxic environments under both high and low sedimentation rates and productivity regimes are expected to have reasonably good source rock potential (Katz, 2005).

Like sulphur, the organic carbon content is also likely to have been affected by the affluent bioturbation (Section 3.5) observed in the sediments on Mariaholmen, where the bioturbation would decrease the amount of organic carbon preserved.

However, it was shown by Raiswell and Berner (1987), that during burial and maturation there is a relationship between temperature and loss of total organic carbon, more specifically, as the vitrinite reflectance (R_o) increase, the amount of organic carbon in their sample material decreased. Raiswell and Berner (1987) analysed fine grained terrigenous material spanning widespread stratigraphic ages (Devonian to Jurassic) at multiple geographic locations achieving consistent results. This thus suggests that the principles of Raiswell and Berner (1987) could also be applied to explain the low organic carbon levels found on Mariaholmen.

The assumptions of Raiswell and Berner (1987) are based on normal marine shales with an average TOC/TS ratio of 2.8. While the sediments on Mariaholmen may not necessarily confine to normal marine shales (as seen from the TOC/TS ratio and V/(V+Ni) ratio in Sec-

tions 4.4.2 and 4.1, respectively), it would still be feasible to assume a similar decrease in TOC value as the exhumation of organic material is due to temperature and not initial chemical composition.

The Rock-Eval studies performed on Mariaholmen show a T_{Max} ranging between 428°C to 513°C (Section 4.3.2) . The T_{Max} on Mariaholmen decrease in the higher part of the investigated section. Considering the massive tectonic disturbances on Mariaholmen, situated immediately adjacent to Midterhuken (Maher et al., 1986) alongside the additional burial, it seems reasonable to have significantly higher T_{Max} temperatures on Mariaholmen than those found in studies done by Karcz (2014) of the immediately overlying and laterally adjacent (~7 km, Figure 1.2.) Middle Triassic succession at Bravaisberget. Karcz (2014) found that the T_{Max} in the Passhatten Member ranges between 449°C to 467°C with an average of 452°C. Also at Passhatten Member, the T_{Max} increa stratigraphically downwards.

At Passhatten Member, vitrinite reflectance was measured at an average of 1.10% R_o. This did not compare well to the T_{Max} calculations, but is explained to result from bitumen impregnation of the vitrinite due to exhumed oil. This is also supported by the variation of unimodal, bimodal and multimodal vitrinite reflectance histograms (Figure 4.8). As such, disregarding the bitumen, the actual vitrinite reflectance should most likely have been higher in the Passhatten Member.

Comparing the vitrinite reflectance values and T_{Max} from Karcz (2014) to Figure 4.5 and Table 4.3 respectively, it is evident that even for the lowest maturity assumptions, the Passhatten Member is well within peak oil, and as Karcz (2014) state, likely within the gas window.

For the succession on Mariaholmen, very low S1 and S2 values (average of 0.07 mg/g and 0.10 mg/g respectively) combined with the high T_{Max} (463.76°C) and Production index (0.30 wt. ratio) indicate that the Mariaholmen is a post mature source rock with poor hydrocarbon potential (when compared to the limits in Table 4.4). Considering the HI (30.23 mg HC/g TOC average) the Mariaholmen is well within the gas window (Table 4.4). This is further supported by the high T_{Max} (Table 4.3).

However, Peters (1986) describe how sediments with low TOC (<0.5%), generally have reduced S2 peaks due adsorption of pyrolyzate by the mineral matrix. Adsorption of oxygen and CO_2 also leads to relatively high S3 peaks due to the low TOC (Peters, 1986). The combination of these two effects lead to an anomalously high oxygen ratio and anomalously low hydrogen ratio (Peters, 1986), also the T_{Max} can be affected by as much as +10°C in low TOC sediments (Peters, 1986). Accounting for a 10°C change in T_{Max}, however, still place the succession well within the kerogen type III window.

Table 4.3: Hydrocarbon generation in relation to T_{Max}. Kerogen type I is not reliable in conjunction with T_{Max}, and is therefore omitted in the table. Modified after Law (1999).

Hydrocarbon Generation Zone	Rock-Eval Pyrolysis T_{Max} (°C)
Immature	<435
Oil (from type II kerogen)	435-455
Oil (from type III kerogen)	435-465
Gas (from type II kerogen)	>455
Gas (from type III kerogen)	>465

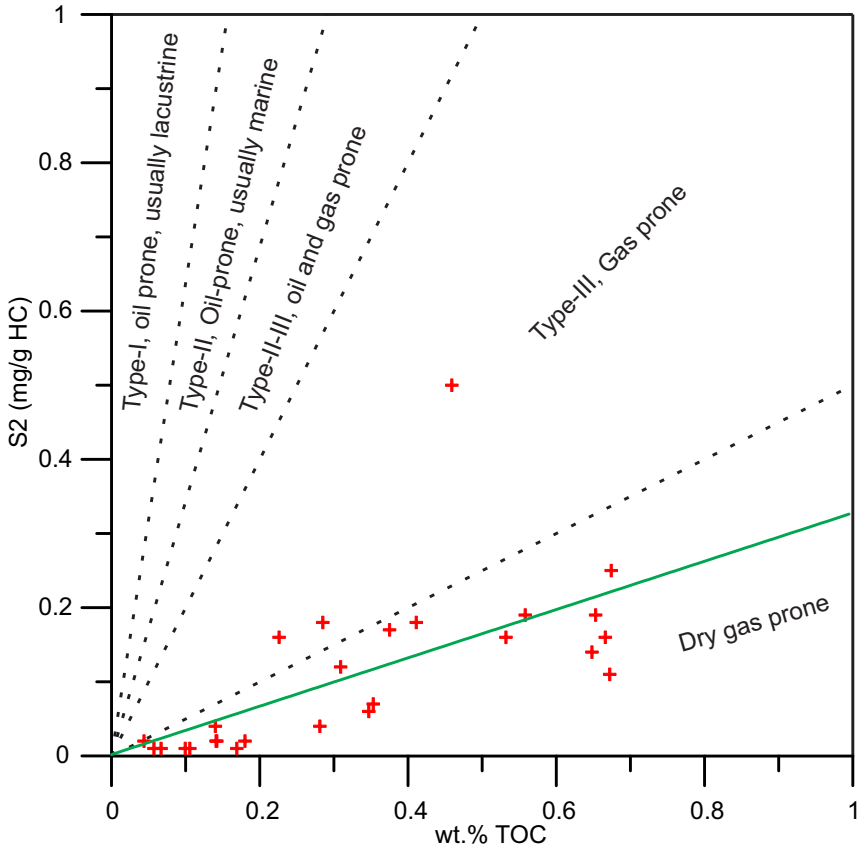

Fig. 4.6: TOC vs. S2 plot. Green line: regression line. Limits from Langford and Blanc-Valleron (1990) and Diasty et al. (2015).

Considering a shift in HI and OI due to the low TOC when analysing the measurements in a hydrogen index vs oxygen index plot (Figure 4.7) and in a S2 vs TOC plot (Figure 4.6) give indications that the sediments from Mariaholmen possibly could contain highly mature type III kerogen. On Figure 4.7, the points would be shifted up and to the left, while the points on 4.6 would have positive shift on the y-axis.

Comparing what Karcz (2014) found at Passhatten Member, to what is seen on Mariaholmen in relation to the findings of Raiswell and Berner (1987) discussed earlier, it seems reasonable to expect that there has been a significant loss of organic carbon as a result of thermal maturation and expulsion on Mariaholmen. However, this does not imply

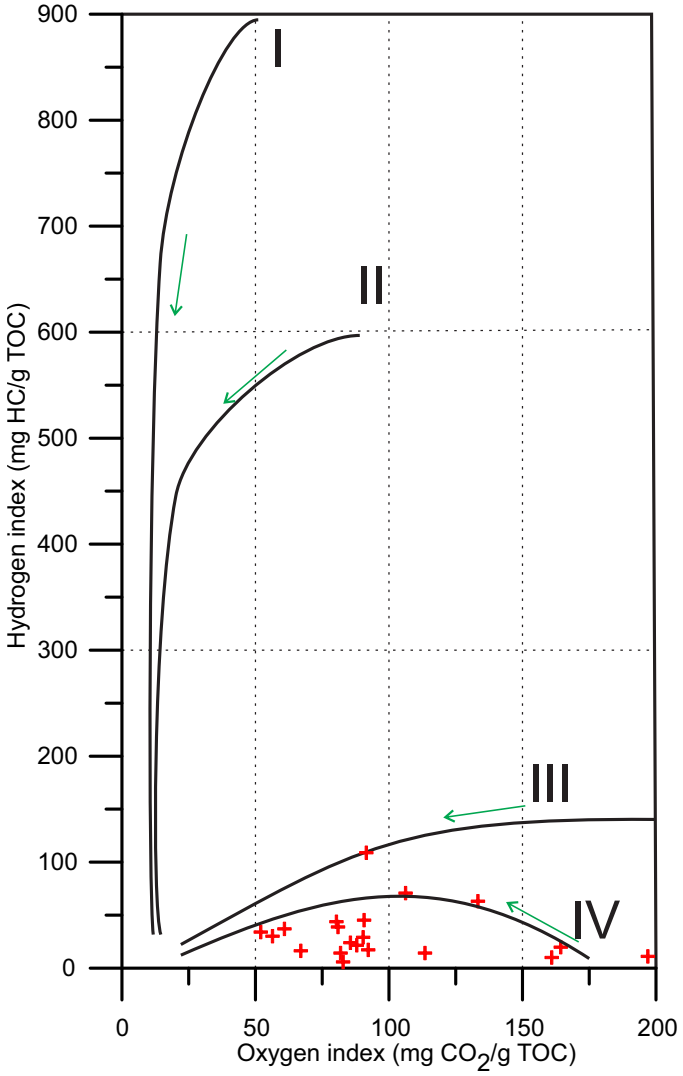

Fig. 4.7: HI vs. OI plot. I-IV indicate kerogen maturation paths. The green arrows indicate increasing maturation. Limits based on those of Espitalie et al. (1977), Peters (1986), Langford and Blanc-Valleron (1990), Dembicki (2009) and Diasty et al. (2015).

that the Mariaholmen sediments were rich in carbon prior to maturation (as can be seen from the extremely low S2 values).

Assuming either a 50% or 70% loss of organic carbon on Mariaholmen due to maturation and exhumation still places the succession only at the brink of the global average TOC for shales. (50% and 70% loss reflect $R_o = 1.0$ and Anthracite grade organic metamorphism, respectively, in Raiswell and Berner (1987)). Given these generally low

Table 4.4: Organic matter limits. Modified after Baskin (1997).

Quantity of Organic Matter	(Wt.% TOC)	S2	**Quality of Organic Matter**	(HI)
Poor:	<0.50	<1.0	Gas:	<100
Fair:	0.5-1.0	1.0-5.0	Gas and Oil:	100 – 200
Good:	1.0-2.0	5.0-10.0	Oil and Gas:	200-350
Very good:	2.0-4.0	10.0-20.0	Oil:	>350
Excellent:	>4.0	>20.0		
Maturity of Organic Matter				
Maturation	(T_{Max})		Generation	PI
Immature:	<430		Immature:	<0.10
Beginning:	430-435		Beginning:	0.10-0.15
Peak:	445-450		Peak:	0.15-0.25
Post:	>460		Post:	>0.20

values, it is still worth noting that there is an increase in the shaly middle unit, with a maximum of 0.67% TOC.

The Vardebukta Formation on Mariaholmen is generally very low in total organic content, and there is no increase before approaching the upper two thirds of the Tvillingodden Formation. Throughout the succession there generally appears to be a positive correlation between TOC and fine-grained material.

It is also worth noticing that the standard deviation is quite a bit lower for the TOC as compared to TS when differentiating the rocks

Table 4.5: Comparison between standard deviations for Total Sulphur and Total Organic Carbon in fine grained shale and shaly silt detrital sediments. Standard deviations have been normalised using the relative standard deviation method (RSD).

Standard Deviation Comparison		
	Total Sulphur	Total Organic Carbon
Light grey sediments	73.29%	48.51%
Grey sediments	69.72%	44.31%
Dark grey sediments	43.51%	32.44%

by powder colour (Table 4.5). In other words, this goes to show that what Berner (1974) and Arthur and Sageman (1994) have shown could most likely also be applied to powdered rock. From the TOC standard deviations, it becomes evident that the dark sediments can be used as an indication of elevated TOC levels.

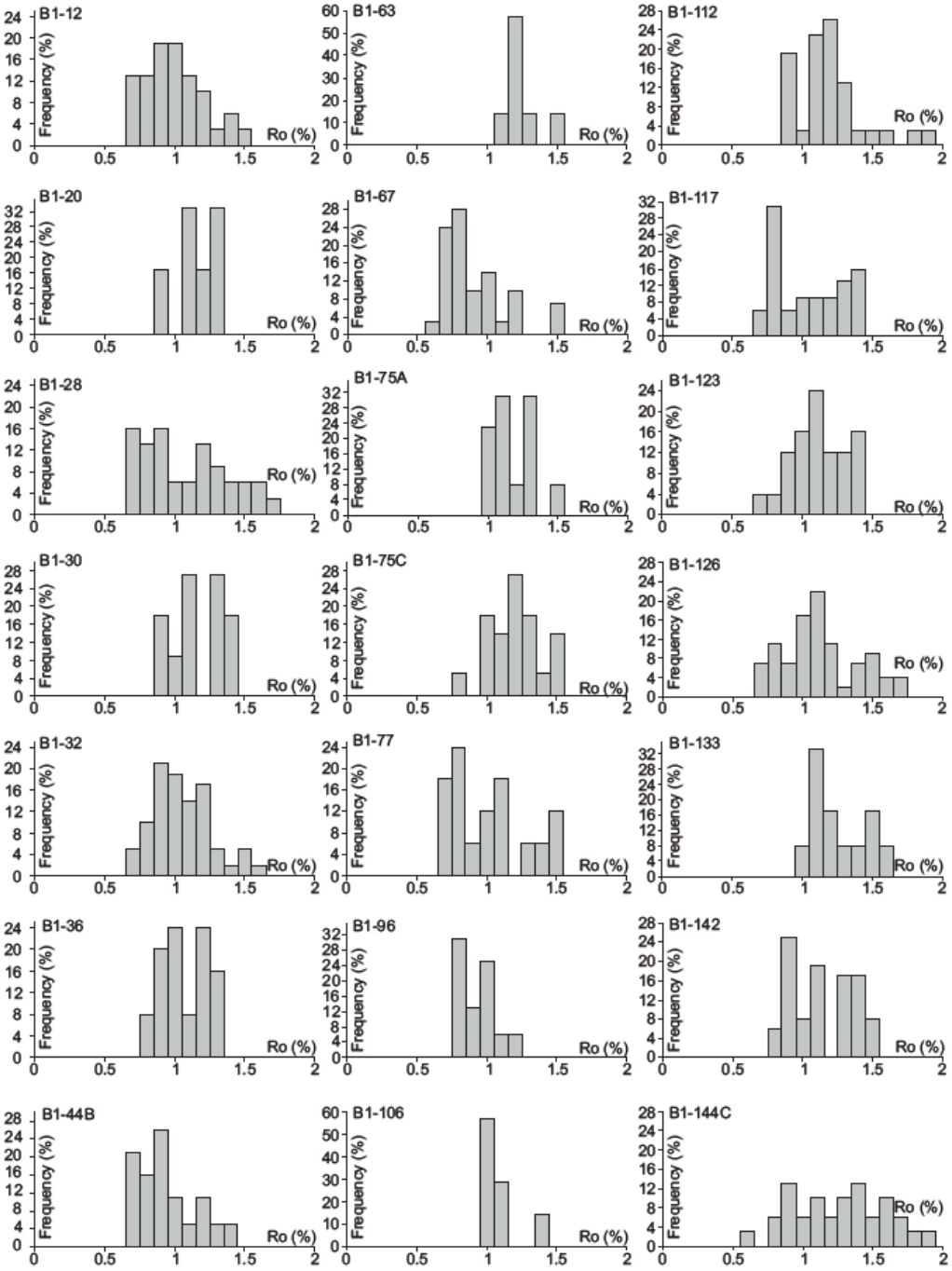

Fig. 4.8: Unimodal, bi-modal and multimodal vitrinite distributions at Passhatten (B1-xxx is stratigraphic height). From Karcz (2014).

4.4 TOTAL ORGANIC CARBON AND TOTAL SULPHUR RATIO

4.4.1 *TOC/TS ratio data*

The ratio is obtained dividing the total organic carbon content by total sulphur content (here, as previously discussed, one assumes all sulphur is derived from pyrite). The average ratio is 0.429 with a standard deviation of 0.383 (89.2% RSD), while the maximum and minimum ratio values are 2.873 and 0.045 respectively.

The lowermost sequence (0 m to 62 m) has an average ratio of 0.49 with a standard deviation of 0.61 (125.45% RSD) which is an indication of a very large spread in ratios. For the second sequence (62 m to 98 m), the average ratio value is 0.33 with a standard deviation of 0.27 (81.00% RSD). The third sequence (98 m to 116 m) has an average ratio of 0.24 with a standard deviation of 0.12 (50.00% RSD). Sequence number four has an average ratio of 0.50 with a standard deviation of 0.37 (73.75% RSD). The fifth sequence has a ratio of 0.45 with a standard deviation of 0.19 (41.96% RSD).

The light grey fine grained siliclastic sediments show an average ratio of 0.44 with a standard deviation of 0.59 (134.73% RSD) indicating a large sample spread. The grey fine grained siliclastic sediments show an average ratio of 0.39 with a standard deviation of 0.30 (77.38% RSD), while the dark grey fine grained siliclastic sediments had an average ratio of 0.46 and a standard deviation of 0.31 (68.53% RSD).

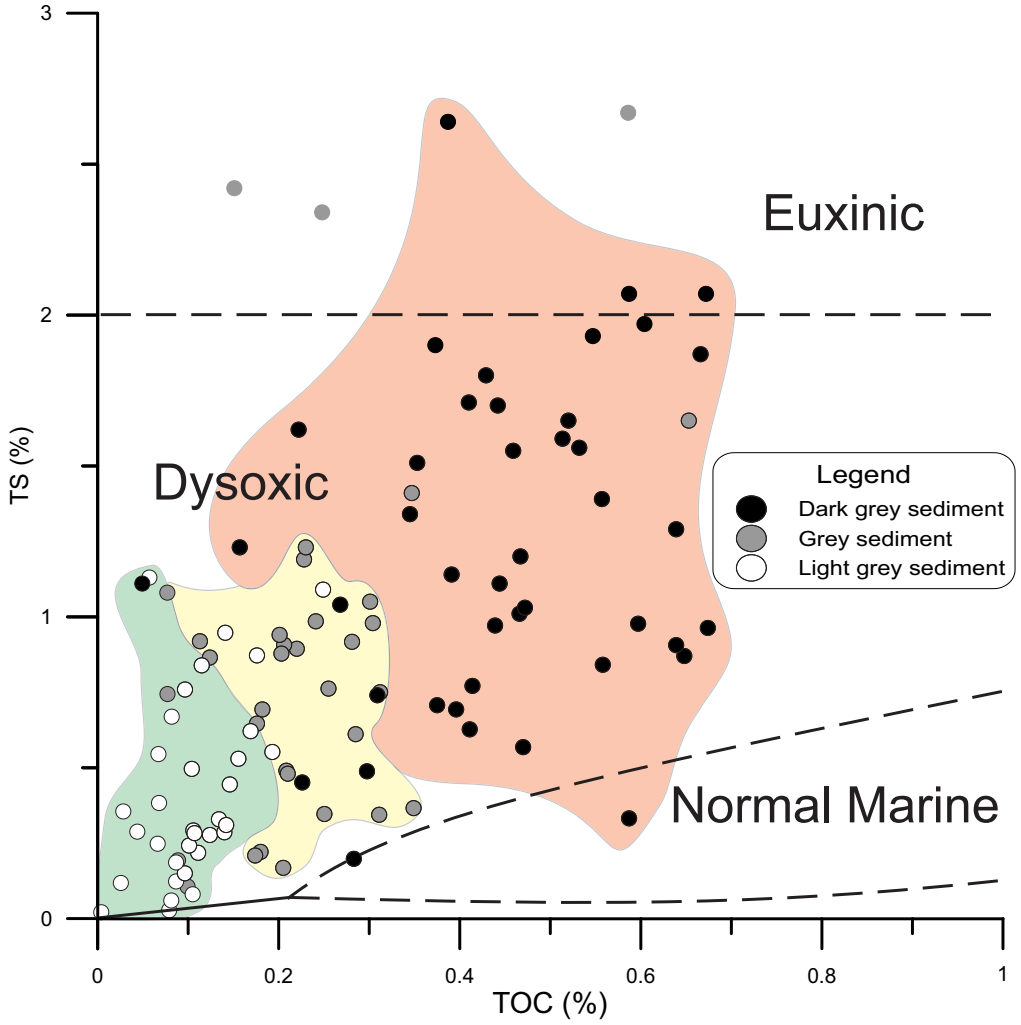

Fig. 4.9: TS vs TOC scatter plot of shale and silty shale with different colours. Notice how the anoxicity of the environment overall increases with darker rock colour and larger TOC values. Green, yellow and red shading is to emphasise position of light, grey and dark grey sediments, respectively. Limits from Leventhal (1983, 1995) and Berner (1983).

4.4.2 *Discussion of TOC/TS ratio*

Several workers such as Berner and Raiswell (1984); Berner (1983); Leventhal (1983, 1995); Arthur and Sageman (1994); Berner and Raiswell (1983); Raiswell and Berner (1986) and Raiswell and Al-Biatty (1989) have shown that there is a strong positive correlation between TOC/TS ratio

and bottom-water conditions at the time of deposition. This is supported by a strong positive correlation between organic carbon and pyrite bound sulphur in both modern and ancient sediments (Leventhal, 1983; Berner, 1983; Berner and Raiswell, 1983). This allows the use of the TOC/TS ratio as an oxygenation proxy.

As seen on Figure 4.9, showing limits for different depositional conditions, most of the Mariaholmen succession has been deposited under dysoxic conditions, with euxinic and normal marine environments as exceptions. Further considering Figure 4.10 which has the oxygenation limits as defined by Berner (1983) and Berner and Raiswell (1984), it becomes evident that the Tvillingodden Formation falls within the limits of an anoxic to dysoxic environment as the majority of the sediments have a ratio below 0.4. The Tvillingodden Formation is largely represented by the dark grey fine grained siliclastic sediments. This can also be seen on the scatter plot where these sediments are shifted more to the right and up towards the euxinic border (Figure 4.9). As expected the more oxic environments are found in the coarser grained high energy environments which are constrained to the lowermost Vardebukta Formation as well as above and below the Skilisen Bed of the Tvillingodden Formation. The onset of the Anisian and the Bravaisberget Formation's shale, does not lead to yet another anoxic/dysoxic event in the sediments found on Mariaholmen albeit borderline.

When situated within sandstone beds, shale and silt beds are still low energy depositional events. As such shale and silty shale beds are generally more prone to dysoxic and anoxic conditions. It should, however, be noted that indications of dysoxic and anoxic environments in

these interbedded shale intervals, does not imply dysoxic and anoxic conditions in the immediately over and underlying sandstone beds. The TOC/TS ratio in the fine grained terrigenous sediments situated in sandier intervals can be seen shifting towards normal marine conditions. Coarser grained sediments are typically deposited in higher energy environments, and as such oxygenated bottom-water is readily available. This allows opportunistic trace fossil fauna to move in and thrive, which can also disturb the underlying fine grained material, and in turn disturb the initial TOC/TS ratio.

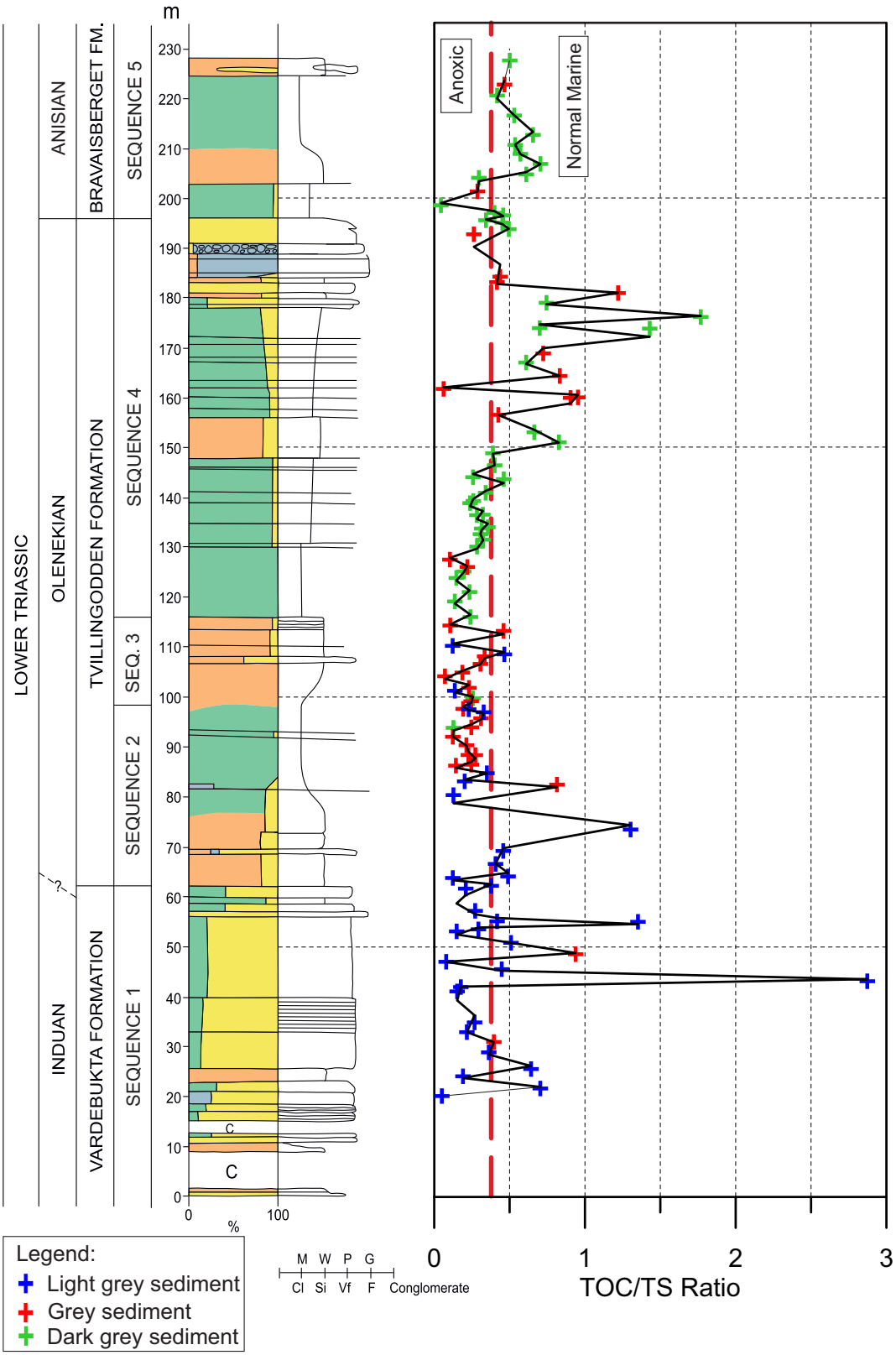

Fig. 4.10: TOC/TS ratio of fine grained clastic sediments against the lithological log. The curve is smoothed with moving average (over 3 points), raw data points are denoted by +. Stippled red line indicated border between anoxic and normal marine environments as per Berner and Raiswell (1984). For lithology legend see Figure 3.3.

4.5 ORGANIC CARBON ISOTOPES - $\delta^{13}C_{Org}$

4.5.1 $\delta^{13}C_{ORG}$ *mass spectrometry data*

Average $\delta^{13}C_{ORG}$ for the entire succession measures at -29.51‰with a standard deviation of 1.44 pmp (per mille points) (4.86‰RSD).

0 m to 62 m representing the lowermost sequence shows average $\delta^{13}C_{ORG}$ values of -27.60‰with a standard deviation of 0.48 pmp (1.75% RSD). The second sequence covering 62 m to 98 m has an average $\delta^{13}C_{ORG}$ value of -30.73‰with a standard deviation of 0.97 pmp (3.22% RSD) while the third sequence (98 m to 116 m) has an average at -30.73 ‰with a standard deviation of 0.59 pmp (1.93% RSD). Sequence 4 (116 m to 196 m) has an average $\delta^{13}C_{ORG}$ value of -29.72‰with a standard deviation of 1.50 pmp (5.04% RSD). The fifth sequence has an average value of -28.26‰with a standard deviation of 0.43 pmp (1.54% RSD).

4.5.2 *Discussion of organic carbon isotopes* - $\delta^{13}C_{Org}$

The $\delta 13C_{Org}$ measurements performed on the fine grained terrigenous sediments from Mariaholmen were found to have one overall large negative excursion from -27‰to -32‰(Figure 4.3). This negative excursion occurs from the onset of Olenekian and Tvillingodden Formation at ~60 m and last until approximately 165 m, covering most of the Olenekian on Mariaholmen. This negative excursion correlates seem-

ingly well with a positive total sulphur excursion over the same interval pointing towards an anoxic event .

$\delta^{13}C_{Carb}$ and to some extent $\delta^{13}C_{Org}$ are widely used for correlation purposes. These are thought to generally correlate, but at different magnitudes. They are believed to correlate as there are no known diagenetic effect that can alter the two measurements in such a way that they will always react similarly (Knoll et al., 1986; Krull et al., 2004; Meyer et al., 2013). For instance, the $\delta^{13}C_{Org}$ shown by Wignall et al. (1998) follows somewhat the various global $\delta^{13}C_{Carb}$ measurements shown by Korte and Kozur (2010). Other workers such as Musashi et al. (2001), Sephton et al. (2002) and Algeo et al. (2007) also show strong covariate behaviour of the two carbon isotope measurements. However, it should be noted that not all $\delta^{13}C_{Org}$ and $\delta^{13}C_{Carb}$ measurements correlate, such records have been used to point towards diagenetic alteration, rothman oceanic model (Rothman et al., 2003) and syn-sedimentary processes (Oehlert and Swart, 2014). Oehlert and Swart (2014) also propose that meteoritic alteration can infer a negative excursion on $\delta^{13}C$ measurements, for both organic carbon and carbonate, and as such, extra care should be taken if there are known instances of meteoric exposure.

The excursion on Mariaholmen correlates seemingly well with the $\delta^{13}C_{Carb}$ records in Payne et al. (2004), Galfetti et al. (2007a), Galfetti et al. (2007b), Horacek et al. (2007b), Horacek et al. (2007a) and Horacek et al. (2009). The $\delta^{13}C_{Org}$ excursion in Grasby et al. (2013) and Galfetti et al. (2007c) correlate very well to the Mariaholmen succession, and somewhat to the $\delta^{13}C_{Carb}$ measurements in Yin et al. (2007) and Saltzman and Sedlacek (2013). These correlations tie the isotope excursion

in the Tvillingodden Formation to the Smithian (249.7 – 247.4 ma) (Figure 4.11), which is contained within Olenekian. As such the Triassic of Mariaholmen most likely show a part of the recurring global anoxia following the Late Permian mass extinction recovery period (Knoll et al., 2007). Although the lowermost parts of the Induan is not exposed, it appears the $\delta^{13}C_{Org}$ values have stabilised by the end of the Induan before yet again declining towards anoxia in the Olenekian period and stabilising at more oxic levels prior to the onset of the Anisian (based on the assumption by Grasby et al. (2013) that $\delta^{13}C_{Org}$ can be used as an anoxia indicator in the period of the Permian-Triassic biotic crisis).

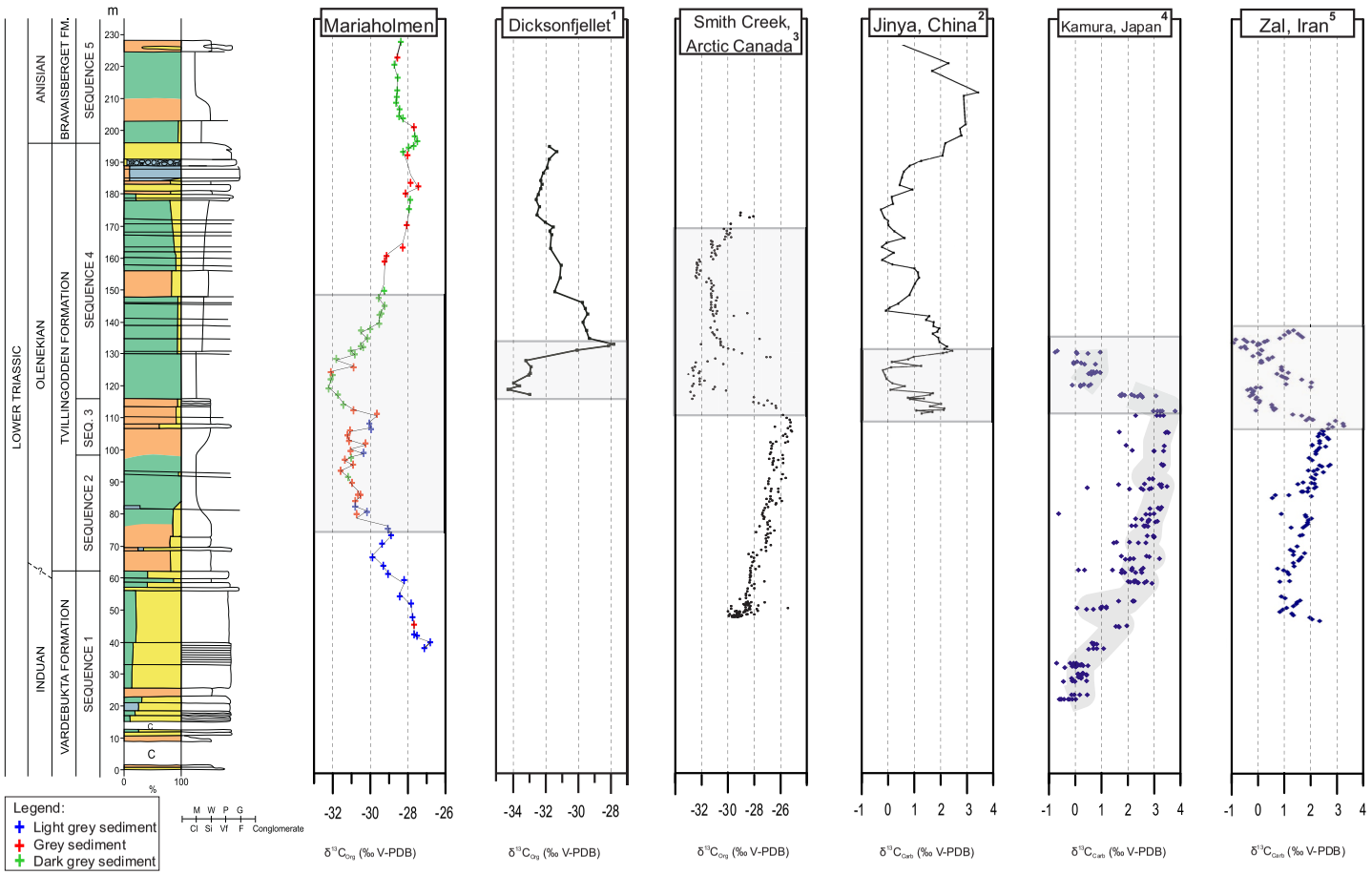

Fig. 4.11: $\delta^{13}C_{Org}$ measurements from shale and silty shale Mariaholmen correlated with various $\delta^{13}C_{Org}$ and $\delta^{13}C_{Carb}$ records. All records were tied to the Mariaholmen Olenekian and/or Anisian boundaries seen in the lithological log. Records were compressed or expanded to fit this interval. Levels (m) only apply to Mariaholmen. Grey area indicate correlation with the Mariaholmen excursion. 1: Galfetti et al. (2007c), 2: Galfetti et al. (2007a), 3: Grasby et al. (2013), 4: Horacek et al. (2009), 5: Horacek et al. (2007b).

5

DISCUSSION

5.1 DEPOSITIONAL ENVIRONMENT

5.1.1 *Sequence 1*

Sequence 1 is interpreted to represent the upper part of the Vardebukta Formation as defined by Mørk et al. (1999a). In Mørk et al. (1982) and Mørk et al. (1999a), the Vardebukta Formation is described as a shallow-marine coastal environment with prograding deltaic lobes with offshore bars present at some localities.

Bioturbation in sequence 1 is characterised by the proximal *Cruziana* ichnofacies with appearances of *Arenicolites* isp. indicating that the environment is close to *Skolithos* ichnofacies suggesting upper/middle to lower shoreface (Figure 5.1), which correlate well with the depositional environment discussed below.

On Mariaholmen, the exposed parts of the Vardebukta Formation consist of a regressive-transgressive cycle. The first 0 m - 20 m encompass the relative regression. It is a coarsening upwards sequence where normally graded bedding (tempestite sandstones rich in skeletal material) transition into sandstone beds with wave interference ripples, and decimetre thick sandstones with current ripples. The interference

ripples indicate that changing wind or current direction or multiple forces are acting upon the sediments such as river current, wind or waves (Davis, 1965; Clifton et al., 1971; Vos, 1977), and as such, relatively shallow water depth.

The lowermost level (0 m - 10 m) of the first sequence is interpreted to represent the transition from a distal delta front, rich in clay and silt (c.f. Olariu and Bhattacharya (2006)), to the sandier subtidal platform (c.f. Roberts and Sydow (2003); Bhattacharya (2010)) where shallower water depths allow multiple forces to act upon the sediments, resulting in the wave interference ripples. The interval from 10 m - 20 m is interpreted to represent the transition across the sandy subtidal platform towards the lower delta shoreface or upper sandy subtidal platform. Here, current ripples indicate unidirectional lamination commonly found in the "clean" sand zone (c.f. Olariu and Bhattacharya (2006)).

The hardground at 19.05 m has been bored (*Trypanites* isp.), and later phosphatised, both indications of very slow and/or no deposition. The *Trypanites* isp. borings are indicative of hard substrate (Bromley, 1972), while phosphatised hardgrounds are an indication of early cementation at a time of reduced sedimentation rates or no deposition (Föllmi, 196; Mutti and Bernoulli, 2003; Brandano et al., 2009). Partially phosphatised *Trypanites* isp. borings show that the boring must have occurred prior to phosphatisation.

This hardground, in combination with the immediately overlying *Myalina* layer and associated carbonate grainstones rich in skeletal fossils, could very well indicate avulsion. When avulsion occur, and the river changes direction, there is a significant reduction or stop in depos-

ition of sediments. Subsequently erosion of the delta front also occurs (Roberts, 1997, 1998; Coleman et al., 1998). As the hardground is formed, adjacent to the abandoned distributary channel, carbonate banks, possibly similar to those in the Mississippi delta (Penland et al., 1988; Roberts, 1998), form in the vicinity. These shells are redeposited during storm events both as tempestites and as the *Myalina* layer. The lower *Myalina* layer has poorly sorted small bivalve shells indicating rapid deposition, while shells with convex up appear more frequently towards the top indicating wave action. The *Myalina* layer were also shown by Nakrem and Mørk (1991) to represent a high energy depositional environment on Mariaholmen.

Mud-flake conglomerates which are formed by the redeposition of material from mud desiccation cracks (Fagerstrom, 1967; Tirsgaard and Øxnevad, 1998) at the $\pm$20 m level, can indicate proximity (Smith, 1972) to subaerially exposed sediments where ephemeral rivers could have picked up and later deposited the mud-flakes (Williams, 1966).

After the hardground event at 20 m passes and deposition resume, there is a relative transgression from 20 m to 62 m with a gradual upwards increase in siltstone bed frequency and thickness with an equal decrease in sandstone bed thickness and frequency.

In the 20 m - 60 m interval initial parallel lamination which reflect high energy depositional environments gradually transition to lower energy structures such as wave interference ripples, wave ripples and hummocky cross-stratification, respectively. This unit is interpreted to represent the transition from the sandy subtidal platform to prodelta clinoforms (c.f. Roberts and Sydow (2003); Bhattacharya (2010)). On the

prodelta clinoform, the sand beds are deposited during storm events, which is observed by their hummocky-cross stratification. Loading of silt and clay sediments subsequently result in the deformation structures seen on Mariaholmen as ball-and-pillows.

Siderite clasts are commonly formed in areas with freshwater influx (Coleman et al., 1998; Bhattacharya and Walker, 1989) are also found from 20 m to 30 m, indicating a relatively close proximity to a delta system. It should, however, be noted that siderite may also form as an early diagenetic effect in marine environments (Mozley, 1989). Siderite formed in normal marine environments is also commonly quite unclean with substantial substitution of Ca and Mg for Fe (Mozley, 1989). However, as all siderite clasts observed on Mariaholmen were well-rounded, it is much more probable that they have been rafted by tree roots from lacustrine or fluvial environments, rather than having been formed, eroded, rounded and redeposited on the subtidal delta platform.

Increasing distance from the shoreline is also reflected by the decreasing amount of clasts. (Figure 3.38). The clasts are generally well-rounded, and were as discussed in Section 3.4, most likely rafted from the river system by suspension in tree roots. A higher number of clasts are more likely to fall out of the rafting agent in vicinity to the delta system than further basinward, where distance between rafting agents increases. This relationship also applies to plant fragments which are also observed only within the coarser sediments.

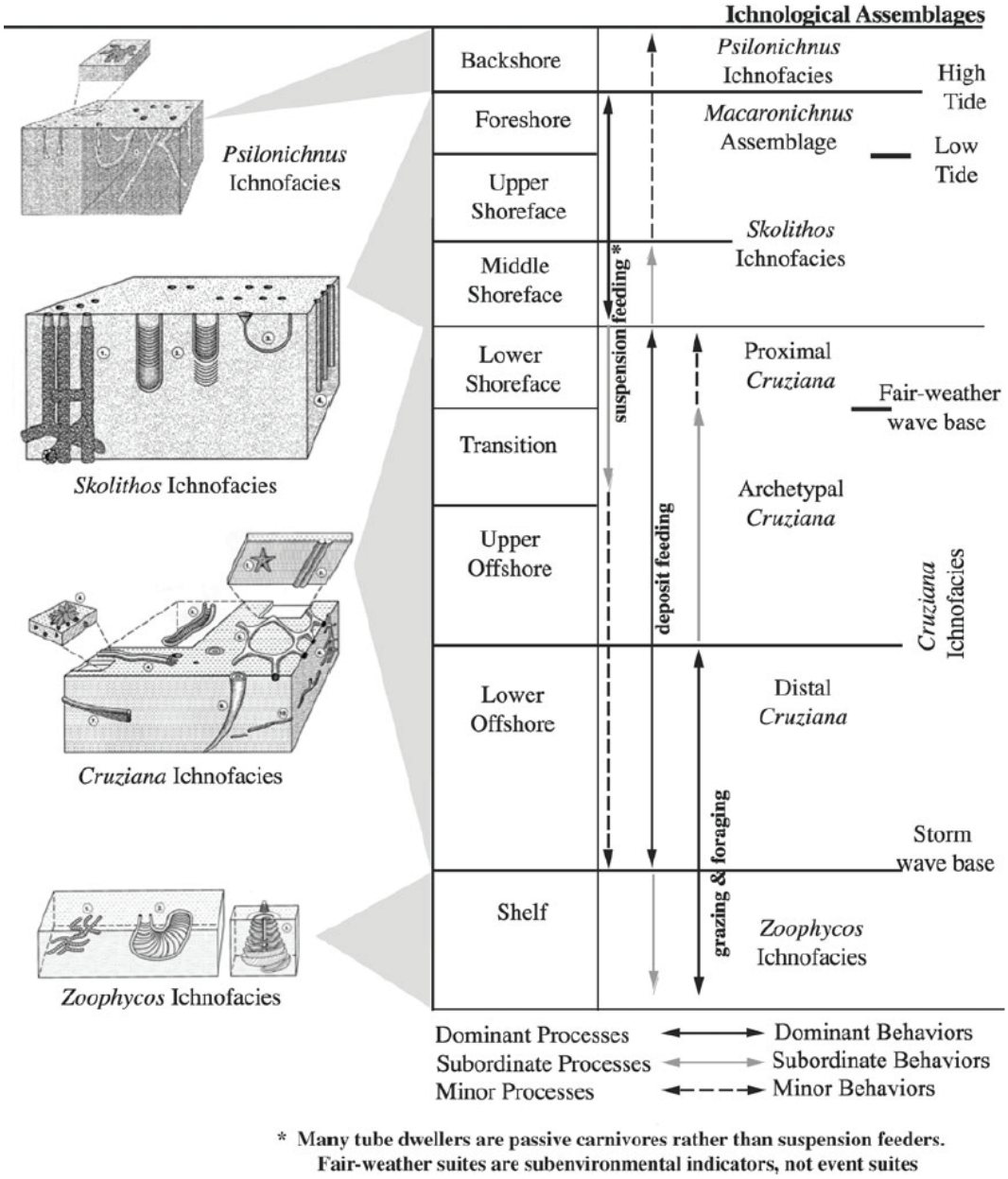

Fig. 5.1: Shoreface model showing the distribution of ichnologic assemblages based on examples from the Cretaceous of the Western Interior of North America. From Pemberton (2003).

5.1.2 *Sequence 2*

The onset of the Tvillingodden Formation is marked by the onset of distinct shale and siltstone with little bioturbation. Sequence 2 is interpreted as the onset of a widely recognised early Smithian transgres-

sion seen throughout the Arctic (Mørk, 1994). The depositional environment is interpreted to transition from deposition of prodelta clinoforms (c.f. Bhattacharya (2010)) consisting of shale and siltstone interbedded with tempestite sandstone beds (c.f. Myrow and Southard (1996)) commonly with hummocky cross-stratification, to prodelta bottomsets (c.f. Bhattacharya (2003, 2010)). The interpreted prodelta bottomsets consist of laminated siltstone and shale with occasional tempestite beds. One instance of convolute lamination directly underneath a silt- and sandstone bed is observed. This is an indication of rapid deposition. However, the convolute lamination is probably relatively common adjacent to tempestites in the silt and shale units, but was not observed in field due to relatively poor exposures.

A phosphatised hardground with *Trypanites* isp. rich in randomly oriented bivalve shells is seen at 68.65 m in the second sequence, which is an indication of slow or no deposition.

Wrinklemarks are found towards the top of sequence 2 at 95.7 m, an indication of deposition approaching fair-weather wave base (Section 3.2.3).

The transition from prodelta clinoforms to prodelta bottomsets is also reflected by the ichnofacies transitioning from proximal *Cruziana* to archetypal *Cruziana* which indicate a transition from lower shoreface to either the transition zone or upper offshore (Figure 5.1).

5.1.3 *Sequence 3*

From the 98 m level, a relative regression is marked by the onset of coarser, distinctly siltier sediments, interpreted to represent prograding clinoforms. The clinoforms are richer in sandstone beds, interpreted to represent either river flooding (c.f. Bhattacharya (2010)) or storm events. Hummocky cross-stratification is common within the sandstone beds, and current ripple cross bedding and planar lamination is seen within the sandstones in the middle of the sequence (107 m). This could possibly indicate deposition on the shallow subtidal platform.

The transition is also indicated by the bioturbation which has shifted back to proximal *Cruziana* ichnofacies with the reappearance of *Arenicolites* isp. in the sandstone beds. The appearance of *Arenicolites* isp. is an indication that the ichnofacies is approaching *Skolithos* ichnofacies. This combination of ichnofacies represents either lower or middle shoreface (Figure 5.1), which matches well with a sandy subtidal platform located immediately below the shoreface, but above the prodelta (c.f. Bhattacharya (2010)). From the 107 m level to the top of sequence 3 at 116 m the frequency of sand beds again decreases, and hummocky-cross stratification, convolute lamination and slumping starts to reoccur, indicating a transition back to the prodelta clinoform facies.

5.1.4 *Sequence 4*

The lower boundary of sequence 4 is marked by the onset of finely laminated dark shales almost devoid of bioturbation. These shales are

Fig. 5.2: Bioturbated sandy subtidal platform deposits. Red arrow indicates 178 m above base. Photo show the base of the layers.

interpreted to represent a transition back to the prodelta bottom sets, and continue to the 130 m level.

Upwards from 130 m the depositional environment gradually transitions to what is interpreted as prograding prodelta clinoforms. They consist of alternating silt and sandstone beds with an upwards increase in sandstone bed frequency and thickness, indicating an increase in relative proximity to the coastline.

The sandstone beds commonly have hummocky cross-stratification with slumping observed in the directly underlying shale and siltstone beds at several levels, which is an indication of tempestite and/or flood based deposition.

Wrinklemarks are found at the 148 m level, indicating deposition close to fair weather wave-base. Graded bedding in the upper third

Fig. 5.3: Slab from 172 m above base, showing the underside of the bed, which is very rich in trace fossils. Found within trace fossil unit VI.

of the sequence can indicate storm deposition (Myrow and Southard, 1996) or flooding as a result of the increasing proximity to the delta system (Bhattacharya, 2010).

Sandstone beds appear more frequently from approximately 172 m. The sandstone beds are also heavily bioturbated (Figure 5.3). From 178 m, sandstone beds are now more common than siltstone beds (Figure 5.2). An indication that the sediments interpreted as prodelta clinoforms have prograded beyond the point of deposition, and that deposition is now occurring on a sandy subtidal platform.

From 185 m to 189.15 m, several pronounced fossiliferous carbonate beds belonging to the Skilisen Bed (Mørk et al., 1982) are found. The Skilisen Bed has been is interpreted to represent open marine bank deposits (Mørk et al., 1982). On Mariaholmen, the Skilisen Bed appear as randomly sorted grainstones which indicate rapid deposition and reworking. Nakrem and Mørk (1991) reported low to intermediate energy at the Skilisen Bed from Bjørnskardet in the Hornsund area. However, despite being deposited a far distance from Mariaholmen, the deposits

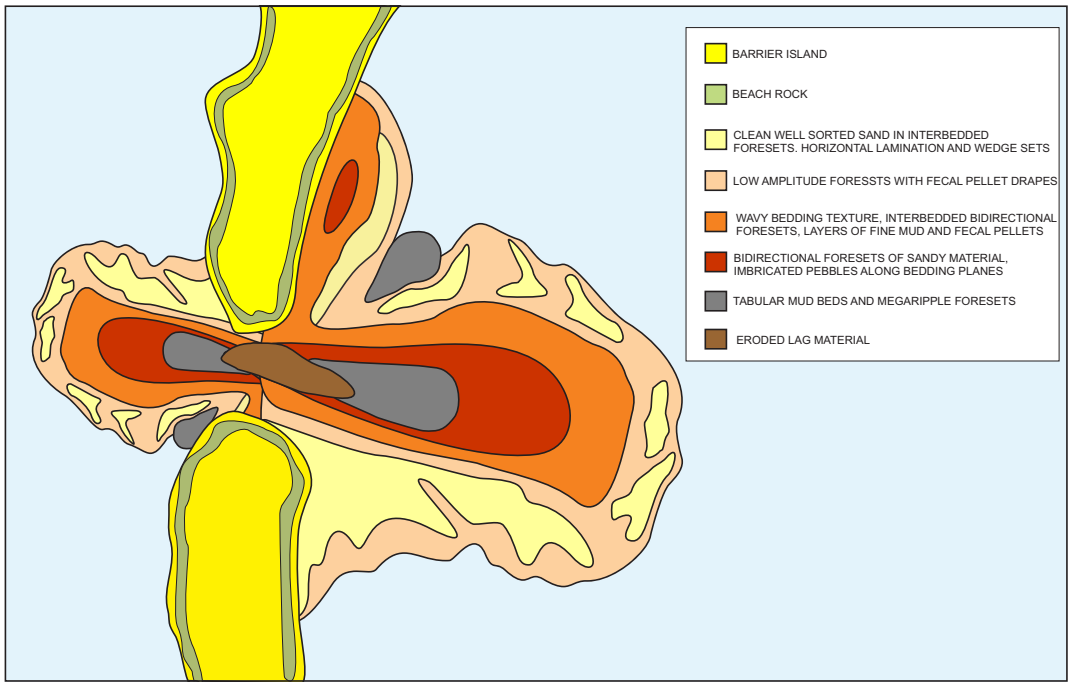

Fig. 5.4: Conceptual tidal inlet depositional features. Note, due to only partial preservation, only collapsed beach rock and the eroded lag material were observed on Mariaholmen. Modified after Oertel (1985).

at Bjørnskardet also have both autochthonous and transported skeletal fossils such as those found on Mariaholmen.

Immediately above the Skilisen Bed, two conglomerates (Section 3.2.6) are found at 189.15 m and 192.65 m (Figures 3.14 and 3.31 respectively). The conglomerates are overlain by fine grained sandstone beds (ending at 196 m level) with parting lineation and abundant large scale cross bedding in the form of trough cross beds, wave ripples and current ripples (Figures 3.19 and 3.18).

This association of sedimentary features is interpreted to represent a partially preserved tidal channel. The first conglomerate, which is a polymict conglomerate with large (~1 m) blocks, is interpreted to be a collapsed beachrock (morphologically similar to those observed by Vousdoukas et al. (2007)) from a barrier adjacent to the tidal inlet (c.f.

Oertel (1985)). The presence of beach rock is an indication very shallow water (Gischler, 2003). Occurrences of bar environments towards the top of the Tvillingodden Formation have previously also been discussed by Mørk et al. (1982) and Mørk et al. (1999a).

The second conglomerate is interpreted as a conventional channel lag deposit (Hayes, 1980). In this context, the upper conglomerates act as the erosional base lag deposit (Reinson, 1979) as the barrier islands tidal channel migrates laterally (Einsele, 2000). The abundant through cross-bedding represent the deeper channel deposits (Reinson, 1979), while the ripple lamination represents the overlying shallow channel deposits (Reinson, 1979).

Tidal inlet morphology varies (Hayes, 1980), however, Reinson (1979) defined four conditions which are largely met in the succession on Mariaholmen:

1. Erosional base marked by a coarse lag deposit
2. Deep channel facies consisting of bidirectional large-scale planar and or medium-scale trough cross-bedding
3. Shallow channel facies with bidirectional small to medium scale trough cross-beds, possible plane beds and ripple laminae
4. Fining upwards textural trend and thinning upwards cross-bed set thickness.

The trace fossils also correlate well with the discussed sedimentological model. The lower part of sequence 4 (<185 m level) consists of archetypal *Cruziana* ichnofacies, where bioturbation amounts gradually increase upwards from close to no bioturbation at the base of the

sequence, to large amounts when approaching the 185 m level. In this interval, the burrows are largely parallel to the bedding and are found within fine grained beds. This implies that there has been long enough time between deposition of sandstone beds to develop favourable conditions for the trace makers — this support the episodic deposition of sandy beds already discussed.

Within the Skilisen Bed (185 m to 189.15 m level), only *Trypanites* isp. burrows are found, and the interval is interpreted to belong to the *Trypanites* ichnofacies, which is characteristic of e.g. reefs, hardgrounds and beach rock (MacEachern et al., 2007). The overlying sandstones belong to the proximal *Cruziana* ichnofacies, an indication of higher energy depositional environments as compared to the underlying archetypal *Cruziana* ichnofacies (Figure 5.1).

In the shallow water interval relatively close to the delta system, clasts reappear at approximately 180 m. The clasts found within the Skilisen Bed contain glauconite, while the clasts above and below have none. Glauconite is an indication of very slow deposition (Amorosi, 2003), and glauconite is mostly restricted to the outer-shelf and slope at water depths between 50 m to 500 m (Amorosi, 1997). As noted earlier, the Skilisen Bed has been interpreted to represent marine bank deposits. Glauconite found on Mariaholmen is thus most likely of allochthonous or parautochthonous origin, where it has been rafted or redeposited by storm events, respectively.

When comparing the shallow water interval in the first sequence with sequence 4 it is evident that the plant material is missing from sequence 4 (Figure 3.38). The tidal channel has too much energy to allow for

deposition of relatively light plant material, while preservation in the well oxygenated Skilisen Beds is not likely.

5.1.5 *Sequence 5*

Sequence 5 marks the onset of the Bravaisberget Formation (Anisian Stage). The onset of the Anisian is marked by a regional transgression recognised across the Arctic (Mørk et al., 1989; Mørk, 1994). On Mariaholmen there is a sharp transition from the tidal inlet channel sediments in sequence 4 to dark laminated shale and siltstone with occasional sandstone beds. As a result of abundant bioturbation, very little primary lamination remains. Where primary lamination exists, it was seen as parallel lamination in hand specimens. Towards the top, a sandstone channel with wave ripples are found within siltstone beds.

The trace fossils in the fifth sequence is constrained to the archetypal *Cruziana* ichnofacies, an indication of a depositional environment in the upper shoreface to transition zone (Figure 5.1).

The lower level of the fifth sequence is interpreted as prodelta bottomsets (196 m to 224 m). This is based on the dark laminated shales with archetypal *Cruziana* ichnofacies. The depositional environment transition to deposits interpreted as prograding prodelta clinoforms in the 224 m to 227 m level, this is based on the occurrence of sandstone beds with wave ripples and an overlying sandstone channel. The presence of wave ripples indicates a change in depositional environment from the underlying dark shales. However, due to a combination of tectonic

disturbances and overburden covering the overlying sediments, there is some uncertainty in this interpretation.

5.1.6 *Depositional environment summary*

As a whole, the succession on Mariaholmen represents a depositional setting located relatively close to a westerly large prograding deltaic environment. The river system(s) supplying the basin must have been quite substantial as the clasts observed are of varying lithologies, indicating a significant provenance area. As the delta was situated west of Mariaholmen and only prodelta sediments are preserved, determining the delta type is difficult. However, the tidal barrier inlet structures points towards a tidally influenced delta, while the tempestite beds points towards some degree of wave influence (c.f. Bhattacharya (2010)), possibly a transition?

Regarding provenance, the spiculite clasts commonly observed throughout the succession on Mariaholmen is of particular interest. On Svalbard, spiculite deposits are found only in the directly underlying Late Permian Kapp Starostin Formation (Artinskian — Kazanian age) (Mørk et al., 1999a). Time equivalent spiculite deposits are also found on eastern Greenland (Stemmerik, 1997). The occurrence of well-rounded spiculite clasts in the Mariaholmen deposits imply burial, uplifting, erosion and subsequent redeposition of the Permian sediments occurring somewhere to the west of Mariaholmen prior to and simultaneously to deposition of the Triassic Mariaholmen sediments.

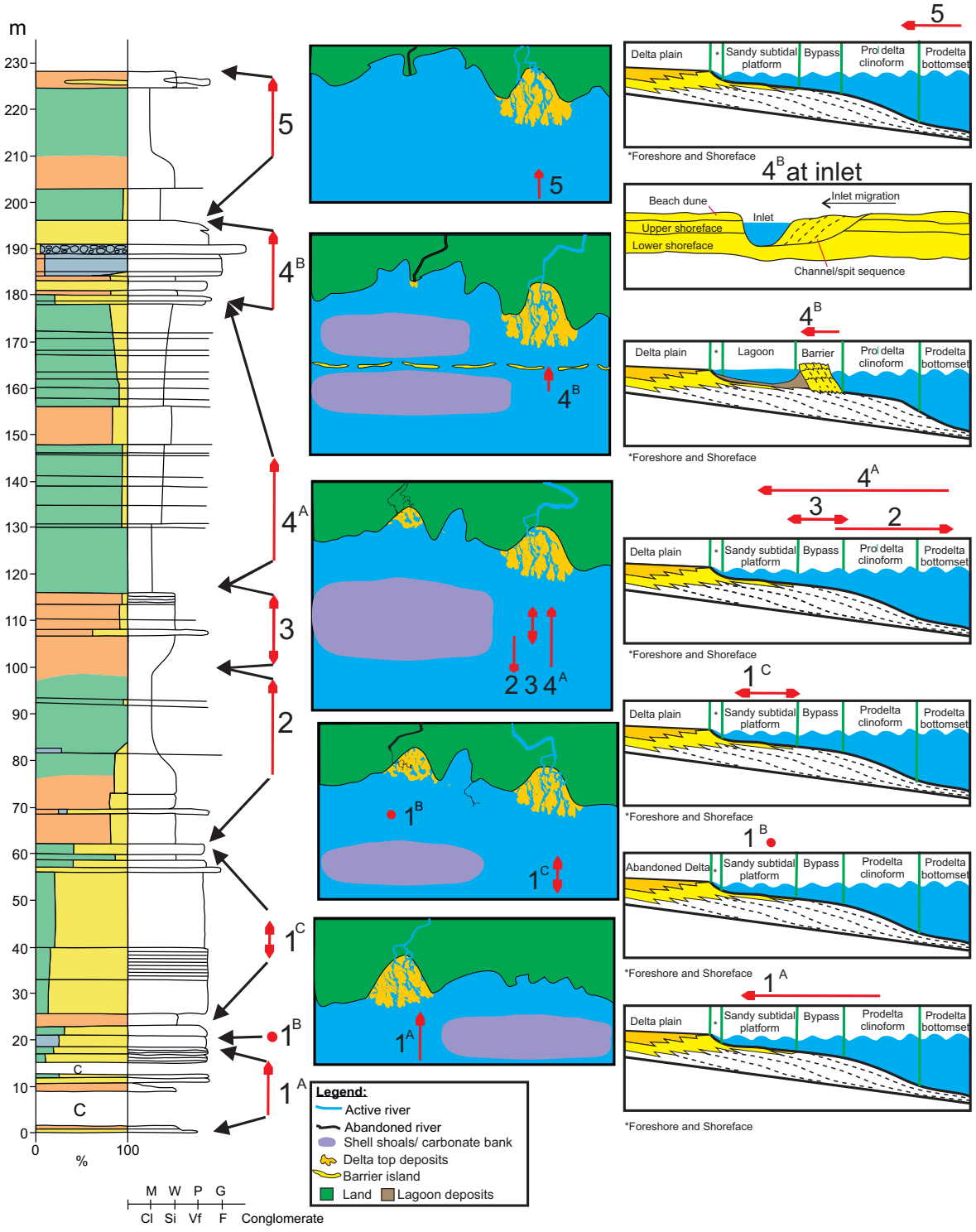

Fig. 5.5: Conceptual palaeoenvironmental model with overview of interpreted changes in depositional setting on Mariaholmen (numbering according to sequences, letters indicate subdivision of sequences). Based on principles from Bhattacharya (2010), Nichols (2009) and McCubbin (1982).

During the Late Permian and Early Triassic there were both uplift and erosion occurring in the western area of the Barents Sea rift system (Gudlaugsson et al., 1998). In the Triassic, land areas were situated immediately to the west of Svalbard (Doré, 1991), Greenland was for example much closer during the Early Triassic (Torsvik and Cocks, 2004). These uplifts are believed to be reactivation of weaknesses inherited from the Caledonian orogeny (Doré, 1991). The occurrence of spiculite clasts indicate that also Permian strata was uplifted and eroded in these areas.

Another indication of erosion is the thin Palaeozoic succession found by Ritzmann et al. (2002) (Figure 1.5). Burial, uplifting, erosion and redeposition of Permian sediments require substantial time. However, the period of time from the top of the Kapp Starostin Formation (Kazanian) (Mørk et al., 1999a) to the onset of Vardebukta Formation (Induan) (Mørk et al., 1999a) is approximately 9 million years if the top of Kapp Starostin is in fact at the very end of the Kazanian(?), such a period of time should be long enough for substantial tectonic activity.

The presence of wrinklemarks in the Early Triassic Tvillingodden Formation, is interpreted to be a product of microbial mats. The mats are believed to be prolific in the Early Triassic as a result of the reduced infaunal bioturbation following the Permian-Triassic extinction event (Section 3.2.3). The algal mats also indicate that the water must have been clear which allowed sunlight to reach the sea bottom.

Pruss et al. (2004) and Mata and Bottjer (2009) discuss how the presence of wrinklemarks is an indication that the faunal recovery after the Permian-Triassic extinction event was possibly still ongoing, and

the levels at which the wrinklemarks occur on Mariaholmen correlate well with the postulated gradual faunal recovery towards the Spathian (Section 1.3).

An overview of the depositional environment is found in Figure 5.5.

5.2 BOTTOM-WATER CONDITIONS AND ORGANIC CARBON SUMMARY

Despite the dysoxic and anoxic conditions during deposition of fine grained terrigenous sediments, which have relatively little bioturbation, the deposition and preservation of organic content on Mariaholmen was poor. The Rock-Eval analysis show that the organic material in the fine grained terrigenous sediments on Mariaholmen is largely land derived material of kerogen type-III and type-IV. These two kerogens are found to prevail in environments related to deltas and environments in the vicinity of delta systems (c.f. Nwachukwu and Chukwura (1986); Tissot et al. (1987) and references therein).

As seen on Figure 4.7, there is no sign of type-I or type-II kerogen in the fine grained terrigenous sediments on Mariaholmen. Kerogen type-I and kerogen type-II is lighter than kerogen type-III and type-IV and there appears to be a strong correlation between kerogen density and offshore deposition distance of kerogen types (Nwachukwu and Barker, 1985). This proposed correlation implies that the heavier kerogen type-III and type-IV fall out of suspension closer to the shoreline proposing and explanation for the lack of kerogen type-I and kerogen type-II on Mariaholmen.

In the fine grained terrigenous deposits, the combination of mainly land derived organic material, fairly high sulphur values, anoxic V/(V+Ni) ratios, anoxic to dysoxic TOC vs TS ratio and sparse bioturbation suggest that the marine productivity at the time of deposition was quite low. However, in the coarser grained deposits containing abundant bioturbation and often skeletal fossils, the organic productivity must have been relatively high.

The dysoxic to anaerobic bottom-water environments develop during the deposition of silt and mud on the interpreted prodelta clinoforms and bottomsets. At intervals, deposition of sand beds due to flooding or storm events bring in fresh oxygenated water where the bioturbating organisms proliferate. The assemblages of skeletal fossils also indicate oxygenated bottom water when sand beds and carbonate beds were deposited. Presence of nektonic organisms at discrete levels in the fine grained shale in sequence 2 and sequence 4 indicate that even though the bottom-water was anoxic to dysoxic, in periods, the overlying watermasses must have been oxygenated.

5.3 DIAGENESIS

Cement generations

Sediments on Mariaholmen have gone through multiple diagenetic events, and three (possibly four) generations of cement is observed within the samples studied.

The first generation of cement exist as hardgrounds found within three distinct levels. This first generation of cement is found as a phos-

phatised zone at the top of the hardgrounds. The phosphorite is formed by carbonate replacement where phosphate replace the calcium in calcite (Ames, Jr., 1959; Kasioptas et al., 2008), which means the hardgrounds were carbonate cemented prior to phosphatisation. As discussed in Section 5.1.1, hardgrounds are occurrences of very early cementation taking place during slow/non-deposition. This implies that the three observed hardgrounds must have formed at discrete periods in time.

The second cement generation consists of calcite cement, and in the smaller voids the calcite cement completely fills the primary pores. In the larger voids (such as those in septaries), the calcite cement is observed as large blocky crystals that does not entirely fill the voids.

In the secondary porosity formed by aragonite dissolution of shells, the second cement generation is observed as large blocky crystals, also here the cement does not completely fill the cavities.

However, there are some occurrences where the large blocky calcite crystals of the second generation completely fill the larger voids and cavities. The second cement generation is often slightly brownish.

Cement generation number three, which is also a calcite cement, is only found in conjunction with larger cavities in septaries and in cavities formed by aragonite dissolution of shells. The third cement generation has grown onto the larger blocky calcite crystals of the second cement generation. The third cement generation is a light coloured calcite cement with a very slight brownish colour tint.

The fourth cement generation, also a calcite cement is only found within concretions. It appears only within large septarian voids where

it is observed as a clear light coloured calcite cement, forming a contrast to the slightly brown coloured calcite cement of the third generation (See Figure 3.58). It could also be that it is a less coloured variant of the third calcite cement generation.

In the secondary porosity formed by aragonite dissolution of skeletal fossils, only the second and third cement generation was observed. This show that the secondary porosity was filled with cement prior to the onset of the fourth cement generation, which is only observed in large voids.

There is one occurrence where a fracture crosses a bivalve shell which is filled with the second and third cement generation. The calcite cement of the fracture cuts the calcite cement in bivalve, and must thus be younger than the second and third cement generation. However, it is important to note that this does not imply that the fracture calcite cement is neither older nor younger than the fourth cement generation, it only shows that the fractures must have occurred after the third calcite cement generation.

Diagenetic quartz was only observed within fractures, where the quartz crystals grow on the calcite crystals that line the fractures, indicating that the quartz crystals are younger than the calcite crystals in the fractures.

Dolomite observed on Mariaholmen is seen either as fully or partly dolomitized matrix (Figure 3.51). The dolomite seen within the bivalve on Figure 3.51 show that the dolomitisation must have occurred after the first calcite cement generation.

Hydrocarbon generation and migration

Pyrobitumen was not observed in the matrix, it is only observed lining fracture walls such as those seen on Figure 3.60. This implies that hydrocarbon generation and migration must have occurred after the first and second calcite cement generation.

The origin of the hydrocarbons found in the sediments on Mariaholmen is unknown, but likely candidates are the underlying unexposed fissile shales of the Vardebukta Formation on Mariaholmen, or the directly underlying biogenic cherts and dark shales of the Late Permian Kapp Starostin Formation (Dallmann, 2015).

Assuming a normal geothermal gradient between 25°C and 40°C (Bjørlykke et al., 1988) for Svalbard, the required overburden for hydrocarbon generation to start is approximately 2 km to 3 km (Waples, 1980). Where Mariaholmen is situated, 2.7 km of overburden was deposited by the Early Cretaceous (top of Carolinefjellet Formation in the Adventdalen Group) (Harland, 1997), indicating that hydrocarbon generation in the Triassic of Mariaholmen started in the Early Cretaceous.

An unknown time after the Early Cretaceous hydrocarbon generation, the hydrocarbons migrated through fractures in formations at Mariaholmen. Most of the hydrocarbon on Mariaholmen is observed lining the walls of fractures which have subsequently been cemented with light coloured calcite cement. However, in some occurrences, hydrocarbons were also observed within calcite crystals on fracture walls and within quartz crystals growing on the calcite crystals. In the Triassic deposits on Mariaholmen, at least two generations of fractures are present, where the hydrocarbon lined fracture walls with hydrocarbon

contaminated calcite cement is cut by fractures containing only light coloured calcite cement (Figure 3.60).

When considering the total overburden for the Triassic formations on Mariaholmen, the Neogene erosion (Dallmann, 2015) must be taken into account. Prior to the Neogene erosion, the Paleocene Firkanten Formation (Mørk et al., 1999a), is estimated to have been under more than 3 km of overburden (Manum and Throndsen, 1978). This gives a total overburden thickness at Mariaholmen of approximately 6 km prior to the erosion events.

Note that the overburden discussed for the deposits on Mariaholmen does not take into account the unknown thickness of Upper Cretaceous succession on Svalbard that was eroded during recurring uplifts in the late Cretaceous (Dallmann, 2015).

An overburden of approximately 6 km, result in temperatures between 150°C and 240°C assuming the discussed geothermal gradients between 25°C/km and 40°C/km. This implies that the sediments on Mariaholmen have been exposed to temperatures well beyond the peak oil and gas windows (c.f. (Tissot and Welte, 1984)), further explaining the low organic carbon levels in the deposits on Mariaholmen.

6

CONCLUSION

In the Early Triassic Vardebukta Formation and Tvillingodden Formation, and the Middle Triassic Bravaisberget Formation on Mariaholmen, five depositional sequences were identified. Each sequence constitutes separate segments of a transgressive-regressive prodelta environment situated next to a westerly delta system.

The Vardebukta Formation on Mariaholmen consists of sandy subtidal platform deposits where river switching occurs in the westerly delta system. Throughout the uncovered part of Vardebukta Formation on Mariaholmen, there is an upwards increase in siltstone bed frequency. At the top of the Vardebukta Formation, a regional transgression marks the onset of the Tvillingodden Formation. Fine grained sediments interpreted as prodelta bottomsets and clinoforms that gradually prograde to higher energy sediments interpreted as sandy subtidal platform deposits characterise the Tvillingodden Formation on Mariaholmen. Towards the top of the Tvillingodden Formation, a barrier island tidal inlet with collapsed beach rock is observed. The onset of the Middle Triassic and the Bravaisberget Formation is marked by another regional transgression where sediments interpreted as prodelta bottomsets are deposited. The prodelta bottomsets at the bottom of the Bravaisberget Formation gradually transition to slightly coarser siltstone and

sandstone sediments interpreted as prodelta clinoforms at the top of the investigated profile.

The varying lithology of dropstone clasts found throughout the succession indicates that the drainage area to the west of Svalbard was quite substantial. The presence of Permian spiculite clasts indicates uplift and erosion to the west in the Late Permian and/or Early Triassic.

Trace fossils assemblages observed throughout the Mariaholmen succession reflects the described depositional environment. Trace fossil assemblages vary between archetypal *Cruziana* ichnofacies and proximal *Cruziana* ichnofacies, where some of the proximal *Cruziana* ichnofacies levels are approaching the *Skolithos* ichnofacies. Such trace fossil assemblages indicate water depths from the middle/lower shoreface transition zone (sandy subtidal platform deposits) to the upper offshore (prodelta bottomset deposits).

Geochemical relationships of the fine grained terrigenous shales and silty shales indicate predominantly anoxic to dysoxic bottom-water conditions. The V/(V+Ni) ratio and TOC:TS ratio both indicate similar conditions with only slight variations. However, abundant bioturbation and skeletal fossils in the coarser grained sediments indicate that bottom-water conditions were likely oxygenated during deposition of the coarser grained sediments.

Kerogen is found only as type-III and type-IV. This shows that the sediments, at best could have been gas-prone if total organic carbon content was somewhat higher.

Global correlation of the $\delta^{13}C_{Org}$ data shows that the isotope excursion in the Tvillingodden Formation is confined to the Smithian

(249.7 ma to 247.4 ma) and part of the recurring anoxia following the end-Permian mass extinction.

The sediments have been cemented in three (four when considering hardgrounds) different phases. Petrographic evidence show that the last generation of fracturing must have occurred subsequent to the hydrocarbon migration. The thickness of the eroded overburden indicates that the hydrocarbon generation and migration through in the Triassic at the western Svalbard occurred at the earliest in the Early Cretaceous.

The depositional environments described herein strengthen the arguments for the existing, and prevailing theories. The barrier structures proposed by aforementioned workers for the upper Lower Triassic is confirmed through the presence of a tidal inlet lag deposit.

Part I

APPENDIX

A

PUBLISHED CRINOID ARTICLE

This article by Salamon et al. (2015a) was published in Polish Polar Research the fall of 2015. In this article, I contributed with the geological profile, write-up of the geological setting, preparation of the material and picking of crinoids for further analysis.

POLISH POLAR RESEARCH
vol. 36, no. 3, pp. 225–238, 2015 doi: 10.1515/popore-2015-0015

Crinoids from Svalbard in the aftermath of the end-Permian mass extinction

Mariusz A. SALAMON [1], Przemysław GORZELAK[2*], Nils-Martin HANKEN [3], Henrik Erevik RIISE [3,4] and Bruno FERRÉ [5]

[1] *Wydział Nauk o Ziemi, Uniwersytet Śląski, ul. Będzińska 60, 41-200 Sosnowiec, Poland* <*paleo.crinoids@poczta.fm*>

[2] *Instytut Paleobiologii, Polska Akademia Nauk, ul. Twarda 51/55, 00-818 Warszawa, Poland* <*pgorzelak@twarda.pan.pl*> * *corresponding author*

[3] *Department of Geology, UiT – The Arctic University of Norway, NO-9037 Tromsø, Norway* <*nils-martin.hanken@uit.no*>

[4] *Present address: Halliburton, Sperry Drilling, P.O. Box 200, NO-4065 Stavanger, Norway* <*henrik.riise@halliburton.com*>

[5] *Dame du Lac 213, 3 rue Henri Barbusse, F-76300 Sotteville-lès-Rouen, France* <*bruno_ferre@yahoo.fr*>

Abstract: The end-Permian mass extinction constituted a major event in the history of crinoids. It led to the demise of the major Paleozoic crinoid groups including cladids, disparids, flexibles and camerates. It is widely accepted that a single lineage, derived from a late Paleozoic cladid ancestor (Ampelocrinidae), survived this mass extinction. Holocrinid crinoids (*Holocrinus*, Holocrinida) along with recently described genus *Baudicrinus* (Encrinida), the only crinoid groups known from the Early Triassic, are considered the stem groups for the post-Paleozoic monophyletic subclass Articulata. Here, we report preliminary data on unexpectedly diverse crinoid faunas comprising at least four orders from the Lower Triassic (Induan and Olenekian) of Svalbard, extending their stratigraphic ranges deeper into the early Mesozoic. These findings strongly imply that the recovery of crinoids in the aftermath of the end-Permian extinction began much earlier at higher palaeolatitudes than in the central Tethys.

Key words: Arctic, Svalbard, echinoderms, crinoids, P/T extinction, recovery.

Introduction

Recovery of most organisms from the end-Permian mass extinction, other than a few nekto-pelagic and reef taxa, is thought to have spanned the entire Early Triassic (*i.e.* ~5 million years; see *e.g.* Benton 2005; Brayard *et al.* 2009, 2011; Foster

and Twitchett 2014). Crinoids were suggested to re-diversify from a single holocrinid lineage achieving great morphological and behavioural innovations not before the Middle–Late Triassic (Simms and Sevastopulo 1993; Simms 1999; Baumiller *et al*. 2010; Hess and Messing 2011; Gorzelak *et al*. 2012).

Although several authors have proposed alternative evolutionary scenarios suggesting polyphyletic and Paleozoic origins of articulate crinoids, supporting evidence is lacking. Similarities between Paleozoic and Mesozoic crinoids have simply been attributed to convergent evolution (Simms and Sevastopulo 1993; Hess and Messing 2011). Notwithstanding the above, the fossil record of crinoids in the Lower Triassic is patchy. For instance, Oji and Twitchett (2015) based solely on columnal remains recently erected a new genus, *Baudicrinus* from the Lower Triassic of Oman. Such findings highlight that the low abundance of crinoids in the aftermath of the end-Permian extinction need not necessarily be attributable solely to extinction but may in part reflect the incompleteness of the fossil record, and the migration of taxa to refuges.

So far, only a few studies have been devoted to fossil crinoids from Svalbard (*e.g.* Holtedahl 1911; Rousseau and Nakrem 2012; Gorzelak *et al*. 2013) and the Triassic representatives have never been the subject of a thorough investigation. Here, we report preliminary data on unexpectedly diverse crinoid faunas from the upper Vardebukta Formation and the Tvillingodden Formation (Lower Triassic) at Mariaholmen (Svalbard).

Geological setting

The paleo-geographical reconstruction of the Early Triassic (Mørk *et al*. 1982) depicts a land area to the west of the southern part of Svalbard while the southwards-extending epi-continental basin delineates an extensive embayment of the Panthalassa Ocean into the northern margin of the Pangea supercontinent (Fig. 1; Riis *et al*. 2008; Worsley 2008). Within a Tertiary fold-thrust belt, the lithological succession at Mariaholmen dips steeply eastward; the Lower Triassic sequence is well exposed along the south and southeast coast of the island (Fig. 2). Due to strong tectonic disturbance and quaternary cover, only a 228 m-thick sequence comprising the upper part of the Vardebukta Formation and the Tvillingodden Formation was investigated (Fig. 3). The stratigraphy of these sediments was revised by Birkenmajer and Trammer (1975) and Mørk *et al*. (1982, 1999).

The Permian–Triassic boundary in Svalbard has usually been placed at the top of the Kapp Starostin Formation based on an abrupt sedimentary change (Mørk *et al*. 1982, 1989, 1999; Gruszczyński *et al*. 1989; Błażejowski 2004). However, palynology, organic chemo-stratigraphy and bio-magnetostratigraphy indicate that the Permian/Triassic boundary lies within the basal part of the Vardebukta Formation.

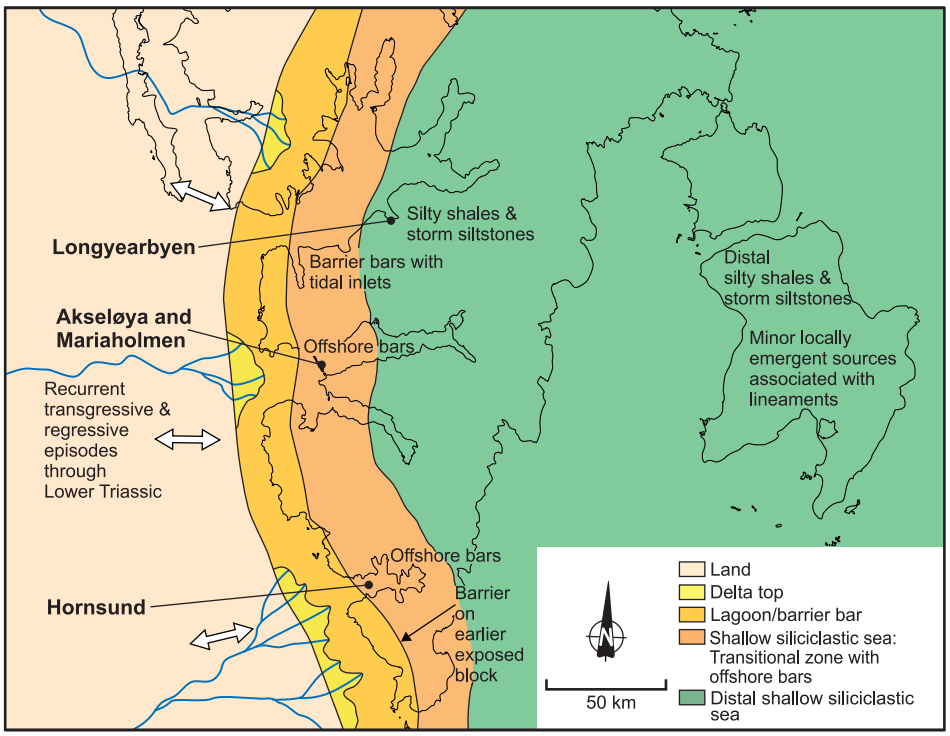

Fig. 1. Palaeogeographic map showing the Lower Triassic facies relationships in Svalbard (modified from Mørk *et al.* 1982). A land area is situated west of the southern part of Svalbard. Shallow siliciclastic marine deposits including lagoonal and barrier bars appear as coast-parallel facies belts adjacent to more distal fine-grained deposits further to the east.

The upper part of the Vardebukta Formation contains the so-called *Myalina* Bed yielding conodonts indicative of the late Griesbachian/early Dienerian (Induan) age (Nakrem *et al*. 2008), whereas bio-magnetostratigraphic analysis (Hounslow and Nawrocki 2008) suggests a late Griesbachian age. The boundary between the Vardebukta Formation and the overlying Tvillingodden Formation is usually regarded as the Induan/Olenekian boundary (see summary in Mørk *et al*. 1999). However, the magnetostratigraphic analysis of Hounslow and Nawrocki (2008) indicates that the Vardebukta Formation may well extend into the Olenekian rather than terminating close to the Induan–Olenekian boundary. Mørk *et al*. (1989, 1994) and Mørk (1994) showed the existence of a major early Olenekian transgression in the circum-Arctic area. Its age is based on a characteristic fossil assemblages (conodonts, ammonoids, bryozoans and bivalves) from the Tvillingodden Formation (Mørk *et al*. 1999; Nakrem *et al*. 2008; Hounslow *et al*. 2008). According to the palynological investigations of Vigran *et al*. (2014), the overlying Tvillingodden Formation corresponds to the *Naumovaspora striata* assemblage zone (early Olenekian/Smithian). In the upper part of the Tvillingodden Formation, the Skilisen Bed (a prominent unit of sandy biosparitic grainstone, formally defined by Mørk *et al*.

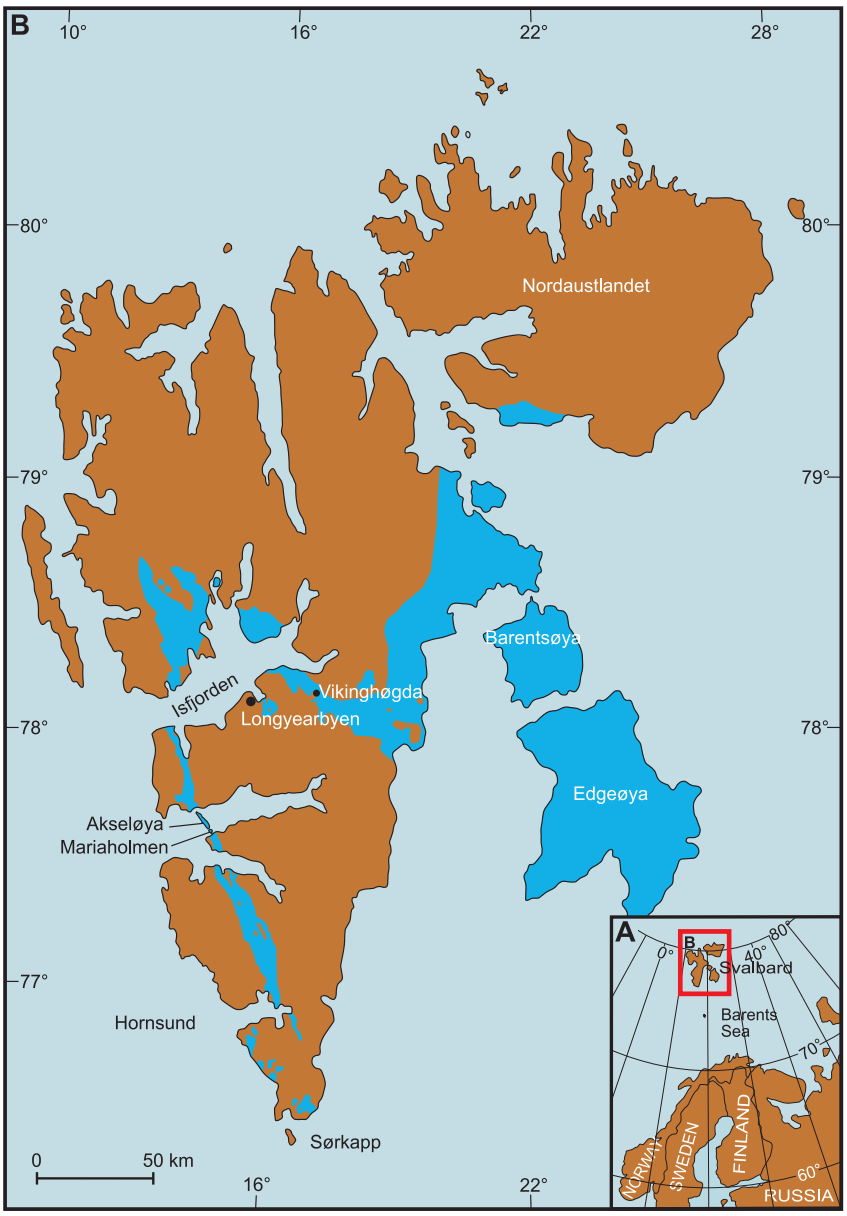

Fig. 2. **A**. Map of northern Europe with enlarged schematic geological map of Svalbard with investigated locality at Mariaholmen indicated (**B**). Triassic deposits in blue while the remaining areas are in brown.

1982; see also Dallmann 1999) contains conodont assemblages of late Smithian age (Nakrem *et al*. 2008). Early Triassic crinoids described herein were collected from the upper part of the Vardebukta Formation and the Tvillingodden Formation at Mariaholmen, Svalbard (70°41'30" N, 14°48'01" E; Fig. 1).

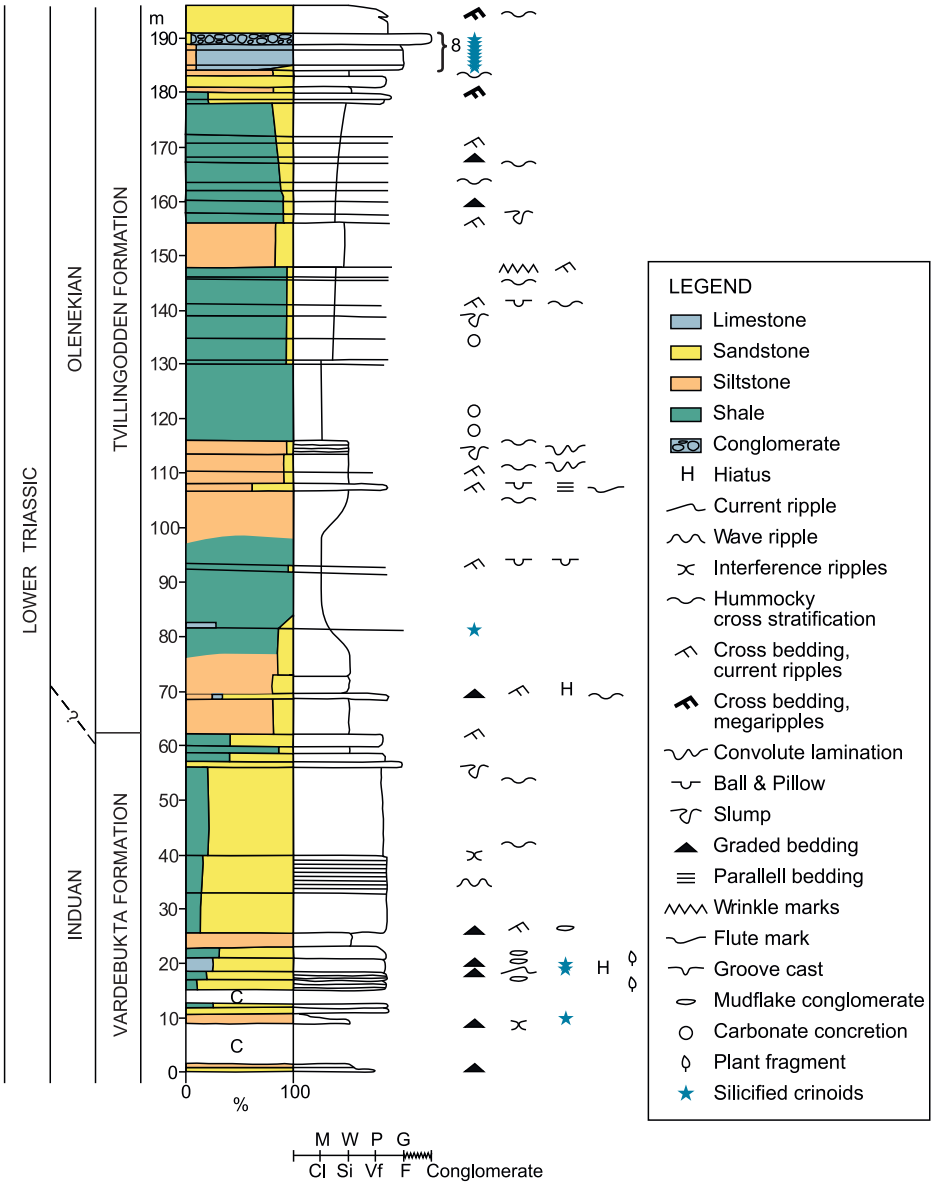

Fig. 3. Fragment (about 195 metres) of the investigated section along the south and southeast coast of Mariaholmen, Svalbard. About 90 meters of the lowermost part of the Vardebukta Formation is covered by Quaternary deposits. The upper part of the Vardebukta Formation consists of shallow-marine (including pro-delta) sediments. The overlying Tvillingodden Formation is characterized by a transgressive system tract in the lower part and a regressive system tract in the upper part. Abundant silicified crinoid ossicles were recovered from eight samples taken from a highly fossiliferous limestone (the Skilisen Bed). Carbonate classification following Dunham (M – mudstone, W – wackestone, P – packstone, G – grainstone) and the grain size of the clastic deposits is based on the Udden-Wentworth grade scale (Cl – clay, Si – silt, Vf – very fine sand, F – fine sand).

Methods

Samples, ranging from 0.4 to 10.5 kg, were collected from different levels of the section with most of the material from the calcareous Skilisen Bed. To optimize the subsequent dissolution process, after weighing the broken samples, rock fragments were placed in a net (mesh size 1.4 mm) over a plastic tank in order to retrieve both silicified and phosphatic fossils (inarticulate brachiopods, conodonts, fish teeth and scales) from the limestone and carbonate cemented sandy deposit. To prevent the destruction of phosphatic material, buffered acetic acid was used following Jeppsson's procedure (Jeppsson *et al.* 1999).

Carbonate dissolution resulted in the fine-grained insoluble residue sinking through the net to the bottom of the container preventing fragments from being smeared with the insoluble residue and allowing the acid to be in contact with the rock surface, increasing the dissolution rate. The dissolution of calcium carbonate usually took between 6 to 7 weeks. Once the reaction ceased, the acid was filtered out, the insoluble residues washed with tap water and wet sieved (standard mesh set from 16 down to 0.25 mm). All fractions >0.5 mm were screened for fossils. Most crinoid elements were found in the 0.5–1 mm and 1–2 mm fractions; they were mostly disarticulated but relatively well preserved implying para-autochthonous assemblages. Only a small portion of ossicles were broken by this procedure.

Morphological description

The upper part of the Vardebukta Formation yielded crinoid plate molds occurring as replacement ghosts after dissolution of calcitic ossicles; only two levels contained a few silicified ossicles of different morphology (Fig. 4A, F, G). Some of them are pentagonal and sub-stellate in outline and can be assigned to those observed in Early Triassic holocrinids (Holocrinida) and/or Middle Triassic iso-

Fig. 4. Early Triassic crinoids from the Vardebukta Formation (Induan: A, F, G) and Tvillingodden Formation (Olenekian: B–E, H–X) of Svalbard. Scale bars equal 0.5 mm. **A**. Medial/proximal? internodal of *Holocrinus*, articular facet ZPALV.42/P-T/h1, sample no. 2. **B**. Proximal nodal of *Isocrinus*, articular facet ZPALV.42/P-T/i1, sample no. 2. **C**. Proximal? nodal of Encrinida, articular facet ZPALV.42/P-T/e1, sample no. 5. **D**. Proximal internodal of Encrinida, articular facet ZPALV. 42/P-T/e2, sample no. 5. **E**. Calyconodal of Encrinida (Ainigmacrinidae), lateral and oblique view view ZPALV.42/P-T/e3, sample no. 5. **F**. Broken fragment of roveacrinid brachial, lateral view ZPALV.42/P-T/r01, sample no. 1. **G**. Broken fragment of roveacrinid? theca, lateral view ZPALV. 42/P-T/r00, sample no. 1. **H**. Holdfast of unknown crinoid, lateral view ZPALV.42/P-T/c1, sample no. 6. **I**. Unassignable columnal?, articular facets view ZPALV.42/P-T/c2. **J–K**. Centrodorsal? of Comatulida?, upper view (J) and lateral and oblique view (K) ZPALV.42/P-T/cc1, sample no. 5. **L–X**. Roveacrinida ossicles. **L**. Distal brachial plate (NBrn) of Roveacrinida, lateral view ZPALV. 42/P-T/r1, sample no. 5. **M**. Secundibrachial plate (IIBrn) of *Osteocrinus*, oblique upper view of outer side ZPALV.42/P-T/r3, sample no. 6. **N**. Primibrachial plate (IBr1) of *Osteocrinus*, oblique →

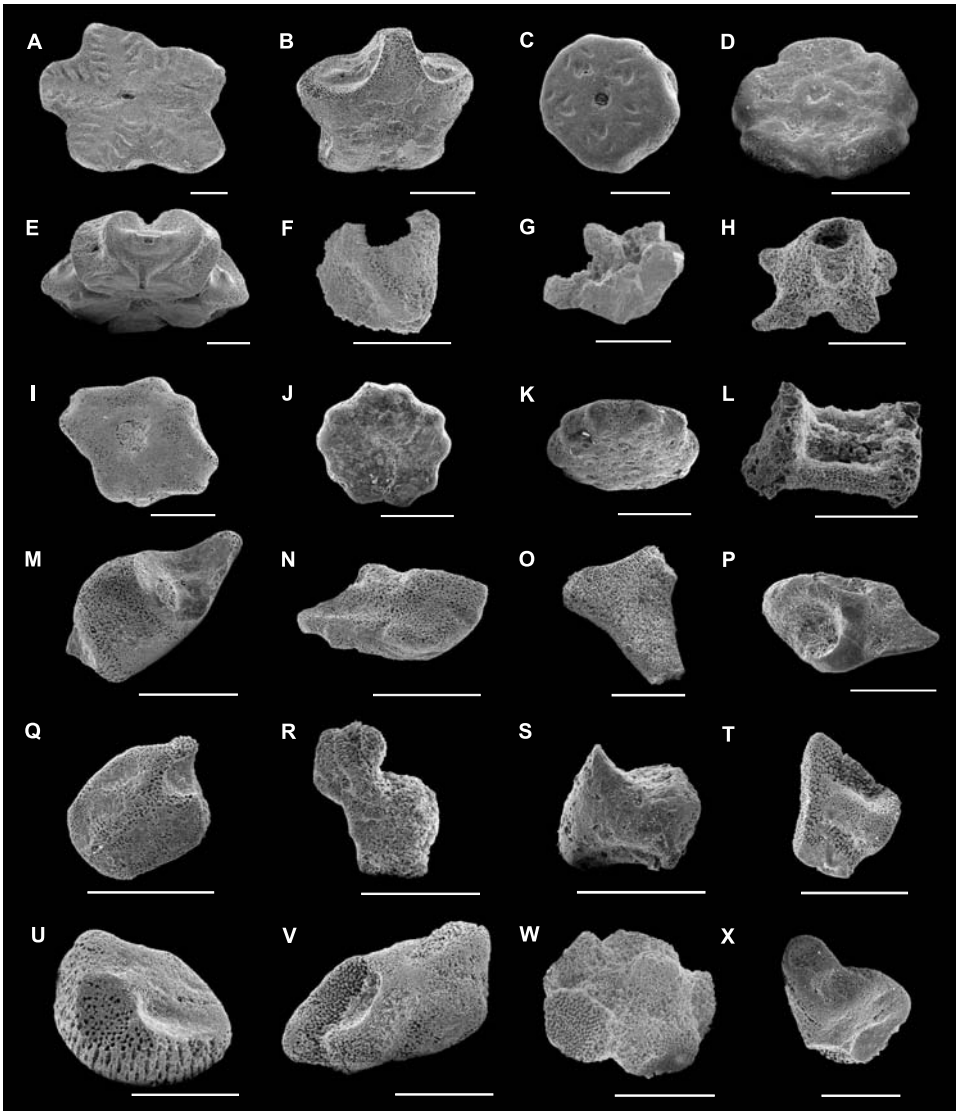

adradial view from above of inner side ZPALV.42/P-T/r4, sample no. 5. **O**. Brachial plate of *Somphocrinus*, lateral view ZPALV.42/P-T/r5, sample no. 9. **P**. Primibrachial plate (IBr2) of *Osteocrinus*, oblique adradial view of outer side ZPALV.42/P-T/r2, sample no. 7. **Q**. First primibrachial plate (IBr1) of *Osteocrinus*, oblique upper view of outer side ZPALV.42/P-T/r6, sample no. 4. **R**. Radial plate (Rad) of *Osteocrinus*, lateral view ZPALV.42/P-T/r7, sample no. 5. **S**. Distal plate (IIBrn) of *Somphocrinus*, abradial outer lateral view ZPALV.42/P-T/r8, sample no. 5. **T**. Primibrachial plate (IBr1) of *Osteocrinus*, oblique abradial view from below of inner side ZPALV. 42/P-T/r9, sample no. 7. **U**. Thecal plate of ?juvenile *Osteocrinus*, tilted lateral view slightly from above ZPALV.42/P-T/r10, sample no. 6. **V**. First primibrachial plate (IBr1) of *Osteocrinus* ZPALV. 42/P-T/r11, sample no. 6. **W**. Thecal plate of juvenile *Osteocrinus*, tilted lateral view slightly from above ZPALV.42/P-T/r12, sample no. 9. **X**. Broken thecal plate of *Somphocrinus*, lateral view ZPALV.42/P-T/r13, sample no. 12. Number of sample refers to profile from Fig. 3.

crinids (Isocrinida; see Hess and Messing 2011). The most noticeable ossicles of this upper part of the Vardebukta Formation are a partially broken and recrystallized thecal plate resembling *Osteocrinus* sp. and three other ossicles, possibly of the pelagic roveacrinids (Roveacrinida; Fig. 4F, G). The Tvillingodden Formation revealed an unexpectedly high number of diversified silicified crinoid ossicles, dominated by columnals and brachial plates of holocrinids (*Holocrinus*) – this difference in the abundance of crinoids throughout the section is most likely related to fossil preservation (extension of diagenetic silicification). The distal internodal plates of these crinoids are sub-circular, sub-pentagonal (basaltiform) and pentagonal whereas the medial and proximal internodals are sub-stellate. The larger columnals have a distinct petaloid pattern. The nodal columnals are higher and wider than the internodals. All nodals display symplectial lower facets. Cirrus scars are deeply depressed and elliptical in outline. They may have a lip at their lower margin. The transverse ridge is inflated on both sides of lumen. Cirrus scar facets are horizontal. Brachials are muscular and small, V- or U-shaped. These holocrinid plates were accompanied by other crinoid ossicles including two holdfasts of unknown crinoids (Fig. 4H).

Among other crinoid elements discovered were strongly stellate columnals with petals (Fig. 4B): their articular facets are smooth, the lumen is large and the lower nodal articular facet is either cryptosymplectial or synostosial which is indicative of isocrinids. Within a single layer of the upper part of the section (sample no. 5 in Table 1), two extremely enlarged and modified nodals are also present (Fig. 4E). These ossicles strongly resemble the so-called calyconodal, a synapomorphic ossicle, of the highly specialized *Ainigmacrinus* (Encrinida) previously known exclusively from the early Late Triassic (Hagdorn 1988). The Svalbard calyconodals have five very deep cirrus sockets with longitudinally depressed latera separated by five protruding and strongly concave lateral surfaces of interradii. The cirrus sockets are cordate and display an inflated transverse ridge with a relatively large lumen. Deep furrows (on both sides of the facet) extend from each socket toward the lumen. Low and subpentagonal columnals with a reduced epifacets may belong to encrinids (Fig. 4C–D; Hagdorn *et al*. 1996). They are of similar diameter and height as holocrinid and isocrinid columnals, but their morphology is different. Similar columnals are known from the Middle Triassic and have been ascribed to immature encrinid columnals (Hagdorn *et al*. 1996).

The Tvillingodden Formation in Svalbard contains possible pelagic roveacrinids (Roveacrinida) similar to those described by Kristan-Tollmann (1975) from the Upper Triassic limestones of Austria. Generic determination is nearly impossible for isolated brachial plates. All brachial ossicles are rather smooth, devoid of any coarse or reticulate ornamentation. Thecal, radial and brachial plates from the upper part of the section have only genera-level features; we assign them to juvenile specimens and/or to new species (to be described elsewhere). These specimens display smooth low aboral projections with short interradial edges and radial

Table 1

Weight of limestone samples used and major crinoid groups identified in each sample. The stratigraphic level refers to profile from Fig. 3.

Sample number	Stratigraphic level [m]	Weight of sample [kg]	Crinoid groups, number and types of ossicle
1	10.65	0.6	roveacrinids (1 incomplete theca and 3 brachials)
2	19.6	1.6	holocrinids (3), isocrinids (2), Crinoidea indet. (2 cirrals)
3	20.3	1.7	–
4	83.7	10.5	holocrinids (3), roveacrinids (1 brachial), Crinoidea indet. (1 columnal, 2 brachials, 3 cirrals)
5	184.4	0.4	holocrinids (9), isocrinids (4), encrinids (2 calyconodals, 10 columnals, 3 brachials), roveacrinids (7 thecae/thecal plates, 10 brachials), Crinoidea indet. (13 columnals, 4 brachials, 9 cirrals)
6	185.0	2.2	holocrinids (41 columnals), isocrinids (6 columnals), encrinids (13 columnals), roveacrinids (8 brachials and 2 thecae/thecal plates), Crinoidea indet. (27 columnals, 3 centrodorsals?, 2 holdfasts, 4 cirrals, 7 brachials)
7	186.9	0.8	holocrinids (7 columnals), isocrinids (1 columnals), roveacrinids (2 theca/thecal plate and 2 brachials), Crinoidea indet. (5 cirrals)
8	187.4	0.5	holocrinids (8 columnals), isocrinids (2 columnals), encrinids (5 columnals)
9	189.2	2.1	holocrinids (3), isocrinids (1), roveacrinids (3 theca/thecal plates and 7 brachials), Crinoidea indet. (12 columnals, 4 cirrals)
10	190.5	2.2	holocrinids (3 columnals), isocrinids (1 columnals)
11	191.9	7.9	holocrinids (9 columnals), isocrinids (3 columnals), roveacrinids (1 brachial), Crinoidea indet. (6 columnals, 2 cirrals, 2 brachials)
12	193.85	2.6	holocrinids (21 columnals), isocrinids (3 columnals) encrinids (2 columnals), Crinoidea indet. (5 columnals, 1 centrodorsal?, 2 cirrals, 6 brachials)

plates with vertical articular facets, weak ridges and prominent edges, both typical of *Osteocrinus* sp. (Fig. 4M–N, P–R, T-W). Individual radials and scarce thecae were found with isolated brachials. Some brachials, triangular in outline (conical to cylindrical, with comminutive articular facets), resemble those of *Somphocrinus* (Fig. 4O, S, X). Distal brachials (NBrn; see Fig. 4L) correspond to those of the saccocomid, *Saccocoma quendstedti* Sieverts-Doreck *et* Hess, 2002 (Hess 2002), known from the Upper Jurassic (Lower Kimmeridgian) of Germany. Their articular facets display spinose extensions on both sides of the food groove. On the whole, the Svalbard somphocrinid (roveacrinid) assemblages show a fairly high level of species diversity. Most could be assigned to three genera: *Somphocrinus* sp. (one species), *Osteocrinus* sp. (at least three species) and a few "saccocomid-

-like" brachial remains here assigned to Roveacrinida (gen. indet., one species). The full taxonomic description will be published elsewhere.

Other echinoderm plates are hard to diagnose and we leave them unassigned. For instance, low and slightly conical ossicles, irregularly pentagonal in outline and devoid of lumen, are present (Fig. 4J–K). On one side they possess irregularly placed depressions and, on the other, they are smooth but slightly depressed in the centre. Such ossicles resemble centrodorsals of stalkless comatulids (Comatulida, *cf.* Hess and Messing 2011, fig. 582e). Intriguing irregular four--sided columnals? with a large lumen, atypical of any post-Paleozoic crinoid taxa, also occur (Fig. 4I).

Discussion

Although it has been suggested that the range of various groups of articulates should be extended down to the Paleozoic and/or Early Triassic (Webster and Jell 1999; Twitchett and Oji 2005; Webster and Lane 2007), this idea has not been widely accepted. For instance, according to the latest edition of the Treatise on Invertebrate Paleontology, the Articulata is retained as a monophyletic, post-Paleozoic clade (Hess and Messing 2011). In accordance with this, recent molecular clocks suggest that articulate crinoids have roots in the Middle–Late Triassic (Rouse *et al*. 2013). The latter study suggested that articulate crinoids likely radiated from a small clade that passed through the end-Permian extinction rather than from several surviving lineages. However, it should be pointed out that the 95% confidence limits on the Beast analyses extend into the Permian (Rouse *et al*. 2013). Indeed, as highlighted by Roux *et al*. (2013), molecular data of extant crinoids need to be treated with caution because they can only support the monophyly of the class Crinoidea, not that of the subclass Articulata.

Our preliminary findings document at least four crinoid orders from the Early Triassic, earlier hypothesized by Twitchett and Oji (2005). This either implies that the recovery of crinoids in the aftermath of the P/T extinction was rapid or that more than a single taxon survived the end-Permian. However, it seems rather unlikely that such a rapid rate of morphological divergence from a single holocrinid lineage could have taken place within a few Myrs following the P/T boundary. More probably at least a few crinoid taxa, survived the end-Permian mass extinction. Consequently, the crown-group divergence of articulate crinoids extends deeper in time. This is consistent with recent data suggesting the presence of crinoids referred to as a new genus *Baudicrinus* (Encrinida) in the Lower Triassic of Oman (Oji and Twitchett 2015; see also Twitchett *et al*. 2004). However, Oji and Twitchett (2015) erected this new genus based on limited and poorly preserved type material. For example, they used symplexial articulation of the crinoid column as a diagnostic feature, but the feature is widely distributed among post-Pa-

leozoic taxa (*e.g. Dadocrinus*, see Salamon and Niedźwiedzki 2005, fig. 2b–d), *Qingyanocrinus* (see Stiller 2000, fig. 4.21, 4.23) and *Silesiacrinus* (see Stiller 2000, fig. 11.14–16), *Lonchocrinus* (see Głuchowski 1987, pl. 3, fig. 1b), *Apsidocrinus* (see Głuchowski 1987, pl. 9, fig. 5) and many Paleozoic taxa (*e.g.* Głuchowski 2002, fig. 2E; Głuchowski and Racki 2005, fig. 4c–f). Futhermore, Oji and Twitchett (2015) illustrated isolated ossicles displaying clear evidence of abrasion and post-diagenetic fracturing; therefore, redeposition from Paleozoic rocks cannot be excluded since highly fossiliferous Permian beds with crinoids are actually known in Oman (*e.g.* Webster *et al*. 2009).

The occurrence of at least four major crinoid clades in the Lower Triassic may have important implications for their phylogenetic relationships, especially with regard to the so-called microcrinoids known from the Paleozoic. From a palaeogeographic perspective, the Svalbard roveacrinid occurrence is consistent with the circum-Tethyan distribution of this crinoid order, extending far north into the Arctic realm due to surface water circulation that allowed the dispersal of somphocrinid larvae as well as of adults during the Late Triassic. The most intriguing discovery may be that of the comatulid-like plates: if these prove to be centrodorsals, they will force a reassessment of previous hypotheses of their Late Triassic origins and imply that the crinoid stalk might have been lost multiple times as previously suggested by molecular data (Rouse *et al*. 2013). Furthermore, discovery of encrinid-like ossicles in the Lower Triassic may solve a long-standing problem concerning the similarities between the late Paleozoic cladid Erisocrinidae and the Triassic encrinids that were long attributable to convergent evolution. Future analysis combining morphological and new temporal data of late Paleozoic and early Mesozoic crinoid taxa (such as in stratocladistics; see Holterhoff and Baumiller 1996) may answer important phylogenetic questions (for instance whether post-Paleozoic crinoids indeed represent descendants of several of the major Paleozoic clades rather than just one).

Conclusions

On the whole, the Svalbard materials are crucial for a number of reasons. Most importantly, it considerably extends the ranges of at least four major crinoid clades back to the Early Triassic, which may radically reassess the previous hypothesis about the timing of post-Paleozoic crinoid radiation. Previous studies suggested that crinoids underwent a major radiation during the Middle–Late Triassic which led to the appearance of many taxa displaying both active and passive mobility (Baumiller *et al*. 2010; Hagdorn 2011; Gorzelak *et al*. 2012). This major morphological and behavioural radiation of crinoids was likely triggered by their interactions with benthic predators during the so-called Mesozoic marine revolution (Baumiller *et al*. 2010). However, our data suggest that the Triassic radiation of crinoids began earlier and was certainly a far more prolonged evolutionary event than previously thought.

The question concerning why crinoid faunas from Svalbard were able to recover so rapidly after the end-Permian extinction is now open. Despite the timing and nature of extinction crisis in higher palaeolatitudes closely resembling those from lower latitude Tethyan settings, previous data also implied a noteworthy rapid recovery in boreal settings (Wignall *et al*. 1998). Strikingly, a recent study also revealed that the Svalbard Archipelago yields one of the most diverse Early Triassic ichthyopterygian assemblages known worldwide (Maxwell and Kear 2013).

Acknowledgements. — This study was supported by grants from the University of Tromsø and Kong Håkon den 7des utdannelsesfond for norsk ungdom. We thank Błażej Błażejowski (Institute of Paleobiology, Polish Academy of Sciences, Warsaw, Poland), Jesper Kresten Nielsen (North Energy ASA, Alta, Norway), Michał Lofek and Alfred Uchman (Jagiellonian University, Cracow, Poland) for fruitful discussions in the field. Comments by Atle Mørk (SINTEF Petroleum Research, Trondheim, Norway), Hans Hess (Natural History Museum, Basel, Switzerland), Hans Hagdorn (Muschelkalkmuseum, Ingelfingen, Germany), Samuel Zamora (University of Zaragoza, Zaragoza, Spain), William Ausich (Ohio State University, Columbus, USA). Special thanks are also due to journal reviewers Tomasz K. Baumiller (University of Michigan, Ann Arbor, USA) and Gary D. Webster (Washington State University, Pullman, USA) for their constructive comments. Figures (1–3) were drawn by Torger Grytå and Jan Petter Holm.

References

BAUMILLER T.K., SALAMON M.A., GORZELAK P., MOOI R., MESSING C.G. and GAHN F.J. 2010. Post-Paleozoic crinoid radiation in response to benthic predation preceded the Mesozoic marine revolution. *Proceedings of the National Academy of Sciences of the United States of America* 107: 5893–5896.

BENTON M.J. 2005. *When life nearly died: the greatest mass extinction of all time*. Thames & Hudson, New York: 336 pp.

BIRKENMAJER K. and TRAMMER J. 1975. Lower Triassic conodonts from Hornsund, south Spitsbergen. *Acta Geologica Polonica* 25: 299–308.

BŁAŻEJOWSKI B. 2004. Shark teeth from the Lower Triassic of Spitsbergen and their histology. *Polish Polar Research* 25 (2): 153–167.

BRAYARD A., ESCARGUEL G., BUCHER H., MONNET C., BRÜHWILER T., GOUDEMAND N., GALFETTI T. and GUEX J. 2009. Good genes and good luck: Ammonoid diversity and the end-Permian mass extinction. *Science* 325: 1118–1121.

BRAYARD A.,VENNIN E., OLIVIER N., BYLUND K.G., JENKS J., STEPHEN D.A., BUCHER H., HOFMANN R., GOUDEMAND N. and ESCARGUEL G. 2011. Transient metazoan reefs in the aftermath of the end-Permian mass extinction. *Nature Geosciences* 4: 693–697.

DALLMANN W.K. (ed.) 1999. *Lithostratigraphic Lexicon of Svalbard. Upper Palaeozoic to Quaternary Bedrock. Review and recommendations for nomenclature use*. Norwegian Polar Institute, Tromsø: 318 pp.

FOSTER W.J. and TWITCHETT R.J. 2014. Functional diversity of marine ecosystems after the Late Permian mass extinction event. *Nature Geoscience* 7: 233–238.

GŁUCHOWSKI E. 1987. Jurassic and Early Cretaceous articulate Crinoidea from the Pieniny Klippen Belt and the Tatra Mts, Poland. *Studia Geologica Polonica* 94: 1–100.

GŁUCHOWSKI E. 2002. Crinoids from the Famennian of the Holy Cross Mountains, Poland. *Acta Palaeontologica Polonica* 47 (2): 319–328.

GŁUCHOWSKI E. and RACKI G. 2005. Disarticulated crinoid stems from the Devonian and Carboniferous of north Devon, England. *Proceedings of the Yorkshire Geological Society* 55 (3): 161–172.

GORZELAK P., SALAMON M.A. and BAUMILLER T.K. 2012. Predator-induced macroevolutionary trends in Mesozoic crinoids. *Proceedings of the National Academy of Sciences of the United States of America* 109: 7004–7007.

GORZELAK P., BŁAŻEJOWSKI B., UCHMAN A. and HANKEN N.-M. 2013. First record of catacrinid crinoid from the Lower Permian of Spitsbergen. *Polish Polar Research* 34: 139–150.

GRUSZCZYŃSKI M., HAŁAS S., HOFFMAN A. and MAŁKOWSKI K. 1989. A brachiopod calcite record of the oceanic carbon and oxygen isotope shifts at the Permian/Triassic transition. *Nature* 337: 64–68.

HAGDORN H. 1988. *Ainigmacrinus calyconodalis* n. g . n. sp., eine ungewöhnliche Seelilie aus der Obertrias der Dolomiten. *Neues Jahrbuch für Geologie und Paläontologie, Monatshefte* 2: 71–96.

HAGDORN H. 2011. Triassic: the crucial period of post-Palaeozoic crinoid diversification. *Swiss Journal of Palaeontology* 130: 91–112.

HAGDORN H., GŁUCHOWSKI E. and BOCZAROWSKI A.B. 1996. The crinoid fauna of the Diplopora Dolomite (Middle Muschelkalk, Upper Anisian) at Piekary Śląskie in Upper Silesia. *Geologisch-Paläontologische Mitteilungen Innsbruck* 21: 47–87.

HESS H. 2002. Remains of Saccocomids (Crinoidea: Echinodermata) from the Upper Jurassic of southern Germany. *Stuttgarter Beiträge zur Naturkunde – Serie B* 329: 1–57.

HESS H. and MESSING C.G. 2011. *Treatise on Invertebrate Paleontology, Part T, Echinodermata 2 Revised, Crinoidea 3*. University of Kansas Press, Lawrence, Kansas: xxix + 261 pp.

HOLTEDAHL O. 1911. Zur Kenntnis der Karbonablagcrungen des westlichen Spitzbergens I. Eine Fauna der Moskauer Stufe. *Videnskabernes Selskabs Skrifter* 10: 1–89.

HOLTERHOFF P.E. and BAUMILLER T.K. 1996. Phylogeny of the proto-articulates (ampelocrinids + basal articulates): implications for the Permo-Triassic extinction and reradiation of the Crinoidea. *Paleontological Society Special Publication* 8: 1–176.

HOUNSLOW M.W. and NAWROCKI J. 2008. Palaeomagnetism and magnetostratigraphy of the Permian and Triassic of Spitsbergen: a review of progress and challenges. *Polar Research* 27: 502–522.

HOUNSLOW M.W., PETERS C., MØRK A., WEITSCHAT W. and VIGRAN J.O. 2008. Biomagnetostratigraphy of the Vikinghøgda Formation, Svalbard (Arctic Norway), and the geomagnetic polarity timescale for the Lower Triassic. *Geological Society of America Bulletin* 120: 1305–1325.

JEPPSSON L., ANEHUS R. and FREDHOLM D. 1999. The optimal acetate buffered acetic acid technique for extracting phosphatic fossils. *Journal of Paleontology* 73: 964–972.

KRISTAN-TOLLMANN E. 1975. Die Osteokrinusfazies, ein Leithorizont von Schwebcrinoiden im Oberladin-Unterkarn der Tethys. *Erdöl und Kohle, Erdgas, Petrochemie vereinigt mit Brennstoff – Chemie* 23: 781–789.

MAXWELL E.E. and KEAR B.P. 2013. Triassic ichthyopterygian assemblages of the Svalbard archipelago: a reassessment of taxonomy and distribution. *GFF* 135: 85–94.

MØRK A. 1994. Triassic transgressive-regressive cycles of Svalbard and other Arctic areas: a mirror of stage subdivision. *In*: J. Guex and A. Baud (eds) Recent developments on Triassic stratigraphy. *Mémoires de Géologie, Lausanne* 22: 69–82.

MØRK A., EGOROV A.Y. and EMBRY A.F. 1994. Base Olenekian and base Anisian sequence boundaries produced by Triassic circumpolar "synchronous" transgressions. *In*: D.K. Thurston and K. Fujita (eds) *International conference on Arctic Margins 1992 Proceedings*. OCS Study MMS 94-0040. Department of the Interior, Mineral Management Service, Anchorage, Alaska OCR Region, U.S.: 9–14.

MØRK A., EMBRY A.F. and WEITSCHAT W. 1989. Triassic transgressive-regressive cycles in the Sverdrup Basin, Svalbard, and the Barents Shelf. *In*: J.D. Collinson (ed.) *Correlation in hydrocarbon exploration*. Norwegian Petroleum Society, Graham & Trotman, London: 113–130.

MØRK A., KNARUD R. and WORSLEY D. 1982. Depositional and diagenetic environments of the Triassic and Lower Jurassic succession of Svalbard. *In*: A.F. Embry and H.R. Baikwill (eds) Arctic Geology and Geophysics. *Canadian Society of Petroleum Geologists Memoir* 8: 371–398.

MØRK A., ELVEBAKK G., FORSBERG A.W., HOUNSLOW M.W., NAKREM H.A., VIGRAN J.O. and WEITSCHAT W. 1999. The type section of the Vikinghøgda Formation: a new Lower Triassic unit in central Spitsbergen and eastern Svalbard. *Polar Research* 18: 51–82.

NAKREM H.A., ORCHARD M.J., WEITSCHAT W., HOUNSLOW M.W., BEATY T.W. and MØRK A. 2008. Triassic conodonts from Svalbard and their Boreal correlations. *Polar Research* 27: 523–539.

OJI T. and TWITCHETT R.J. 2015. The Oldest Post-Palaeozoic Crinoid and Permian–Triassic Origins of the Articulata (Echinodermata). *Zoological Science* 32: 211–215.

RIIS F., LUNSCHIEN T., HØY T., MØRK A. and MØRK M.B. 2008. Evolution of the Triassic shelf in the northern Barents Sea region. *Polar Research* 27: 318–338.

ROUSE G.W., JERMIIN L.S., WILSON N.G., EECKHAUT I., LANTERBECQ D., OJI T., YOUNG C.M., BROWNING T., CISTERNAS P., HELGEN L.E., STUCKEY M. and MESSING C.G. 2013. Fixed, free and fixed: The fickle phylogeny of extant Crinoidea (Echinoderma) and their Permian–Triassic origin. *Molecular Phylogenetics and Evolution* 66: 161–181.

ROUSSEAU J. and NAKREM H.A. 2012. An Upper Jurassic Boreal echinoderm Lagerstätte from Janusfjellet, central Spitsbergen. *Norwegian Journal of Geology* 92: 133–161.

ROUX M., ELEAUME M., HEMERY L.G. and AMEZIANE N. 2013. When morphology meets molecular data in crinoid phylogeny: a challenge. *Cahiers de Biologie Marine* 54: 541–548.

SALAMON M.A. and NIEDŹWIEDZKI R. 2005. Triassic crinoids from the Tatra Mountains and their stratigraphic significance (Poland). *Geologica Carpathica* 57 (2): 69–77.

SIMMS M.J. 1999. Systematics, phylogeny and evolutionary history. *In*: H. Hess, W.I. Ausich, C.E. Brett and M.J. Simms (eds) *Fossil Crinoids*. Cambridge University Press, Cambridge: 31–40.

SIMMS M.J. and SEVASTOPULO G.D. 1993. The origin of articulate crinoids. *Palaeontology* 36: 91–109.

STILLER F. 2000. Two new early millericrinids and an unusual crinoid of uncertain systematic position from the lower Upper Anisian (Middle Triassic) of Qingyan, southwestern China. *Journal of Paleontology* 74: 32–51.

TWITCHETT R.J., KRYSTYN L., BAUD A., WHEELEY J.R. and RICHOZ S. 2004. Rapid marine recovery after the end-Permian mass extinction event in the absence of marine anoxia. *Geology* 32: 805–808.

TWITCHETT R.J. and OJI T. 2005. Early Triassic recovery of echinoderms. *Comptes Rendus Palevol* 4: 531–542.

VIGRAN J.O., MANGERUD G., MØRK A. WORSLEY D. and HOCHULI P.A. 2014. Palynology and geology of the Triassic succession of Svalbard and the Barents Sea. *Geological Survey of Norway Special Publication* 14: 1–270.

WEBSTER G.D. and JELL P.A. 1999. New Permian crinoids from Australia. *Memoirs of the Queensland Museum* 43: 279–339.

WEBSTER G.D. and LANE N.G. 2007. New Permian crinoids from the Battleship Wash patch reef in southern Nevada. *Journal of Paleontology* 81: 951–965.

WEBSTER G.D., TINTORI A. and ANGIOLINI L. 2009. Permian crinoids from the Saiwan and Khuff formations, southeastern Oman. *Revista Italiana di Paleontologia e Stratigrafia* 115 (1): 27–48.

WIGNALL P.B., MORANTE R. and NEWTON R. 1998. The Permo-Triassic transition in Spitsbergen: δ^{13}Corg chemostratigraphy, Fe and S geochemistry, facies, fauna and trace fossils. *Geological Magazine* 135: 47–62.

WORSLEY D. 2008. The post-Caledonian development of Svalbard and the western Barents Sea. *Polar Research* 27: 298–317.

Received 6 July 2015
Accepted 10 August 2015

B

CRINOID CONFERENCE ABSTRACT

The following abstract was presented at GSA Annual Meeting in Baltimore, Maryland, USA (1 – 4 November 2015). See Appendix A for my contributions.

UNEXPECTEDLY DIVERSE CRINOID FAUNA FROM SVALBARD IN THE AFTERMATH OF THE END-PERMIAN MASS EXTINCTION

SALAMON, Mariusz A., Department of Paleontology and Stratigraphy, Faculty of Earth Sciences, University of Silesia in Katowice, Bedzinska Street 60, Sosnowiec, 41-200, Poland, GORZELAK, Przemyslaw, Institute of Paleobiology, Polish Academy of Sciences, Twarda Str. 51/55, Warsaw, 00-818, Poland, HANKEN, Nils-Martin, Department of Geology, UiT - The Arctic University of Norway, NO-9037 11 Tromsø, Tromsø, NO-9037, Norway, RIISE, Henrik Erevik, Halliburton, Sperry Drilling, P.O. Box 200, Stavanger, NO-4065, Norway and FERRE, Bruno, Sotteville-lès-Rouen, F-76300, France, paleo.crinoids@poczta.fm

The end-Permian mass extinction constitutes the major breakdown in the history of life. With regards to crinoids (Crinoidea), it led to the demise of the major Paleozoic crinoid groups including cladids, disparids, flexibles and camerates. It has been argued that only a single lineage derived from a Late Paleozoic ancestor survived this mass extinction. Holocrinids (Holocrinida), the oldest Mesozoic crinoids, are considered the stem group for the post-Paleozoic monophyletic subclass Articulata. New findings of crinoids from the Lower Triassic (Induan and Olenekian) of Svalbard radically reassess the previous hypothesis about the severity of the end-Permian mass extinction on crinoids and provide new insights into the origins and early evolution of post-Paleozoic crinoids. More specifically, we show that at least several taxa belonging to at least four orders already existed in the Early Triassic of Svalbard. This implies that the aftermath recovery of crinoids should have begun much earlier in higher paleolatitudes than in central Tethys. It seems highly improbable that such a rapid rate of morphological divergence from a single holocrinid lineage could have taken place within few Myrs following the P/T boundary. More probably, the divergence of the crown-group articulates could have likely occurred in the Late Paleozoic implying the survival of more than a single crinoid lineage from the end-Permian extinction.

C

POSTER

The poster on the following page was presented at the University of Tromsø in conjunction with a geoscience conference.

UNIVERSITY OF TROMSØ UiT
FACULTY OF SCIENCE AND TECHNOLOGY
DEPARTMENT OF GEOLOGY

Sedimentological, geochemical and diagenetic investigations with emphasis on hydrocarbon migration

N.M. Hanken, Henrik E. Riise

PROJECT 1:

Title: The hydrocarbon potential of Lower Triassic sediments on Svalbard based on sedimentological, palaeoecological, sequence stratigraphical and diagenetic investigations at Mariaholmen, Svalbard.
Financed by: Statoil
Participants: Dr. Blazej Blazejowski (University of Warszawa), Assoc. Prof. Nils-Martin Hanken (University of Tromsø), Master student Krysztof Lofek (Jagiellonian University, Krakow), Dr. Jesper Kresten Nielsen (SINTEF Petroleum Research, Trondheim), Master student Henrik Erevik Riise (University of Tromsø), Prof. Alfred Uchman (Jagiellonian University, Krakow).

Abstract: The project is interdisipliniary involving the cooperation of 6 participants. The fieldwork was carried out on Mariaholmen, which is situated at the west coast of Spitsbergen, during 4 weeks in 2010. The main focus is to achieve a better understanding of the lower Triassic basin development in this area involving a combination of sedimentological research, sequence stratigraphy and palaeoecology mainly based on trace fossil assemblages. The petrographic part concentrates upon the relative timing of the different cement generations. Hydrocarbon residues incorporated in the cement or in cavities will be related to the sequence of diagenetic minerals precipitated during burial. The lower Triassic dark organic rich shales will be characterized from a geochemical point of view, and their potential as source rocks will be evaluated.

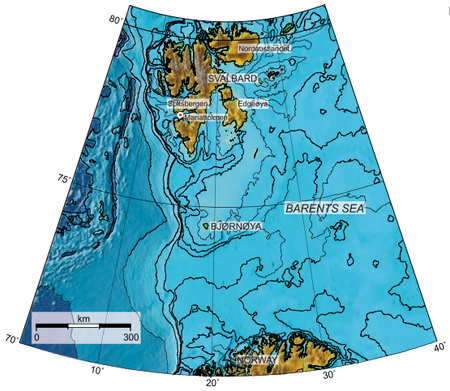

Fig. 1. Map showing the location of Mariaholmen on Svalbard.

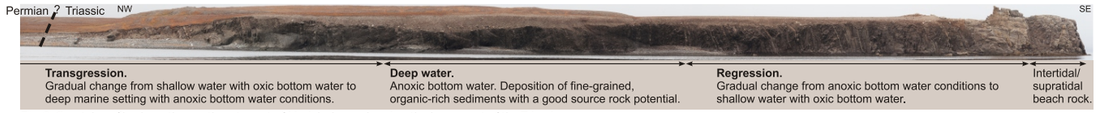

Fig. 2. Coastal profile along the southeast coast of Mariaholmen showing the lower part of the Triassic sequence.

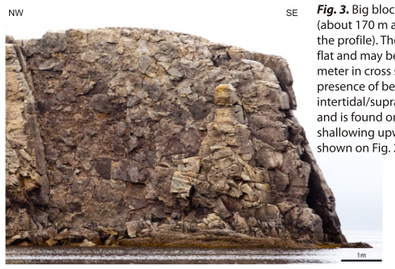

Fig. 3. Big blocks of beach rock (about 170 m above the base of the profile). The blocks are fairly flat and may be up to about one meter in cross section. The presence of beach rock indicates intertidal/supratidal conditions and is found on the top of the shallowing upward sequence shown on Fig. 2.

Fig. 5. A vein with brown/black petroliferous diagenetic quartz crystals. About 122 m above the base of the profile.

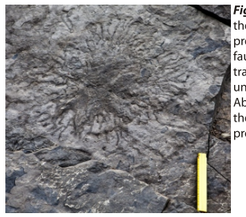

Fig. 4. An example of the rich and well preserved trace fossil fauna. This circular trace fossil is a new undescribed species. About 180 m above the base of the profile.

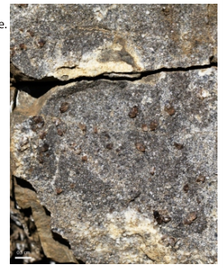

PROJECT 2

Title: An exhumed Upper Ordovician hydrocarbon reservoir in the Oslo Region, Norway: burial and fluid flow in the Ringerike area.
Financed by: ENI Norge
Participants: Dr. Bjørn Buchardt (University of Copenhagen), Malene Hansen (Statoil), Tor Eggebø (Halliburton), Assoc. Prof. Nils-Martin Hanken (University of Tromsø), Dr. Jesper Nielsen (SINTEF Petroleum Research), Prof. Snorre Olaussen (UNIS), Reidar Steinsland (Statoil), Prof. Alfred Uchman (Jagiellonian University, Krakow).

Abstract: The uppermost Ordovican sediments in the Ringerike area, Oslo Region, are characterized by an interfingering of shallow-water siliciclastic and carbonate facies. The outcrops at Ringerike exhibit a very well exposed example and analogue of potential hydrocarbon plays of mixed shallow marine siliciclastic deposits and carbonates. A combination of petrographic investigations, stable isotope analysis and conodont colour analysis indicates a maximum temperature of about 150°C or slightly higher. This temperature is due to a combination of burial and Carboniferous-Permian magmatic activity. The first migration phase probably took place during the Caledonian Orogeny (Late Silurian-Early Devonian) while the second phase took place during the Carboniferous magmatic activity and rifting.

Fig. 1. Map showing the location of the investigated area at Ringerike.

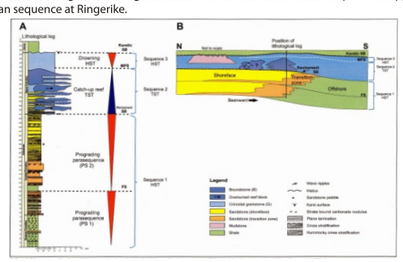

Fig. 2. A. The uppermost Ordovician section at Tyrifjorden can be distinguished by a Lower Unit of siliciclastics and an Upper Unit of mainly carbonates. The Lower Unit is interpreted as an inner shelf to shoreface with tidal inlets in upper part. This unit comprise a prograding highstand system tract and a transgressive system tract separated by a third order sequence boundary.
A third order sequence boundary (ravinement surface) defines the base of the Upper Unit which comprises a complex pattern with patch reefs interfingering with shallow marine sandstones, crinoidal banks to the south and mudbanks to the north. A combination of subaeril exposures and karstification spanning the Ordovician-Silurian is interpreted as a 2nd order sequence boundary.
B. Simplified fence diagram showing the lateral and vertical facies relationships in the upper Ordovician sequence at Ringerike.

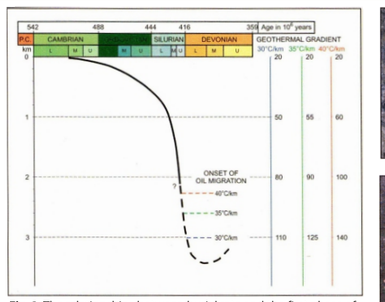

Fig. 3. The relationships between burial rate and the first phase of hydrocarbon migration in the Oslo Region.

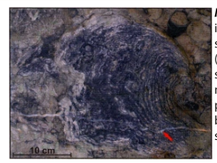

Fig. 4. Pyrobitumen (black) in primary cavities of a stromatoporoid. The vein (red arrow) cutting both the stromatoporoid and the matrix contain some pyrobitumen which has been incorporated in the sparry cement.

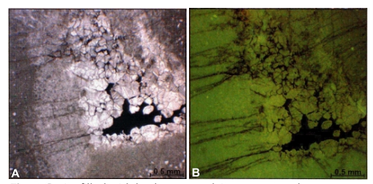

Fig. 5. Cavity filled with both sparry calcite cement and pyrobitumen as seen in normal light (**A**) and UV-light (**B**). The tiny cracks in the matrix are also filled with pyrobitumen.

PROJECT 3

Title: Late Pleistocene – early Holocene polychaete borings in north-east Spitsbergen and their palaeoceological and climate implications: an example from the Basissletta area.
Financed by: The Norwegian Petroleum Directorate and the Norske Oljeselskap
Participants: Assoc. Prof. Nils-Martin Hanken (University of Tromsø), Sten Jakobsen (University of Copenhagen), Prof. Alfred Uchman (Jagiellonian University, Krakow).

Abstract: Several marine invertebrates bore in rocks, mostly carbonates, producing characteristic microscopic and macroscopic bioerosion structures which have a high fossilization potential. *Caulostrepsis* is a widely distributed shallow-marine boring produced by polychaetes, but is rarely known from Polar Regions. Together with the related boring, *Meandropolydora*, it was discovered for the first time in Svalbard (the Basissletta area in north-east Spitsbergen). The borings occur about 9-78 m above present sea level. ^{14}C datings of wood, whalebone and bivalves in the vicinity and in neighboring areas indicate that the borings have a radiocarbon age spanning from about 7 to 11 ky. It is well known that the boring polychates are restricted to areas where the water temperature is at least 7°C in summer, and the presence of their borings can thus be used as a measure of the minimum surface water temperature.

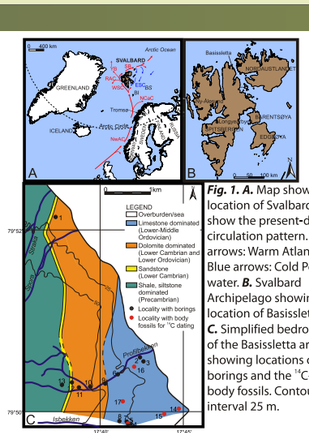

Fig. 1. A. Map showing the location of Svalbard. Arrows show the present-day ocean circulation pattern. Red arrows: Warm Atlantic water. Blue arrows: Cold Polar water. ***B.*** Svalbard Archipelago showing the location of Basissletta. ***C.*** Simplified bedrock map of the Basissletta area showing locations of borings and the ^{14}C-dated body fossils. Contour interval 25 m.

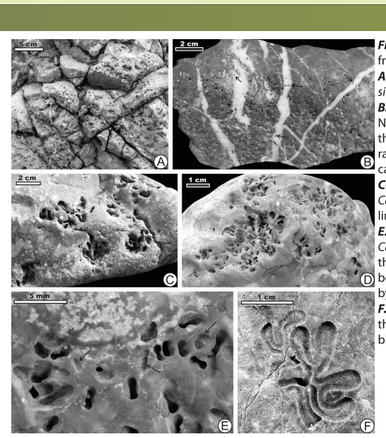

Fig. 2. Examples of borings from the Basissletta area.
A. *Caulostrepsis taeniola in situ* in limestone substrate.
B. *Caulostrepsis taeniola*. Note common borings in the grey limestones and rare borings in the white calcite veins (arrows).
C-D. Patches of *Caulostrepsis taeniola* in a limestone block.
E. Insert of B, showing *Caulostrepsis taeniola*. Note the shallow, basal part of borings (arrows) truncated by erosion.
F. *Maeandropolydora* isp. on the surface of a limestone block.

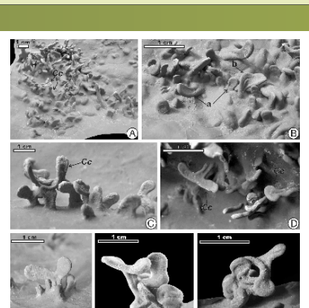

Fig. 3. Silicone rubber casts of *Caulostrepsis*. ***A.*** A patch of *Caulostrepsis taeniola* and *Caulostrepsis contorta* (Cc). ***B.*** *Caulostrepsis taeniola* with specimens showing arcuate corrugations in concordance with the distal curvature (a) or the marginal tube (b). ***C-D.*** *Caulostrepsis taeniola* and *Caulostrepsis contorta* (Cc). ***E.*** *Caulostrepsis contorta*. ***F-G.*** *Caulostrepsis contorta* on the surface.

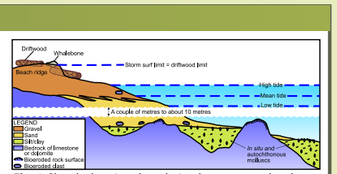

Fig. 4. Sketch showing the relation between sea level (mean tide), beach ridges and sea-level indicators (driftwood, whalebone and molluscs). Bioeroded rock surfaces are limited to vertical to gently dipping surfaces or boulders which were exposed to sea water on the sea floor. *In situ* and autochthonous molluscs are mostly found in patchily distributed fine-grained sediments selectively preserved in topographical depressions which were little affected by later erosion during the glacio-isostatic regression phase and subaerial exposure.

D

GEOCHEMICAL DATA

D.1 LECO DATA

Raw data used for the plots containing data from LECO analysis. Blank TOC/TS ratio are due to either negative TOC or TS values.

Table D.1: LECO data.

Level (m)	TS (%)	TOC (%)	TOC/TS ratio	Powder colour
20.15	1.13	0.06	0.05	Light grey
21.65	0.12	0.09	0.70	Light grey
24.10	0.02	0.00	0.19	Light grey
25.55	0.15	0.10	0.64	Light grey
29.40	0.29	0.11	0.36	Light grey
30.97	1.65	0.65	0.40	Dark grey
32.95	0.12	0.03	0.22	Light grey
34.90	0.25	0.07	0.27	Light grey
39.55	0.22	−0.01		Light grey
41.10	0.29	0.04	0.15	Light grey
41.35	−0.09	0.07		Light grey

Continued on next page

Table D.1 – *Continued from previous page*

Level (m)	TS (%)	TOC (%)	TOC/TS ratio	Powder colour
41.98	0.38	0.07	0.18	Light grey
43.15	0.03	0.08	2.87	Light grey
45.15	−0.01	0.07		Light grey
45.55	0.28	0.12	0.45	Light grey
47.05	0.36	0.03	0.08	Light grey
48.55	0.11	0.10	0.94	Grey
50.85	0.22	0.11	0.51	Light grey
53.15	0.95	0.14	0.15	Light grey
53.55	0.53	0.16	0.29	Light grey
55.05	0.06	0.08	1.35	Light grey
55.15	0.24	0.10	0.42	Light grey
57.25	0.62	0.17	0.27	Light grey
57.30	0.77	0.11	0.15	Grey
61.70	0.50	0.10	0.21	Light grey
62.25	0.28	0.11	0.38	Light grey
63.85	0.55	0.07	0.12	Light grey
64.15	0.29	0.14	0.49	Light grey
66.65	0.33	0.13	0.41	Light grey
69.25	0.31	0.14	0.46	Light grey
73.45	−0.06	0.09		Light grey
73.55	0.08	0.11	1.30	Light grey
76.05	−0.01	0.05		Light grey

Continued on next page

Table D.1 – *Continued from previous page*

Level (m)	TS (%)	TOC (%)	TOC/TS ratio	Powder colour
78.05	−0.03	0.07		Light grey
80.45	0.76	0.10	0.13	Light grey
82.55	0.22	0.18	0.81	Grey
83.20	0.87	0.18	0.20	Light grey
84.85	0.55	0.19	0.35	Light grey
86.35	0.87	0.12	0.14	Grey
86.55	0.89	0.22	0.25	Grey
88.45	0.65	0.18	0.27	Grey
88.50	0.91	0.21	0.23	Grey
90.45	0.94	0.20	0.21	Grey
92.15	0.92	0.11	0.12	Grey
93.95	1.23	0.16	0.13	Dark grey
94.03	1.41	0.35	0.25	Grey
95.85	0.98	0.30	0.31	Grey
97.05	0.44	0.15	0.33	Light grey
97.65	1.09	0.25	0.23	Light grey
97.75	1.19	0.23	0.19	Grey
99.25	0.99	0.24	0.24	Grey
99.85	1.04	0.27	0.26	Dark grey
101.35	0.84	0.12	0.14	Light grey
101.95	0.88	0.20	0.23	Grey
104.26	1.08	0.08	0.07	Grey

Continued on next page

Table D.1 – *Continued from previous page*

Level (m)	TS (%)	TOC (%)	TOC/TS ratio	Powder colour
105.00	1.23	0.23	0.19	Grey
106.75	0.92	0.28	0.31	Grey
108.25	0.76	0.26	0.33	Grey
108.65	0.19	0.09	0.47	Light grey
110.35	0.67	0.08	0.12	Light grey
113.35	0.19	0.09	0.46	Grey
114.45	2.34	0.25	0.11	Grey
116.15	1.71	0.41	0.24	Dark grey
119.25	1.62	0.22	0.14	Dark grey
121.15	1.51	0.35	0.23	Dark grey
123.95	2.64	0.39	0.15	Dark grey
125.25	1.90	0.37	0.20	Dark grey
126.15	2.67	0.59	0.22	Grey
127.65	0.74	0.08	0.10	Grey
130.25	2.07	0.59	0.28	Dark grey
131.65	2.07	0.67	0.32	Dark grey
132.75	1.97	0.60	0.31	Dark grey
133.85	1.65	0.52	0.32	Dark grey
134.15	1.87	0.67	0.36	Dark grey
136.55	1.93	0.55	0.28	Dark grey
136.65	1.59	0.51	0.32	Dark grey
138.95	1.80	0.43	0.24	Dark grey

Continued on next page

Table D.1 – *Continued from previous page*

Level (m)	TS (%)	TOC (%)	TOC/TS ratio	Powder colour
139.40	1.70	0.44	0.26	Dark grey
141.05	1.56	0.53	0.34	Dark grey
143.75	1.01	0.47	0.46	Dark grey
144.15	1.34	0.35	0.26	Dark grey
146.55	1.39	0.56	0.40	Dark grey
148.95	1.20	0.47	0.39	Dark grey
151.15	0.57	0.47	0.83	Dark grey
153.15	0.84	0.56	0.66	Dark grey
156.65	0.49	0.21	0.43	Grey
160.05	0.34	0.31	0.90	Grey
160.15	0.37	0.35	0.95	Grey
161.85	2.42	0.15	0.06	Grey
164.45	0.21	0.17	0.83	Grey
167.15	0.49	0.30	0.61	Dark grey
168.95	0.35	0.25	0.72	Grey
171.35	−0.02	0.20		Grey
173.95	0.20	0.28	1.43	Dark grey
174.05	0.96	0.67	0.70	Dark grey
176.25	0.33	0.59	1.77	Dark grey
179.10	0.87	0.65	0.74	Dark grey
181.05	0.17	0.21	1.22	Grey
183.25	0.75	0.31	0.42	Grey

Continued on next page

Table D.1 – *Continued from previous page*

Level (m)	TS (%)	TOC (%)	TOC/TS ratio	Powder colour
184.35	0.48	0.21	0.44	Grey
192.85	0.69	0.18	0.26	Grey
193.85	1.29	0.64	0.50	Dark grey
195.15	0.97	0.44	0.45	Dark grey
195.65	1.14	0.39	0.34	Dark grey
196.65	1.03	0.47	0.46	Dark grey
197.15	1.11	0.44	0.40	Dark grey
198.65	1.11	0.05	0.04	Dark grey
201.45	1.05	0.30	0.29	Grey
204.15	1.55	0.46	0.30	Dark grey
204.85	0.98	0.60	0.61	Dark grey
206.95	0.91	0.64	0.71	Dark grey
208.95	0.69	0.40	0.57	Dark grey
210.75	0.77	0.41	0.54	Dark grey
212.75	0.63	0.41	0.66	Dark grey
216.65	0.71	0.38	0.53	Dark grey
220.65	0.74	0.31	0.42	Dark grey
222.85	0.61	0.29	0.47	Grey
227.65	0.45	0.23	0.50	Dark grey

D.2 XRF DATA

Raw data used for the plots containing data from XRF measurements.

Table D.2: XRF data.

Level (m)	V (ppm)	Ni (ppm)	V/(V+Ni) ratio	Powder colour
20.15	89.20	39.50	0.693	Light grey
21.65	107.10	35.00	0.738	Light grey
25.55	116.30	28.50	0.803	Light grey
29.40	129.80	38.25	0.772	Light grey
30.97	119.80	49.90	0.706	Dark grey
32.95	87.90	38.00	0.698	Light grey
34.90	103.60	42.90	0.707	Light grey
39.55	76.20	31.60	0.707	Light grey
41.10	102.80	40.10	0.719	Light grey
41.35	96.40	36.30	0.726	Light grey
41.98	105.70	44.70	0.703	Light grey
43.15	136.70	44.50	0.754	Light grey
45.15	105.80	37.80	0.737	Light grey
45.55	141.10	47.60	0.748	Light grey
47.05	95.90	44.10	0.685	Light grey
48.55	127.70	40.90	0.757	Grey
50.85	133.50	44.40	0.750	Light grey
53.15	121.20	52.70	0.697	Light grey
53.55	135.15	46.55	0.744	Light grey
55.05	113.90	39.50	0.743	Light grey

Continued on next page

Table D.2 – *Continued from previous page*

Level (m)	V (ppm)	Ni (ppm)	V/(V+Ni) ratio	Powder colour
55.15	97.70	34.70	0.738	Light grey
57.25	146.80	49.10	0.749	Light grey
57.30	119.60	49.10	0.709	Grey
61.70	130.50	48.00	0.731	Light grey
62.25	128.70	42.40	0.752	Light grey
63.85	97.70	44.80	0.686	Light grey
64.15	150.40	49.30	0.753	Light grey
66.65	147.40	46.40	0.761	Light grey
69.25	153.50	48.80	0.759	Light grey
73.45	109.40	40.60	0.729	Light grey
73.55	102.50	34.20	0.750	Light grey
76.05	84.00	31.40	0.728	Light grey
78.05	102.10	33.90	0.751	Light grey
80.45	91.10	40.30	0.693	Light grey
82.55	101.60	36.70	0.735	Grey
83.20	116.60	40.10	0.744	Light grey
84.85	106.60	38.90	0.733	Light grey
86.35	72.60	36.70	0.664	Grey
86.55	113.40	42.60	0.727	Grey
88.45	93.60	34.40	0.731	Grey
88.50	110.20	39.60	0.736	Grey
90.45	82.20	34.60	0.704	Grey
92.15	67.60	29.50	0.696	Grey
93.95	91.30	31.10	0.746	Dark grey

Continued on next page

Table D.2 – *Continued from previous page*

Level (m)	V (ppm)	Ni (ppm)	V/(V+Ni) ratio	Powder colour
94.03	126.20	51.35	0.711	Grey
95.85	102.20	38.70	0.725	Grey
97.05	90.90	32.60	0.736	Light grey
97.65	133.50	48.30	0.734	Light grey
97.75	119.90	52.40	0.696	Grey
99.25	110.10	38.60	0.740	Grey
99.85	139.70	42.80	0.765	Dark grey
101.35	84.10	31.60	0.727	Light grey
101.95	131.90	40.80	0.764	Grey
104.26	80.70	33.90	0.704	Grey
105.00	105.00	50.20	0.677	Grey
106.75	120.20	45.60	0.725	Grey
108.25	137.20	52.50	0.723	Grey
108.65	81.80	29.50	0.735	Light grey
110.35	80.90	36.70	0.688	Light grey
113.35	96.90	34.20	0.739	Grey
114.45	129.50	52.00	0.713	Grey
116.15	112.40	37.60	0.749	Dark grey
119.25	78.70	25.50	0.755	Dark grey
121.15	82.60	30.00	0.734	Dark grey
123.95	78.60	35.90	0.686	Dark grey
125.25	91.70	39.80	0.697	Dark grey
126.15	150.50	51.50	0.745	Grey
127.65	62.10	23.40	0.726	Grey

Continued on next page

Table D.2 – *Continued from previous page*

Level (m)	V (ppm)	Ni (ppm)	V/(V+Ni) ratio	Powder colour
130.25	96.70	38.50	0.715	Dark grey
131.65	137.40	42.00	0.766	Dark grey
132.75	124.20	44.90	0.734	Dark grey
133.85	118.40	41.40	0.741	Dark grey
134.15	110.70	44.90	0.711	Dark grey
136.55	103.80	43.90	0.703	Dark grey
136.65	117.45	39.55	0.748	Dark grey
138.95	110.90	40.80	0.731	Dark grey
139.40	97.70	42.00	0.699	Dark grey
141.05	121.40	42.00	0.743	Dark grey
143.75	96.60	31.90	0.752	Dark grey
144.15	80.70	32.60	0.712	Dark grey
146.55	110.2	42.30	0.723	Dark grey
148.95	85.60	38.90	0.688	Dark grey
151.15	74.70	28.30	0.725	Dark grey
153.15	96.50	33.25	0.744	Dark grey
156.65	61.55	23.30	0.725	Grey
160.05	89.30	30.90	0.743	Grey
160.15	80.70	27.10	0.749	Grey
161.85	53.50	23.30	0.697	Grey
164.45	48.10	19.90	0.707	Grey
167.15	77.85	24.20	0.763	Dark grey
168.95	61.20	20.25	0.751	Grey
171.35	53.30	15.90	0.770	Grey

Continued on next page

Table D.2 – *Continued from previous page*

Level (m)	V (ppm)	Ni (ppm)	V/(V+Ni) ratio	Powder colour
173.95	60.40	20.35	0.748	Dark grey
174.05	102.60	34.90	0.746	Dark grey
176.25	95.90	35.30	0.731	Dark grey
179.10	104.10	40.00	0.722	Dark grey
181.05	42.60	16.60	0.720	Grey
183.25	64.60	26.00	0.713	Grey
184.35	51.70	20.90	0.712	Grey
192.85	32.40	13.30	0.709	Grey
193.85	86.10	33.10	0.722	Dark grey
195.15	57.50	25.40	0.694	Dark grey
195.65	54.10	23.70	0.695	Dark grey
196.65	60.70	31.10	0.661	Dark grey
197.15	67.60	32.10	0.678	Dark grey
197.65	56.90	29.40	0.659	Dark grey
198.65	60.90	30.00	0.670	Dark grey
201.45	55.70	25.50	0.686	Grey
204.15	53.70	30.20	0.640	Dark grey
204.85	62.10	29.40	0.679	Dark grey
206.95	62.30	27.90	0.691	Dark grey
208.95	41.90	19.00	0.688	Dark grey
210.75	48.00	22.60	0.680	Dark grey
212.75	46.10	20.30	0.694	Dark grey
216.65	40.90	18.60	0.687	Dark grey
220.65	42.60	19.70	0.684	Dark grey

Continued on next page

Table D.2 – *Continued from previous page*

Level (m)	V (ppm)	Ni (ppm)	V/(V+Ni) ratio	Powder colour
222.85	41.50	18.20	0.695	Grey
227.65	34.00	14.40	0.702	Dark grey

D.3 MASS SPECTROMETRY DATA

Raw data used for all plots containing data from Mass Spectrometry measurements.

Table D.3: Mass spectrometry data.

Level (m)	TOC (%)	$\delta^{13}C_{Org}$ (‰)	Powder colour
41.35	0.12	−27.13	Light grey
43.15	0.11	−26.81	Light grey
45.15	0.09	−27.52	Light grey
45.55	0.17	−27.67	Light grey
48.55	0.13	−27.67	Grey
50.85	0.09	−27.75	Light grey
55.05	0.09	−27.83	Light grey
57.25	0.20	−28.44	Light grey
62.25	0.10	−28.20	Light grey
64.15	0.17	−29.06	Light grey
66.65	0.14	−29.31	Light grey
69.25	0.15	−29.89	Light grey
73.45	0.12	−29.38	Light grey
76.05	0.08	−28.90	Light grey
78.05	0.07	−29.07	Light grey
82.55	0.14	−30.73	Grey
83.20	0.22	−30.18	Light grey
84.85	0.20	−30.81	Light grey
86.55	0.22	−30.80	Grey

Continued on next page

Table D.3 – *Continued from previous page*

Level (m)	TOC (%)	$\delta^{13}C_{Org}$ (‰)	Powder colour
88.45	0.18	−30.53	Grey
88.50	0.19	−30.66	Grey
92.15	0.15	−30.98	Grey
93.95	0.19	−31.18	Dark grey
95.85	0.31	−31.58	Grey
97.75	0.29	−30.92	Grey
99.25	0.28	−31.36	Grey
99.85	0.30	−31.02	Dark grey
101.35	0.17	−30.36	Light grey
101.95	0.23	−31.05	Grey
104.26	0.15	−30.25	Grey
105.00	0.29	−31.13	Grey
106.75	0.32	−31.22	Grey
108.25	0.30	−31.09	Grey
108.65	0.15	−29.96	Light grey
110.35	0.15	−30.05	Light grey
113.35	0.15	−29.65	Grey
114.45	0.30	−30.90	Grey
116.15	0.43	−31.44	Dark grey
119.25	0.25	−31.72	Dark grey
121.15	0.38	−32.22	Dark grey
123.95	0.39	−32.11	Dark grey
125.25	0.39	−32.01	Dark grey
126.15	0.59	−32.11	Grey

Continued on next page

Table D.3 – *Continued from previous page*

Level (m)	TOC (%)	$\delta^{13}C_{Org}$ (‰)	Powder colour
127.65	0.14	−30.90	Grey
130.25	0.60	−31.81	Dark grey
131.65	0.66	−30.83	Dark grey
132.75	0.63	−31.05	Dark grey
133.85	0.55	−30.38	Dark grey
134.15	0.70	−30.52	Dark grey
136.55	0.56	−30.15	Dark grey
138.95	0.43	−30.50	Dark grey
139.4	0.47	−30.00	Dark grey
141.05	0.56	−29.53	Dark grey
143.75	0.49	−29.51	Dark grey
144.15	0.40	−29.42	Dark grey
146.55	0.57	−29.24	Dark grey
148.95	0.52	−29.56	Dark grey
151.15	0.48	−29.27	Dark grey
160.15	0.33	−29.25	Grey
161.85	0.20	−29.14	Grey
164.45	0.23	−28.28	Grey
171.35	0.22	−28.06	Grey
176.25	0.62	−27.94	Dark gGrey
179.10	0.65	−27.88	Dark grey
181.05	0.20	−28.13	Grey
183.25	0.32	−27.45	Grey
184.35	0.24	−27.86	Grey

Continued on next page

Table D.3 – *Continued from previous page*

Level (m)	**TOC (%)**	**$\delta^{13}C_{Org}$ (‰)**	**Powder colour**
192.85	0.23	−28.02	Grey
193.85	0.65	−28.26	Dark grey
195.15	0.48	−27.96	Dark grey
195.65	0.42	−27.70	Dark grey
197.15	0.46	−27.50	Dark grey
198.65	0.48	−27.64	Dark grey
201.45	0.32	−27.68	Grey
204.15	0.48	−28.26	Dark grey
204.85	0.59	−28.47	Dark grey
206.95	0.73	−28.45	Dark grey
208.95	0.45	−28.63	Dark grey
210.75	0.44	−28.59	Dark grey
212.75	0.44	−28.57	Dark grey
216.65	0.40	−28.55	Dark grey
220.65	0.30	−28.72	Dark grey
222.85	0.36	−28.56	Grey
227.65	0.25	−28.38	Dark grey

Rock-Eval data. Any missing values in hydrogen and oxygen index is due to either negative or missing TOC values.

Table D.4: Rock-Eval data.

Level (m)	S1 (mg/g)	S2 (mg/g)	S3 (mg/g)	T_{Max} (°C)	PI (wt. ratio)	Hydrogen Index (mg HC/g TOC)	Oxygen Index (mg HC/g TOC)	Powder colour
11.75	0	0	0.62	513	0			Light grey
17.15	0	0.01	0.20	490	0			Light grey
20.15	0	0.01	0.77	488	0	17.48	1346.15	Light grey
29.4	0.01	0.01	0.44	474	0.50	9.47	416.67	Light grey
30.97	0.13	0.19	0.59	463	0.41	29.10	90.35	Dark grey
39.55	0	0.01	0.26	492	0			Light grey
41.1	0	0.02	0.61	473	0	45.56	1389.52	Light grey
48.55	0.01	0.01	0.16	475	0.50	10.06	160.97	Grey

Continued on next page

Table D.4 – *Continued from previous page*

Level (m)	S1 (mg/g)	S2 (mg/g)	S3 (mg/g)	T_{Max} (°C)	PI (wt. ratio)	Hydrogen Index (mg HC/g TOC)	Oxygen Index (mg HC/g TOC)	Powder colour
53.15	0	0.02	0.16	470	0	14.18	113.48	Light grey
57.25	0	0.01	0.14	473	0	5.92	82.84	Light grey
64.15	0.02	0.04	1.50	478	0.33	28.57	1071.43	Light grey
69.25	0.01	0.02	0.72	484	0.33	14.08	507.04	Light grey
78.05	0	0.01	0.30	487	0	14.95	448.43	Light grey
82.55	0	0.02	0.36	463	0	11.11	200.00	Grey
94.03	0.02	0.06	0.32	465	0.25	17.29	92.22	Grey
106.75	0.02	0.04	0.23	471	0.33	14.23	81.85	Grey
121.15	0.07	0.07	0.58	453	0.5	19.83	164.31	Dark grey
131.65	0.13	0.11	0.45	454	0.54	16.37	66.96	Dark grey
134.15	0.17	0.16	0.57	284	0.52	24.02	85.59	Dark grey
141.05	0.15	0.16	0.30	459	0.48	30.08	56.39	Dark grey

Continued on next page

Table D.4 – *Continued from previous page*

Level (m)	S1 (mg/g)	S2 (mg/g)	S3 (mg/g)	T_{Max} (°C)	PI (wt. ratio)	Hydrogen Index (mg HC/g TOC)	Oxygen Index (mg HC/g TOC)	Powder colour
153.15	0.10	0.19	0.29	464	0.34	34.05	51.97	Dark grey
174.05	0.09	0.25	0.41	461	0.26	37.09	60.83	Dark grey
179.1	0.07	0.14	0.57	457	0.33	21.60	87.96	Dark grey
204.15	0.41	0.5	0.42	472	0.45	108.93	91.50	Dark grey
212.75	0.09	0.18	0.33	467	0.33	43.80	80.29	Dark grey
216.65	0.13	0.17	0.34	458	0.43	45.33	90.67	Dark grey
220.65	0.10	0.12	0.25	456	0.45	38.83	80.91	Dark grey
222.85	0.13	0.18	0.38	452	0.42	63.16	133.33	Grey
227.65	0.09	0.16	0.24	453	0.36	70.80	106.19	Dark grey

E

MEASURED CURRENT DIRECTIONS

Table E.1: Current and wind directions measured on Mariaholmen (directions are structurally restored compass measurements).

Height	Sedimentary feature	Current direction
19.75	Current ripples	260°
36.70	Wave ripples	260°/80°
41.15	Interference ripples	295°/115° and 355°/175°
192.15	Parting lineation	255°/80°
192.65	Wave ripples	290°/110 °
192.65	Wave ripples	205°/25°
192.65	Wave ripples	225°/45°
192.65	Wave ripples	275°/95°
192.65	Trough cross-bedding	360°
192.65	Trough cross-bedding	355°
192.65	Trough cross-bedding	355°
192.65	Trough cross-bedding	355°
192.65	Trough cross-bedding	315°
192.65	Trough cross-bedding	315°
192.65	Trough cross-bedding	345°
192.65	Trough cross-bedding	345°
192.65	Trough cross-bedding	345°

Continued on next page

Table E.1 – *Continued from previous page*

Level (m)	Sedimentary feature	Current direction
192.65	Trough cross-bedding	330°
192.65	Trough cross-bedding	330°
192.65	Trough cross-bedding	350°
192.65	Trough cross-bedding	325°
195.50	Wave ripples	270°/90°
195.55	Current ripples	270°
225.85	Wave ripples	280°/100°
226.95	Wave ripples	185°/5°

F

SAMPLES TREATED WITH ACETIC ACID

The following carbonate samples were dissolved in acetic acid following the method described in Section 2.7.

Table F.1: Samples dissolved in acetic acid

Level (m)	**Sample name**
8.55	M−10.1
19.55	M0.5
19.58	M0.93
20.30	M1.65
20.35	M1.7
68.65	M50
83.65	M65
87.65	M69
184.40	M165.75
185.00	M166.35
185.35	M166.70
185.75	M167.10
186.90	M168.25
187.40	M168.75

Continued on next page

Table F.1 – *Continued from previous page*

Level (m)	**Sample name**
189.15	M170.50
191.75	M173.10
192.65	M174.00
193.75	M175.10

G

SEM ANALYSIS

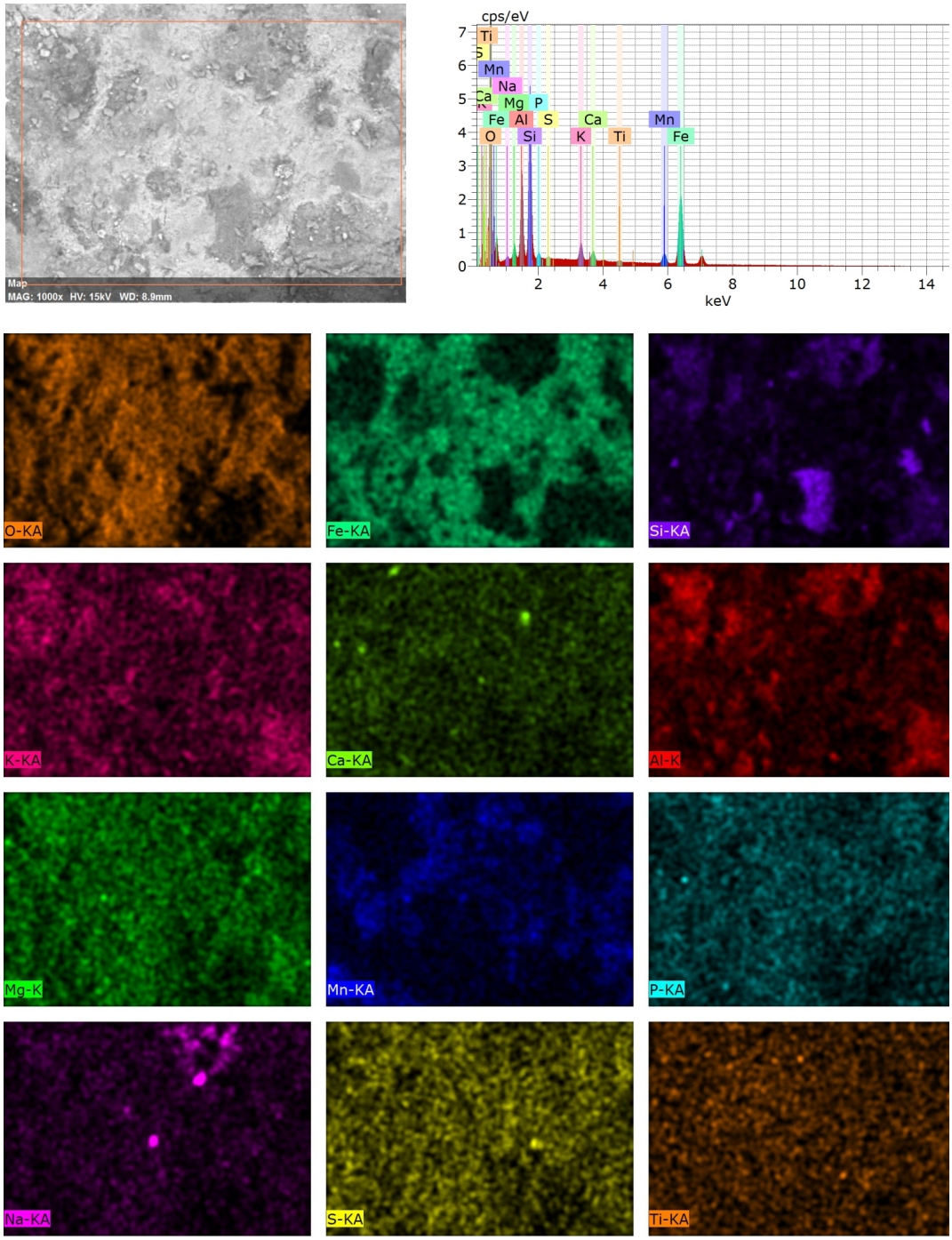

Fig. G.1: SEM-EDS scan of clast (18.95 m) in Figure 3.36A.

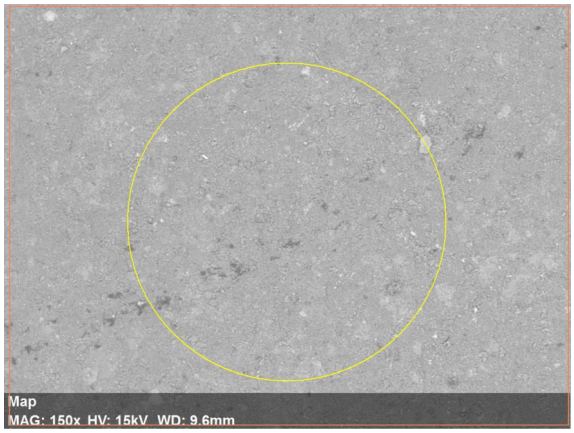

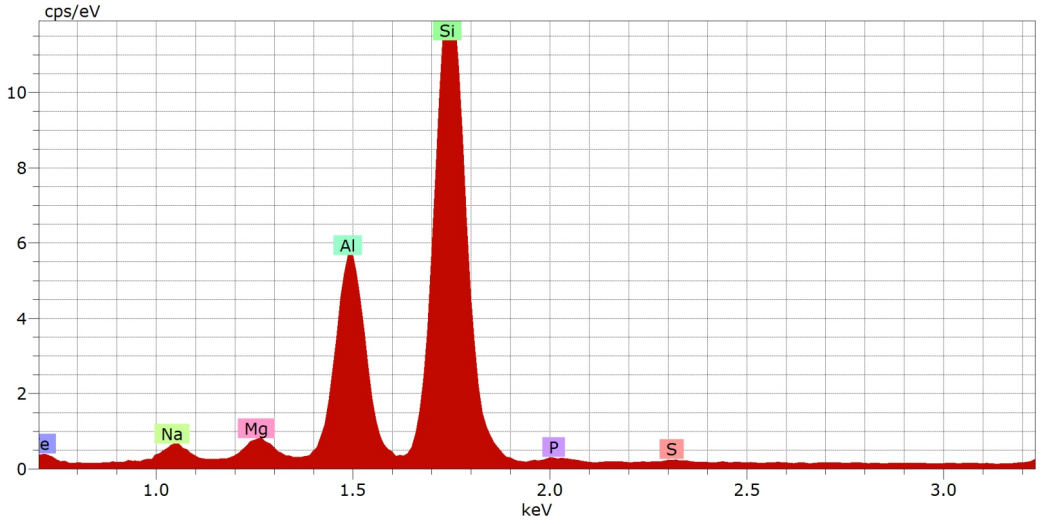

Spectrum: Point

Element	AN	Series	unn. C [wt.%]	norm. C [wt.%]	Atom. C [at.%]	Error [%]
Oxygen	8	K-series	51.59	50.16	65.47	5.6
Silicon	14	K-series	26.80	26.05	19.37	1.1
Aluminium	13	K-series	10.57	10.28	7.96	0.5
Iron	26	K-series	5.42	5.27	1.97	0.2
Potassium	19	K-series	3.02	2.94	1.57	0.1
Sodium	11	K-series	1.44	1.40	1.27	0.1
Magnesium	12	K-series	1.29	1.26	1.08	0.1
Calcium	20	K-series	0.89	0.86	0.45	0.1
Titanium	22	K-series	0.80	0.78	0.34	0.0
Manganese	25	K-series	0.57	0.56	0.21	0.0
Phosphorus	15	K-series	0.31	0.30	0.21	0.0
Sulfur	16	K-series	0.15	0.15	0.09	0.0

Fig. G.2: SEM-EDS scan of clast (18.95 m) in Figure 3.36B.

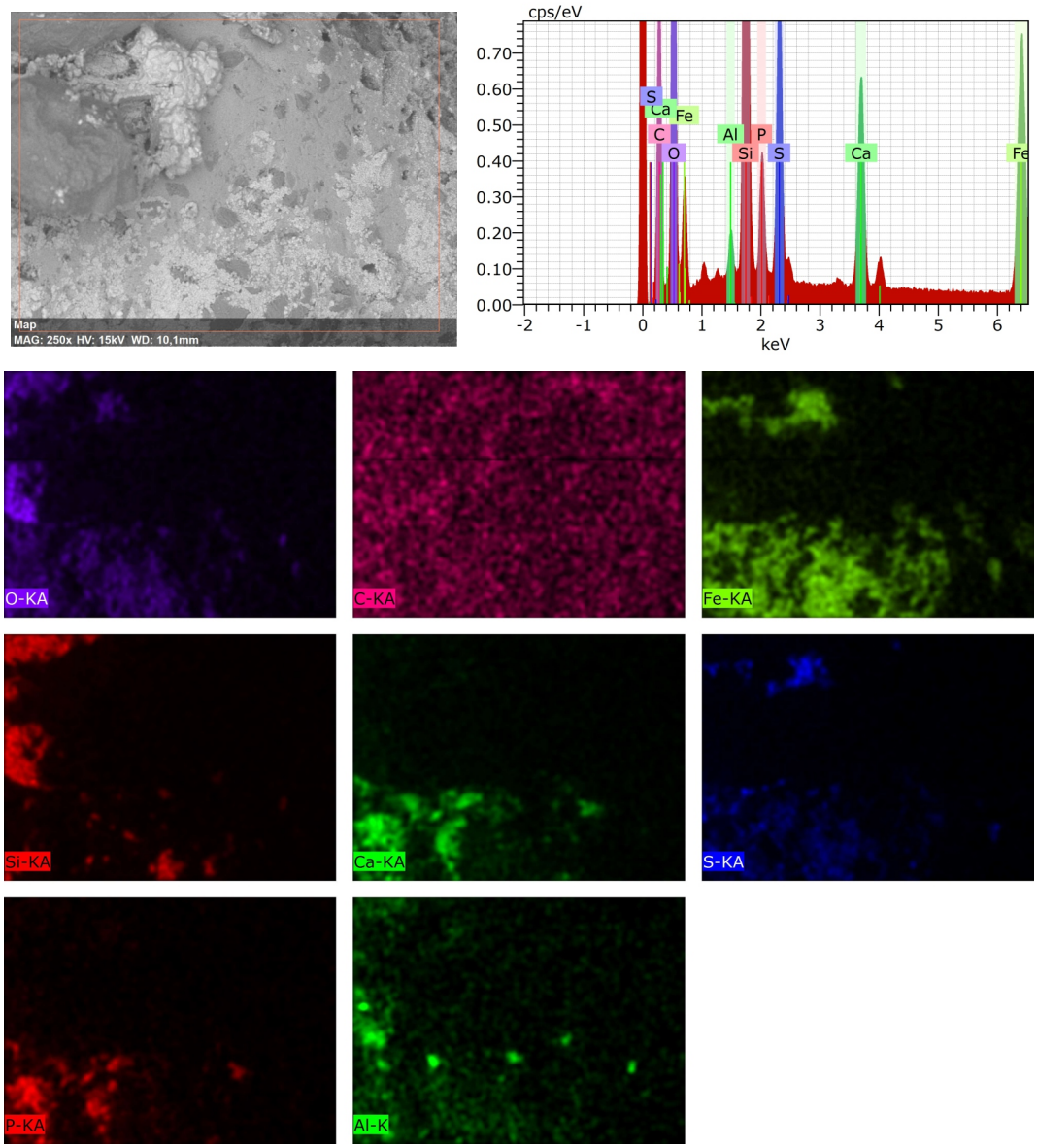

Fig. G.3: SEM-EDS scan of clast (192.65 m) in Figure 3.37A.

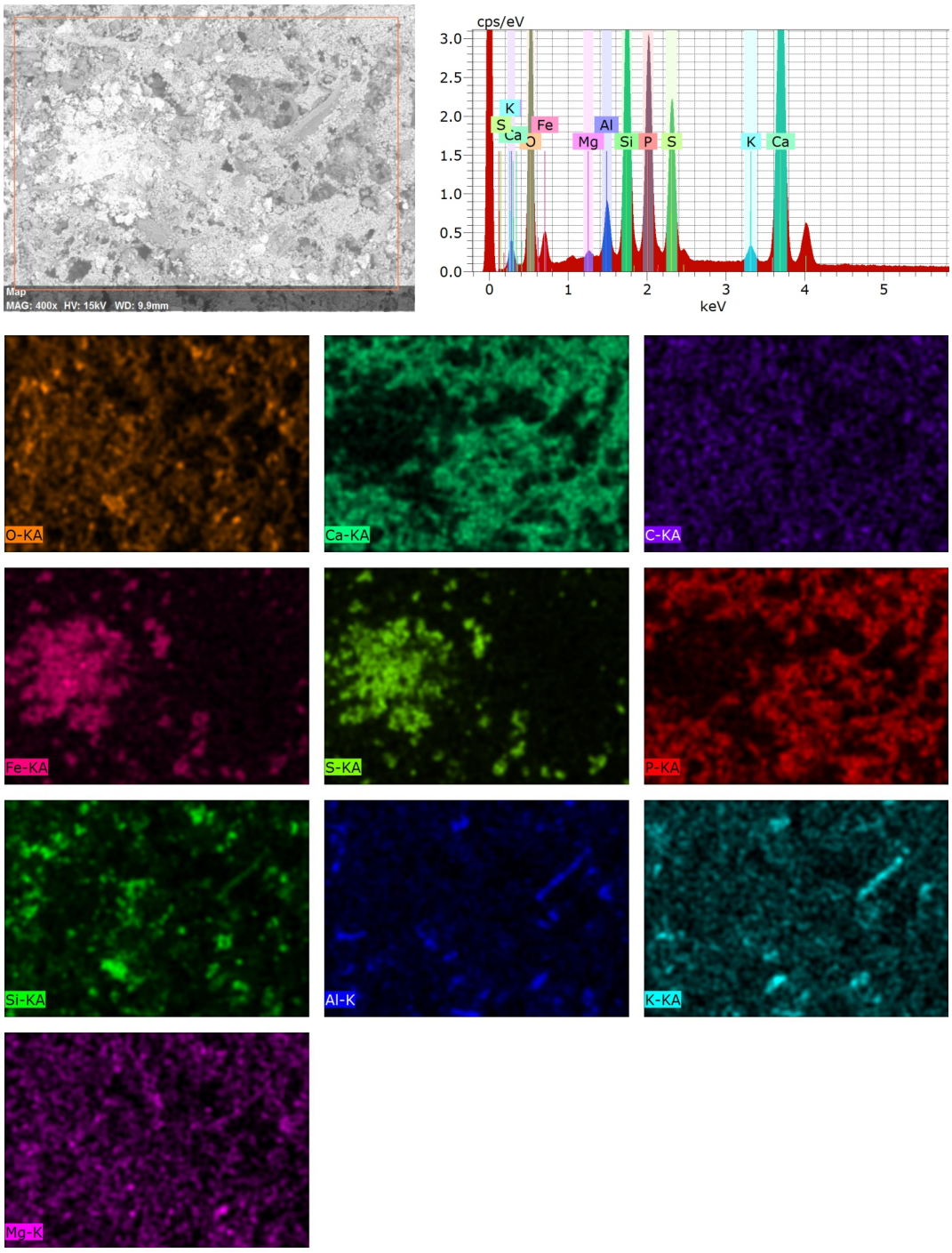

Fig. G.4: SEM-EDS scan of clast (191.75 m) in Figure 3.37B.

REFERENCES

Aigner, T., Reineck, H.-E., 1982. Proximality trends in modern sands from the Heligoland Bight (North Sea) and their implications for basin analysis. Senckenbergiana maritima 14 (5), 183–215.

Algeo, T. J., Hanningan, R., Rowe, H., Brookfield, M., Baud, A., Krystyn, L., Ellwood, B. B., 2007. Sequencing events across the Permian-Triassic boundary, Guryl Ravine (Kashmir, India). Palaeogeography, Palaeoclimatology, Palaeoecology 252, 328–346.

Allen, J. R. L., 1977. The possible mechanics of convolute lamination in graded sand beds. Journal of the Geological Society, London 134, 19–31.

Allen, J. R. L., 2003. Load structures. In: Middleton, G. V. (Ed.), Encyclopaedia of Sediments and Sedimentary Rocks. Kluwer Academic Publishers.

Ames, Jr., L. L., 1959. The genesis of carbonate apatites. Economic Geology 54, 829–841.

Amorosi, A., 1997. Detecting compositional, spatial and temporal attributes of glaucony: a tool for provenance research. Sedimentary Geology 109, 135–153.

Amorosi, A., 2003. Glauconi and verdine. In: Middleton, G. V. (Ed.), Encyclopaedia of Sediments and Sedimentary Rocks. Kluwer Academic Publishers, pp. 331–333.

Arthur, M. A., Sageman, B. B., 1994. Marine black shales: depositional mechanisms and environments of ancient deposits. Annual Review of Earth and Planetary Sciences 22, 499–551.

Basilici, G., de Luca, P. H. V., Poiré, D. G., 2012. Hummocky cross-stratification-like structures and combined-flow ripples in the Punta Negra Formation (Lower-Middle Devonian, Argentine Precordillera): a turbidite deep-water or strom-dominated prodelta inner-shelf system? Sedimentary Geology 267-268, 73–92.

Baskin, D. K., 1997. Atomic (H/C) ratio of kerogen as an estimate of thermal maturity and organic matter conversion. AAPG Bulletin 81 (9), 1437–1450.

Becker, L., 2002. Repeated blows. Scientific American, 62–69.

Becker, L., Porenda, R. J., Hunt, A. G., Bunch, T. E., Rampino, M., 2001. Impact event at the Permian-Triassic boundary: evidence from extraterrestrial noble gases in fullerenes. Science 291 (5508), 1530–1533.

Behar, F., Beaumont, V., Penteado, H. L. D. B., 2001. Rock-Eval 6 technology: performances and developments. Oil & Gas Science and Technology 56 (2), 111–134.

Bennett, M. R., Doyle, P., Mather, A. E., 1996. Dropstones: their origin and significance. Palaeogeography, Palaeoclimatology, Palaeoecology 121, 331–339.

Benton, J. M., Twitchett, J. R., 2003. How to kill (almost) all life: the end-Permian extinction event. Trends in Ecology and Evolution 18 (7), 358–365.

Benton, M. J., 2015. When life nearly died: the greatest mass extinction of all time, revised Edition. Thames & Hudson.

Berner, R. A., 1974. Iron sulfides in Pleistocene deep Black Sea sediments and their paleo-oceanographic significance. In: The Black Sea Geology, Chemistry and Biology. No. 20 in Memoir. AAPG, pp. 524–531.

Berner, R. A., 1982. Burial of organic carbon and pyrite sulfur in the modern ocean: Its geochemical and environmental significance*. American Journal of Science 282, 451–473.

Berner, R. A., 1983. Sedimentary pyrite formation: an update*. Geochimica et Cosmochimica Acta 48, 605–615.

Berner, R. A., Raiswell, R., 1983. Burial of organic carbon and pyrite sulfur in sediments over Phanerozoic time: a new theory. Geochimica et Cosmochimica Acta 47, 855–862.

Berner, R. A., Raiswell, R., 1984. C/S method for distinguishing freshwater from marine sedimentary rocks. Geology 12, 365–368.

Berner, R. A., Westrich, J. T., 1985. Bioturbation and the early diagenesis of carbon and sulfur. American Journal of Science 285, 193–206.

Bhattacharya, J. P., 2003. Deltas and estuaries. In: Middleton, G. V. (Ed.), Encyclopaedia of Sediments and Sedimentary Rocks. Kluwer Academic Publishers, pp. 195–203.

Bhattacharya, J. P., 2010. Deltas. In: Dalrymple, R. G., James, N. P. (Eds.), Facies Models 4. Vol. 6. Geological Association of Canada. Geotext, pp. 233–264.

Bhattacharya, J. P., Walker, R. G., 1989. River- and wave-dominated depositional systems of the Upper Cretaceous Dunvegan Formation, northwestern Alberta. Bulletin of Canadian Petroleum Geology 39 (2), 165–191.

Bjørlykke, K., Høeg, K., 1997. Effects of burial diagenesis on stresses, compaction and fluid flow in sedimentary basins. Marine and Petetroleum Geology 14 (3), 267–276.

Bjørlykke, K., Mo, A., Palm, E., 1988. Modelling of thermal convection in sedimentary basins and its relevance to diagenetic reactions. Marine and Petetroleum Geology 5, 338–251.

Błażejowski, B., 2004. Shark teeth from the Lower Triassic of Spitsbergen and their histology. Polish Polar Research 25 (2), 153–167.

Blomeier, D., Dustria, A., Forke, H., Scheibner, C., 2011. Environmental change in the Early Permian of NE Svalbard: from a war water carbonate platform (Gipshuken Formation) to a temperate, mied siliclastic-carbonate ramp (Kapp Starostin Formation). Facies 57 (3), 493–523.

Bond, D. P. G., Hilton, J., Wignall, P. B., Ali, J. R., Stevens, L. G., Sun, Y.-D., Lai, X.-L., 2010. The Middle Permian (Captinian) mass extinction on land and in the oceans. Earth-Science Reviews 102, 100–116.

Bond, D. P. G., Wignall, P. B., Joachimski, M. M., Sun, Y., Savov, I., Grasby, S. E., Beauchamp, B., Blomeier, D. P. G., 2015. An abrupt extinction in the Middle Permian (Captinian) of the Boreal Realm (Spitsbergen and its link to anoxia and acidification. Geologic Society of America Bulletin 127, 1411–1421.

Bowring, S. A., Erwin, D. H., Jin, Y. G., Martin, M. W., Davidek, K., Wang, W., 1998. U/Pb zircon geochronology and tempo of the end-Permian mass extinction. Science 280, 1039–1045.

Brandano, M., Mateu-Vicens, G., Gianfagna, A., Corda, L., Billi, A., Quaresima, S., Simonetti, A., 2009. Hardground development and drowning of a Miocene carbonate ramp (Latium-Abruzzi): from tectonic to paleoclimate. Journal of Mediterranean Earth Sciences 1, 47–56.

Breit, G. N., Wanty, R. B., 1991. Vanadium accumulation in carbonaceous rocks: a review of geochemical controls during deposition and diagenesis. Chemical Geology 91, 83–97.

Brett, C. E., 1988. Paleoecology and evolution of marine hard substrate communities: An overview. Palaios 3 (4), 374–378.

Bromley, R. G., 1972. On some ichnotaxa in hard substrates, with a redefenition of *Trypanites* Mägdefrau. Paläontologische Zeitschrift 46 (1), 93–98.

Buchan, S. H., Callinor, A., Harland, W. B., Parker, J. R., 1965. The Triassic stratigraphy of Svalbard. Norsk Polarinstitutt Skrifter 135, 1–94.

Calvert, S. E., Pedersen, T. F., 1993. Geochemistry of recent oxic and anoxic marine sediments: implications for the geological record. Marine Geology 113, 67–88.

Campbell, C. V., 1966. Truncated wave-rippled laminae. Journal of Sedimentary Petrology 36 (3), 825–828.

Canfield, D. E., Thamdrup, B., 1994. The production of ^{34}S-depleted sulfide during bacterial disproportionation of elemental sulfur. Science 266 (5193), 1973–1975.

Cheel, R. J., Leckie, D. A., 1993. Hummocky cross-stratification. In: Wright, V. P. (Ed.), Sedimentology Review. No. 1. Blackwell Scientific Publications, Ch. 7, pp. 103–122.

Chen, Z.-Q., Kaiho, K., George, A. D., 2005. Early Triassic recovery of the brachiopod faunas from the end-Permian mass extinction: A global review. Palaeogeography, Palaeoclimatology, Palaeoecology 224, 270–290.

Chinn, W. E., 1991. The role of organic geochemistry in petroleum exploration. Basin Research Institure Bulletin, 15–23.

Choquette, P. W., Pray, L. C., 1970. Geologic nomenclature and classification of porosity in sedimentary carbonates. The American Association of Petroleum Geologists Bulletin 54 (2), 207–250.

Clapham, M. E., Shen, S.-Z., Bottjer, D. J., 2009. The double mass extinction revisited: reassessing the severity, selectivity and causes of the end-Guadalupian biotic crisis (Late Permian). Paleobiology 35, 32–50.

Clifton, H. E., Hubter, R. E., Phillips, R. L., 1971. Depositional structures and processes in the non-barred high-energy nearshore. Journal of Sedimentary Petrology 41 (3), 651–670.

Cohen, K. M., Finney, S. C., Gibbard, P. L., Fan, J.-X., 2013. The ics international chronostratigraphic chart. Episodes 36 (3), 199–204.

Coleman, J. M., Roberts, H. H., Stone, G. W., 1998. Missisippi River delta: an overview. Journal of Coastal Research 14 (3), 698–716.

Dallmann, W. K. (Ed.), 2015. Geoscience Atlas of Svalbard. No. 148 in Report Series. Norwegian Polar Institute.

Dar, A., Laor, A., Shaviv, N. J., 1998. Life extinctions by cosmic ray jets. Physical Review Letters 80 (26), 5813–5816.

Davis, R. A., 1965. Underwater study of ripples, southeaster Lake Michigan. Journal of Sedimentary Petrology 35 (4), 857–866.

DeCelles, P. G., Cavazza, W., 1992. Constraints on the formation of Pliocene hummocky cross-stratification in Calabriia (Southern Italy) from consideration of hydraulic and dispersive equivalence, grain-flow theory, and suspended-load fallout rate. Journal of Sedimentary Petrology 62 (4), 555–568.

Dembicki, H., 2009. Three common source rock evaluation errors made by geologists during prospect or play appraisals. AAPG Bulletin 93 (3), 341–356.

Diasty, W. S., Beialy, S. Y. E., Mostafa, A. R., Ghonaim, A. A. A., Peters, K. E., 2015. Crude oil geochemistry and source rock potential of the

upper cretaceous-euocene succession in the Belayim oifields, Central Gulf of Suez, Egypt. Journal of Petroleum Geology 38 (2), 193–216.

Dietz, R. S., Holden, J. C., 1970. Reconstruction of Pangea: Breakup and dispersion of continents, Permian to present. Journal of Geophysical Research 75 (26), 4939–4956.

Doré, A. G., 1991. The structural foundation and evolution of Mesozoic seaways between Europe and the Arctic. Palaeogeography, Palaeoclimatology, Palaeoecology 87, 441–492.

Dott, R. H., Bourgeois, J., 1982. Hummocky stratification: Significance of its variable bedding sequences. Geologic Society of America Bulletin 93, 663–680.

Doyle, L. J., Garrels, R. M., 1985. What does percent organic carbon in sediments measure? Geo-Marine Letters 5, 51–53.

Duke, W. L., Arnott, R. W. C., Cheel, R. J., 1991. Shelf sandstones and hummocky cross-stratification: New insights on a stormy debate. Geology 19, 625–628.

Dunham, R. J., 1962. Classification of carbonate rocks according to depositional textures. In: Ham, W. E. (Ed.), Classification of carbonate rocks - a symposium. American Assoiciation of Petrolem Geologists, pp. 108–121.

Dunham, R. J., 1969. Early vadose silt in Townsend Mound (reef), New Mexico. In: Friedman, G. M. (Ed.), Depositional Environments in Carbonate Rocks: a Symposium. Vol. 14. Special Publications of SEPM, pp. 139–181.

Dustria, A. M., Wignall, P. B., Joachimski, M., Blomeier, D., Hartkopf-Fröder, C., Bond, D. P. G., 2013. Gradual onset of anoxia across the Permian-Triassic boundary in Svalbard, Norway. Palaeogeography, Palaeoclimatology, Palaeoecology 374, 303–313.

Dzulynski, S., Smith, A. J., 1963. Convolute lamination, its origin, preservation, and directional significance. Journal of Sedimentary Petrology 33 (3), 616–627.

Ehrenberg, S. N., Pickard, N. A. H., Henriksen, L. B., Svånå, T. A., Gutteridge, P., Macdonald, D., 2001. A depositional and sequence stratigraphic model for cold-water, spiculitic strata based on the Kapp Starostin Formation (Permian) of Spitsbergen and equivalent deposits from the Barents Sea. AAPG Bulletin 85 (12), 2061–2087.

Einsele, G., 2000. Sedimentart Basins: Evolution, Facies and Sediment Budget, 2nd Edition. Springer-Verlag.

Ellis, J., Fields, B. D., Schramm, D. N., 1996. Geological isotope anomalies as signatures of nearby supernovae. Astrophysical Journal 470, 1227–1236.

Embry, A. F., Klovan, J. E., 1971. A late Devonian reef tract on Northeastern Banks Island, N.W.T. Bulletin of Canadian Petroleum Geology 19 (4), 730–781.

Erwin, D. H., 1993. The great Paleozoic crisis: life and death in the Permian. Columbia University Press.

Erwin, D. H., 1994. The Permo-Triassic extinction. Nature 367, 231–235.

Erwin, D. H., 2015. Extinction: how life on earth nearly ended 250 million years ago, updated Edition. Princeton University Press.

Espitalie, J., Madec, M., Tissot, B., Menning, J. J., Leplat, P., 1977. Source rock characterization method for petroleum exploration. In: Offshore Technology Conference. pp. 439–444.

Fagerstrom, J. A., 1967. Development, flotation, and transportation of mud crusts - neglected factors in sedimentology. Journal of Sedimentary Petrology 37 (1), 73–79.

Flügel, E., 2010. Microfacies of carbonate rocks: Analysis, interpretation and application. Springer-Verlag, pp. 206–211.

Föllmi, K. B., 196. The phosphorus cycle, phosphogenesis and marine phosphate-rich deposits. Earth-Science Reviews 40 (55-124).

Fossilworks, 2015. *Hybodus sp.* http://fossilworks.org/bridge.pl?a=taxonInfo&taxon_no=34498 (accessed October 10th, 2015).

Gadov, S., Reineck, H. E., 1969. Ablandiger sandtransport bei sturmfluten. Senckenbergiana maritima 1, 63–78.

Galfetti, T., Bucher, H., Brayard, A., Hochuli, P. A., Weissert, H., Guodun, K., Atudorei, V., Guex, J., 2007a. Late Early Triassic climate change: insights from carbonate carbon isotopes, sedimentary evolution and ammonoid paleobiogeopgraphy. Palaeogeography, Palaeoclimatology, Palaeoecology 243, 394–411.

Galfetti, T., Bucher, H., Ovtcharova, M., Shaltegger, U., Brayard, A., Brühwiler, T., Goudemand, N., Weissert, H., Hochuli, P. A., Cordey, F.,

Guodun, K., 2007b. Timing of the Early Triassic carbon cycle perturbations inferred from new U-Pb ages and ammonoid biochronozones. Earth and Planetary Science Letters 258, 593–604.

Galfetti, T., Hochuli, P. A., Brayard, A., Bucher, H., Weissert, H., Vigran, J. O., 2007c. Smithian-Spathian boundary event: evidence for global climatic change in the wake of the end-Permian biotic crisis. Geology 35, 291–294.

Gischler, E., 2003. Beach rock. In: Middleton, G. V. (Ed.), Encyclopaedia of Sediments and Sedimentary Rocks. Kluwer Academic Publishers, pp. 71–82.

Glenn, C. R., Garrison, R. E., 2003. Phosphorites. In: Middleton, G. V. (Ed.), Encyclopaedia of Sediments and Sedimentary Rocks. Kluwer Academic Publishers.

Glørstad-Clark, E., Faleide, J. I., Lundschien, B. A., Nystuen, J. P., 2010. Triassic seismic sequence stratigraphy and paleogeograpy of the western Barents Sea area. Marine and Petetroleum Geology 27, 1448–1475.

Grasby, S. E., Beauchamp, B., Embry, A., Sanei, H., 2013. Recurrent Early Triassic ocean anoxia. Geology 41 (2), 175–178.

Groves, J. R., Wang, Y., 2013. Timing and size selectivity of the Guadalupian (Middle Permian) fusulinoidean extinction. Journal of Paleontology 87, 183–196.

Gruszczyński, M., Halas, S., Hoffman, A., Malkowski, K., 1989. A brachiopod calcite record of the oceanic carbon and oxygen isotope shifts at the Permian/Triassic transition. Nature 337, 64–68.

Gudlaugsson, S. T., Faleide, J. I., Johansen, S. E., Breivik, A. J., 1998. Late Palaeozoic structural development of the south-western Barents Sea. Marine and Petetroleum Geology 15 (73-102).

Habicht, K. S., Canfield, D. E., 2001. Isotope fractionation by sulfate-reducing natural populations and the isotopic composition of sulfide in marine sediments. Geology 29 (6), 555–558.

Hagadorn, J. W., Bottjer, D. J., 1997. Wrinkle structures: microbially mediated sedimentary structures common in subtidal siliclastic settings at the Proterozoic - Phanerozoic transition. Geology 25 (11), 1047–1050.

Hallam, A., 1991. Why was there a delayed radiation after the end-Palaeozoic extinction? Historical Biology 5, 257–262.

Hansen, J., Nielsen, J. K., Hanken, N.-M., 2009. The relationships between Late Ordovician sea-level changes and faunal turnover in western Baltica: geochemical evidence of oxic and dysoxic bottom-water conditions. Palaeogeography, Palaeoclimatology, Palaeoecology 271, 268–278.

Harfield, C. B., Camp, M. J., 1970. Mass extinctions correlated with periodic galactic events. Geologial Society of America Bulletin 81, 911–914.

Harland, W. B. (Ed.), 1997. The Geology og Svalbard. No. 17 in Memoir. Geological Society London.

Harms, J. C., 1979. Primary sedimentary structures. Annual Review of Earth and Planetary Sciences 7, 227–248.

Harms, J. C., Southard, J. B., Spearing, D. R., Walker, R. G., 1975. Depositional environments as interpreted from primary sedimentary structures and stratification sequences. In: Short Course. No. 2. S. E. P. M.

Hatch, J. R., Leventhal, J. S., 1992. Relationship between inferred redox potential of the depositional environment and geochemistry of the Upper Pennsylvanian (Missourian) Sark Shale Member of the Dennis Limestone, Wabaunsee County, Kansas, U.S.A. Chemical Geology 99, 65–82.

Hayes, M. O., 1980. General morphology and sediment patterns in tidal inlets. Sedimentary Geology 26, 139–156.

Hochuli, P. A., Hermann, E., Vigran, O. J., Bucher, H., Weissert, H., 2010. Rapid demise and recovery of plant ecosystems across the end-Permian extinction-event. Global and Planetary Change 74, 144–155.

Hoffman, D. L., Algeo, T. J., Maynard, J. B., Joachimski, M. M., Hower, J., Jaminski, J., 1998. Regional and strategraphical variation in bottom-water anoxia in the offshore core shales of Upper Pennsylvanian cyclotherms from eastern midcontinent shelf (Kansas), U.S.A. In: Schieber, J., Zimmerle, W., Sethi, O. (Eds.), Shales and Mudstones. Schweizerbart'che Verlagsbuchandlung (Nägele u.Obermiller), Stuttgart, pp. 243–269.

Holser, W. T., Schönlaub, H.-P., Jr, M. A., Boeckelmann, K., Klein, P., Magaritz, M., Orth, C. J., Fenninger, A., Jenny, C., Kralik, M., Mauritsch, H., Pak, E., Schramm, J., Stattegger, K., Schmöller, R., 1989. A unique geochemical record at the Permian/Triassic boundary. Nature 337, 39–44.

Hongfu, Y., Kexin, Z., Jinnan, T., Zunyi, Y., Shunbao, W., 2001. The global stratotype section and point (GSSP) of the Permian-Triassic boundary. Episodes 24 (2), 102–114.

Horacek, M., Brandner, R., Abart, R., 2007a. Carbon isotope record of the P/T boundary and the Lower Triassic in the southern Alps: evidence for rapid changes in storage of organic carbon. Palaeogeography, Palaeoclimatology, Palaeoecology 252 (347-354).

Horacek, M., Koike, T., Richoz, S., 2009. Lower Triassic $\delta^{13}C$ isotope curve from shallow-marine carbonates in Japan, Panthalassa realm: confirmation of the Tethys $\delta^{13}C$ curve. Journal of Asian Earth Sciences 36 (481-490).

Horacek, M., Richoz, S., Brandner, R., Krystyn, L., Spötl, C., 2007b. Evidence for recurrent changes in Lower Triassic oceanic circulation of the Tethys: The $\delta^{13}c$ record from marine sections in Iran. Palaeogeography, Palaeoclimatology, Palaeoecology 252, 355–369.

Hounslow, M., Peters, C., Mørk, A., Weitschat, W., Vigran, J. O., 2014. Biomagnetostratigraphy of the Vikinghøgda Formation, Svalbard (Arctic Norway), and the geomagnetic polarity timescale for the Lower Triassic. Geologic Society of America Bulletin 120, 1305–1325.

Hounslow, M. W., Nawrocki, J., 2008. Palaeomagnetism and magnetostratigraphy of the Permian and Triassic of Spitsbergen; a review of progress and challenges. Polar Research 27, 502–522.

Huc, A. Y., Nederlof, P., Debarre, R., Carpentier, B., Boussafir, M., Laggoun-Défarge, F., Lenail-Chouteau, A., Floch, N. B.-L., 2000.

Pyrobitumen occurrence and formation in a Cambro-Ordovician sandstone reservoir, Fahud Salt Basin, North Oman. Chemical Geology 168, 99–112.

Hunter, R. E., Clifton, E. H., 1982. Cyclic deposits and hummocky cross-stratification of probable storm origin in Upper Cretaceous rocks of the Cape Sebastian area, southwestern Oregon. Journal of Sedimentary Petrology 62, 127–143.

Ibach, L. E. J., 1982. Relationship between sedimentation rate and total organic carbon content in ancient marine sediments. AAPG Bulletin 66 (2), 170–188.

J. John Sepkoski, J., 1989. Periodicity in extinction and the problem of catastrophism in the history of life. Journal of the Geological Society, London 146, 7–19.

Jeppson, L., Anehus, R., Fredholm, D., 1999. The optimal acetate buffered acetic acid technique for extracting phospathe fossils. Journal of Paleontology 73 (5), 964–972.

Jin, Y. G., Wang, Y., Wang, W., Shang, Q. H., Cao, C. Q., Erwin, D. H., 2000. Patterns of marine mass extinction near the Permian-Triassic boundary in south China. Science 289, 432–436.

Jin, Y.-G., Zhang, J., Shang, Q.-H., 1994. Two phases of the end-Permian mass extinction. In: Embry, A. F., Beauchamp, B., Glass, D. J. (Eds.), Pangea: Globsl Environments and Resources. Canadian Society of Petroleum Geologists Memoir 17, pp. 813–822.

Johnsen, S., 1980. A sedimentary, paleontological and paleoecological investigation of Lower Triassic outcrops on the west coast of Spitsbergen, Svalbard, unpublished Cand. Scient. thesis, University of Oslo.

Jørgensen, B. B., 1994. A thiosulfate shunt in the sulfur cycle of marine sediments. Science 249 (4965), 152–154.

Kaiho, K., Kajiwara, Y., Nakano, T., Miura, Y., Kawahata, H., Tazaki, K., Ueshima, M., Chen, Z., Shi, G. R., 2001. End-Permian catastrophe by a bolide impact: evidence of gigantic release of sulfur from the mantle. Geology 29 (9), 815–818.

Karcz, P., 2014. Depositional conditions and petroleum potential of the Middle Triassic Passhatten Member (Bravaisberget Formation), Spitsbergen. Polish Polar Research 35 (1), 41–71.

Kasioptas, A., Perdikouri, C., Putnis, C. V., Putnis, A., 2008. Pseudomorphic replacement of single calcium carbonate crystals by polycrystalline apatite. Mineralogical Magazine 72 (1), 77–80.

Katz, B. J., 2005. Controlling factors on source rock development - a review of productivity, preservation, and sedimentation rate. In: The Deposition of Organic-Carbon-Rich Sediments: Models, Mechanisms, and Consequences. No. 82 in Special Publications of SEPM. pp. 7–16.

Kidder, D. L., Worsley, T. R., 2004. Causes and consequences of extreme Permo-Triassic warming to globally equable climate and relation to the Permo-Triassic extinction and recovery. Palaeogeography, Palaeoclimatology, Palaeoecology 203, 207–237.

Knoll, A. H., Bambach, R. K., Payne, J. L., Pruss, S., Fischer, W. W., 2007. Paleophysiology and end-Permian mass extinction. Earth and Planetary Science Letters 256, 295–313.

Knoll, A. H., Hayes, J. M., Kaufman, A. J., Swett, K., Lambert, I. B., 1986. Secular variation in carbon isotope ratios from Upper Proterozoic successions of Svalbard and East Greenland. Nature 321, 832–838.

Korte, C., Kozur, H. W., 2010. Carbon-isotope stratigraphy across the Permian-Triassic boundary: a review. Journal of Asian Earth Sciences 39, 215–235.

Krajewski, K. P., 2000. Phosphogenic facies and processes in the Triassic of Svalbard. Studia Geologicoa Plonica 116, 7–84.

Krajewski, K. P., 2008. The Botnheia Formation (Middle Triassic) in Edgeøya and Barentsøya, Svalbard: lithostratigraphy, facies, phosphogenesis, paleoenvironment. Polish Polar Research 29 (4), 319–364.

Krajewski, K. P., Cappellen, P. V., Trichet, J., Kuhn, O., Lucas, J., Martín-Algarra, A., Prévôt, L., Tewari, V. C., Gaspar, L., Knight, R. I., Lamboy, M., 1994. Biological processes and apatite formation in sedimentary environments. Eclogae Geologicae Helvetiae 3, 701–745.

Krajewski, K. P., Karcz, P., Woźny, E., Mørk, A., 2007. Type section of the Bravaisberget Formation (Middle Triassic) at Bravaisberget, western Nathorst Land, Spitsbergen, Svalbard. Polish Polar Research 28 (2), 79–122.

Krasil'ščikov, A. A., Livšic, J. J., 1974. Tektonika ostrova Medvežij (Tectonics of Bjørnøya). Geotektonika, 39–51.

Kristensen, E., Ahmed, S. I., Devol, A. H., 1995. Aerobic and anaerobic decomposition of organic matter in marine sediment: which is fastest? Limnology and Oceanography 40 (8), 1430–1437.

Krull, E. S., Lehrmann, D. J., Druke, D., Kessel, B., Yu, Y., Li, R., 2004. Stable carbon isotope stratigraphy across the Permian-Triassic boundary in shallow marine carbonate platforms, Nanpanjiang Basin, south China. Palaeogeography, Palaeoclimatology, Palaeoecology 204, 297–315.

Labandeira, C. C., Sepkoski, J. J., 1993. Insect diversity in the fossil record. Science 261, 310–315.

Langford, F. F., Blanc-Valleron, M. M., 1990. Interpreting Rock-Eval pyrolysis data using graphs of pyrolizable hydrocarbons vs. total organic carbon. The American Association of Petroleum Geologists Bulletin 74 (6), 799–804.

Law, C. A., 1999. Evaluating source rocks. In: Beaumont, E. A., Foster, N. H. (Eds.), Treatise of Petroleum Geology / Handbook of Petroleum Geology: Exploring for Oil and Gas Traps. American Assoiciation of Petrolem Geologists, Ch. 6, pp. 6,1–6,41.

Leeder, M., 2011. Sedimentology and Sedimentary Basins - From Turbulence to Tectonics, 2nd Edition. Wiley Blackwell, Ch. 7, pp. 158–159.

Leventhal, J. S., 1983. An interpretation of carbon and sulfur relationships in Black Sea sediments as indicators of environments of deposition. Geochimica et Cosmochimica Acta 47, 133–137.

Leventhal, J. S., 1995. Carbon-sulfur plots to show diagenetic and epigenetic sulfidation in sediments. Geochimica et Cosmochimica Acta 59 (6), 1207–1211.

Lewan, M., 1984. Factors controlling the proportinality of vanadium to nickel in crude oils. Geochimica et Cosmochimica Acta 48, 2231–2238.

Lewan, M., Maynard, J. B., 1982. Factors controlling enrichment of vanadium and nickel in the bitumen of organic sedimentary rocks. Geochimica et Cosmochimica Acta 46, 2547–2560.

Lofek, M., 2012. Skamieniałości śladowe z utworów permu i triasu wysp Akseløya i Mariaholmen, Svalbard Zachodni (Trace fossils from the Permian and Triassic sediments of the Akseløya and Mariaholmen islands, West Svalbard). Master's thesis, Uniwersytet Jagielloński w Krakowie.

Lundschien, B. A., Høy, T., Mørk, A., 2014. Triassic hydrocarbon potential in the Northern Barents Sea; integrating Svalbard and stratigraphic core data. Norwegian Petroleum Directorate Bulletin 11, 3–20.

Lynch, J., 1990. Provisional elemental values for eight new geochemical lake sediment and stream sediment reference materials LKSD-1, LKSD-2. LKSD-3, LKSD-4, STSD-1, STSD-2, STSD-3 and STSD-4. Geostandards Newsletter 14 (1), 153–167.

MacEachern, J. A., Bann, K. L., Pemberton, G., Gingras, M. K., 2007. The ichnofacies paradigm: High-resolution paleoenvironmental interpretation of the rock record. In: SEPM Short Course 52. pp. 27–64.

Macintyre, I. G., Reid, R. P., 2003. Micritization. In: Middleton, G. V. (Ed.), Encyclopaedia of Sediments and Sedimentary Rocks. Kluwer Academic Publishers, pp. 436–438.

Maher, H. D., Craddock, C., Maher, K., 1986. Kinematics of Tertiary structures in upper Paleozoic and Mesozoic strata on Midterhuken, west Spitsbergen. Geologic Society of America Bulletin 97, 1411–1421.

Manum, S. B., Throndsen, T., 1978. Rank of coal and dispersed organic matter and its geological bearing in the Spitsbergen Tertiary. Norsk Polarinstitutt Årbok 1977, 159–177.

Mariotti, G., Pruss, S. B., Perron, J. T., Bosak, T., 2014. Microbial shaping of sedimentary wrinkle structures. Nature Geoscience 7, 736–740.

Mata, S. A., Bottjer, D. J., 2009. The paleoenvironmental distribution of Phanerozoic wrinkle structures. Earth-Science Reviews 96, 181–195.

McCubbin, D. G., 1982. Barrier-island and strand-plain facies. In: Scholle, P. A., Spearing, D. (Eds.), Sandstone Depositional Environments. Vol. 31 of Memoir. AAPG, pp. 247–279.

Meyer, K. M., Yu, M., Lehrmann, D., van de Schootbrugge, B., Payne, J. L., 2013. Constraints on early triassic carbon cycle dynamics from paired organic and inorganic carbon isotope records. Earth and Planetary Science Letters 361, 429–435.

Miles, J. A., 1989. Illustrated glossary of petroleum geochemistry. Clarendon Press, p. 105.

Miller, C. B., Wheeler, P. A., 2012. Biological oceanography. John Wiley & Sons, p. 186.

Møller, L. N. N., Friis, H., 1999. Petrographic evidence for hydrocarbon migration in Lower Cambrian sandstones, Bornholm, Denmark. Bulletin of the Geological Society of Denmark 45 (117-127).

Mørk, A., 1994. Triassic transgressive-regressive cycles of Svalbard and other Arctic areas: a mirror of stage subdivision. In: Guex, G., Baud, A. (Eds.), Recent developments on Triassic stratigraphy. Mémories de Géologie (Lausanne), pp. 69–82.

Mørk, A., Dallmann, W. K., Dypvik, H., Johannesen, E. P., Larsen, G. B., Nagy, J., Nøttvedt, A., Olaussen, S., Pchelina, T. M., Worsley, D., 1999a. Mesozoic lithostratigraphy. In: Dallmann, W. K. (Ed.), Lithostratigraphic lexicon of Svalbard. Upper Palaeozoic to Quarternary bedrock. Review and recommendations for nomenclature use. Norwegian Polar Institute, Tromsø, pp. 127–213.

Mørk, A., Egorov, A. Y., Embry, A. F., 1994. Base Olenekian and base Anisian sequence boundaries produced Triassic circumpolar "synchronous" transgressions. In: Thurston, D. K., Fujita, K. (Eds.), 1992 proceedings, International Conference on Arctic Margins : Anchorage, Alaska, September 1992. pp. 9–14.

Mørk, A., Elvebakk, G., 1999. Lithological description of subcropping Lower and Middle Triassic rocks from the Svalis Dome, Barents Sea. Polar Research 18 (1), 83–104.

Mørk, A., Elvebakk, G., Forsberg, A. W., Hounslow, M. W., Nakrem, H. A., Vigran, J. O., Weitschat, W., 1999b. The type section of the Vikinghøgda Formation: a new Lower Triassic unit in central and eastern Svalbard. Polar Research 18 (1), 51–82.

Mørk, A., Embry, A. F., Weitschat, W., 1989. Triassic transgressive-regressive cycles in the Sverdrup Basin, Svalbard and the Barents Shelf. In: Collinson, J. D. (Ed.), Correlation in Hydrocarbon Exploration. Graham & Trotman, London, pp. 113–130.

Mørk, A., Knarud, R., Worsley, D., 1982. Depositional and diagenetic environments of the Triassic and Lower Jurassic succession of Svalbard. In: Embry, A. F., Balkwill, H. R. (Eds.), Artic geology and geophysics: proceedings of the Third International Symposium on Arctic Geology. Vol. 8. pp. 371–398.

Morsilli, M., Pomar, L., 2012. Internal waves vs. surface storm waves: a review on the origin of hummocky cross-stratification. Terra Nova 24, 273–282.

Mozley, P. S., 1989. Relation between depositional environment and the elemental composition of early diagenetic siderite. Geology 17, 704–706.

Musashi, M., Isozaki, Y., Koike, T., Kreulen, R., 2001. Stable carbon isotope signature in mid-Panthalassa shallow-water carbonates across the Permo-Triassic boundary: evidence for δ^{13}C-depleted superocean. Earth and Planetary Science Letters 191, 9–20.

Mutti, M., Bernoulli, D., 2003. Early marine lithification and hardground development on a Miocene ramp (Maiella, Italy): Key surfaces to track changes in trophic resources in nontropical carbonate settings. Journal of Sedimentary Research 73 (2), 296–308.

Myrow, P. M., Southard, J. B., 1996. Tempestite deposition. Journal of Sedimentary Research 66 (5), 875–887.

Nakrem, H. A., Ernst, A., 2008. Arcticoporidae Fam. Nov. (Bryozoa, Trepostomata) from the Lower Triassic of Ellesmere Island (Canada) with remarks on some other Triassic Bryozoans. In: Winston, J. E., Key, M. M., Hageman, J., Hageman, S. J. (Eds.), 14th International Bryozology Association Conference Volume, Special Publication Series. Virginia Museum of Natural History Press.

Nakrem, H. A., Mørk, A., 1991. New early Triassic Bryozoa (Trepostomata) from Spistbergen, with some remarks on the stratigraphy of the investigated horizons. Geolgical Magazine 128 (2), 129–140.

Nakrem, H. A., Orchard, M. J., Wolfgang, W., Hounslow, M. W., Beatty, T. W., Mørk, A., 2008. Triassic conodonts from Svalbard and their Boreal correlations. Polar Research 27, 523–539.

Nelson, C. H., 1982. Modern shallow-water graded sand layers from stor surges, Bering shelf: A mimic of bouma sequences and turbidite systems. Journal of Sedimentary Petrology 52 (2), 537–545.

Nichols, G., 2009. Sedimentology and Stratigraphy. Wiley Blackwell.

Nielsen, J. K., Shen, Y., Piasecki, S., Stemmerik, L., 2010. No abrupt change in redox condition caused the end-Permian marine ecosystem collapse in the East Greenland Basin. Earth and Planetary Science Letters 291, 32–38.

Noffke, N., Gerdes, G., Krumbein, T. K. N. W. E., 2001. Microbially induced sedimentary structures - a new category within the classification of primary sedimentary structures. Journal of Sedimentary Research 71 (5), 649–656.

Noffke, N., Knoll, A. H., Grotzinger, J. P., 2002. Sedimentary controls on the formation and preservatuin if microbial mats in siliclastic deposits: a case study from the upper Neoporoterozoic Nama Group, Namibia. Palaios 17 (6), 533–544.

Nwachukwu, J. I., Barker, C., 1985. Variations in kerogen densities of sediments from the Oringco delta, Venezuela. Chemical Geology 51, 193–198.

Nwachukwu, J. I., Chukwura, P. I., 1986. Organic matter of Agbada Formation, Niger Delta, Nigeria. AAPG Bulletin 70 (1), 48–55.

Oehlert, A. M., Swart, P. K., 2014. Interpreting carbonate and organic carbon isotope covariance in the sedimentary record. Nature Communications 5 (4672).

Oertel, G. F., 1985. The barrier island system. Marine Geology 63, 1–18.

Olariu, C., Bhattacharya, J. P., 2006. Terminal distributary channels and delta front architecture of river-dominated delta systems. Journal of Sedimentary Research 76, 212–233.

Owen, G., 1987. Deformation processes in unconsolidated sands. In: Jones, M. E., Preston, R. M. F. (Eds.), Deformation of Sediments and Sedimentary Rocks. No. 29. Geological Society Special Publication, pp. 11–24.

Owen, G., 2003. Ball-and-pillow (pillow) structures. In: Middleton, G. V. (Ed.), Encyclopaedia of Sediments and Sedimentary Rocks. Kluwer Academic Publishers, pp. 39–40.

Payne, J. L., Lehrmann, D. J., Wei, J., Orchard, M. J., Schrag, D. P., Knoll, A. H., 2004. Large perturbations of the carbon cycle during recovery from the end-Permian extinction. Science 305 (506-509).

Pčelina, T. M., 1983. Novye dannye po stratigrafii mezozoja archipelaga Špisbergen (New material on the Mesozoic stratigraphy of the Spitsbergen Archipelago). In: Krasilnikov, A. A., Basov, V. (Eds.), Geologija Špisbergen. PGO Sevmorgeologija, Leningrad, pp. 121–141.

Pemberton, S. G., 2003. Biogenic sedimentary structures. In: Middleton, G. V. (Ed.), Encyclopaedia of Sediments and Sedimentary Rocks. Kluwer Academic Publishers, pp. 71–82.

Penland, S., Boyd, R., Suter, J. R., 1988. Transgressive depositional systems of the Mississippi delta plain: a model for barrier shoreline and shelf sand development. Journal of Sedimentary Petrology 58 (6), 932–949.

Peters, K. E., 1986. Guidelines for evaluating petroleum source rock using programmed pyrolysis. The American Association of Petroleum Geologists Bulletin 7 (3), 318–329.

Peters, K. E., Cassa, M. R., 1994. Applied source rock geochemistry. In: Magoon, L. B., w. G. Dow (Eds.), The petroleum system - from source to trap. No. 60 in AAPG Memoir. AAPG.

Peters, S. E., Loss, D. P., 2012. Storm and fair-weather wave base: a relevant distinction? Geology 40 (6), 511–514.

Pettijohn, F. J., Potter, P. E., Siever, R., 1987. Sand and Sandstone, 2nd Edition. Springer-Verlag.

Porada, H., Ghergut, J., Bouougri, E. H., 2008. Kinneyia-type wrinkle structures - critical review and model of formation. Palaios 23, 65–77.

Pruss, S., Fraiser, M., Bottjer, D. J., 2004. Proliferation of Early Triassic wrinkle structures: implications for environmental stress following the end-Permian mass extinction. Geology 32 (5), 461–464.

Raiswell, R., 1976. The microbiological formation of carbonate concretions in the Upper Lias of NE England. Chemical Geology 18, 227–244.

Raiswell, R., Al-Biatty, H. J., 1989. Depositional and diagenetic C-S-Fe signatures in early Paleozoic normal marine shales. Geochimica et Cosmochimica Acta 53, 1147–1152.

Raiswell, R., Berner, R. A., 1986. Pyrite and organic matter Phanerozoic normal marine shales. Geochimica et Cosmochimica Acta 50, 1967–1976.

Raiswell, R., Berner, R. A., 1987. Organic carbon losses during burial and thermal maturation of normal marine shales. Geology 15, 853–856.

Raiswell, R., Fisher, Q. J., 2000. Mudrock-hosted carbonate concretions: a review of growth mechanisms and their influence on chemical and isotopic composition. Journal of the Geological Society, London 157, 239–251.

Ramberg, I. B., Bryhni, I., Nøttvedt, A., 2007. Landet blir til: Norges Geologi. Norges Geologiske Forening.

Ravna, E. K., 2011. X-ray fluorescence spectrometry and sample preparation. Department of Geology, University of Tromsø.

Reichow, M. K., Pringle, M. S., Al'Mukhamedov, A. I., Allen, M. B., Andreichev, V. L., Buslov, M. M., Davies, C. E., Fefoseev, G. S., Fitton, J. G., Inger, S., Medvedev, A. Y., Mitchell, C., Puchkov, V. N., Safonova, I. Y., Scott, R. A., Saunders, A. D., 2009. The timing and extent of the eruption of the Siberian Traps large igneous province: implications for the end-Permian environmental crisis. Earth and Planetary Science Letters 277, 9–20.

Reineck, H. E., Singh, I. B., 1986. Depositional Sedimentary Environments. Springer-Verlag.

Reinson, G. E., 1979. Facies models 14. Barrier island systems. Geoscience Canada 6 (2), 51–68.

Renne, P. R., Basu, A. R., 1991. Rapid eruption of the Siberian Traps flood basalts at the Permo-Triassic boundary. Science, New Series 253 (5016), 176–179.

Riis, F., Lunschien, T., Høy, T., Mørk, A., Mørk, M., 2008. Evolution of the Triassic shelf in the northern Barents Sea region. Polar Research 27, 318–338.

Rimmer, S. M., Thompson, J. A., Goodnight, S. A., Robl, T. L., 2004. Multiple controls on the preservation of organic matter in Devonian-Mississippian marine black shales: geochemical and petrographic evidence. Palaeogeography, Palaeoclimatology, Palaeoecology 215, 125–154.

Ritzmann, O., Jokat, W., Mjelde, R., Shimamura, H., 2002. Crustal structure between the Knipovich Ridge and the Van Mijenfjorden (Svalbard). Marine Geophysical Researches 23, 379–401.

Roberts, H. H., 1997. Dynamic changes of the Holocene Mississippi River delta plain: the delta cylce. Journal of Coastal Research 13 (3), 605–627.

Roberts, H. H., 1998. Delta Switching: early responses to the Atchafalaya river diversion. Journal of Coastal Research 14 (3), 882–899.

Roberts, H. H., Sydow, J., 2003. Late Quarternary stratigraphy and sedimentology of the offshore Mahakam delta, east Kalimantan (Indonesia). In: Tropical Deltas of Souteast Asia - Sedimentology, Stratigraphy and Petroleum Geology. No. 76 in Special Publications. SEPM, pp. 125–145.

Rothman, D. H., Hayes, J. M., Summons, R. E., 2003. Dynamics of the Neoproterozoic carbon cycle. Proceedings of the National Academy of Sciences 100 (14), 8124–8129.

Sahney, S., Benton, M. J., 2008. Recovery from the most profound mass extinction of all time. Proceedings of the Royal Society B 275, 759–765.

Salamon, M. A., Gorzelak, P., Hanken, N.-M., Riise, H. E., Ferré, B., 2015a. Crinoids from Svalbard in the aftermath of the end-Permian mass extinction. Polish Polar Research 36 (3), 225–238.

Salamon, M. A., Gorzelak, P., Hanken, N.-M., Riise, H. E., Ferré, B., 2015b. Unexpectedly diverse Crinoid fauna from Svalbard in the af-

termath of the End-Permian mass extinction. In: Abstracts with Programs. Vol. 47. Geological Society of America, p. 765.

Saltzman, M. R., Sedlacek, A. R. C., 2013. Chemostratigraphy indicates a relatively complete Late Permian to Early Triassic sequence in the western United States. Geology 41 (4), 399–402.

Sawlowicz, Z., 1993. Pyrite framboids and their development: a new conceptual mechanism. Geologische Rundschau 82, 148–156.

Schoepfer, S. D., Shen, J., Wei, H., Tyson, R. V., Ingall, E., Algeo, T. J., 2015. Total organic carbon, organic phosphorus and biogenic barium fluxes as proxies for paleomarine productivity. Earth-Science Reviews 149, 23–52.

Seilacher, A., 1967. Bathymetry of trace fossils. Marine Geology 5, 413–428.

Sephton, M. A., Looy, C. V., VEefkind, R. J., Brinkhuis, H., Leeuw, J. W. D., Visscher, H., 2002. Synchronous record of $\delta^{13}C$ shifts in the oceans and atmosphere at the end of the Permian. In: Koeberl, C., MacLeod, K. G. (Eds.), Catastrophic Events and Mass Extinctions: Impacts and Beyond. Vol. 356 of Special Paper. Geological Society of America, pp. 455–462.

Shen, S., Crowley, J. L., Wang, Y., Bowring, S. A., Erwin, D. H., Sadler, P. M., qun Cao, C., Rothman, D. H., Henderson, C. M., Ramezani, J., Zhang, H., Shen, Y., dong Wang, X., Wang, W., Mu, L., zhong Li, W., gang Tang, Y., lei Liu, X., jun Liu, L., Zeng, Y., fa Jiang, Y., gan Jin, Y., 2011. Calibrating the end-Permian mass extinction. Science 334, 1367–1372.

Shen, S.-Z., Shi, G.-R., 1996. Diversity and extinction patterns of Permian brachiopods of south China. Historical Biology 12, 93–110.

Siedlecka, A., 1970. Investigations of Permian cherts and associated rocks in southern Spitsbergen. Norsk Polarinstitutt Skrifter 147, 5–86.

Smith, A. G., Briden, J. C., 1977. Mesozoic and Cenozoic paleocontinental maps. Cambridge University Press.

Smith, N. D., 1972. Flume experiments on the durability of mud clasts. Journal of Sedimentary Petrology 42 (2), 378–383.

Stanley, S. M., Yang, X., 1994. A double mass extinction at the end of the Paleozoic Era. Science 266, 1340–1344.

Stemmerik, L., 1997. Permian (Artinksian - Kazanian) Cool-Water Carbonates in North Greenland, Svalbard and the Western Barents Sea. In: James, N. P., Clarke, J. A. D. (Eds.), Cool-Water Carbonates. Vol. 56 of Special Publication. AAPG, pp. 349–364.

Stemmerik, L., Bendix-Almgreen, S. E., Piasecki, S., 2001. The Permian-Triassic boundary in central East Greenland: past and present views. Bulletin of the Geological Society of Denmark 48, 159–167.

Stensiö, E. A., 1921. Triassic fishes from Spitzbergen, part I. Vienna: Holzhausen.

Sun, Y., Joachimski, M. M., Wignall, P. B., Yan, C., Chen, Y., Jian, H., Wand, L., Lai, X., 2012. Lethally hot temperatures during the Early Triassic greenhouse. Science 338, 366–370.

Surlyk, F., Noe-Nygaard, 1986. Hummocky cross-stratification from the Lower Jurrasic Hasle Formation of Bornholm Denmark. Sedimentary Geology 46, 259–273.

Svensen, H., Planke, S., Polozov, A. G., Schmidbauer, N., Corfu, F., Podladchikov, Y. Y., Jamtveit, B., 2009. Siberian gas venting and the end-Permian environmental crisis. Earth and Planetary Science Letters 277, 490–500.

Taylor, J. M., 1950. Pore-space reduction in sandstones. AAPG Bulletin 34 (4), 701–716.

Taylor, P. D., Wilson, M. A., 2003. Palaeoecology and evolution of marine hard substrate communities. Earth-Science Reviews 62, 1–103.

Tirsgaard, H., Øxnevad, I. E. I., 1998. Preservation of pre-vegetational mixed fluvio-aeolian deposits in a humid climatic setting: an example of the Middle Proterozoic Eriksfjord Formation, southwest Greenland. Sedimentary Geology 120, 295–317.

Tissot, B. P., Pelet, R., Ungerer, P., 1987. Thermal history of sedimentary basins, maturation indices, and kinetics of oil and gas generation. AAPG Bulletin 12, 1445–1466.

Tissot, B. P., Welte, D. H., 1984. Petroleum formation and occurrence, 2nd Edition. Springer-Verlag, p. 518.

Torsvik, T., Carlos, D., Mosar, J., Cocks, R., Malme, T., 2008. Global reconstructions and North Atlantic paleogeography 440 Ma to recent. Norges Geologiske Undersøkelse.

Torsvik, T. H., Cocks, L. R. M., 2004. Earth geography from 400 to 250 Ma: a palaeomagnetic, faunal and facies review. Journal of the Geological Society 161, 555–572.

Twitchett, R. J., 1999. Palaeoenvironments and faunal recovery after the end-Permian mass extinction. Palaeogeography, Palaeoclimatology, Palaeoecology 154, 27–37.

Twitchett, R. J., Krystyn, L., Baud, A., Wheeley, J. R., Richoz, S., 2004. Rapid marine recovery after the end-Permian mass-extinction event in the absence of marine anoxia. Geology 32 (9), 805–808.

Uchman, A., Drygant, D., Paszkowski, M., Porębski, S. J., Turnau, E., 2004. Early Devonian trace fossils in marine to non-marine redbeds in Podolia, Ukraine: palaeoenvironmental implications. Palaeogeography, Palaeoclimatology, Palaeoecology 214, 67–83.

Uchman, A., Hanken, N.-M., Nielsen, J. K., Grundvåg, S.-A., Pasecki, S., In Press. Depositional environment, ichnological features and anoxicity of Permian to earliest Triassic marine sediments in central Spitsbergen, Svalbard. Polar Research.

Vigran, J., Mangerud, G., Mørk, A., Worsley, D., Hochuli, P., 2014. Palynology and geology of the Triassic succession of Svalbard and the Barents Sea. In: Special Publication 14. Geologica Survey of Norway, p. 270.

Vogt, P. R., Parrish, M., 2012. Driftwood dropstones in Middle Miocene climate optimum shallow marine strata Calvert Cliffs, Maryland coastal plain: erratic pebbles no certain proxy for cold climate. Palaeogeography, Palaeoclimatology, Palaeoecology 323-325, 100–109.

Vos, R. G., 1977. Sedimentology of an upper paleozoic river, wave and tide influenced delta system in southern Morocco. Journal of Sedimentary Petrology 47 (3), 1242–1260.

Vousdoukas, M. I., Velegrakis, A. F., Plomaritis, T. A., 2007. Beachrock occurrence, characteristics, formation beachrock occurrence, characteristics, formation mechanisms and impact. Earth-Science Reviews 85, 23–46.

Wanty, R. B., Goldhaber, M. B., 1992. Thermodynamics and kinietics of reactions involving vanadium in natural systems: accumulaton of vanadium in sedimentary rocks. Geochimica et Cosmochimica Acta 56, 1471–1483.

Waples, D. W., 1980. Time and temperature in petroleum formation: Application of Lopatin's method to petroleum exploration. AAPG Bulletin 64 (6), 916–926.

Wehrli, B., Stumm, W., 1989. Vanadyl in natural waters: Adsorption and hydrolysis promote oxygenation. Geochimica et Cosmochimica Acta 53, 69–77.

Wentworth, C. K., 1922. A scale of grade and class terms for clastic sediments. The Journal of Geology 30 (5), 377–392.

Wignall, P., Morante, R., Newton, R., 1998. The Permo-Triassic transition in Spitsbergen: $\delta^{13}C_{Org}$ chemostratigraphy, Fe and S geochemistry, facies, fauna and trace fossils. Geolgical Magazine 135, 47–62.

Wignall, P. B., 1994. Black shales. In: Oxford Monographs on Geology and Geophysics. Vol. 30. Oxford University Press, p. 127.

Wignall, P. B., Hallam, A., 1992. Anoxia as a cause of the Permian/Triassic mass extinction: facies evidence from northern Italy and the western United States. Palaeogeography, Palaeoclimatology, Palaeoecology 93, 21–46.

Wignall, P. B., Twitchett, R. J., 1996. Oceanic anoxia and the end Permian mass extinction. Science 272 (5265), 1155–1158.

Wignall, P. B., Twitchett, R. J., 2002. Extent, duration and nature of the Permian-Triassic superanoxic event. Geologic Society of America Special Paper 356, 395–413.

Williams, G. D., 1966. Origin of shale-pebble conglomerate. AAPG Bulletin 50 (3), 573–577.

Wilson, J. C., McBride, E. F., 1988. Compaction and porosity evolution of Ppliocene sandstones, Ventura Basin, California. The American Association of Petroleum Geologists Bulletin 72 (6), 664–681.

Woods, A. D., 2014. Assessing Early Triassic paleoceanographic conditions via unusual sedimentary fabrics and fatures. Earth-Science Reviews 137, 6–18.

Worsley, D., 2008. The post-Caledonian development of Svalbard and the western Barents Sea. Polar Research 27, 298–317.

Worsley, D., Johansen, R., Kristensen, S. E., 1988. The Mesozoic and Cenozoic succession of Tromsøflaket. In: Dalland, A., Worsley, D., Ofstad, K. (Eds.), A lithostratigraphic scheme for the Mesozoic and Cenozoic succession offshore mid- and northern Norway. No. 4 in Bulletin. Norwegian Petroleum Directorate, pp. 42–65.

Wright, V. P., 1992. A revised classification of limestones. Sedimentary Geology 76, 177–185.

Yang, X.-N., Shi, G.-J., Liu, J.-R., Chen, Y.-T., Zhou, J.-P., 2000. Inter-taxa differences in extinction process of Maokouan (Middle Permian) fusulinaceans. Science in China (SeriesD) 43, 633–637.

Yin, H., Feng, Q., Lai, X., Baud, A., Tong, J., 2007. The protracted Permo-Triassic crisis and multi-episode extinction around the Permian-Triassic boundary. Global and Planetary Change 55, 1–20.

Zonneveld, J.-P., Beatty, T. W., Pemberton, S. G., 2007. Lingulide brachiopods and the trace fossil lingulichnus from the Triassic of western Canada: Implications for faunal recovery after the end-Permian mass extinction. Palaios 22, 74–97.